

Nanoscopic supramolecular architectures based on Pi-conjugated oligomers

Citation for published version (APA):

Jonkheijm, P. (2005). *Nanoscopic supramolecular architectures based on Pi-conjugated oligomers*. [Phd Thesis 1 (Research TU/e / Graduation TU/e), Chemical Engineering and Chemistry]. Technische Universiteit Eindhoven. <https://doi.org/10.6100/IR591737>

DOI:

[10.6100/IR591737](https://doi.org/10.6100/IR591737)

Document status and date:

Published: 01/01/2005

Document Version:

Publisher's PDF, also known as Version of Record (includes final page, issue and volume numbers)

Please check the document version of this publication:

- A submitted manuscript is the version of the article upon submission and before peer-review. There can be important differences between the submitted version and the official published version of record. People interested in the research are advised to contact the author for the final version of the publication, or visit the DOI to the publisher's website.
- The final author version and the galley proof are versions of the publication after peer review.
- The final published version features the final layout of the paper including the volume, issue and page numbers.

[Link to publication](#)

General rights

Copyright and moral rights for the publications made accessible in the public portal are retained by the authors and/or other copyright owners and it is a condition of accessing publications that users recognise and abide by the legal requirements associated with these rights.

- Users may download and print one copy of any publication from the public portal for the purpose of private study or research.
- You may not further distribute the material or use it for any profit-making activity or commercial gain
- You may freely distribute the URL identifying the publication in the public portal.

If the publication is distributed under the terms of Article 25fa of the Dutch Copyright Act, indicated by the "Taverne" license above, please follow below link for the End User Agreement:

www.tue.nl/taverne

Take down policy

If you believe that this document breaches copyright please contact us at:

openaccess@tue.nl

providing details and we will investigate your claim.

NANOSCOPIC SUPRAMOLECULAR ARCHITECTURES

BASED ON π -CONJUGATED OLIGOMERS

PROEFSCHRIFT

ter verkrijging van de graad van doctor aan de Technische
Universiteit Eindhoven, op gezag van de Rector Magnificus,
prof.dr.ir. C. J. van Duijn, voor een commissie aangewezen door
het College voor Promoties in het openbaar te verdedigen op
maandag 20 juni 2005 om 16.00 uur

door

Pascal Jonkheijm

geboren te Hontenisse

Dit proefschrift is goedgekeurd door de promotor:

prof.dr. E.W. Meijer

Copromotor:

dr. A.P.H.J. Schenning

Druk: Universiteitsdrukkerij, Technische Universiteit Eindhoven

CIP-DATA LIBRARY TECHNISCHE UNIVERSITEIT EINDHOVEN

Jonkheijm, Pascal

Nanoscopic Supramolecular Architectures based on π -Conjugated Oligomers/ by
Pascal Jonkheijm. - Eindhoven: Technische Universiteit Eindhoven, 2005.

Proefschrift. - ISBN 90-386-2607-X

NUR 913

Trefwoorden: supramoleculaire chemie / π -geconjugeerde oligomeren ;
poly(aryleenalkenylenen) / organische halfgeleiders ; nanostructuren / aggregatie /
zelf-assemblage / waterstofbruggen / chiraliteit

Subject headings: supramolecular chemistry / π -conjugated oligomers ;
poly(arylenealkenylenes) / organic semiconductors ; nanostructures / aggregation /
self-assembly / hydrogen-bonding / chirality

De manuscriptcommissie:

prof.dr. E.W. Meijer

dr. A.P.H.J. Schenning

prof.dr. T. Swager (Massachusetts Institute of Technology)

prof.dr. W.J. Feast (University of Durham)

prof.dr.ir. R.A.J. Janssen

<i>CONTENTS IN BRIEF</i>	<i>page</i>
VOORWOORD	1
1 ABOUT SUPRAMOLECULAR ASSEMBLIES OF π-CONJUGATED SYSTEMS	3
2 SELF-ASSEMBLY OF OLIGO(P-PHENYLENEVINYLENE)S INFLUENCED BY HYDROPHILICITY	25
3 SELF-ASSEMBLY OF OLIGO(P-PHENYLENEVINYLENE)S INTO ROSETTES AND THEIR TUBULAR SELF-ASSEMBLY	41
4 COLUMNAR SELF-ASSEMBLY OF OLIGO(P-PHENYLENEVINYLENE)S HAVING QUADRUPLE HYDROGEN-BONDS	51
5 CONTROLLED DEPOSITION AT DEVICE SURFACES OF SELF-ASSEMBLED OLIGO(P-PHENYLENEVINYLENE)S	73
6 HYDROGEN-BONDED SELF-ASSEMBLY OF DONOR AND ACCEPTOR MOLECULES	87
7 CHIROPTICAL STUDIES AND MANIPULATION OF SELF-ASSEMBLED OLIGOTHIOPHENE CAPSULES	101
EXPERIMENTAL SECTION	113
REFERENCES AND NOTES	123
SUMMARY	135
SAMENVATTING	139
CURRICULUM VITAE	143

VOORWOORD

Het verschijnen van dit proefschrift schenkt mij, na een aantal jaren wetenschappelijk werk, veel voldoening. Bij deze gelegenheid zou ik willen benadrukken dat het voltooiën van het promotieonderzoek slechts gerealiseerd kon worden dankzij de directe of indirecte betrokkenheid van vele vroegere en huidige collegae. Ook de leden van de manuscriptcommissie ben ik bijzonder erkentelijk voor hun constructieve bijdrage aan dit proefschrift.

Dat ik het in dit proefschrift beschreven onderzoek kon uitvoeren in het Laboratorium Macromoleculaire en Organische Chemie (SMO) beschouw ik als een gelukkige omstandigheid. Immers, de goede sfeer op deze afdeling schept een klimaat waarin op ontspannen wijze gewerkt en samengewerkt kan worden. Niet alleen dat, maar vooral de toegang tot uitgebreide voorzieningen om op hoog wetenschappelijk niveau te kunnen experimenteren is een lust voor elke onderzoeker. Niet alleen hiervoor gaat mijn dank uit naar prof. Bert Meijer maar ook vanwege zijn motiverende en toegewijde wijze waarop hij wetenschappelijk onderzoek uitvoert. Een voortdurende stimulans is uiteraard ook dr. Albert Schenning geweest. Hem hebben als begeleider is niet eenvoudig te omvatten in een paar woorden; een boekje erover uitgeven zou beslist een bestseller worden. Ik ben ontzettend blij dat jullie mij de ruimte en vrijheid in het onderzoek hebt laten nemen gedurende de afgelopen jaren. De afgelopen jaren waren fantastisch en het was een genot om met jullie beiden te kunnen werken.

Ik heb ook het geluk gehad enige tijd in een andere onderzoeksomgeving te kunnen verblijven. Aan de universiteit in Leuven, heeft dr. André Gesquière zijn passie voor de scanning tunneling microscopy op mij overgebracht. Zijn invloed, en later ook die van dr. Atsushi Miura, hebben er voor gezorgd dat deze techniek een voorname plaats heeft gekregen in mijn onderzoek. Speciale dank gaat uit naar dr. Steven De Feyter die mij de ruimte heeft geboden om me mijn gang te laten gaan in hun desolate bunker. In de afronding van menig artikel zijn de discussies met hem en prof. Frans De Schryver zeer waardevol geweest, mijn dank daarvoor. De fijne kneepjes van een andere scanning probe techniek, AFM, heb ik tijdens mijn kort verblijf in Mons gretig afgekeken van dr. Phillipe Leclère. Many thanks and lots of succes with your research. Mons turned out to be a very pleasant place to learn new things but certainly also to relax. It was here that I met dr. Oliver Henze, a handsome young man from Germany and with dr. Natalie Stutzmann. It was interesting to see that Swiss charm is very efficiently convincing people to drink another beer in the pub. I am very happy we still chat about life every now and then over a few of those Belgian beers. To reassure the readers, Natalie performed FET measurements later when she was working at Philips for which I like to thank the continuous interest of dr. Dago de Leeuw. And Olli, I hope you are relieved that I had a look at all of your oligothiophenes after spending the many hours cooking them. In this respect, I thank with pleasure prof. Jim Feast for the very stimulating and educational collaboration. Another set of molecules was prepared by Zhijian Chen in the laboratories of prof. Frank Würthner; many thanks for the successful collaboration.

In de eerste fase van het onderzoek vonden ook de verstrooiingsexperimenten plaats waarbij Dr. Ralf Kleppinger een onmisbare schakel bleek. Ik ben zeer erkentelijk dat je me hebt geïntroduceerd in deze discipline. Een inspirerende samenwerking met dr. Paul van der Schoot heeft een grote verdieping gebracht in het begrijpen van moleculaire assemblage; mijn oprechte dank hiervoor. Tijdens een latere fase in het onderzoek, toen de fibers vanuit de

oplossing op de substraten lagen, kwamen ir. Murat Durkut en dr. Peter Hadley van de universiteit in Delft op bezoek. Helaas hebben we nooit een signaal gedetecteerd, maar ik denk dat we beiden wel veel geleerd hebben over elkaars vakgebied. Hartelijk bedankt voor de vele inspanningen en succes met de afronding met je promotie. Gedurende mijn hele AIO periode was het hoge magneetveld laboratorium in Nijmegen betrokken in het onderzoek. Ook hier leek aanvankelijk de keuze van onze moleculen geen doorslaand succes op te leveren. Onze set moleculen hebben dr. Igor Shklyarevskiy er tot gebracht zijn bril op te eten, dr. Cécile Jeukens haar minutieus inelkaar gebouwde NSOM in te ruilen voor een FM opstelling, en dr. Peter Christianen te verleiden tot beklagenswaardige opmerkingen als 'toen we nog werkten aan anorganische halfgeleiderstructuren...'. Het is echter zeker niet teveel gezegd dat dankzij jullie volhardendheid en de verfrissende kijk op onze structuren mooie resultaten zijn behaald en ik verwacht dat dit nog maar een begin is van wat er mogelijk is.

Voor aanvang van mijn AIO periode hadden dr. Emiel Peeters en dr. Ky Hirschberg de SMO-vakgroep net verlaten, maar beiden hebben een grote invloed gehad op het gemak waarmee ik mijn moleculen heb kunnen synthetiseren. Ook de synthetische 'handigheidjes' van dr. Abdelkrim El-Ghayoury en Michel Fransen zijn niet te verwaarlozen geweest. De bijdragen van ir. Freek Hoeben (de metaalfabriek voor de beste kwaliteit), drs. Jeroen van Herrikhuizen (compileert De Beste Alle 21 van elke goeie artiest behalve Dennie Christiaan), Maarten Pouderoijen (beste tapper van SMO) en ir. Pim Janssen hebben tot een grote versnelling geleid van het 'aptronics'-onderzoek; bedankt, het was een genot er deel van uit te maken. Succes met het vervolg van jullie promotie en werkzaamheden. Dank ook voor de assistentie van ir. Frank van der Meer, ir. Leandra Cornelissen, Martin Veld en Robin de Bruin. Binnen SMO bedank ik verder dr. Jeroen van Duren (jij kunt beter je Brabantse nachten kort houden) voor het karakteriseren van zonnecellen, ir. Edwin Beckers (al klagend het bejaardentehuis in) voor CV en PIA metingen, dr. Martijn Kemerink voor de altijd geïnteresseerde en helpende hand toereikende momenten in en rond de AFM en dr. Stefan Meskers voor CPL metingen. Natuurlijk ook dank aan de kamergenoten voor de betere interpretaties van de dagelijkse beslommeringen. Bijzondere dank ook voor de mensen die de SMO-machine gesmeerd laten draaien; Hans, Hannie en Henk, Joost, Lou en Ralf, en het uitdijende secretariaat; Hanneke, Joke, Carinne, Ingrid en Sagitta.

Tenslotte spreek ik mijn dank uit aan mijn ouders die mij altijd gestimuleerd hebben tot leren en studeren. En natuurlijk Dodo; ik ben dankbaar dat je mijn geraas hebt doorstaan, het komend jaar zal het omgekeerd zijn.

Pascal.

1 ABOUT SUPRAMOLECULAR ASSEMBLIES OF π -CONJUGATED SYSTEMS¹

ABSTRACT

Ever since the first demonstration of organic semiconductors in opto-electronic applications such as light emitting diodes, field effect transistors and photovoltaic cells, one characteristic feature of these materials received continuous attention; namely the effect of the structure and organization of the functional components on the performance of the device. The lack of control over the organization going from π -conjugated molecules to macroscopic materials hampers the performance of these materials in devices. In this Chapter, an overview is given of the supramolecular organization of π -conjugated oligomers with a strong focus on the important interactions involved in their nanoscopic structural arrangement. Challenged by the required control over dimensions and shape of the supramolecular architectures, the area of supramolecular electronics is introduced. With this new area of supramolecular electronics as a target, the aim and scope of the thesis are formulated.

CONTENTS IN BRIEF

	<i>page</i>
1.1 <i>Supramolecular Assemblies based on π-Conjugated Systems inspired by Nature</i>	4
1.1.1 <i>Self-Assembly Principles of π-Conjugated Systems</i>	5
1.1.2 <i>Polymers versus Oligomers</i>	6
1.2 <i>Self-Assembly of Block-copolymers</i>	7
1.2.1 <i>Monodisperse π-Conjugated Blocks in the Main chain</i>	7
1.2.2 <i>Monodisperse π-Conjugated Blocks in the Side chain</i>	10
1.3 <i>Supramolecular Organization of π-Conjugated Oligomers</i>	11
1.3.1 <i>Self-Assembly of Liquid Crystalline Molecules</i>	11
1.3.1.1 <i>Thermotropic Rod-like Molecules</i>	12
1.3.1.2 <i>Thermotropic Discotic Molecules</i>	13
1.3.1.3 <i>Lyotropic Liquid Crystals</i>	16
1.3.2 <i>Self-Assembly by Specific Interactions in Solution</i>	19
1.3.2.1 <i>Assembly by π-π Interactions</i>	19
1.3.2.2 <i>Assembly by Amphiphilic Interactions</i>	20
1.3.2.3 <i>Assembly by Hydrogen-bonding Interactions</i>	21
1.4 <i>Aim of the Thesis</i>	23
1.5 <i>Outline of the Thesis</i>	23
1.6 <i>Selected Publications</i>	24

¹ For a complete review of 'Supramolecular Assemblies based on π -Conjugated Systems', you are referred to Hoeben, F. J. M.; Jonkheijm, P.; Meijer, E. W.; Schenning, A. P. H. J. *Chem. Rev.* **2005**, *105*, 1491-1546.

1.1 SUPRAMOLECULAR ASSEMBLIES BASED ON π -CONJUGATED SYSTEMS INSPIRED BY NATURE

The fundamental building principle for biological materials is the assembly of a variety of molecular building blocks through non-covalent interactions forming well-defined supramolecular structures. The appeal that nature holds, lies in the fact that the information at the molecular level guides organization at the supramolecular level via a hierarchy of assembly steps. Making use of supramolecular interactions is a challenging task in developing π -conjugated functional materials. Knowing the limitations involved in ordering π -conjugated systems at different length scales will surely hasten the development of future applications, supramolecular electronics being the most prominent.¹ The construction of supramolecular assemblies of π -conjugated systems in the 5 to 100 nm regime provides an excellent tool to construct organized electronic components in the nanometer range. Supramolecular electronics narrows the gap between molecular electronics and bulk, 'plastic', electronics (Figure 1.1). The latter is well established resulting in commercially available polymer-based light-emitting diodes. In the field of molecular electronics, properties of single molecules are investigated at the Ångstrom length scale and simple device structures have been demonstrated.²⁻⁴ However, applications of single molecule devices remain hampered by orientational and conformational motion of the molecule as well as contact problems at the molecule-electrode interface.

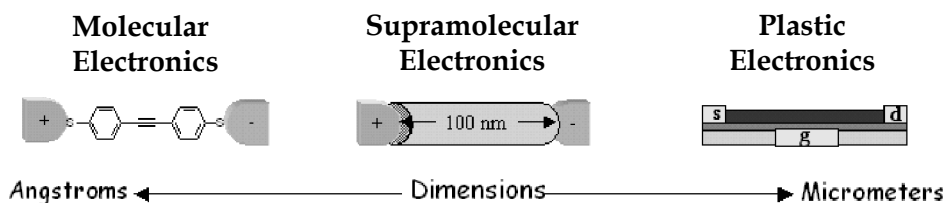


Figure 1.1: Schematic representation illustrating the dimensional gap between molecular electronics, where single molecules are studied, and plastic electronics, which relies on bulk properties of π -conjugated polymers. Supramolecular electronics aims at an intermediate length scale, searching for self-assembled architectures of about 100 nm long and 5 nm in diameter.

Self-assembly is an attractive and efficient bottom-up strategy governing thermodynamic control which aims to position well-defined shape-persistent objects at predefined locations. Limitations in bulk materials can arise by connecting well-ordered domains with the size range of about 100 nm. Single molecules, in comparison, possessing a size of 1 to 5 nm, have limitations in shape selectivity. It is proposed that self-assembled structures with the dimensions of 5 to 100 nanometers are ideal components for creating supramolecular opto-electronic devices. They would combine the smallest dimensions with well-ordered organization in the object. Bottom-up approaches have been reported for inorganic nanowires⁵⁻⁷ and carbon nanotubes^{8,9} and both show promising electrical characteristics.

For electronic devices made from π -conjugated systems the intrachain electronic coupling will determine the device performance, which has steadily improved as synthetic chemists have gained more control over chemical structure¹⁰ and purity¹¹⁻¹⁸ of the π -conjugated materials. The dependence of properties with control over structure, purity and organization is not unique for semiconducting materials but is also valid for functional polymers in general. However, the importance of control at every point in the assembly

process is crucial in determining the overall semiconducting polymer properties. For example, charge transfer between chains is required for conduction in a well-ordered or mesoscopic phase.¹⁹⁻²⁴ To arrive at controlled microcrystallinity, it is often necessary to have solubilizing side chains on the π -conjugated material. These side chains while useful at the mesoscopic level for microcrystallization, are sometimes detrimental to macroscopic ordering.²⁵⁻³⁰ It is evident that materials research in the area of semiconducting polymers requires macromolecular engineering by organic synthesis combined with investigations aimed at control of molecular architecture at all levels of organization (Figure 1.2). Only in that way can control over all length scales in the organic electronic device be achieved.

Tremendous progress in controlling the morphology of the active layer has been realized through variations in processing conditions³¹ of the conjugated polymeric materials. This has been accomplished by the introduction of alignment layers,^{32,33} or through thermal³⁴⁻³⁷ and mechanical³⁸ treatments. Nonetheless, most polymeric films are highly amorphous and inhomogeneous; for example, small domains of 15 to 30 nm are observed for polyfluorenes³⁹, while for polypyridylvinylene⁴⁰, polythiophenes⁴¹ and poly-p-phenylenevinylene⁴² partially aligned regions of the film with dimensions of typically 200 to 300 nm are found. However, device structures are roughly in the micrometer range. Therefore, additional techniques to control the morphology of the active layers are necessary to improve performance.

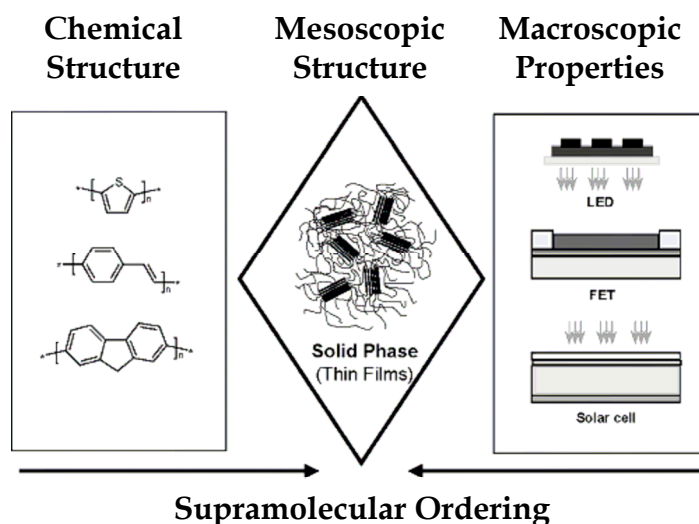


Figure 1.2: Schematic representation of how the properties of opto-electronic devices such as light emitting diodes (LEDs), field effect transistors (FETs) and solar cells are related to chemical structure and supramolecular organization. Chemists and material scientists have aimed for control of supramolecular organization of π -conjugated polymers by using chemical modification or various processing conditions.

1.1.1 Self-Assembly Principles of π -Conjugated Systems

The strongest interactions within π -conjugated systems are covalent bonds formed directly between two atoms. They are very stable, stiff, highly directional, and dissociation of e.g. carbon-carbon bonds needs normally about 350 kJ/mol. However, non-covalent bonds, formed between different parts of the same molecule or connecting different molecules, play a major role in determining both the three-dimensional structure of molecular chains and how these structures interact with one another. A variety of non-covalent bonds exist: ionic bonds (300–800 kJ/mol), ion-dipole (50–200 kJ/mol), hydrogen-bonds (4–120 kJ/mol), dipole-dipole (4–40 kJ/mol), π - π stacking (1–20 kJ/mol) and van der Waals (dispersion)

attractions (1–10 kJ/mol). Another important weak force is created by the solvent. Of course, a single non-covalent bond – unlike a single covalent bond – is too weak to withstand the thermal motions that keep molecules apart, however, they are strong enough to provide tight binding when many of them are formed simultaneously and act collaboratively.

Two important secondary interactions in the design of supramolecular π -conjugated materials, described in this thesis, are π - π and hydrogen-bond interactions. Logically, π - π interactions often exist in π -conjugated systems. The strength as well as the causes of these interactions, however, varies considerably. In water, the stacking interaction between aromatic molecules is mainly caused by the hydrophobic effect. Water molecules solvating the aromatic surface have a higher energy than bulk water resulting in stacking of the aromatic surfaces, which reduces the total surface exposed to the solvent. In solvents other than water, the interactions between solvent molecules are weaker and therefore solvophobic forces play a minor role.

Hydrogen-bonds are ideal secondary interactions to construct supramolecular architectures since they are highly selective and directional. In nature, beautiful examples of these effects are present in DNA and proteins. Hydrogen-bonds are formed when a donor with an available acidic hydrogen atom interacts with an acceptor carrying available non-bonding electron lone pairs. The strength depends largely on the solvent, number and sequence of the hydrogen-bonds.^{43,44}

1.1.2 Polymers versus Oligomers

π -Conjugated systems having a base structure of alternating single and double/triple bonds can roughly be divided into oligomers and polymers. Due to the viscosity of polymer solutions, π -conjugated polymers can be processed from solution and therefore offer low-cost manufacture. The processing conditions of the polymers dictates the film morphology and interchain interactions. These both features are difficult to tune and, moreover, small defects in the polymer backbone can have a negative influence on the performance of opto-electronic devices.

Opto-electronic devices can also be constructed from small molecules, *i.e.*

π -conjugated oligomers. Synthetic procedures to produce monodisperse π -conjugated oligomers have considerably improved during the past decades.^{45,46} The ability to vacuum evaporate these oligomers results in crystalline films and mobilities are generally 1 order of magnitude higher than those observed in solution processed materials.^{20,47-52} However, especially for large area electronics, solution processing is preferred since vacuum deposition techniques are more expensive.

Exciting results have been obtained in plastic electronic devices based on polymers and small organic molecules; however, it remains a challenge to create materials that will give highly ordered thin layers by less expensive means. An attractive approach would be applying

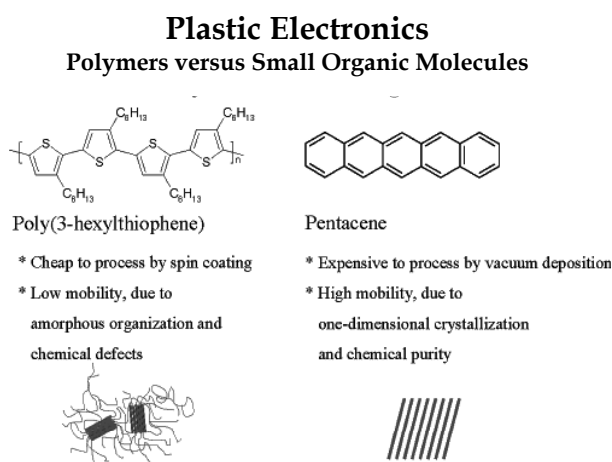


Figure 1.3: Advantages and disadvantages of π -conjugated polymers compared to those of small molecules.

the principles of supramolecular self-assembly to organize π -conjugated oligomers into well-defined supramolecular structures through programmed information inserted in the molecule.

This introductory Chapter will briefly sketch the areas of supramolecular assembly, based on monodisperse π -conjugated oligomers, in relation to their ability to create nanoscopic architectures using secondary interactions since this is the topic of this thesis. For a description of the rich area of the self-assembly of polydisperse π -conjugated systems, the reader is referred to the review that forms the basis of this Chapter (see page 3).

1.2 SELF-ASSEMBLY OF BLOCK-COPOLYMERS

As an alternative to physical blending of polymers it is synthetically possible to link oligomeric conjugated building blocks to other blocks that are able to enhance the positioning of the conjugated blocks in the active layer and improve the mechanical and processing properties. The block-copolymer approach can display phase separation, and therefore, a rich variety of nanoscopic organizations can be realized ranging from lamellar, spherical, and cylindrical to vesicular morphologies. This Section surveys two classes of block-copolymers; namely those having the π -conjugated oligomeric block in the main chain (Section 1.2.1) and those having them as a side chain (Section 1.2.2).

1.2.1 Monodisperse π -Conjugated Blocks in the Main chain

One of the first examples in this class of block-copolymers was provided by Miller *et al.*, who have prepared block-copolymers **1**, having bis-, quarter- or octathiophenes alternating with a polyester chain^{53,54} and Jenekhe *et al.*⁵⁵ connected terthiophenes **2** via single carbon atoms carrying an alkyl group. Leclerc *et al.* prepared block-copolymers having a range of well-defined oligothiophene blocks and polyester chains (**3–6**). The polyester with pentathiophene segments showed the highest conductivity of this set, 0.4 S/cm, due to favorable π -stacking.⁵⁶ The behavior of oligothiophenes alternating with polyethyleneoxide (PEO) blocks ($M_n = 2000, 1000$ and 600) (**11–13**) was studied by Feast *et al.*⁵⁷ Aggregation of the oligothiophenes occurs in dioxane-water mixtures, which was manifested by a blue shift of the absorption maximum and quenching of the emission. An oligothiophene length of three

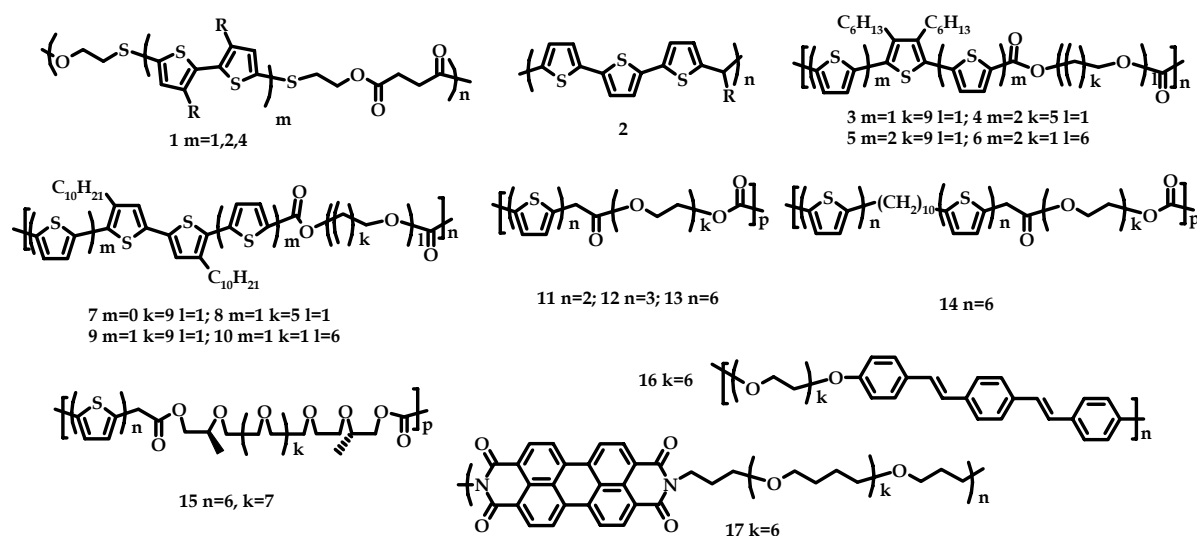


Figure 1.4: Amphiphilic block-copolymers containing monodisperse π -conjugated blocks. (only the indices of rod- and coil-segments that are monodisperse are specified as k, l, m, n, p, q)

thiophenes was necessary to observe aggregation.⁵⁸ When a sexithiophene is alternated with chiral undeca(ethyleneoxy) blocks (**15**), aggregation also occurs in dioxane. However, no helicity was found in this aggregate, in contrast with the monodisperse chiral monomeric unit (**85**, *vide infra*). This illustrates, that although the processability and mechanical robustness of block-copolymers may be superior to those of analogous oligomers, the degree of order found in oligomer-based systems may be lost in alternating polymers.⁵⁹ Oligo(ethyleneoxide)s can also be used in alternation with distyrylbenzene units (**16**) providing efficient light emitting diodes, presumably by efficient ion conducting pathways.^{60,61} Polymers consisting of alternating perylenebisimide (PBI) chromophores and flexible polytetrahydrofuran (PTHF) segments of different length (**17**) have been studied using several spectroscopic techniques. In poor solvents, the chromophores self-organize into H-type aggregates (face-to-face stacking), a process which could be enhanced by shortening the flexible spacer.^{62,63}

Yu *et al.* reported the synthesis of a polystyrene (PS)-nonathiophene diblock-copolymer (**18**) without specifying phase separation.⁶⁴ Hempenius *et al.* have made a triblock-copolymer of PS-undecathiophene-PS (**19**, polydispersity 1.1) and phase separation was observed in films cast from a poor solvent. Transmission electron microscopy (TEM) and atomic force microscopy (AFM) show that the cast copolymer is self-assembled into irregular, spherical, micellar structures having an average diameter of 12 nm (Figure 1.5). This value corresponds to about 60 block-copolymer molecules per aggregate. The optical properties are in agreement with aggregated unsubstituted oligothiophenes. Electrochemical doping was hampered by the PS shell, however, chemical doping afforded small nanoscopic charged aggregates that were soluble in organic solvents.⁶⁵

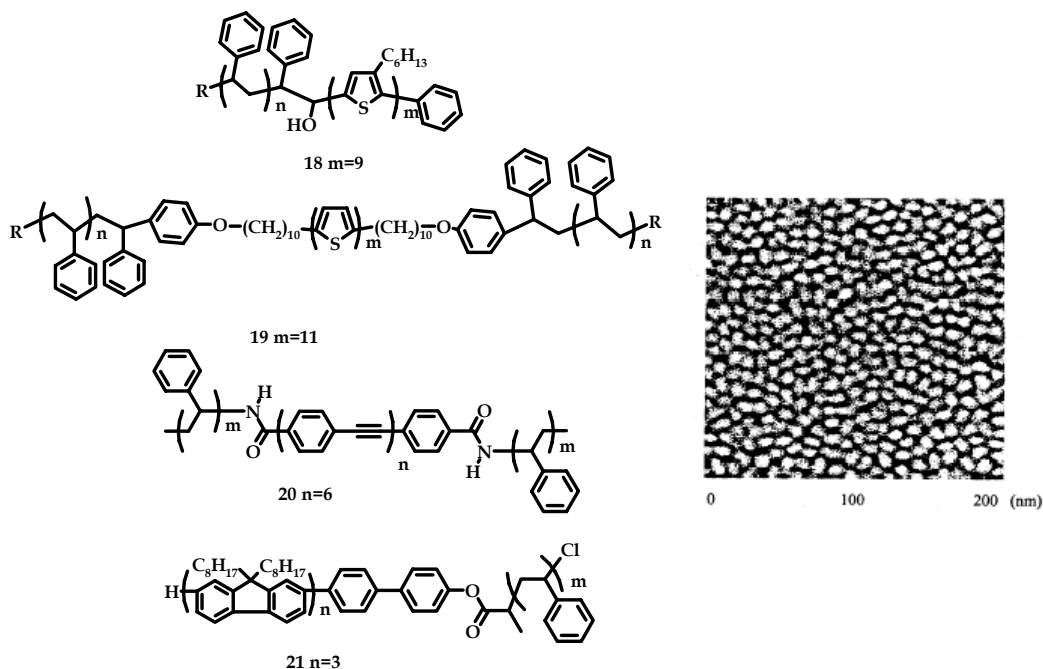


Figure 1.5: Various di- and triblock-copolymer of PS and π -conjugated oligomeric blocks. AFM image shows that phase separation into micellar aggregates occurs in films of **19** cast from a poor solvent.

The triblock-copolymer approach has been expanded to other π -conjugated blocks such as oligo(p-phenylenethynylene) **20** and phase separation was observed in films cast from poor solvents.^{66,67} In the case of oligofluorene-PS block-copolymer **21**, nanofibrillar morphologies were obtained. The polymers can be applied in light emitting diodes (LEDs) giving stable blue emission.⁶⁸

A more systematic study of the phase separation behavior in this class of block-copolymers is reported by Stupp *et al.* who made and characterized the set of triblock rod-coil molecules **22–26**. These block-copolymers consist of diblock coil segments of PS and polyisoprene (PiP), with oligo(*p*-phenylenevinylene)s (OPVs) as the rod segments. Based on TEM and X-ray diffraction data, it was shown that **23–26** formed self-organized nanostructures in films (Figure 1.6), whereas films of **22** lacked any order, showing that π -aggregation of OPV units is not the only or not always the dominant factor in the self-assembly process.

Furthermore, the regularity of the nanostructures depends on the rod:coil volume fraction. If the diblock coil segments are still solvated during rod-block crystallization, the steric effects of the coil segments will be relatively larger leading to the stabilization of smaller nanostructures. Long range order was disrupted in samples derived from structures **25** and **26**, resulting in polydisperse nanostructures, in contrast to samples from **24**, where a regular strip morphology was observed. The latter may be the result of a more favorable enthalpy of aggregation for OPV rod segments in **24** relative to those in **25** and **26**. The supramolecular strips arranged further into anti-parallel sheets. Absorption and emission spectra showed strong photoluminescence facilitated by the herringbone packing of the chromophores.^{69,70} The self-assembled macroscopic material **25** is polar and the authors showed films with piezoelectric activity.⁷¹

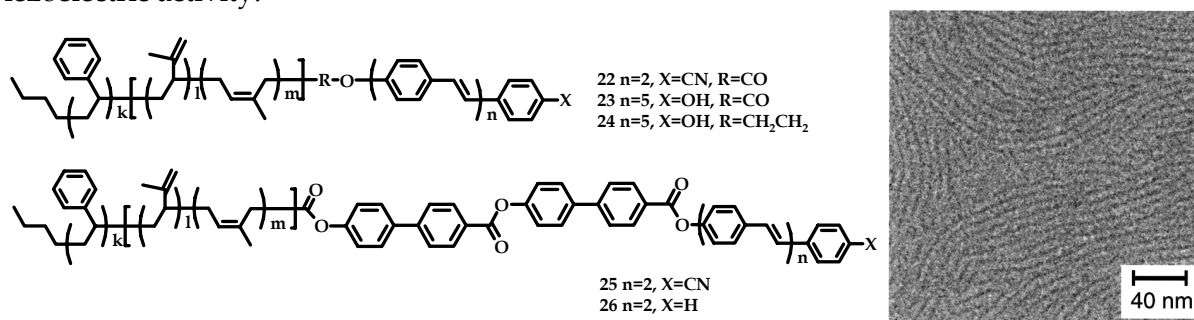


Figure 1.6: Rod-coil triblock-copolymers **22–26** containing OPV units. TEM micrograph of a sample of **24** reveals the formation of strips with nanoscale dimensions. The strips are about 8 nm in width and approximately 80 nm in length, and rod segments are perpendicular to the plane of the micrograph.

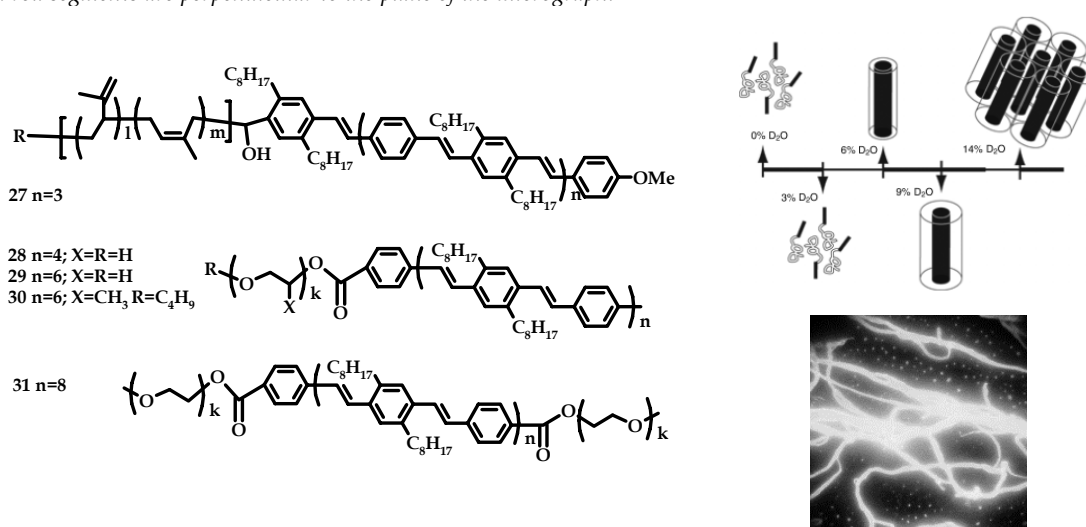


Figure 1.7: Schematic representation of the self-assembly of block-copolymers **27–31** in aqueous solution and fluorescence micrograph of **30** with long PPO blocks.

The influence of the nature of the coil on the phase behavior in these systems was studied in further detail by Yu *et al.* in rod-coil molecules **27–31** consisting of a monodisperse OPV block⁷² and a coil segment of varying length of PEO, poly(propylene oxide) (PPO)^{73–75} and PiP⁷⁶. All block-copolymers showed a polydispersity of less than 1.1. Small angle neutron scattering (SANS) data for the copolymers based on PEO or PPO in water revealed a strong tendency to self-assemble into cylindrical micelles in which the cylindrical OPV core is surrounded by the PEO or PPO corona. In the case of the PiP based polymer, a layered phase of alternated PiP and OPV was observed. In addition, the semi-flexible character of PiP blocks dramatically decreases the processability of the molecule. In the case of the hydrophilic blocks, the supramolecular structure could be manipulated by changing the ratio of poor (water) to good (THF) solvent. Stable and ordered cylinders are formed in the case of long PPO coil segments (Figure 1.7). At higher ratios of poor solvent, initial swelling of the corona occurs, followed by aggregation among the cylinders into a hexagonal close packing. This phase is stable upon further increasing the amount of poor solvent. In the case of the PEO based systems, however, regular and interwoven fibers of micrometers long with diameters around 10 nm were observed.

1.2.2 Monodisperse π -Conjugated Blocks in the Side chain

Another approach to create block-copolymers is to introduce pendant conjugated oligomers onto non-conjugated polymer backbones. It was expected that these polymers would form films that would exhibit unique properties characteristic of the pendant oligomers. Shirota *et al.* studied the correlation between the length of pendant oligothiophenes and the electrical properties of the resulting methacrylate polymers (**32**, **33**).^{77–79} The electrical conductivity of films of these polymers increased with increasing conjugation length of the oligothiophene segment. Furthermore, films made from polymers having longer oligothiophene segments exhibited a reversible color change upon doping which could be of interest for applications in the field of electrochromic materials. By substituting the pendant oligomers with other structures, *e.g.* PBI,⁸⁰ the emission could be tuned. Soluble polyacetylenes with dangling terfluorene (**34**)⁸¹ and tetra(*p*-phenylenevinylene) (**35**) units have also been prepared. The latter system could be applied in a photovoltaic devices when blended with a C₆₀ derivative.⁸²

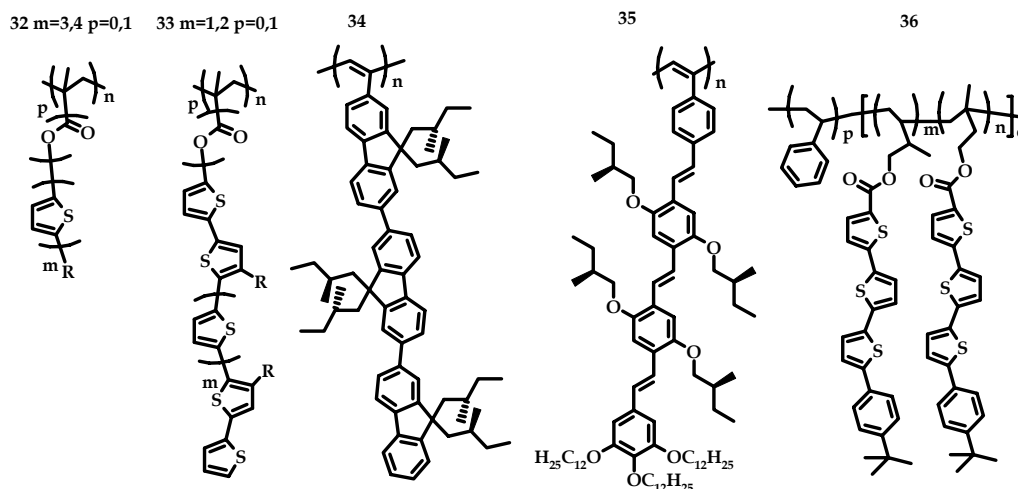


Figure 1.8: Graft copolymers with pendant π -conjugated oligomers. The schematic self-assembly of **36** is displayed on the next page in Figure 1.9.

The full potential of pendant oligomers to construct functional organized materials was recently shown by Hayakawa *et al.* who created extremely regular hierarchical structures from low polydispersity copolymers of coiled PS blocks with semi-rod PiP segments bearing terthiophene side chains (**36**, Figure 1.9). Self-organization at three different length scales occurred in films cast from CS₂, Figure 1.9a). Scanning electron microscopy (SEM) and polarized optical microscopy images showed single layers of hexagonally packed micropores (b) with a narrow size distribution; the pores being 1.5 μm in diameter and having walls as thin as 100 nm. A sulfur-distribution TEM image of films cross sections indicated a 50 nm spacing of lamellar layers (c) of PS and PiP blocks perpendicular to the substrate. DSC and X-ray data showed characteristics of a liquid crystalline smectic mesophase of the π-stacked oligothiophene blocks (d). Annealing changed the direction of the cylinders from perpendicular to parallel at the bottom of the film, while the upper side of the film remained the same. The depth of the pores could be adjusted by the annealing conditions and their diameter by the polymer concentration.⁸³

1.3 SUPRAMOLECULAR ORGANIZATION OF π-CONJUGATED OLIGOMERS

This Section surveys the tools that are available to organize oligomers by self-assembly. The first part (Section 1.3.1) deals with the self-assembly of liquid crystalline oligomers in the bulk, and the second part (Section 1.3.2) covers the influence of different supramolecular interactions on the self-assembled structures of oligomers in solution.

1.3.1 Self-Assembly of Liquid Crystalline Molecules

Liquid crystalline molecules combine the properties of mobile liquids and the orientational order of crystals. The mesophases and the temperatures at which they exist reflect the internal organization of liquid crystals. Different degrees of orientational order arise from the relative anisotropy of the molecules, which can be controlled by varying the size of the rigid segment and the nature of any side chains. Liquid crystals may be thermotropic (rod-like: Section 1.3.1.1; discotic: Section 1.3.1.2), being a state of matter in between the solid and the liquid phase, or they may be lyotropic (Section 1.3.1.3), that is when ordering is induced by the solvent. In the latter case, the solvent usually solvates a certain part of the molecule while the other part of the molecule helps aggregation, leading to mesoscopic assemblies.

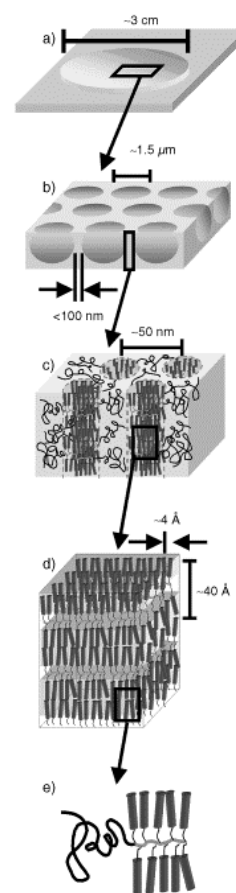


Figure 1.9: Schematic drawing of hierarchical self-assembly of rod-coil **36**.

1.3.1.1 Thermotropic Rod-like Molecules

In the field of opto-electronic applications it is important to have access to films that are cheap and easy to produce without forfeiting the high charge carrier mobilities that are common in crystal structures obtained via vacuum deposition. Charge transport in smectic systems is generally considered to be two-dimensional. A highly ordered smectic phase formed by a terthiophene derivative **37** showed a charge carrier mobility (μ) of $0.01 \text{ cm}^2/\text{Vs}$.⁸⁴ End-substitution of quarter- and sexithiophene **38–46** with varying alkyl chain lengths leads to highly soluble conjugated oligomers, which exhibits smectic mesophases that shift to higher temperatures.^{85–88} This result was interpreted by a model involving alkyl chain movements, yielding shrinkage in spacing, whereas the thiophene units remained face-to-face at typical van der Waals distances. The liquid crystal formed by **44** resulted in a charge carrier mobility of $0.03 \text{ cm}^2/\text{Vs}$. The electron-diffraction pattern of the crystals indicated two-dimensional side-by-side and end-to-end packing of the molecules (Figure 1.10).⁸⁹ However, when oxygen substituents were introduced in **47** the mobilities deteriorated. Asymmetric substitution of the oligothiophene **48** also allowed a smectic phase to be formed. Photocurrent measurements showed a high hole mobility of $0.1 \text{ cm}^2/\text{Vs}$ in this mesophase and this value is comparable to those reported for discotic columnar phases (*vide infra*). Smectic phases can be stabilized by additional hydrogen-bonding as shown by naphthalene,⁹⁰ triphenylene^{91,92} and terthiophene⁹³ derivatives bearing either carboxylic acids, carboxamides or oxyethylenes. Long-range order in OPVs was studied as a function of the conjugation length (**49**), it was found that only strong π - π interactions in the longest oligomer could cause phase separation from the tridodecyl chains.^{94,95} Columnar order in OPVs was also reached using hydrogen-bonded dimers between carboxylic acids aided by strong phase separation of the tridodecyloxyphenyl groups (**50, 51**).⁹⁶ Also dimerization of OPVs by coordination (**52**), ionic and fluorophilic interactions have led to discrete liquid crystalline supramolecular structures that further organize into columnar mesophases.⁹⁷

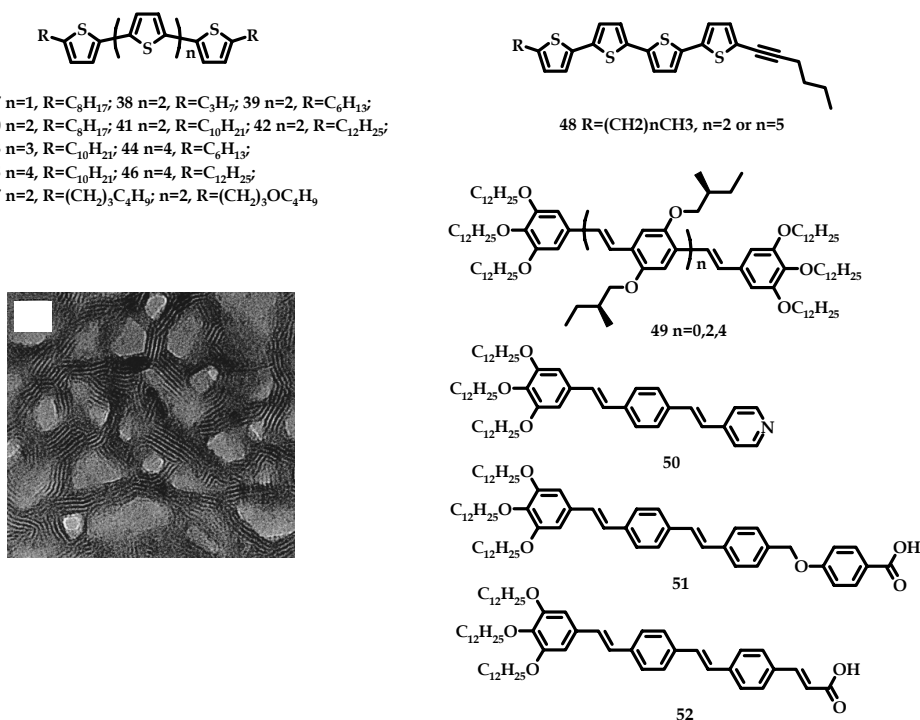


Figure 1.10: Various rod-like π -conjugated oligomers. The TEM image of a film of **44** shows a network morphology of interconnected crystals with random orientations and lattice fringes having a periodicity of 3.6 nm , consistent with the thickness of end-to-end molecular layers.

1.3.1.2 Thermotropic Discotic Molecules

Whereas rod-like molecules predominantly form smectic phases, discotic molecules preferably form columnar mesophases. Since the first discotic liquid crystal was discovered in 1977,⁹⁸ a phenylene derivative that exhibited a columnar mesophase, structural factors that influence the short-range intracolumnar order and long-range intercolumnar order have been studied intensively by varying the substituents on the core. Columnar stacking was also observed by Chandrasekhar *et al.*, however their mesophase (N_{col}) lacked a 2D lattice structure in contrast with the one found by Destrade *et al.*⁹⁹⁻¹⁰¹ The exchange of the oxygens for sulfur atoms in the side chains resulted ultimately in two mesophases with intracolumnar liquid order, Col_{hd} , and intracolumnar fixed order, Col_{ho} . The latter being hexagonal arrays of columns with a periodic, positional and helical columnar order due to the steric bulk of the sulfur atoms limiting the rotation of discs but preserving π - π interactions. The effects of the different degrees of order on the photoconduction was shown by Haarer *et al.*, who injected charges into discotic liquid crystals sandwiched between transparent conducting electrodes (Figure 1.11).

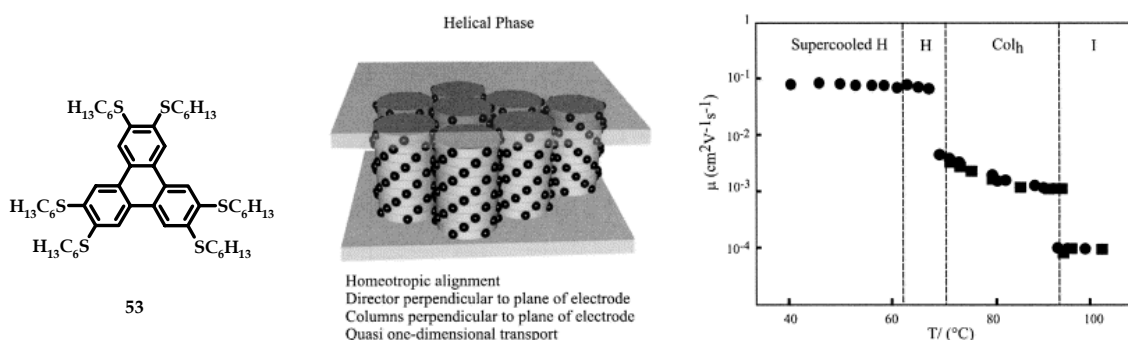


Figure 1.11: Schematic representation of the helical phase formed by triphenylene **53** and its orientation with respect to the electrode surface (middle). Variation of TOF charge carrier mobility as function of temperature for **53** (right, H corresponds to Col_{ho} and Col_h to Col_{hd}).

The transient time-of-flight (TOF) measurement for **53** showed increasing charge carrier mobilities with decreasing temperature in the Col_{hd} phase, which correlates with the increase in short-range interactions. A two orders of magnitude jump in the charge carrier mobility up to 0.1 cm^2/Vs was observed around the transition to the Col_{ho} phase.¹⁰² The high mobility and the time dependence of the currents were taken as evidence of an efficient short-range transport mechanism provided by the face-to-face stacking of the triphenylene units. Moreover, these values are representative of the bulk sample conductivity, since they

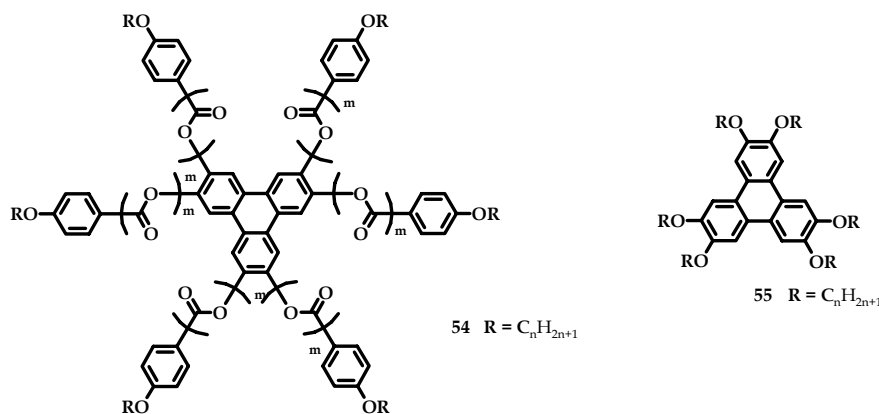


Figure 1.12: Various triphenylene derivatives.

correspond well with high-frequency time-resolved microwave conduction studies (TRMC).¹⁰³ It was found on cooling further into the glassy matrix, that the high mobilities were maintained but defects were locked in causing a significant number of traps.

The thermodynamic stability of the columnar mesophase can be increased by introducing additional aromatic interactions (**54**, **56**) giving rise to similar high mobilities at room temperature.¹⁰⁴⁻¹⁰⁸ The charge carrier mobility is determined by the extent of electronic overlap between the triphenylene cores.¹⁰⁸⁻¹¹⁰ Short side chains (**55** ($n = 3$), 10^{-2} cm²/Vs) allow for better interaction of the cores resulting in higher mobilities in comparison with long side chains (**55** ($n = 11$), 10^{-4} cm²/Vs).¹¹¹ Not only the size of the peripheral side chains, but also the nature of the aromatic core affects the charge carrier mobility.

Larger aryl cores, such as hexabenzocoronenes (HBC, **56–58**), give rise to both higher mobilities (0.7 cm²/Vs)^{103,112-114} due to the large overlap integral between the aromatic rings and more efficient charge injection due to the low band gap as pioneered by Müllen *et al.*¹¹⁵ The larger aryl cores also widen the mesophase temperature range. The phase transition temperatures can be engineered by control of the length, the degree of branching and aromaticity of the side chains.¹¹⁶⁻¹¹⁸

The HBC molecules can be processed from the melt or from solution into columns of high persistence length. However, macroscopically, the films contain isotropically distributed columns yielding numerous grain boundaries. Solid state NMR studies revealed that the HBC discs can rotate uniaxially within the columns and mobility gradients along the alkyl chains can exist,¹¹⁹ thereby allowing the dynamic nature of liquid crystals to self-repair defects on the mesoscopic scale. A variety of methods for inducing macroscopically uniform films were studied.

Annealing at the isotropic transition temperature can induce reorientation in films.¹²⁰ When HBC molecules are deposited in the source-drain channel of organic transistors coated with alignment layers of rubbed teflon, micrometer long columns between source and drain generate charge mobilities of 10^{-3} cm²/Vs.^{121,122} X-ray diffraction studies confirmed that the columnar stacks were indeed oriented parallel to the underlying teflon chains. The charge carrier mobility is lower than measured by TRMC, indicating polycrystallinity. In a LED configuration, it was shown that the onset of the current decreases in homeotropically aligned columns.

Uniaxially aligned thin films of HBCs could also be prepared by a simple solution zone-casting method as developed by Müllen *et al.* (Figure 1.13). Deposition of a solution of **56** from a stationary nozzle onto a moving substrate produces concentration and temperature gradients, dictating uniaxial columnar growth driven by π -stacking interactions. AFM together with X-ray diffraction data reveal large uniform domains with slight columnar defects presumably caused by the folding of columns during final evaporation.¹²³

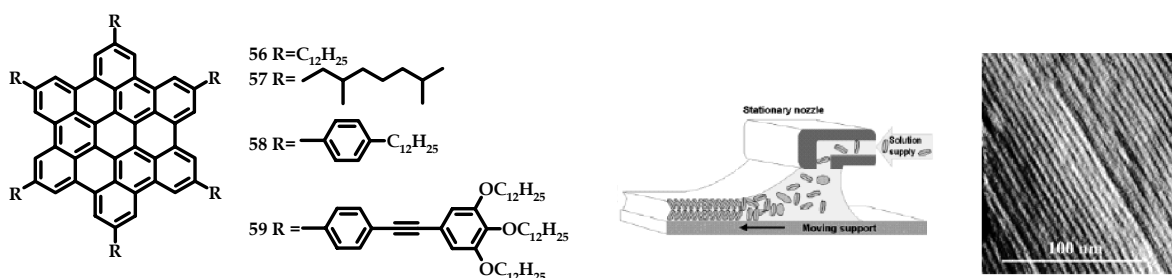


Figure 1.13: HBC derivatives **56–59**. A zone-casting process was developed for controlled deposition of columns of **56** producing a nanofibrillar morphology.

The additional aromatic interactions in **59** and the out-of-plane orientation of the peripheral phenyl rings induces a helical orientation of the HBC cores giving a helical crystalline phase with a high persistence length.¹²⁴ Spin cast films revealed arrays of uniform parallel nanoribbons with lengths of 300 nm as studied by AFM. Slow evaporation of the solvent resulted in long, isolated regular ribbons of 3.8 nm in height and 21 nm in width representing parallel single columns with the columnar axis oriented parallel to the substrate.¹²⁵ The increased tendency to spontaneously aggregate is supported by the red shifted solution emission spectra compared to the alkyl-substituted HBC **56**.

Most columnar liquid crystals are electron rich aromatic systems that are good hole-transporters; *i.e.* p-type materials. Electron poor aromatic systems are required for electron-transporters; *i.e.* n-type materials (**60**). Such compounds are obtained when coronene derivatives were functionalized with carboximide groups. These compounds give rise to mesophases depending on the substitution pattern (**61–64**).^{126–130} Coronenemonoimides (**61**) showed a large intracolumnar electron charge carrier mobility of 0.2 cm²/Vs with room-temperature liquid crystallinity.¹³¹ Related compounds such as alkyl substituted naphthalenes (**65**) and PBIs (**66**) also formed columnar mesophases^{132–135} with similar high

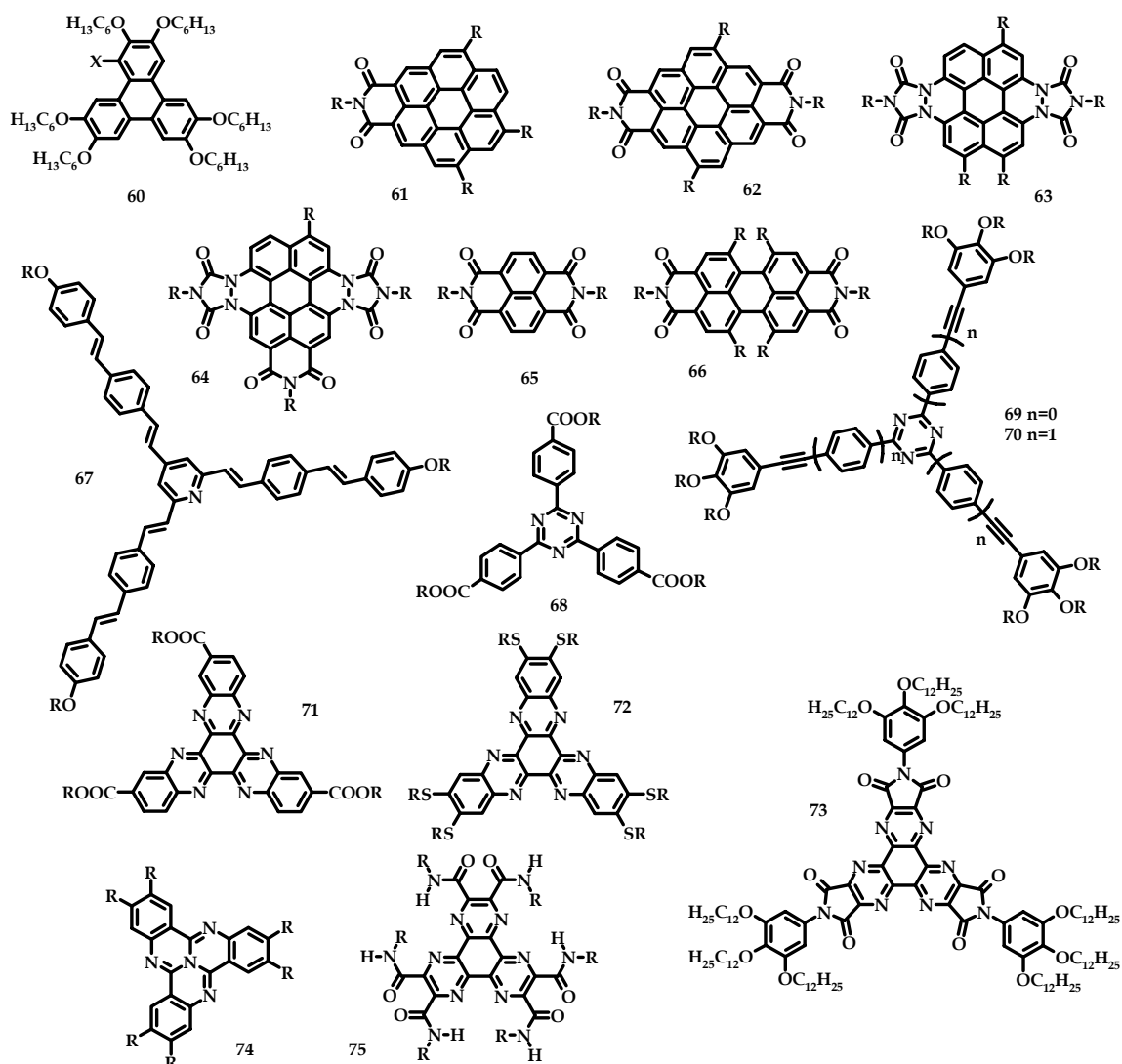


Figure 1.14: Several general chemical structures of n-type liquid-crystalline materials bearing electron-withdrawing substituents or with electron-deficient cores.

The synthesis of asymmetric HBC derivatives^{160,161} allows the creation of amphiphilic HBCs. Depending on the applied pressure, these amphiphiles can be organized in Langmuir layers resulting in two different packing arrangements. Under low pressure well-ordered, π -stacked lamellae of HBC **76** were observed.¹⁶² The thickness of the first layer can be controlled by the ionic interactions between the carboxylate HBC derivative and polyethylene imine anchored on a silicon oxide wafer (Figure 1.15).^{163,164} Polarized absorption confirmed the orientation of the columns with their main axis parallel to the dipping direction. In another experiment, the complexation of the carboxylate functionalized HBC with an aminoethyl-proline functionalized poly(dimethylsiloxane) results in a polymeric complex (**77**), which forms highly ordered discotic columnar structures. The polymeric nanostructures, which contain three incompatible elements, *i.e.* aromatic cores embedded in a matrix of alkyl chains which itself is embedded in a matrix of polysiloxane, have lengths of at least 200 nm (see TEM image Figure 1.15). The columns show two different degrees of internal order; low order was found when HBC cores were tilted with respect to the column axis and higher order when HBCs were oriented perpendicularly to the column axis.¹⁶⁵ Since polyelectrolytes can be deposited in a controlled way, this approach of ionic self-assembly can tremendously aid the orientation and positioning on a surface.¹⁶⁶

Another approach to direct the morphology of the liquid crystalline film is using organogelators (Figure 1.16). Oriented columns of triphenylene derivative **55** are formed when **55** was mixed with a gelator cooled from the isotropic liquid states. The different phases of the mixture determines the size of the domains. Phase separation occurs after the triphenylene enters the liquid crystalline state upon cooling and the aggregates of the gelator develop in the boundary of the liquid crystalline domains because this mesophase and the isotropic liquid phase are immiscible. In this way, uniform domain sizes of approximately 30 μm are obtained. If the phase sequence is reversed, the gelator forms aggregates in the isotropic state of the triphenylene, which is a miscible mixture. Then, fibers of **55** are able to form finer networks resulting in the formation of the liquid crystalline domains at the submicrometer level.¹⁶⁷

Interestingly, vertical alignment of HBC stacks can be achieved by using an amphiphilic PEO-poly(*L*-lysine) block-copolymer. PEO-poly(*L*-lysine) forms a vertical 2D hexagonal lattice at the air/water interface, in which six discotic columns of HBC surrounding an α -helix of poly(*L*-lysine), the resulting ordered structure being held together by acid base interactions. The height of the columns could be tuned by changing the length the *L*-lysine polymer.¹⁶⁸

Organogelators based on π -conjugated systems are relatively rare in contrast to systems based on dyes (anthracene¹⁶⁹⁻¹⁷⁶, porphyrine¹⁷⁷⁻¹⁸⁸, (phtalo¹⁸⁹⁻¹⁹⁸)cyanine¹⁹⁹⁻²⁰⁸, pyrene²⁰⁹, and squaraine²¹⁰⁻²¹²). Cholesterol (**78**) and phospholipid tethered trans-stilbenes (**79**) are able to gelate different organic solvents in which the steroid or lipid unit serves as a template to form one-dimensional stacks.^{213,214}

Ajayaghosh *et al.* have serendipitously extended this concept to longer OPV derivatives (**80**) and reported a completely thermoreversible self-assembly process from single OPV

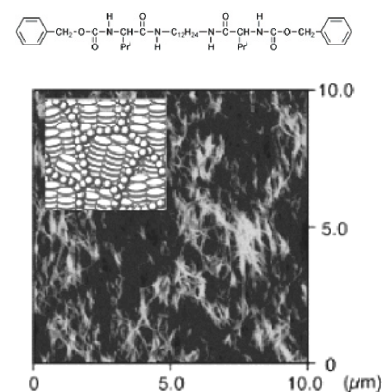


Figure 1.16: AFM image of **55**/*L*-amino acid with a cartoon representing the LC domains.

molecules to fibers and ultimately to an entangled network structure (Figure 1.17). The absorption and emission properties shifted during gelation indicative of intermolecular π -electronic coupling of the OPV segments. In a comparative study, it was shown that the gelation was strongly dependent on the choice of hydrogen-bonding motif, the length of the alkoxy side chains and the conjugation length. An alcohol OPV trimer equipped with six lateral dodecyl chains forms easily a gel at moderate concentrations in hexane, whereas the aldehyde analogue did not gelate the solvent and methyl ether analogue gels only at high concentrations. Studies on the gels using SEM, X-ray diffraction and IR revealed an entangled network of filaments up to micrometer lengths and 100 – 150 nm in width, consisting of well-ordered lamellae of stacked molecules positioned by hydrogen-bonds.²¹⁵ In a recent paper, left-handed helical nanostructures of OPVs with lateral chiral side chains were reported.²¹⁶

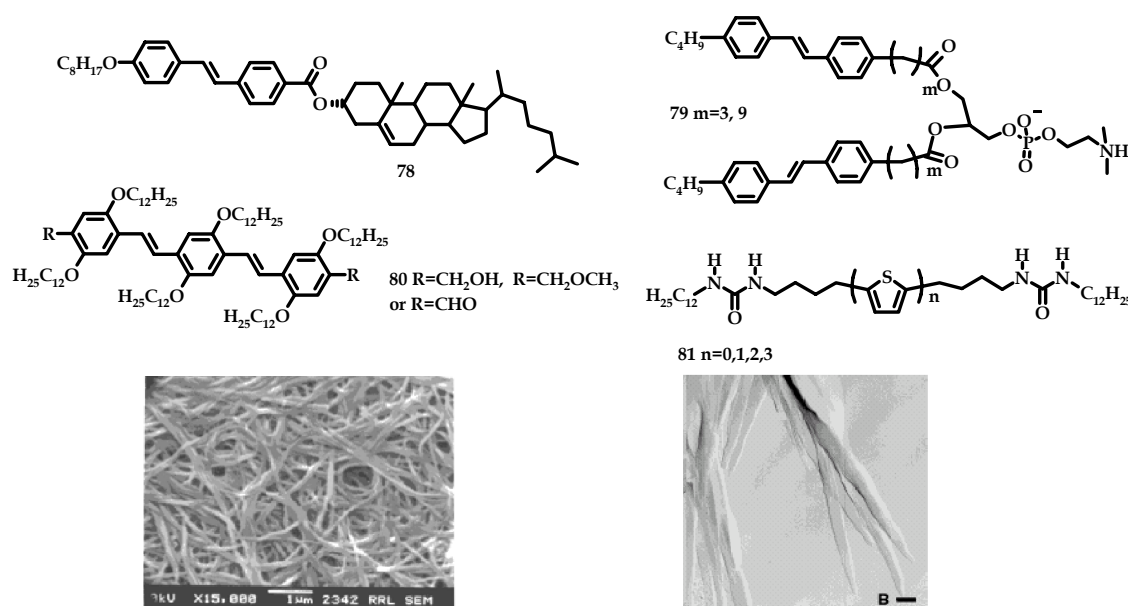
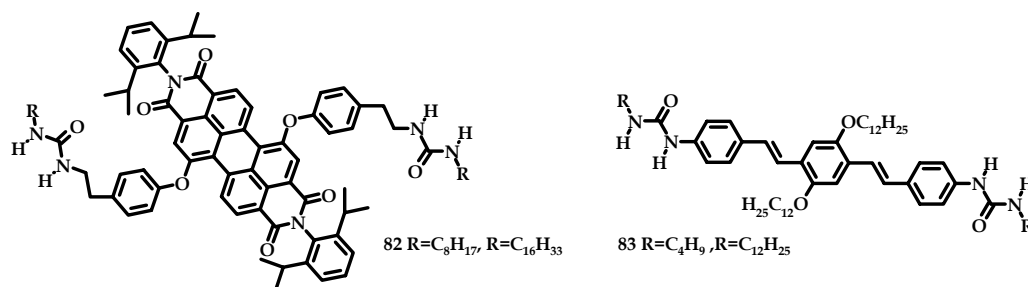


Figure 1.17: Nanofibrillar morphologies based on π -conjugated organogelators (left: **80**, right: **81** ($n = 2$)).

Van Esch *et al.* have shown that charge carrier mobilities up to $5 \times 10^{-3} \text{ cm}^2/\text{Vs}$ can be realized in gel networks built from thiophene derivatives modified with bisurea units (**81**). The thiophene moieties formed closely packed arrays enforced by the urea hydrogen-bonding units, thereby creating an efficient pathway for charge transport.²¹⁷ The nanostructures were studied on several substrates, such as SiO_2 , mica, and highly oriented pyrolytic graphite (HOPG). Elongated twisted fibers were observed on SiO_2 with lengths of 20 – 100 μm and widths of 2 – 10 μm (Figure 1.17). These fibers are strongly birefringent indicating a high degree of molecular ordering. After annealing, extended monolayers are formed consisting of upright one-dimensional arrays standing side-by-side.²¹⁸ On HOPG, the 1D-arrays lie flat on the surface with tilted thiophene rings allowing partially overlapping π -systems.²¹⁹ Scanning tunneling spectroscopy indicate that an effective conjugation in the π -stacks upon increasing the length of the oligothiophenes.²²⁰

Recently, the class of bis-urea compounds equipped with π -conjugated oligomers was extended with PBI **82**²²¹ and OPV **83**.²²² **83** turned strongly emissive in the presence of tetrabutylammonium fluoride due to the competitive hydrogen-bond interaction of the halide ions with the urea groups.



1.3.2 Self-Assembly by Specific Interactions in Solution

Controlled self-assembly of oligomers in solution is of interest for obtaining objects of discrete size and shape. The self-assembly process depends strongly on the nature of the interactions and the shape of the building blocks and a large variety of architectures can be formed in solution. Structures ranging from random coil polymers to intertwined helices and discrete multimolecular objects have been obtained. A typical feature of these assemblies is the dynamic behavior of the molecules within the aggregates. The molecules located in the aggregates may still be mobile, or have some positional disorder. Understanding how self-assembly is controlled by the molecular architecture is expected to enable the design of increasingly complex structures.

In the self-assembly of π -conjugated oligomers, different specific interactions are in operation simultaneously and the strength of the overall binding and the resulting structures are the result of many cooperative processes. In an attempt to simplify the discussion of this complex topic, we will consider situations where π - π (Section 1.3.2.1), amphiphilic (Section 1.3.2.2) or hydrogen-bonding (1.3.2.3) interactions are taken as the leading factor. Not included in the discussion are ligand-metal interaction which have been used to link *e.g.* OPVs and PBIs, both bearing terpyridine receptor groups.^{223,224} Reversibility, that is typical for non-covalent architectures, was established recently by coordination of PBI chromophores with zinc ions.²²⁵

1.3.2.1 Assembly by π - π Interactions

The study of supramolecular organization of well-defined oligomers in solution is a relatively recent activity.²²⁶ The relation between intermolecular interactions and optical properties of substituted ter- and quarterthiophenes or tetrathienylenevinylene was studied by means of UV/vis and fluorescence spectroscopy in linear and branched alkanes or in matrices of polymethylmethacrylate.^{227,228} The results obtained from these studies show that aggregates of oligothiophenes display a blue-shifted absorption spectrum with respect to the molecularly dissolved state. This behavior was attributed to the formation of H-aggregates, assemblies in which the conjugated segments have an orientation perpendicular to the packing axis.^{229,230}

Fréchet *et al.* synthesized the triblock system **84** by symmetrically substituting undeca- and heptadecathiophene cores with oligo(benzylether)dendrons (Figure 1.18). In this way, macromolecular architectures²³¹ were obtained, similar dendritically substituted oligothiophylenevinylenes²³² and oligoimides have been reported by others.^{233,234} Janssen *et al.* obtained TEM images of rod-like 20 nm nanoaggregates of **84** from dichloromethane at low temperatures (Figure 1.18). Detailed analysis of the self-assembly in solution indicated a temperature-induced aggregation in which an intrachain planarization preceded the

intermolecular π - π stacking. The favorable interactions led to an interchain delocalization of the photo-excited singlet, triplet and charged states. Quantitative analysis of the solution aggregation process shows that the supramolecular aggregates were relatively small involving 5 to 6 molecules, which contrasts with the dimensions observed in TEM.²³⁵⁻²³⁷ The apparent size limitation of the solution aggregates is ascribed to steric constraints imparted by the dendritic wedges.²³⁸

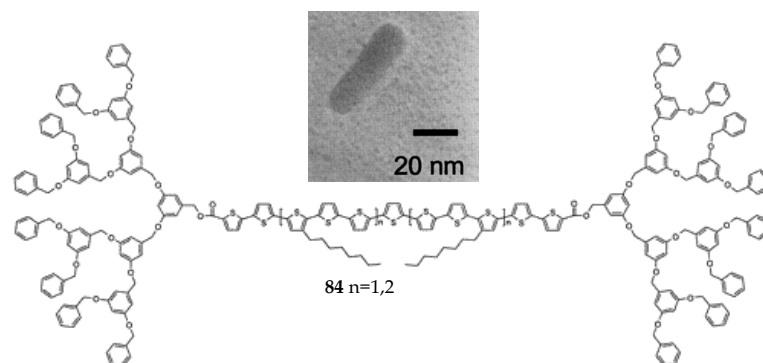


Figure 1.18: Dendritically substituted oligothiophenes that aggregate into nanorods as image by TEM.

1.3.2.2 Assembly by Amphiphilic Interactions

Advincula *et al.* designed sexithiophenes bearing cationic alkyl substituents at either end of the hydrophobic aromatic core. The objective was to prepare ordered ultrathin films by layer-by-layer self-assembly either from a molecularly dissolved or an aggregated state.^{239,240} The self-assembly process of amphiphilic sexithiophene derivatives substituted with chiral penta(ethyleneoxide) chains enabled control of the interplay of hydrophobic and hydrophilic interactions, guiding the π - π stacking of the oligomeric units, and allowing this material to be used for the fabrication of a thin film transistor.²⁴¹ When deposited from THF solution onto silicon wafers, the aggregation of **85** led to rope-like structures with exclusively left-handed

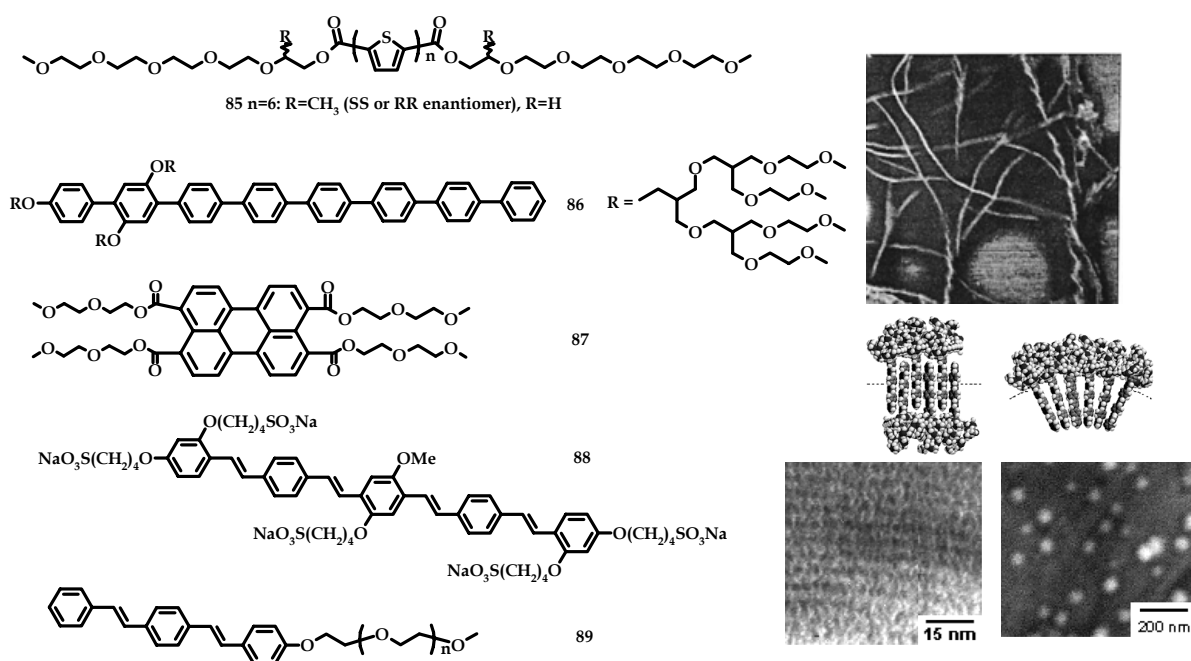


Figure 1.19: Amphiphilic π -conjugated oligomers designed to self-assemble in water. AFM (upper image) shows left-handed helical fibers on silicon oxide surfaces for **85** (SS). Schematic drawing of the molecular arrangement of **86** either into an interdigitated parallel arrangement (lammellae in TEM, lower left image) or into a radial orientation (nanocapsules in AFM, lower right image).

supramolecular helicity (Figure 1.19). This structure was not present when the achiral analogue was deposited; in this case ribbons were observed.^{242,243} The oligomers adopt an edge-on orientation on oxide surfaces by minimizing the contact area between hydrophobic parts of the molecule and the surface; whereas a face-on lamellar array of π -stacked oligomers, typically 3 – 5 molecules in width, was observed on HOPG. In protic media, such as water and butanol, the sexithiophenes **85** aggregate,^{244,245} the self-assembly being accompanied by a blue-shift in the absorption spectrum, reduced fluorescence intensity and a bisignate CD effect indicating chiral superstructures. Thermochromic CD and UV/vis measurements showed a reversible transition at 303 K, demonstrating that the chiral aggregates break up. The shape of these supramolecular assemblies in solution was not elucidated by the authors; however, recent studies by Sasaki *et al.* on an analogous asymmetric quarterthiophene bearing only one oligo(ethyleneoxide) chain, showed that multilamellar vesicles were formed in water.²⁴⁶

Recently, amphiphilic perylenes were reported that self-assemble into flexible rods in water²⁴⁷ (**87**) and chloroform²⁴⁸ as was demonstrated by absorption and scattering measurements. Other molecules which have been reported to self-assemble through hydrophobic π - π interactions are OPVs bearing sulfonic acid side groups (**88**)²⁴⁹ or oligo(ethyleneoxide)s (**89**)^{250,251}. The strong influence of solvophobic interactions on the change of the shape of the structures in water compared to bulk morphology was shown by Lee *et al.* In the bulk, the octa-*p*-phenylenes equipped with oligo(ethyleneoxide) dendrons (**86**) formed an interdigitated parallel arrangement with a 2 nm periodicity, whereas in dilute solution an ordered radial arrangement was obtained resulting in nanocapsules of on average 46 nm in diameter (Figure 1.19).²⁵²

1.3.2.3 Assembly by Hydrogen-bonding Interactions

Supramolecular

polymers are constructed from monomeric units that are glued together by reversible non-covalent hydrogen-bond interactions, and as such consist of a special class of self-assembled systems.²⁵³ Recently Meijer *et al.* reported on supramolecular hydrogen-bonded OPV dimers (**90**) and polymers (**91**) in which the specific electronic and optical properties of conjugated OPV oligomers and the material properties of polymers were combined.^{254,255} These polymeric systems are based on the strong dimerization of quadruple hydrogen-bonding ureido-

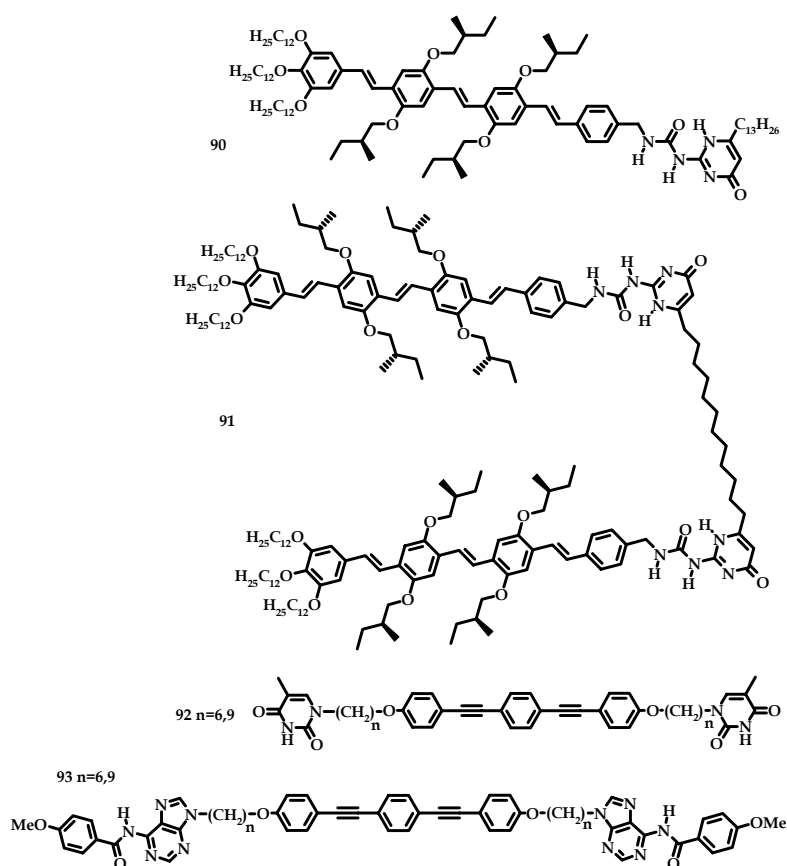


Figure 1.20: π -Conjugated oligomers provided with hydrogen-bonding interacting units.

pyrimidinone units, resulting in a random coil polymer in solution lacking higher mesoscopic order. The supramolecular polymer could be processed easily to give smooth films and photo-induced electron-transfer was observed in films blended with a C_{60} derivative. This film blend was successfully incorporated in a photovoltaic device.

Hydrogen-bonds have also been used to obtain liquid crystalline phases in analogy with the behavior of compounds **50–53**. When nucleobases like adenine and thymine were attached to known mesogens such as alkoxyphenylethynyls (**92, 93**), no liquid crystal phase could be observed. However, the 1:1 blends of the complementary nucleobase derivatives resulted in the formation of fairly stable lyotropic liquid crystalline phases.²⁵⁶

Hydrogen-bond mediated complexes **94** of naphthalenebisimide and complementary dialkylated melamines can result in mesoscopic tube-like nanostructures as shown by Kimizuka *et al.* (Figure 1.21). Molecular stacking of the hydrogen-bonded aromatic sheets was accompanied by a red shift in the onset of the naphthalenebisimide absorption in the UV/vis spectra. The flexible alkyl chains that surround the aggregate probably stabilize the weak hydrogen-bonds. Flexible rod-like aggregates with widths of 12 – 15 nm were observed by electron microscopy and a stacked cyclic dodecameric structure or a helically grown structure was proposed.^{257,258}

Würthner *et al.* extended this process of superstructure formation to PBI derivatives (**95**). The self-assembly is hierarchical and involves multiple supramolecular interactions, appropriate solubilizing substituents and a solvent of low polarity. NMR, optical spectroscopy and dynamic light scattering (DLS) measurements revealed that large aggregates, of ca. 200 nm, were present in dilute methylcyclohexane solution and complexation of PBI with chiral melamines gave rise to exciton-coupled Cotton effects for the PBI absorption bands. SEM images of these mesoscopic superstructures (Figure 1.21) showed a densely intertwined network with cylindrical strands having diameters in the range of 15 – 500 nm. These dimensions indicate that further aggregation takes place. Confocal fluorescence microscopy studies showed the excellent photostability of these superstructures in the solid state.²⁵⁹⁻²⁶¹

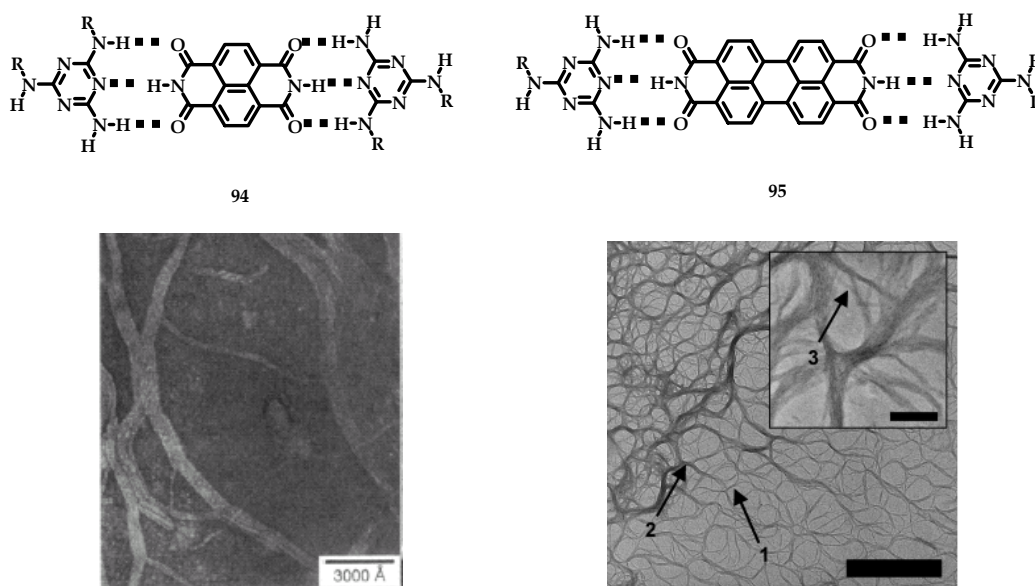


Figure 1.21: Nanofibrillar morphologies based on π -conjugated oligomers equipped with hydrogen-bonding moieties (image to the right has a scale bar indicating 2000 nm, inset: 250 nm).

1.4 AIM OF THE THESIS

The review of literatureⁱ shows that self-assembly is an attractive tool to construct well-organized π -conjugated assemblies. Many types of secondary interactions exist such as π - π stacking, amphiphilic or hydrogen-bonding interactions. However, to date, only one of these secondary interactions has been used to control the position of π -conjugated systems and the dimension of nanoscopic architectures. Furthermore, the previous research has been mainly driven by efforts to improve the supramolecular organization of π -conjugated systems in the active layer of plastic electronic devices. The objective of the work reported in this thesis is the programmed self-assembly²⁶² of π -conjugated oligomers into architectures at the nanometer-scale using several secondary interactions simultaneously, thus following nature's paradigm. The construction of such architectures is thought to be not only important for plastic electronics but also for the new field of supramolecular electronics. This relatively unexplored field of research relies on structures having controlled dimension and shape, *e.g.* wires; 5 nm in diameter and 100 nm in length.

To this end, this thesis will focus on the design and the synthesis of new molecules carrying different types of secondary interacting units. Special attention will be drawn to issues that concern the mechanism of the self-assembly process and how to accurately measure such processes. Another important issue that will be addressed, is the controlled deposition of self-assembled architectures from solution to surfaces, which is crucial for the construction of devices. Finally, issues involving the external manipulation of supramolecular structures will be discussed. The literature review demonstrates the wealth of nanoscopic self-assembled structures that have been described in the last decade or so. A thorough study is necessary to evaluate these nanoscopic structures for their ultimate use in supramolecular electronics.

1.5 OUTLINE OF THE THESIS

The supramolecular structures in solution described in this thesis were studied in solution by optical spectroscopy and scattering experiments, which revealed insight into their stability and shape. Scanning probe microscopy techniques were used to characterize the supramolecular architectures in the solid state.

Chapter 2 describes the influence of the hydrophobic/hydrophilic balance on the self-assembly in solution and solid state of a series of chiral oligo(*p*-phenylenevinylene)s.^{ii,iii} In the next two chapters, self-complementary hydrogen-bonding interactions of different strength are introduced and evaluated in the self-assembly process of oligo(*p*-phenylenevinylene)s at surfaces^{iv,v} and in solution.^{vi-vii} Chapter 4 closes with a detailed analysis of the optical measurements following the self-assembly process and providing, for the first time, a more detailed description of that process. Chapter 5 describes the transfer process of self-assembled oligomers in solution to the solid state,^{viii} which is important for construction of devices.^{ix} Supramolecular fibrils generated by this process were analyzed optically in the solid state and evaluated in devices. In Chapter 6, the use of complementary hydrogen-bond interactions to selectively join different types of π -conjugated components at surfaces^x and in solution^{xi,xii,xiii} is described. After transfer of these structures to the solid state, ambipolar transistors were constructed via a supramolecular approach. The last chapter describes use of the insights gained in the preceding chapters on the self-assembly of chiral

oligo(*p*-phenylenevinylene)s to the interpretation of experimental data on the self-assembly of chiral oligothiophenes. These studies revealed odd-even effects based on the location of the stereocenter and a novel stereomutation process. Chapter 7 ends with a discussion of the contact-free manipulation of supramolecular objects using strong magnetic fields.^{xiv}

1.6 SELECTED PUBLICATIONS^{xv}

- (i) Hoeben, F. J. M.; Jonkheijm, P.; Meijer, E. W.; Schenning, A. P. H. J. *Chem. Rev.* **2005**, *105*, 1491-1546.
- (ii) Gesquière, A.; Jonkheijm, P.; Schenning, A. P. H. J.; Mena-Osteritz, E.; Bäuerle, P.; de Feyter, S.; de Schryver, F. C.; Meijer, E. W. *J. Mater. Chem.* **2003**, *13*, 2164-7.
- (iii) Jonkheijm, P.; Franssen, M.; Schenning, A. P. H. J.; Meijer, E. W. *J. Chem. Soc., Perkin Trans. 2* **2001**, 1280-6.
- (iv) Miura, A.; Jonkheijm, P.; De Feyter, S.; Schenning, A. P. H. J.; Meijer, E. W.; De Schryver, F. C. *Small* **2005**, *1*, 131-7.
- (v) Gesquière, A.; Jonkheijm, P.; Hoeben, F. J. M.; Schenning, A. P. H. J.; De Feyter, S.; De Schryver, F. C.; Meijer, E. W. *Nano Lett.* **2004**, *4*, 1175-9.
- (vi) Jonkheijm, P.; Miura, A.; Zdanowska, M.; Hoeben, F. J. M.; De Feyter, S.; Schenning, A. P. H. J.; De Schryver, F. C.; Meijer, E. W. *Angew. Chem. Int. Ed.* **2004**, *43*, 74-8.
- (vii) Schenning, A. P. H. J.; Jonkheijm, P.; Peeters, E.; Meijer, E. W. *J. Am. Chem. Soc.* **2001**, *123*, 409-16.
- (viii) Jeukens, C. R. L. P. N.; Jonkheijm, P.; Wijnen, F. J. P.; Gielen, J. C.; Christianen, P. C. M.; Schenning, A. P. H. J.; Meijer, E. W.; Maan, J. C. *J. Am. Chem. Soc.* accepted.
- (ix) Jonkheijm, P.; Hoeben, F. J. M.; Kleppinger, R.; Van Herrikhuyzen, J.; Schenning, A. P. H. J.; Meijer, E. W. *J. Am. Chem. Soc.* **2003**, *125*, 15941-9.
- (x) De Feyter, S.; Miura, A.; Yao, S.; Chen, Z.; Würthner, F.; Jonkheijm, P.; Schenning, A. P. H. J.; Meijer, E. W.; De Schryver, F. C. *Nano Lett.* **2005**, *5*, 77-81.
- (xi) Schenning, A. P. H. J.; van Herrikhuyzen, J.; Jonkheijm, P.; Chen, Z.; Würthner, F.; Meijer, E. W. *J. Am. Chem. Soc.* **2002**, *124*, 10252-3.
- (xii) Würthner, F.; Chen, Z.; Hoeben, F. J. M.; Osswald, P.; You, C.-C.; Jonkheijm, P.; van Herrikhuyzen, J.; Schenning, A. P. H. J.; van der Schoot, P. P. A. M.; Meijer, E. W.; Beckers, E. H. A.; Meskers, S. C. J.; Janssen, R. A. J. *J. Am. Chem. Soc.* **2004**, *126*, 10611-8.
- (xiii) Jonkheijm, P.; Schenning, A. P. H. J.; Meijer, E. W. *Polym. Prepr.* **2004**, *91*, 131-2.
- (xiv) Shklyarevskiy, I. O.; Jonkheijm, P.; Christianen, P. C. M.; Schenning, A. P. H. J.; Meijer, E. W.; Henze, O.; Kilbinger, A. F. M.; Feast, W. J.; Del Guerzo, A.; Desvergne, J.-P.; Maan, J. C. *J. Am. Chem. Soc.* **2005**, *127*, 1112-3.
- (xv) For other research performed in the last four years and that is not described in this thesis, the reader is referred to the curriculum vitae.

2 SELF-ASSEMBLY OF OLIGO(*p*-PHENYLENEVINYLENE)S INFLUENCED BY HYDROPHILICITY

ABSTRACT

The self-assembly of a series of oligo(*p*-phenylenevinylene)s (OPVs) having a varying hydrophobic/hydrophilic balance is described. First, the synthesis of OPVs of different π -conjugation length end capped with either hydrophobic or hydrophilic groups is described. Tridodecyloxybenzene units were used as hydrophobic groups and either tri-(tetra(ethyleneoxide))benzene units or crownether moieties were used as hydrophilic groups. In addition, tridodecyloxybenzene units were also combined with tri-(tetra(ethyleneoxide))benzene units in one OPV derivative.

At the liquid/solid interface, only the hydrophobic OPVs self-assemble in highly organized monolayers. In the case of hydrophilic OPVs, the monolayers could not be visualized by scanning tunneling microscopy. The organization of the hydrophobic OPVs in monolayers depends on the conjugation length while the chiral OPVs show a preferred adsorption excluding one possible diastereomeric packing. At the air/water interface no stable monolayers were produced by the amphiphilic OPVs.

Remarkably, the hydrophobic/hydrophilic balance did not have an influence on the supramolecular organization in the solid state after slow evaporation of a solvent in which OPVs were molecularly dissolved. In all cases, on graphite a rod-like morphology appeared, on an initially formed monolayer. On silicon oxide, left-handed helical fibrils of chiral OPVs were observed while, in the case of an achiral OPV, non-helical fibrils were present showing that the chirality in the molecular building block is expressed at the supramolecular level. The self-assembly of crownether functionalized OPVs could be influenced by adding alkaline salts.

The hydrophilic OPVs could also be self-assembled in water. Vesicles were formed that show a helical to non-helical transition. The emission from a single vesicle on a glass surface was similar to emission from vesicles in water. Interestingly, vesicles could be manipulated by optical tweezers providing a tool to position nanoscopic architectures.

CONTENTS	page
2.1 Introduction	26
2.2 Synthesis	26
2.3 Self-Assembly at Interfaces	28
2.3.1 Liquid/Solid Interface	28
2.3.2 Air/Water Interface	30
2.4 Self-Assembly at Surfaces	31
2.5 Self-Assembly in Solution	34
2.5.1 Self-Assembly in Water	34
2.5.2 Self-Assembly in Chloroform by Ions	36
2.6 Conclusions	38
2.7 Towards Positioning Nanoscopic Supramolecular Objects	39

2.1 INTRODUCTION

Cells are fluid aggregates composed of small lipid molecules, phospholipids being the most abundant. The phospholipids have an amphiphilic character, *i.e.* a hydrophobic and a hydrophilic part, and the self-assembly is driven by the hydrophobic effect.²⁶³ The hydrophobic effect is not only a well-known phenomenon in nature, it has also been adopted by synthetic chemists to self-assemble π -conjugated systems and different approaches have been developed to construct nanoscopic architectures. For example, the spontaneous self-assembly in water of amphiphilic π -conjugated oligomers has yielded rods and vesicles (see Chapter 1).^{75,250,264-267} Furthermore, Langmuir layers have been constructed at the air/water interface which could be used in light-emitting diodes (LEDs) and field effect transistors.^{41,268-275} Monolayers of π -conjugated systems can also be constructed at the liquid/solid interface and studied with scanning tunneling microscopy (STM).^{219,276-284} Another method to construct nanoscopic architectures is the slow evaporation of a solvent in which molecules are molecularly dissolved.²⁸⁵⁻²⁹¹ Ionochromic response of π -conjugated systems can create an additional tool to control polymer aggregation in solution.²⁹² PPV equipped with crownether substituents formed wormlike nanoribbons on a substrate through first complexation with potassium in dilute chloroform solution.^{293,294}

This Chapter describes the study of the self-assembly of a range of OPVs having different conjugation lengths and a varying hydrophilic/hydrophobic balance. The self-assembly has been studied in solution, at interfaces and at surfaces. To this end, hydrophobic tridodecyloxybenzene endcapped OPV_{*x*}s (*x* denotes the number of phenyl rings), *i.e.* a dimer (OPV₂), a tetramer (OPV_{4a}) and a hexamer (OPV₆) (Chart 2.1) have been used. In addition, hydrophilic OPVs, *i.e.* a tetramer endcapped with one tridodecyloxybenzene and one tri-(tetra(ethyleneoxide))benzene (OPV_{4b}), and two pentamers having two tri-(tetra(ethyleneoxide))benzene units (OPV_{5a}) or two crownether moieties (OPV_{5b}), were synthesized (Scheme 2.1).

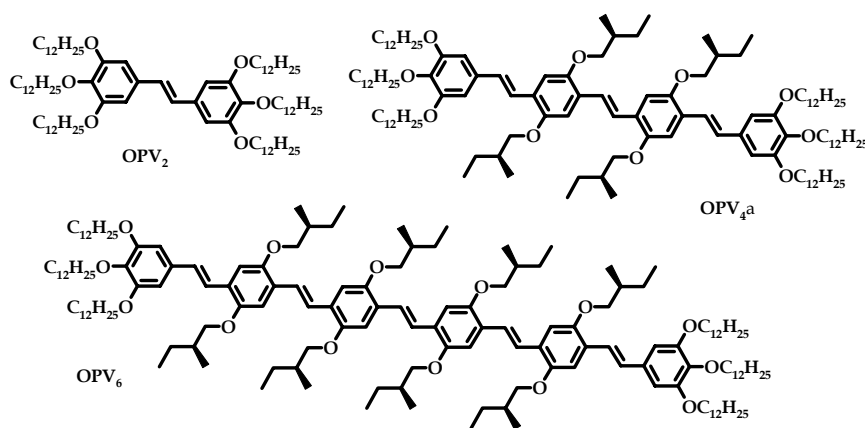
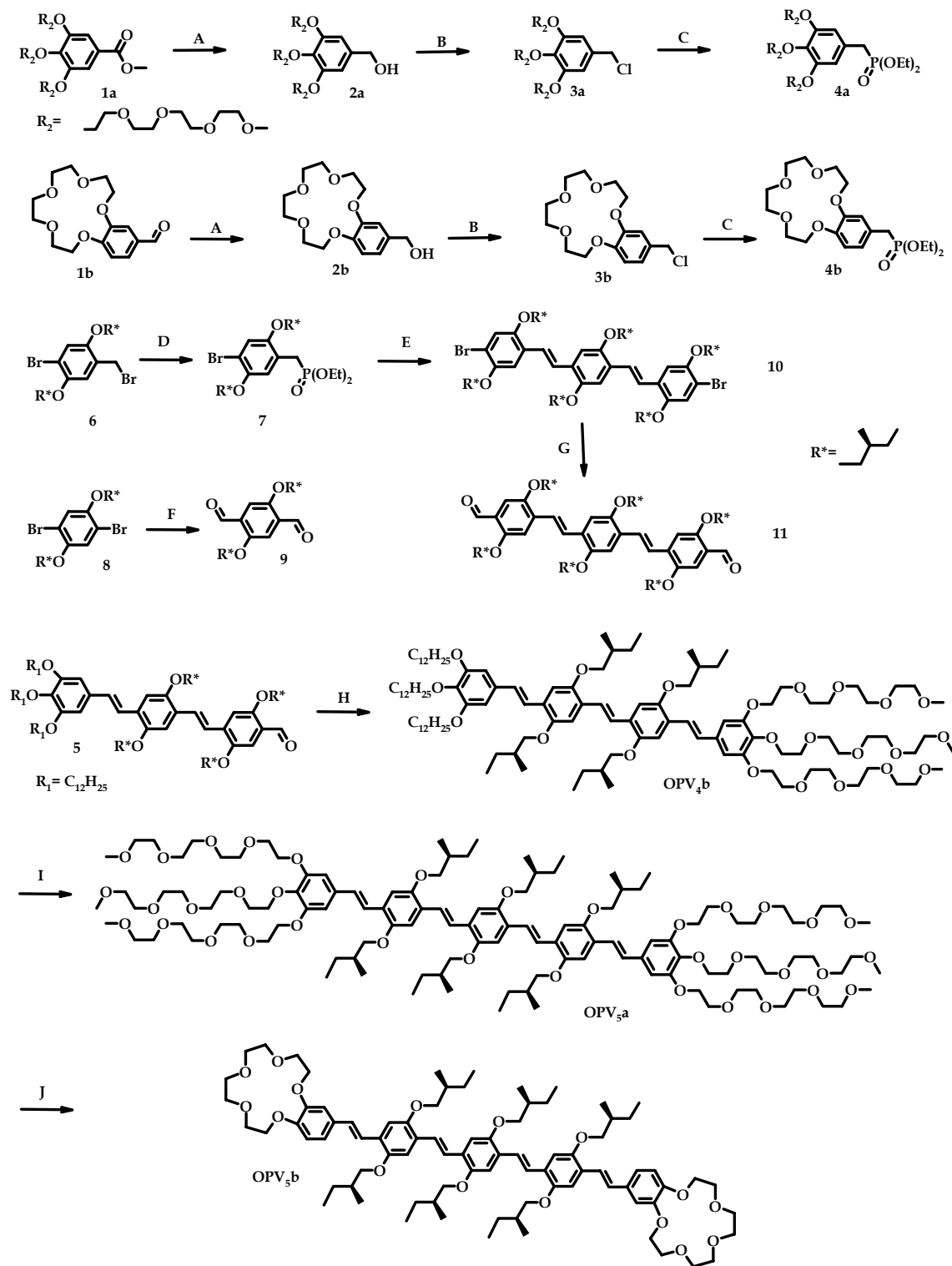


Chart 2.1: Hydrophobic OPV_{*x*}s (*x* = 2, 4, 6).

2.2 SYNTHESIS

Optically active amphiphilic π -conjugated oligomers OPV_{4b}, OPV_{5a} and OPV_{5b} (Scheme 2.1) were synthesized from the phosphonate precursors, **4a** or **4b**, the former bearing tetraethyleneglycol chains, the latter bearing a 15-crown-5 moiety. The synthesis of these

precursors required similar steps starting from the benzoate **1a** and aldehyde **1b**, respectively. Reduction by LiAlH_4 of **1a** and **1b** afforded the corresponding alcohol derivatives **2a** and **2b**, in 95% and 42% yield, respectively. Chlorination of **2a** and **2b** in refluxing thionylchloride with a catalytic amount of DMF yielded 100% chloride derivatives **3a** and **3b**. The obtained products were subsequently converted to **4a** and **4b** by performing Michaelis–Arbuzow reactions with



Scheme 2.1: Synthetic route to hydrophilic OPVs (**OPV_{4b}**, **OPV_{5a}** and **OPV_{5b}**) A) LiAlH_4 , 8h, 0 °C. B) SOCl_2 , 1h. C) and D) $\text{P}(\text{OEt})_3$, 8h, 160 °C. E) **9**, DMF/THF, $\text{KOC}(\text{CH}_3)_3$, 3h. F) and G) 1. *n*-BuLi, -10 °C; 2. DME, 1h. H), I) and J) DMF/THF, $\text{KOC}(\text{CH}_3)_3$, 8h, **5** and **4a**, **11** and **4a**, **11** and **4b**, respectively.

triethylphosphite in 100% yields. Pure **OPV_{4b}** was obtained via a Wittig–Horner coupling reaction of aldehyde derivative **5** with **4a** in 73% yield. **OPV_{5a}** and **OPV_{5b}** were synthesized starting from the dibromide derivative **8**. Reacting **8** with *n*-BuLi in diethylether and by adding DMF resulted in the substitution of the bromines by formyl groups, to give **9** in 52% yield. Wittig–Horner coupling of **9** with phosphonate **7** yielded dibromide OPV derivative **10** (53% yield) which was subsequently converted to the dialdehyde **11** (69% yield) according to the same procedure as applied for **9**. After coupling **4a** to **11**, bolaamphiphile **OPV_{5a}** was isolated in 54% yield, while coupling of **4b** to **11** gave **OPV_{5b}** in 12% yield. The yields of **OPV_{5a}** and **OPV_{5b}** are lower compared to **OPV_{4b}** due to the more extensive purification, which required a combination of column chromatography and size exclusion chromatography.

All amphiphiles were fully characterized by ¹H-NMR, ¹³C-NMR, IR, MALDI-TOF mass spectrometry and elemental analysis and are highly soluble in organic solvents such as tetrahydrofuran (THF), chloroform, and methanol. The UV/vis absorption maxima lie at λ_{max} = 333 (**OPV₂**), 433 (**OPV_{4a}**), 434 (**OPV_{4b}**), 450 (**OPV_{5a}**), 453 (**OPV_{5b}**) and 464 nm (**OPV₆**), respectively. The fluorescence maxima in chloroform are positioned at λ_{max} = 470 (**OPV₂**), 500 (**OPV_{4a}**), 495 (**OPV_{4b}**), 525 (**OPV_{5a}**) 520 (**OPV_{5b}**) and 550 nm (**OPV₆**). The absorption and fluorescence maxima shift with increasing conjugation length is analogous to that described by Meier *et al.*²⁹⁵

2.3 SELF-ASSEMBLY AT INTERFACES

2.3.1 Liquid/Solid Interface

STM experiments were carried out at the liquid/solid interface (1,2,4-trichlorobenzene/highly oriented pyrolytic graphite (HOPG)). For the three hydrophobic compounds, **OPV₂**, **OPV_{4a}** and **OPV₆**, monolayers could be observed by physisorption from a 1 g/L solution.²⁹⁶ The amphiphilic **OPV_{4b}** and the hydrophilic/amphiphilic **OPV_{5a}** and **OPV_{5b}** also organize into monolayers on graphite (*vide infra*), but were virtually impossible to image by STM, presumably because of the strong repulsion between the tip and substrate during scanning over the polar ethylene glycol chains. STM images of **OPV₆** (Figure 2.1) show that the molecules are arranged in lamellae, in which the π -conjugated moieties appear brighter than the alkyl chains due to the higher detected tunneling current.²⁹⁷ It is evident that the OPVs lie flat on the surface, isolated from each other with a spacing between the π -systems of about 1.5 nm, prohibiting interaction between chiral side chains of 0.5 nm. The chiral side chains attached to the π -system could also be observed on a few occasions as dots (Figure 2.1c). Six benzene units could be visualized in one **OPV₆**, that are, in all cases, connected by trans-vinylene bonds. *In-situ* calibration with respect to the graphite lattice allows the unit cell parameters to be calculated ($a = 2.0$ nm, $b = 5.1$ nm, $\gamma = 55^\circ$ in Figure 2.1a). Two out of three dodecyloxy chains were nicely resolved in several images. These chains are oriented along one of the main symmetry axes of the graphite substrate. The exact location of the third chain could not be determined.

The lamellae further order into domains. Lamellae in adjacent domains are rotated by 60° dictated by the symmetry of the graphite substrate and the interactions of the alkyl chains with the substrate. The orientation of the lamellae does not express the molecular chirality: the long lamella-axis in all domains runs parallel to one of the main graphite symmetry axes.²⁹⁸⁻³⁰¹ However, molecular chirality is expressed by the orientation of the molecules within the

lamellae: the π -conjugated backbones are oriented counterclockwise (35°) with respect to the normal on a lamella axis (indicated in Figure 2.1d).³⁰² It is known that molecule–substrate interactions may lead to preferred adsorption of the enantiomer eliminating one of the diastereomeric configurations (*i.e.* unit cells).³⁰² Interestingly, in Figure 2.1d a single trapped molecule can be seen at the domain boundary.

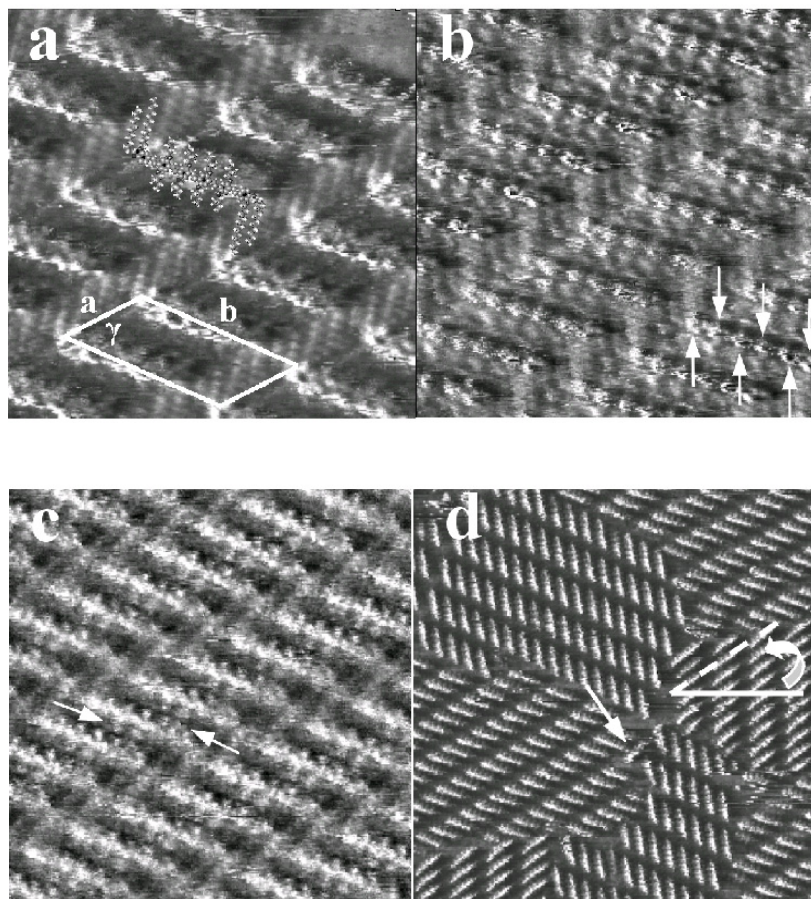


Figure 2.1: STM images of **OPV₆** monolayers on graphite. (a) $10.7 \times 10.7 \text{ nm}^2$, $I_{\text{set}} = 1.0 \text{ nA}$, $V_{\text{bias}} = -0.54 \text{ V}$; a molecular model and unit cell are drawn on the experimental data. (b) $11.8 \times 11.8 \text{ nm}^2$, $I_{\text{set}} = 1.0 \text{ nA}$, $V_{\text{bias}} = -0.89 \text{ V}$; arrows indicate benzene rings. (c) $15.3 \times 15.3 \text{ nm}^2$, $I_{\text{set}} = 1.0 \text{ nA}$, $V_{\text{bias}} = -0.82 \text{ V}$; arrows indicate chiral side chains. (d) $50.0 \times 50.0 \text{ nm}^2$, $I_{\text{set}} = 1.0 \text{ nA}$, $V_{\text{bias}} = -0.80 \text{ V}$; arrow indicates a trapped single molecule.

Although STM images of **OPV_{4a}** show the same contrast features as **OPV₆**, the orientation of the molecules in the 2D crystal is different (Figure 2.2). Now, the OPV–backbones adsorb in an end–to–end fashion on graphite leaving sufficient space (about 1.7 nm) for all six fully extended dodecyloxy chains. Most likely, additional stability is gained by adsorbing all alkyl chains on the surface. The unit cell packing parameters of **OPV_{4a}** ($a = 2.9 \text{ nm}$, $b = 3.1 \text{ nm}$, $\tilde{a} = 60^\circ$ (Figure 2.2b)) give 7.6 nm^2 as the unit cell surface area. If the **OPV_{4a}** packed in a similar way to **OPV₆**, this would require only 6.2 nm^2 , showing that the packing of **OPV₆** is more efficient than that of **OPV_{4a}**. It seems that the packing of **OPV₆** is determined by the π -conjugated backbones, while the alkyl chains of **OPV_{4a}** direct the packing, thereby pushing the OPV–units in an end–to–end type assembly. Surprisingly, the row of end–to–end **OPV_{4a}** also propagates parallel with a main symmetry axis of the graphite lattice, which is similar to the long lamellae–axis observed in the **OPV₆** case. The π -systems show a small counterclockwise rotation with respect to the propagation direction of the row (Figure 2.2b).

The expression of the chirality of **OPV_{4a}** and **OPV₆** in their respective crystals is confirmed by examining monolayers of **OPV₂**, an achiral compound. The packing of **OPV₂** is analogous to **OPV_{4a}**; π -systems are aligned in rows, with the alkyl chains residing between the rows (unit cell: $a = 2.3$ nm, $b = 2.4$ nm, $\tilde{\alpha} = 60^\circ$ Figure 2.2c). The rows formed by the **OPV₂** units make both positive (clockwise) and negative (counterclockwise) angles with respect to the main symmetry axis of the HOPG lattice of about 13° . Moreover, the **OPV₂** units now have both a small clockwise and counterclockwise rotation with respect to the propagation direction of the rows formed by the π -conjugated moieties. Domains with six distinct propagation directions of the rows can be observed, indicative of two sets of enantiomorphous domains. In addition, the unit cells of the enantiomorphous domains are related as mirror images.

In conclusion, only the hydrophobic OPVs self-assemble in highly organized monolayers. The configuration of the monolayers of the hydrophobic OPVs depends on conjugation length and the chiral OPVs show a preferred adsorption excluding one possible diastereomeric packing.

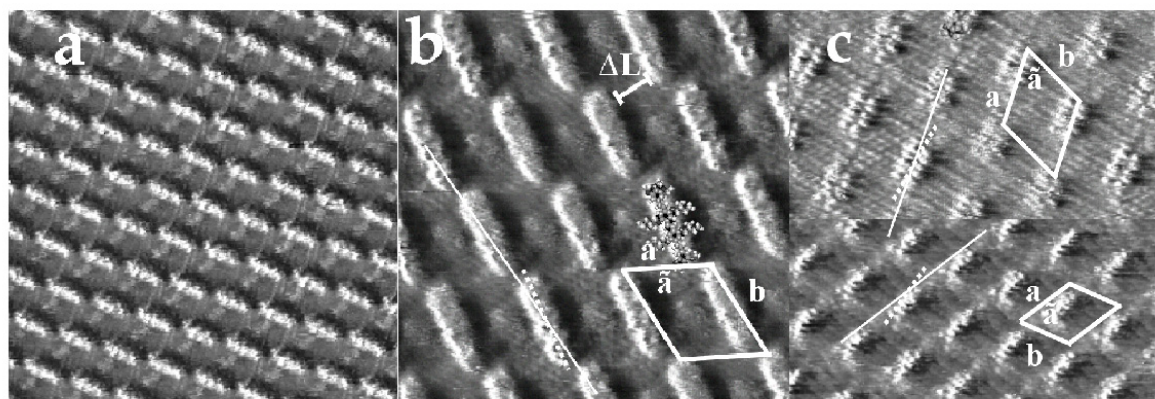


Figure 2.2: STM images of (a) **OPV_{4a}**, 25.1×25.1 nm², $I_{\text{set}} = 1.0$ nA, $V_{\text{bias}} = -0.54$ V. (b) **OPV_{4a}**, 11.8×11.8 nm², $I_{\text{set}} = 1.0$ nA, $V_{\text{bias}} = -0.20$ V; a molecular model are drawn on the experimental data. (c) **OPV₂**, 14.5×14.5 nm², $I_{\text{set}} = 1.0$ nA, $V_{\text{bias}} = -0.98$ V (bottom) and 11.1×11.1 nm², $I_{\text{set}} = 1.0$ nA, $V_{\text{bias}} = -0.62$ V (top). Unit cells and the rotation of the π -system with respect to the propagation direction of a row is depicted.

2.3.2 Air/Water Interface

The amphiphilic **OPV_{4b}** and **OPV_{5a}** were spread at the air/water interface on a Langmuir trough. The pressure–area isotherms (Figure 2.3) display in both cases a slow increase in surface pressure with onsets at areas of 3.8 and 7.5 nm²/molecule for **OPV_{4b}** and **OPV_{5a}**, respectively. In the case of **OPV_{4b}** a collapse was found at a pressure of $\pi = 45$ mN/m and a mean molecular area of 0.8 nm²/molecule was obtained by extrapolating the steep rise in the condensed region to zero pressure. This value is consistent with the hypothesis that **OPV_{4b}** is oriented perpendicularly with respect to the air/water interface, similar as found for other OPV amphiphiles.^{266,267} Stability measurements at constant area lead to an immediate pressure drop indicating that the monolayer is not very stable. In addition, a large hysteresis was found in the isotherm upon expanding (Figure 2.3). In the case of **OPV_{5a}** also unstable monolayers were formed. The increase in pressure found at larger surface area per molecule for **OPV_{5a}** probably indicates that these molecules lie flat on the subphase with the hydrophilic ethyleneglycol tails pointing into the water.

The behavior of these hydrophilic OPVs at the air/water interface is remarkably different from that of related amphiphilic OPVs,^{266,267} and the analogous amphiphilic

oligothiophenes polymers and molecules³⁰³ all of which form stable and transferable monolayers. Presumably, the subtle structural variations change the hydrophobic/hydrophilic balance sufficiently to render the amphiphilic OPV monolayers of interest here unstable with respect to slow dissolution in the subphase or to the formation of multilayers.

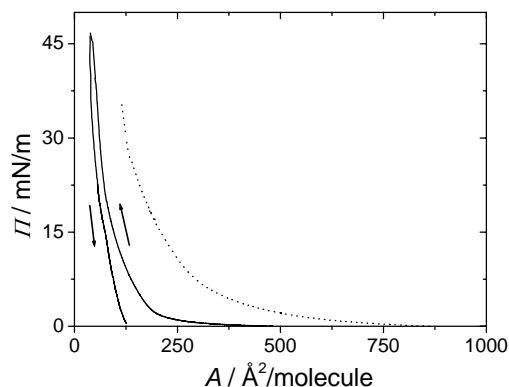


Figure 2.3: Surface pressure–area isotherms of **OPV_{4b}** (solid) and **OPV_{5a}** (dash) at 295 K.

2.4 SELF-ASSEMBLY AT SURFACES

The aggregation processes of **OPV₂**, **OPV_{4b}**, **OPV_{5a}** and **OPV₆** when deposited on a solid support from solution were investigated using tapping mode atomic force microscopy (TM–AFM). Figure 2.4 shows the typical morphology for deposits of **OPV₆** on graphite obtained from 0.01 g/L THF solutions in which the OPVs are molecularly dissolved. Fibrils (III) were formed on top of a monolayer (II in Figure 2.4); as the measured height differences of 0.5 to 0.6 nm relative to the substrate (I) corresponds roughly to the thickness of one absorbed molecule. STM showed that OPVs with aliphatic chains have a strong tendency to form stable monolayers at the liquid/graphite interface while the ethyleneglycol OPV

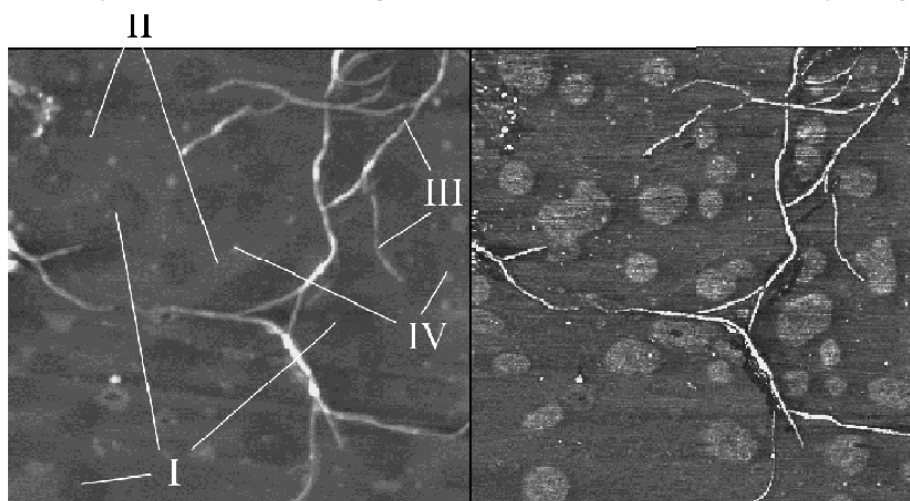


Figure 2.4: TM–AFM image of $2 \times 2 \mu\text{m}^2$ (left) height, z -scale 10 nm and (right) phase, z -scale 25° of **OPV₆** (0.01 g/L) on graphite from THF. Substrate surface (I), monolayer (II), fibril (III) and some non-aggregated material (IV) are indicated for guidance.

derivatives, **OPV_{4b}** and **OPV_{5a}**, were impossible to image by STM. However, when **OPV_{4b}** and **OPV_{5a}** were deposited on graphite, monolayers were observed with fibrils over the monolayers (data not shown).

In all cases the fibrils resemble more ribbon-like objects, as their width (after tip deconvolution³⁴⁵) is much larger than their height (the width ranges from 30 to 50 nm, while the height varies between 1.5 and 9 nm). The formation of ribbons, as in the case of other π -conjugated homopolymers and block-copolymers, probably takes place by self-assembly governed by π - π stacking of the OPV units. These π -stacks most probably form the core of the ribbons, with the ethylene glycol or alkyl segments located on either side. Interestingly, the dimensions estimated for **OPV₆** with the six lateral dodecyloxy segments fully extended is about 6.8 nm. This suggests that the ribbons are constructed from multiple molecule-wide stacks lying side-by-side and that the ribbons can stack on top of each other. The length of the ribbons indicates that such π -stacking can extend over hundreds of nanometers, that is, thousands of molecules. Completely uniform orientation of the ribbons is presumably prevented by the initially formed monolayer, which contains multiple lamellar domains with different orientations which may influence the nucleation and growth of the supramolecular organization into ribbons.

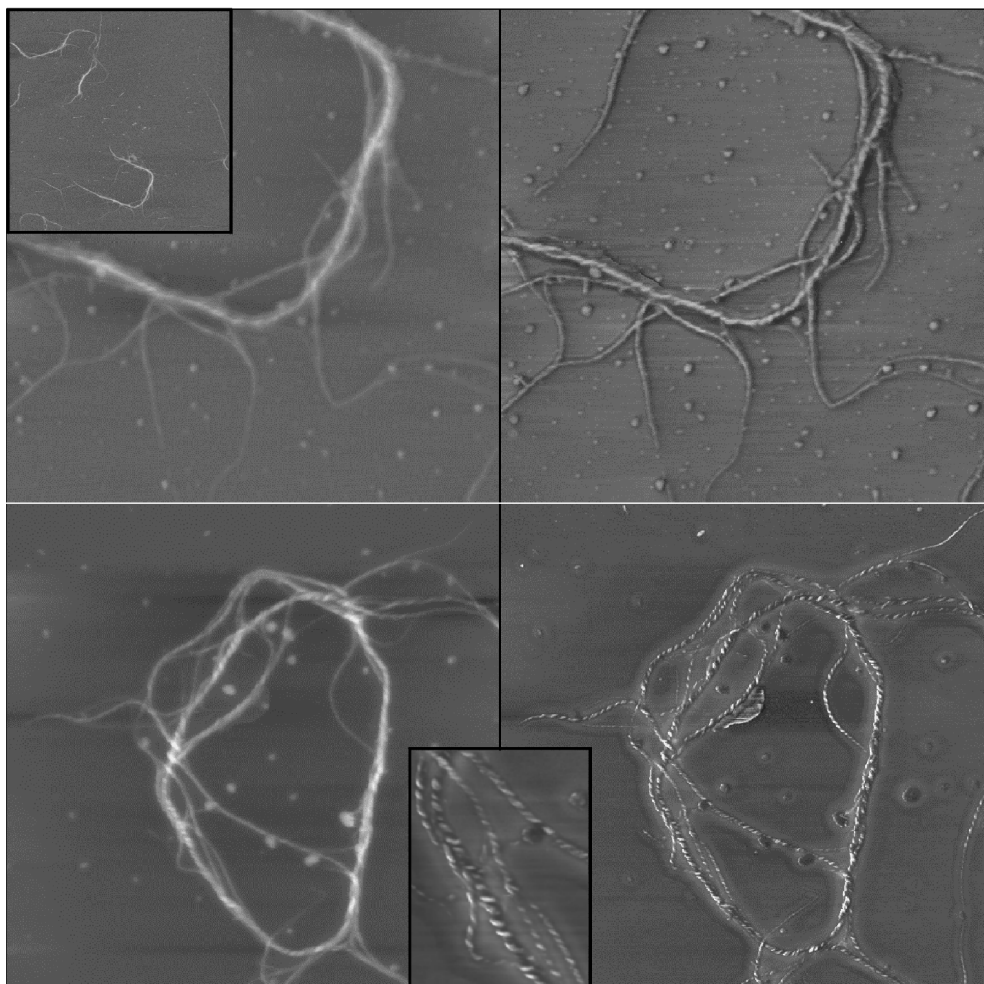


Figure 2.5: TM-AFM images from THF solution (0.01 g/L) on silicon oxide surfaces. Top: **OPV₆**, $3 \times 3 \mu\text{m}^2$, height (left, z-scale 50 nm), phase (right, z-scale 60°), inset: overview of $10 \times 10 \mu\text{m}^2$, height, z-scale 50 nm. Bottom: **OPV_{4b}**, $3 \times 3 \mu\text{m}^2$, height (left, z-scale 50 nm), phase (right, z-scale 25°), inset: enlarged area of phase image, $750 \times 750 \text{ nm}^2$ which left-handed helical structure.

Interestingly, when **OPV_{4b}** and **OPV₆** are deposited on a silicon oxide surface, helical fibers are formed (Figure 2.5). Only left-handed helices are observed. In the case of **OPV₂** non-helical fibers are formed indicative that the chirality present in the molecular building blocks influences the supramolecular chirality observed.

For **OPV_{4b}**, helices of different diameters (based on the height) are observed. Detailed examination reveals diameters of on average 3.4, 6.8 and 15.4 nm, (the spread is indicated in the graph in Figure 2.6). The pitch angle is around 44°, however, it seems that large helices show larger pitch angles. The ribbon width (*W*) is on average 9.3, 17.9 and 26.7 nm for the smallest observed helices and is nicely correlated with the determined diameters; larger widths give larger diameters (Figure 2.6).

Based on molecular modeling, a fully extended **OPV_{4b}** is about 5.1 nm while the core is 2.5 nm which is in agreement with the 2.4 nm found by STM. Depending on the amount of interdigitation of the lateral wedges (about 1.3 nm in length), the length of a bilayer of **OPV_{4b}** will vary between 8.5 and 10.1 nm. Depending on how far the alkyl tails are interdigitated, which also exists in the monolayers studied by STM, this bilayer-length strikingly corresponds to the measured increase in ribbon widths. A proposed molecular arrangement is depicted in Figure 2.6; with ribbon-widths of the thinnest fibers representing bilayers (8.7 nm), two bilayers (17.4 nm) and three bilayers (26.1 nm). The narrowest helix has a pitch length of approximately 25 nm corresponding to roughly 90 molecules, assuming a π - π stacking distance of 0.34 nm.

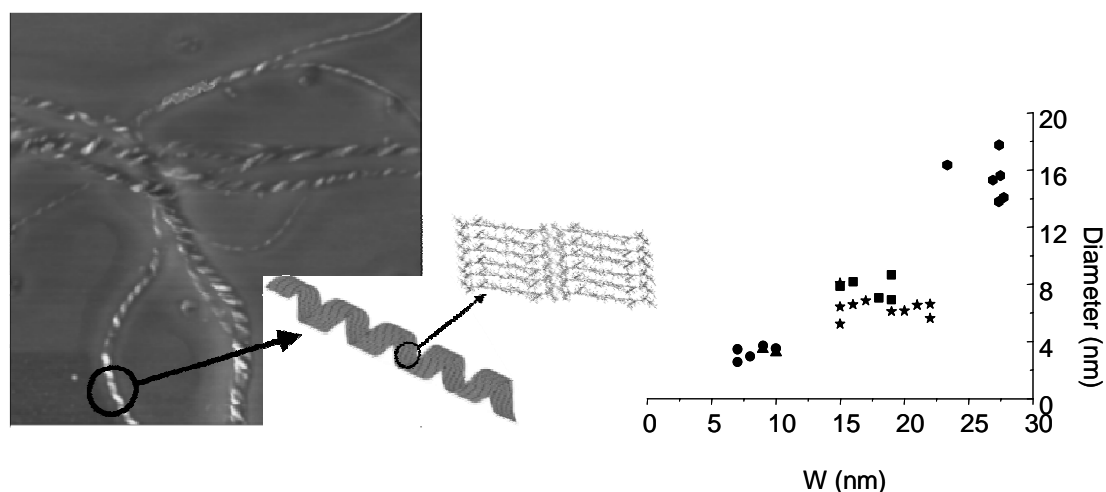


Figure 2.6: Phase image ($1 \times 1 \mu\text{m}^2$, z -scale 25°) of **OPV_{4b}** (left) with proposed model for the thinnest helices based on a curling bilayer ribbon. The graph represents the relation between the ribbon widths and diameters of various narrowest helices on the silicon oxide surface. HyperChem V7.04 was used for geometry optimization.

The balance between molecule-surface and molecule-molecule interactions, must be decisive to the type of OPV assemblies observed. In all cases the starting point is molecularly dissolved species. In the case of graphite, a monolayer is initially formed in which the oligomers are lying flat on the substrate. During evaporation, individual molecules adsorb at this monolayer and due to π - π interactions other molecules stack, forming ribbons in which the molecules are oriented upright. The interactions of the molecules in the ribbons with the underlying monolayer prevents the formation of helical fibers. The self-assembly of the OPV molecules at silicon oxide surfaces can probably be interpreted as follows: the interaction between the π -conjugated segments is slightly stronger than their interaction with the substrate, allowing the OPV molecules to adsorb relatively upright to the substrate. These molecules act as nuclei for the growth of ribbons via π - π interactions with free OPV

molecules. Curling of the ribbons occurs with one preferred supramolecular chirality imposed by the stereochemistry of the single OPV molecules; a small local helicity, that enforces the long-range chiral order of the fibers.

2.5 SELF-ASSEMBLY IN SOLUTION

2.5.1 Self-Assembly in Water

The self-assembly of the amphiphilic OPV derivatives was studied in water. In comparison with chloroform solutions, the UV/vis absorption spectra in water are blue shifted to $\lambda_{\text{max}} = 402$ (OPV_{4b}), 426 (OPV_{5a}) and 435 nm (OPV_{5b}) with the appearance of a shoulder at $\lambda = 467$, 486 and 505 nm, respectively (Figure 2.7) which is a sign of exciton coupled chromophores. The fluorescence is strongly quenched in water and red shifted to $\lambda_{\text{em,max}} = 548$ (OPV_{4b}). For OPV_{5a} and OPV_{5b} two emission maxima are observed at $\lambda = 546$ and 585 nm (OPV_{5a}) and 543 and 583 nm (OPV_{5b}). The absorption and fluorescence data show that the OPV oligomers are aggregated in an H-type fashion. A bisignate Cotton effect (Figure 2.7) was observed for OPV_{4b} in water at the π - π^* band with a positive Cotton effect at $\lambda = 384$ nm and a negative Cotton effect at $\lambda = 424$ nm. The zero crossing of the CD signal ($\lambda = 400$ nm) lies close to the absorption maximum of the chromophore. OPV_{5a} gave a similar strong bisignate Cotton effect with positive and negative peaks at $\lambda = 405$ and 447 nm, respectively, and with a zero-crossing of the CD signal at $\lambda = 423$ nm, close to the absorption maximum of the π - π^* band. Similar results are obtained for OPV_{5b} with peaks at $\lambda = 404$ and 464 nm with the zero-crossing at $\lambda = 425$ nm.

The aggregation process of the amphiphiles was further investigated by temperature dependent UV/vis, fluorescence and CD spectroscopy (Figure 2.7). By plotting the CD intensity against the temperature, OPV_{4b} shows a transition at 321 K (Figure 2.8). The transition is fully reversible, however, with a hysteresis of about 40 K (data not shown). Fluorescence measurements reveal that the emission of OPV_{4b} is still quenched³⁰⁴ at a temperature above 321 K, while the maximum is red-shifted compared to that in chloroform. This behavior indicates that the amphiphiles of OPV_{4b} are still aggregated above this transition temperature. The disappearance of the Cotton effect above 321 K shows, however,

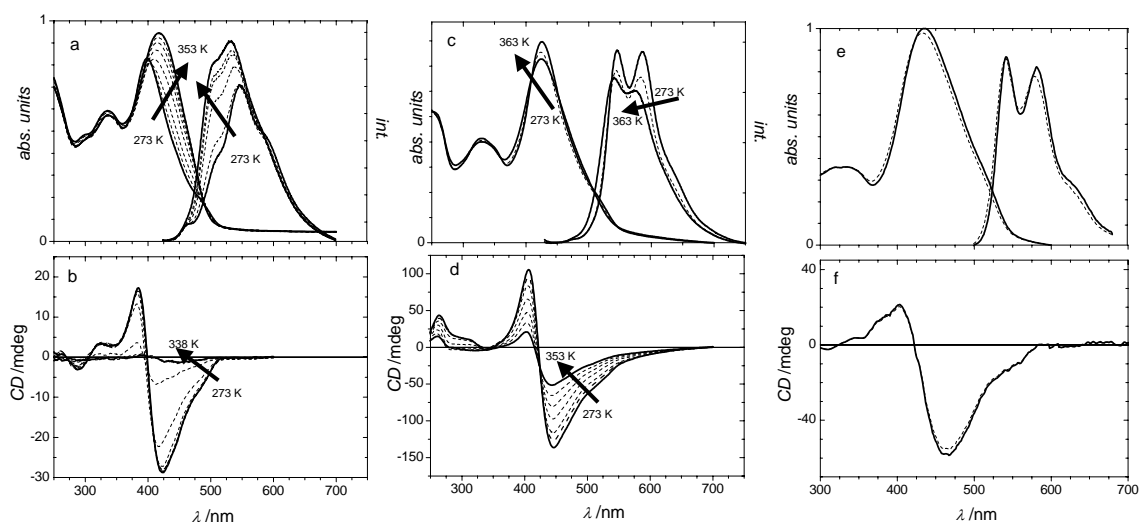


Figure 2.7: Temperature dependent UV/vis, fluorescence and CD measurements for OPV_{4b} (a,b), OPV_{5a} (c,d) and OPV_{5b} (e,f) (only 293 K (solid) and 353 K (dashed) are plotted) at 1.6×10^{-5} mol/L in water.

that the transition is due to the transformation of chiral aggregates into non-chiral aggregates. In the UV/vis spectra, a red shift from $\lambda_{\max} = 400$ nm to $\lambda_{\max} = 417$ nm is observed upon heating, which could point to conformational changes of the oligomers. Another explanation is that the disorder in the aggregates lead to more distance between the oligomers in the aggregates resulting in a weaker exciton coupling.

OPV_{5a} displays similar features, although in this case, a dampened transition occurs. The Cotton effect shows a nearly linear decrease with increasing temperature (Figure 2.8) while the fluorescence and absorption spectra show only modest changes with temperature. Therefore, we assume that the transition occurs from well-ordered chiral aggregates to disordered aggregates. In contrast, aggregates of **OPV_{5b}** are very stable, upon increasing the temperatures nearly no spectral changes are observed.

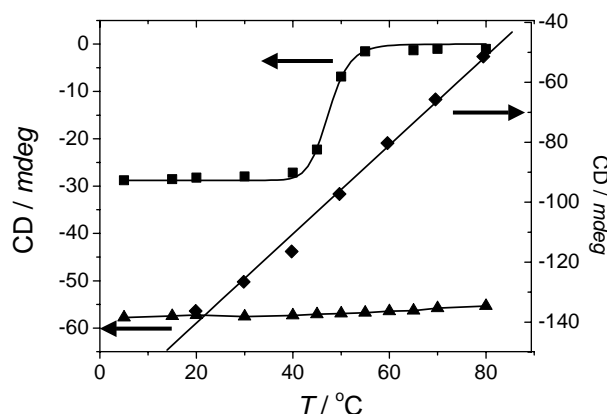


Figure 2.8: Change of the Cotton effect of **OPV_{4b}** (squares), **OPV_{5a}** (diamonds) and **OPV_{5b}** (triangles) as a function of temperature at 1.6×10^{-5} mol/L in water. Lines are drawn to guide the eye.

TM-AFM was used to determine the aggregate structures of **OPV_{4a}**, **OPV_{5a}** and **OPV_{5b}** in water; Figure 2.9 shows an image where a 5 μ L droplet of **OPV_{5a}** in water (1.6×10^{-5} mol/L) is evaporated on a silicon oxide surface. The images show regular shaped individual spheres of 47 nm in diameter, on average after correction for tip-broadening,³⁰⁵ and 18 nm in height. Dynamic light scattering (DLS) experiments confirmed spherical objects in water for **OPV_{5a}**. Confocal microscopy allows the measurement of fluorescence images at several nodal

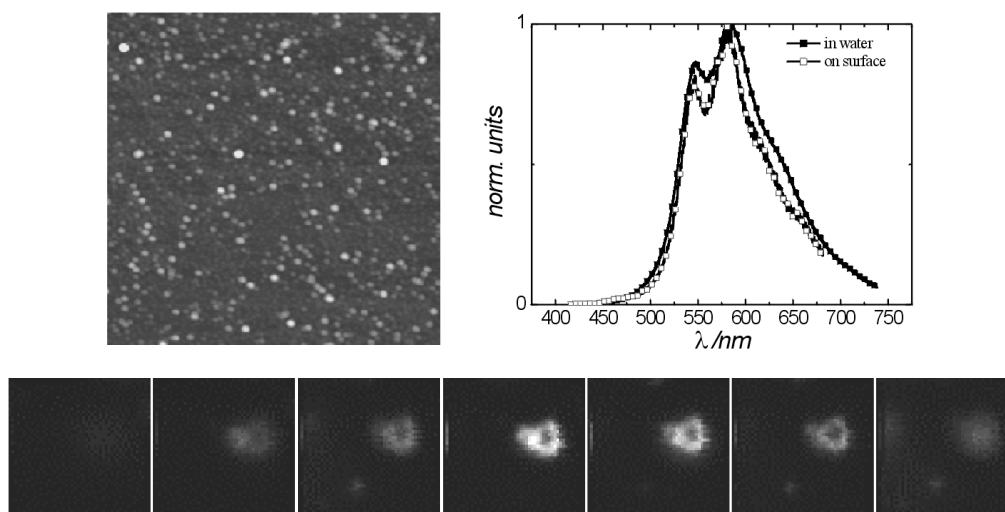


Figure 2.9: TM-AFM height image (top left) of **OPV_{5a}** ($2.5 \times 2.5 \mu\text{m}^2$ z-scale 25 nm) deposited from water (1.6×10^{-5} mol/L) on a silicon oxide surface. Fluorescence spectra (top right) of vesicles in water (closed squares) and on a glass surface (open squares). At the bottom is shown a series of z-sliced fluorescence images of one vesicle.

planes through the spheres. A series of z -scans through the spheres are displayed in Figure 2.9, and the doughnut-shaped substructure confirms that the **OPV_{5a}** assembles into hollow spheres, *i.e.* vesicles. The fluorescence spectrum of a single vesicle is the same as recorded in solution.

It is well-known that ethyleneglycol and crownethers can harbor cations as guests and, if attached to π -conjugated systems, the spectral responses observed are often different from the host system; a phenomenon which is the basis of a sensor.²⁹² The influence of cations on the vesicles in water was studied. Adding the smallest alkali ion, lithium, to **OPV_{5a}** (2.5×10^{-5} mol/L) resulted in a decrease in the Cotton effect. The sensitivity was low, a large excess of salt being needed per tetraethyleneglycol chain. Moreover, once the ions have penetrated into the shell of the vesicles, they may induce flexibility between the OPV oligomers; this results in a decrease of CD effect in the supramolecular aggregates (Figure 2.10). Adding LiClO_4 to vesicles of **OPV_{5b}** (2.5×10^{-5} mol/L), showed similar effects, however, only at even higher salt equivalents. Adding KCl to **OPV_{5b}** did not show any spectral changes, even upon heating, sonicating or at very high salt concentrations. Similar results were obtained for adding NaCl. The response of the vesicles is presumably inhibited by favorable solvation of ions by water or the lack of space for the alkali ions to penetrate the aggregate. The next Section describes a study of the response of molecularly dissolved **OPV_{5b}** on the presence of sodium and potassium ions.

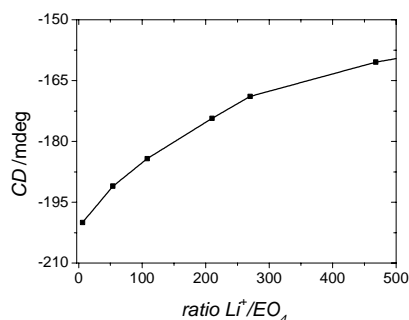


Figure 2.10: Change of the Cotton effect for **OPV_{5a}** in water (2.5×10^{-5} mol/L) as function of salt/ EO_4 ratio.

2.5.2 Self-Assembly in Chloroform by Ions

The effect of the addition of salts was studied in chloroform, a solvent in which **OPV_{5b}** is molecularly dissolved. Adding NaPF_6 to **OPV_{5b}** was followed by emission spectroscopy. Initially, titrating the first molar equivalent of Na^+ , an isobestic point at $\lambda = 568$ nm develops and the emission maximum shifts from $\lambda = 518$ nm to $\lambda = 525$ nm. Upon adding the next molar equivalent of salt, the emission maximum remains at $\lambda = 525$ nm. The titration curve (Figure

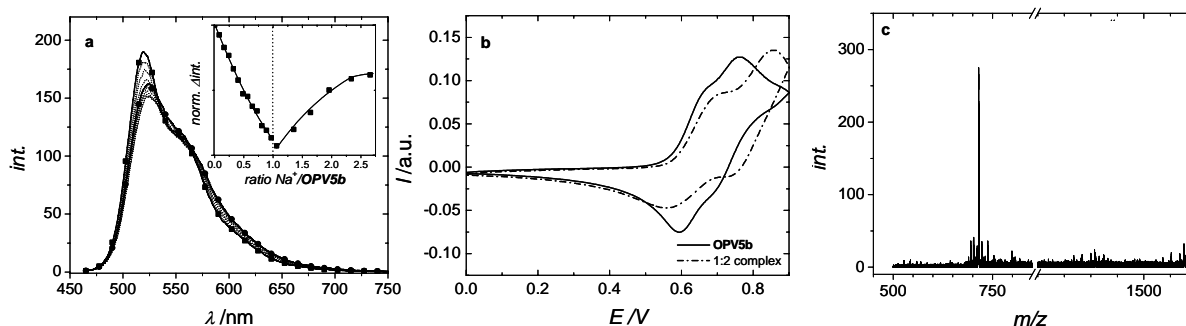


Figure 2.11: (a) Emission spectra of **OPV_{5b}** upon adding NaPF_6 (4.4×10^{-6} mol/L, chloroform, squares, 0 eq.; spheres, 2 eq.), inset shows change in emission intensity at $\lambda = 518$ nm as function of the ratio $\text{Na}^+/\text{OPV}_5\text{b}$. (b) Cyclic voltammogram of **OPV_{5b}** and 1:2 complex vs Fc^+/Fc . (c) ESI-MS spectrum of the 1:2 complex.

2.11a), shows that a 1:2 ($\text{OPV}_5\text{b}:\text{Na}^+$) complex is formed. Remarkably, the changes in intensity are minor and first a drop and then an increase is observed while the UV/vis spectra did not change during the titration. Adding a large excess of Na^+ did not alter the emission and absorption spectra further. The binding could be analyzed with 1:2 binding model resulting in two step-wise association constants, $K_1 = 1.5 \times 10^7 \text{ M}^{-1}$ and $K_2 = 2.5 \times 10^5 \text{ M}^{-1}$ and an overall association constant $K_a = 3.8 \times 10^{12} \text{ M}^{-2}$.³⁰⁶ The interaction parameter $\alpha < 0.1$, indicating that there exist negative cooperativity between the binding sites. The voltammetric response (Figure 2.11b) of the 1:2 complex showed that the first oxidation potential hardly changed and the peak potential separation increased. The complexes were also examined with electrospray ionisation mass spectrometry (ESI-MS), a technique known to probe intact non-covalent molecular ions in the gas phase.³⁰⁷ The principal mass of 715.0 m/z corresponds to the formation of 1:2 complex (Figure 2.11c).

The addition of KPF_6 to OPV_5b ($7.1 \times 10^{-7} \text{ mol/L}$) showed a different behavior. The emission maximum shifted 26 nm to the red and a clear isobestic point at $\lambda = 568 \text{ nm}$ developed in the emission spectra (Figure 2.12a). The intensity change of the fluorescence spectra at $\lambda = 518 \text{ nm}$ is plotted in the inset of Figure 2.12a and the straight line saturates at equimolar ratios. In the presence of excess salt, the 2:2 complex can dissociate into a 1:2 ($\text{OPV}_5\text{b}:\text{K}^+$) complex. The binding isotherm could be analysed with a 2:2 binding model resulting in $K_F = 3 \times 10^{18} \text{ M}^{-3}$ for the formation of a 2:2 complex and a $K_B = 4 \times 10^2 \text{ M}^{-1}$ for breaking up the 2:2 complex to form a 1:2 complex.³⁰⁶ Assuming that OPV_5b has two independent binding sites, this gives for the association between one potassium ion and one binding site $K_a = 10^5 \text{ M}^{-1}$. Another interesting value in this model is the c_{50} value, *i.e.* the concentration necessary to break up 50% of the 2:2 complex by dilution, this turns out to be around $3 \times 10^{-7} \text{ M}$. Under these dilute conditions there is no significant concentration of the dissociated 1:2 complex, however, above this concentration, the dissociation may cause some divergence from linearity before stoichiometric amounts of salt are added. The voltammetric response showed that the oxidative redox potential of 0.64 V for OPV_5b does not shift upon adding potassium. In the ESI mass spectrum, the principal mass found was 1421.8 m/z corresponding to a 2:2 complex indicating that at low concentrations a sandwich-type structure ($7.1 \times 10^{-7} \text{ mol/L}$) is formed predominantly. Low intensity peaks at 1076, 961 and 730 m/z could be related to 3:4, 2:3 and 1:2 complexes.

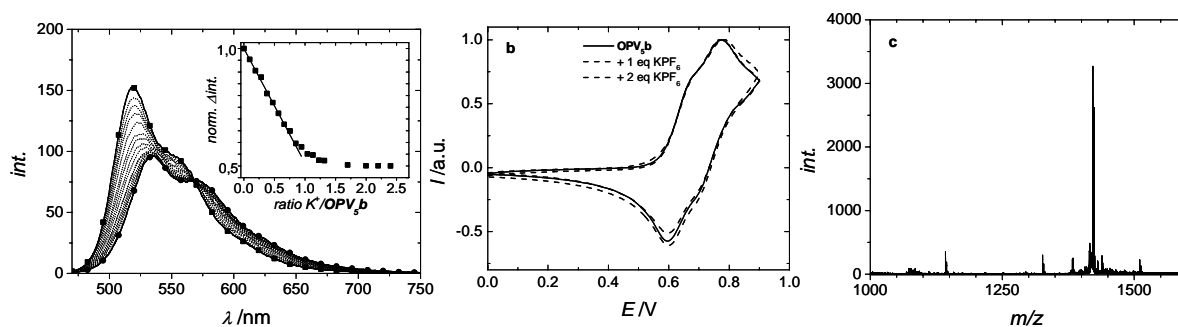


Figure 2.12: (a) Emission spectra of OPV_5b upon adding KPF_6 ($7.1 \times 10^{-7} \text{ mol/L}$, chloroform, squares, 0 eq. salt; spheres, 2 eq.), inset shows change in emission intensity at $\lambda = 518 \text{ nm}$ as function of the ratio $\text{K}^+/\text{OPV}_5\text{b}$. (b) Cyclic voltammogram of OPV_5b , 1 eq and 2 eq. KPF_6 . (c) ESI-MS spectrum of the complex.

TM-AFM images also show the effect of the potassium on the morphology of OPV_5b when small deposits from $7.1 \times 10^{-7} \text{ mol/L}$ in chloroform were cast to silicon oxide surfaces. When no salt and up to 2 equivalents of potassium are added, small blobs of material are

formed (Figure 2.13c), whereas in the presence of excess of potassium, elongated structures are observed (Figure 2.13d). The worm-like structures are about 2 nm in height and range over micrometers long and are constructed from assembling OPVs promoted by the interaction of potassium with adjacent crownether moieties. In contrast to other amphiphiles, for **OPV_{5b}** another type of morphology is now possible on silicon oxide wafers. Vesicles are observed when drop cast from a bad solvent (water, 5×10^{-6} M, Figure 2.13a) and helical ribbons from a good solvent (THF, 1×10^{-5} M, Figure 2.13b).

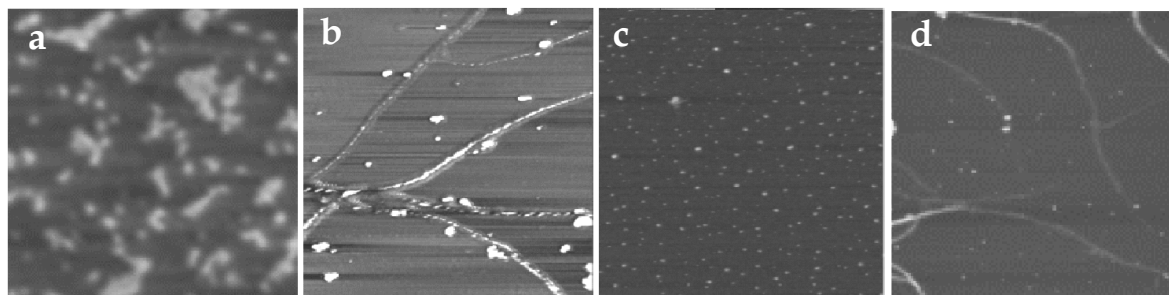


Figure 2.13: TM-AFM images of **OPV_{5b}** from (a) water (5×10^{-6} M), (b) THF (10^{-5} M) and chloroform (7.1×10^{-7} M) (c) without and (d) with KPF_6 (40 moleq.) on silicon oxide surfaces. All images are $1.5 \times 1.5 \mu\text{m}^2$. (a) height (z-scale 50 nm), (b) phase (z-scale 20°), (c) height (z-scale 5 nm), (d) height, (z-scale 10 nm).

2.6 CONCLUSIONS

The self-assembly of a series of oligo(p-phenylenevinylene)s (OPVs) having a different hydrophobic/hydrophilic balances has been studied. Stable monolayers could only be constructed from hydrophobic OPVs on the liquid/solid interface with an internal structure that depends on the conjugation length and the chirality of the OPV. Fibrils have been created after slow evaporation of a solvent in which the OPVs were molecularly dissolved. This was found to be independent of the hydrophobic/hydrophilic balance in the OPV derivatives. In all cases, on graphite, a rod-like morphology appeared, on an initially formed monolayer. On silicon oxide, left-handed helical ribbons of chiral OPVs were observed while in the case of an achiral OPV non-helical ribbons were present. The self-assembly of hydrophilic OPVs could be influenced by adding alkaline salts. Vesicles were constructed in water by the hydrophilic OPVs having a helical to non-helical phase transition. The emission of a single vesicle on the surface was similar to emission of vesicles in water.

These results show that a variety of self-assembled architectures can be obtained using similar building blocks. The approach of pre-organizing the π -conjugated oligomers in solution offers a valuable tool to control the properties in the solid state. This is an important observation for using such objects in the field of supramolecular electronics. However, enhanced control over the positioning of the conjugated building blocks in these objects is highly required. So far, the supramolecular assemblies have a distribution of dimensions. In the next chapter hydrogen-bonding interactions are introduced to increase the level of control as they are known to be directional and selective. However, addressing, positioning and manipulating nanoscopic objects on surfaces remain critical issues. The following Section indicates one possible route to solving these problems.

2.7 Towards Positioning Nanoscopic Supramolecular Objects

Rod-like and spherical aggregates were formed by dendrimers functionalized with OPVs (**G3OPV**, Figure 2.14a),²⁶⁷ kindly provided by M. Fransen. When **G3OPV** was dispersed in decanol a blue shift of the absorption maximum of $\Delta\lambda = 42$ nm was observed in comparison with dichloromethane ($\lambda_{\text{max}} = 417$ nm (CH_2Cl_2) vs $\lambda_{\text{max}} = 375$ nm (decanol), data not shown). At the same time, the onset of the spectrum red shifts from $\lambda = 480$ to 500 nm. This behavior is typical for H-type aggregated OPV units. TEM and TM-AFM revealed the formation of rod-like aggregates (Figure 2.14b and c) of micrometer dimensions (lengths of 3.2 to 0.3 μm , widths of about 0.20 μm). When **G3OPV** was dispersed in water (pH = 1) also a blue shift of the absorption maximum was observed ($\lambda_{\text{max}} = 402$ nm, data not shown) with at $\lambda = 480$ nm a shoulder as a sign of exciton coupling. DLS revealed an average particle size distribution of 300 nm. The spherical aggregates were shown by TEM to have an average diameter of 300 nm. The size of the aggregates strongly depends on the pH of the aqueous solution. For example, at pH 5.5 aggregates are as large as 3 μm were observed.

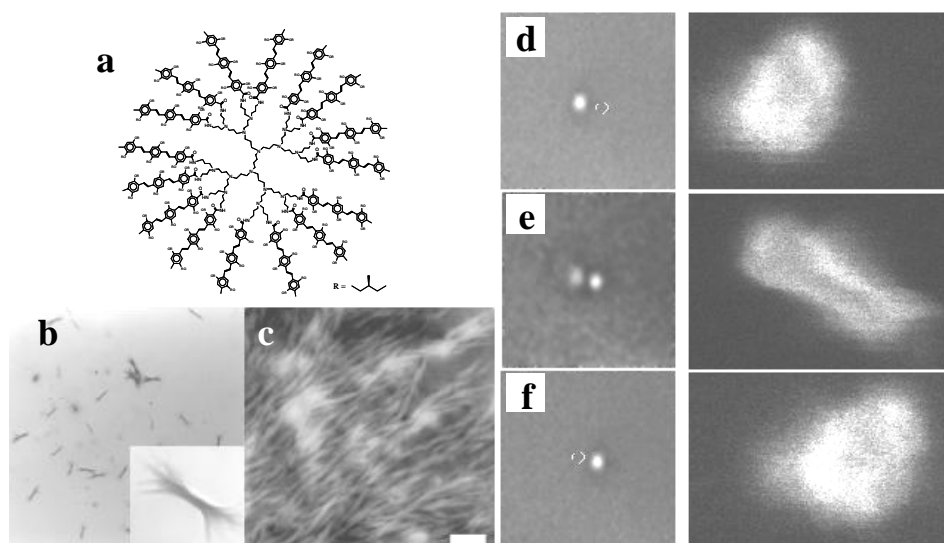


Figure 2.14: (a) **G3OPV** (b) TEM ($50 \times 50 \mu\text{m}^2$ and $1.5 \times 1.5 \mu\text{m}^2$) (c) TM-AFM image (height, z -scale 22 nm; bar 120 nm) of a deposited solution of **G3OPV** in decanol. The 'switch' process in the dual trap visualized in transmission (left d,e,f) and fluorescence (right d,e,f); the diameter of the structures formed is $\sim 1 \mu\text{m}$ in both cases. The distance between the traps is about 3 μm . The dashed circles in the transmission images indicate the position of the turned off traps: (d) trap 1 is turned on (e) trap 1 is turned off and trap 2 is turned on (f) trap 2 is turned on.

The aggregates, which are formed in protic polar media could be built up from bilayers formed by the amphiphilic OPV dendrimers in which the conformation is similar to that found previously in the Langmuir layers.²⁶⁷ In these layers the OPVs are arranged in H-type aggregates.

Studies to trap and manipulate these vesicles in water by the aid of optical tweezers have been performed in acidified aqueous solutions (pH = 5.5). By optical trapping, an object is forced to stay near to the focal point of a highly focussed, non-absorbed beam of light.^{308b} The highly focussed infrared beam forces the vesicles to accumulate near the focus of the beam which results in a very high, local concentration of vesicles in the optical trap (Figure 2.14). Dual trapping provided insight into the effect of trapping and the accumulation of vesicles in a small volume. The dual trap consists of two diffraction limited trapping spots a few μm apart from each other, which can be turned on and off independently. After releasing the optical beam where the vesicles were trapped originally (Figure 2.14d) and turning on the second trap, the gathered vesicles 'jump' to the second trap (Figure 2.14e), thus demonstrating the attractive interaction between vesicles or the formation of a new assembly, created by the second trap (Figure 2.14f). This result shows that manipulation of nanoscopic objects by optical tweezers is a new and promising tool for gaining control over their position.

3 SELF-ASSEMBLY OF OLIGO(*p*-PHENYLENEVINYLENE)S INTO ROSETTES AND THEIR TUBULAR SELF-ASSEMBLY

ABSTRACT

*The self-assembly of diaminotriazine equipped oligo(*p*-phenylenevinylene)s having different π -conjugation lengths has been studied at the liquid/solid interface and in solution. On graphite, either dimers or rosettes are formed; strongly depending on the length of the OPV. The difference in length changes the balance between hydrogen-bond formation, van der Waals interactions between the alkyl chains and the substrate, and the space-filling of the surface, as probed by scanning tunneling microscopy. Surprisingly, the 'rotation direction' of the rosette is dependent on the length of the OPV and is presumed to result from efficient packing of the rosettes on graphite. Optical techniques and small angle neutron scattering showed the presence of long helical columnar aggregates in apolar solutions comprised of stacked rosettes. These tubules could be visualized in the solid state by atomic force microscopy.*

CONTENTS

	<i>page</i>
3.1 Introduction	42
3.2 Synthesis	42
3.3 Self-Assembly at the Liquid/Solid Interface	43
3.4 Self-Assembly in Solution	46
3.4.1 Optical Properties	46
3.4.2 Structure Properties	48
3.5 Conclusions	49

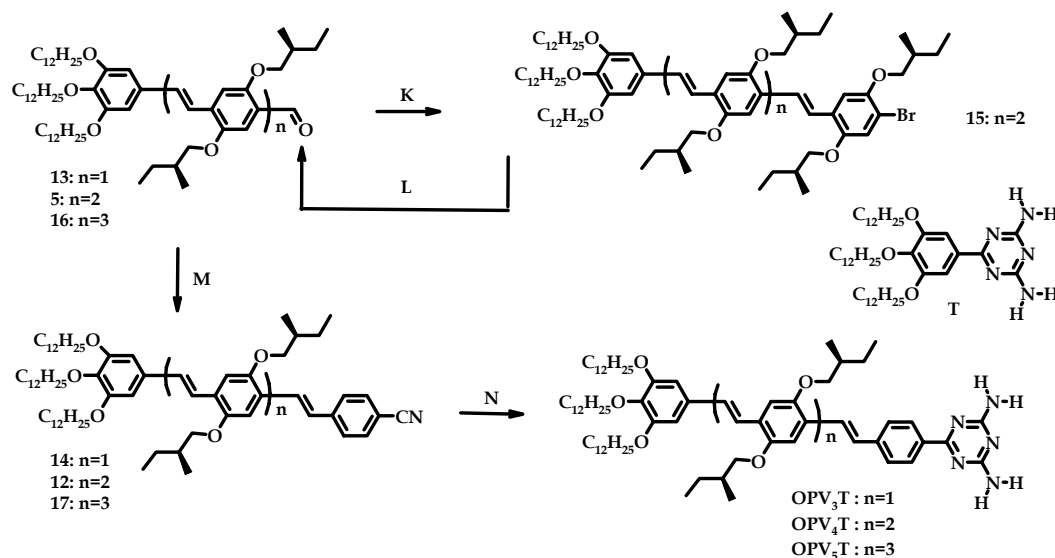
3.1 INTRODUCTION

Artificial cylindrical and tubular aggregates of specifically programmed molecules are of interest as sensing, transporting, and bioactive systems. An important design motif for the formation of these aggregates is ring stacking and most of these stacks are composed of molecular rings, *e.g.* cyclic oligopeptides.³⁰⁹ Hydrogen-bond interactions between molecules are attractive candidates for the formation of the well-defined supramolecular cyclic structures due to their spatial arrangement and directionality.³¹⁰ Multiple examples exist of cyclic structures in solution based on hydrogen-bonding building blocks.³¹¹⁻³¹⁷ Also at surfaces, cyclic hydrogen-bond structures have been observed by STM.^{219,276,318-326} Further aggregation of cyclic supramolecular structures into extended aggregates is, however, relatively scarce.³²⁷⁻³³⁰ Recently, Stupp *et al.* described an elegant example of the self-assembly of dendron rod-coil molecules into tetrameric hydrogen-bonded cycles that further organize into helical nanoribbons by additional hydrogen-bonding and π - π interactions.^{5,331} Nanohelices of cadmium sulfide were made by the mineralization of such aggregates. Fennire *et al.* demonstrated the formation of rosette nanotubes in which the helicity could be tuned by using amino acids.³³²

So far, π -conjugated building blocks have never been used to create tubular aggregates and up to now, most if not all π -conjugated oligomers self-assemble through the stacking of rods into ribbons. To create cylindrical or, even more exciting, tubular aggregates with perfect space filling, requires another, hierarchical assembly process. This Chapter, describes a unique and unexpected process for the construction of hexameric π -conjugated rosettes that self-assemble into chiral tubular objects.

3.2 SYNTHESIS

The structures of oligo(*p*-phenylenevinylene) derivatives **OPV_xT** (*x* indicates the number of phenyl rings) and an achiral analogue (**T**) are displayed in Scheme 3.1. These oligomers are endcapped at one end with a tridodecyloxybenzene wedge and at the other end with a diaminotriazine hydrogen-bonding group. Depending on the length of the oligo(*p*-phenylenevinylene) moiety, the molecules contain a different number of enantiomerically pure (*S*)-2-methylbutoxy groups; namely no (**T**), two (**OPV₃T**), four (**OPV₄T**) or six (**OPV₅T**). The synthesis of the four compounds require similar reaction conditions. The synthesis of **T** and **OPV₃T** are described elsewhere.^{333,334} **OPV₄T** was synthesized from aldehyde derivative **5**³³⁵ which was converted through a Wittig-Horner coupling reaction to nitrile derivative **12** in high yield (91%) by using diethyl(4-cyanobenzyl)phosphonate (Scheme 3.1). After reaction with dicyandiamide, **OPV₄T** was obtained in 74% yield. The synthesis of the pentamer **OPV₅T** followed an additional cycle, with respect to **OPV₄T** (step K and L) of Wittig-Horner and Bouveault reactions to elongate the conjugation length. The synthesis of trimer **OPV₃T** required one cycle less. Analytically pure materials were obtained after extensive purification procedures (column chromatography). The ¹H-NMR and ¹³C-NMR spectra of **OPV₄T** were completely assigned with help of 1D and 2D NMR techniques and used as a references for the other compounds.



Scheme 3.1: Synthetic route to OPV_nT carrying diaminotriazine units. K) DMF/THF, 7, $KOC(CH_3)_3$, 4h, 91% L) 1. diethylether, $n-BuLi$, $-10^\circ C$; 2. DMF, 1h, 88% M) DMF/THF, diethyl(4-cyanobenzyl)phosphonate, $KOC(CH_3)_3$, 4h, 91% for 12, 82% for 17 N) dicyandiamide, 2-methoxyethanol, KOH, 8h, reflux, 74% for OPV_4T , 60% for OPV_5T .

3.3 SELF-ASSEMBLY AT THE LIQUID/SOLID INTERFACE

Typical STM images of monolayer structures appear immediately after bringing the molecules, dissolved in 1-phenyloctane, onto highly oriented pyrolytic graphite (HOPG) (Figure 3.1). Domains span a few tens to several hundreds of nanometers. Smaller scan-areas provide a closer look into the positioning of the molecules. Each bright rod in the large scale images is resolved into individual bright spots in these higher magnifications. In the monolayers of **T**, the length of the bright rods is 1.7 nm, which is almost twice the length of the aromatic backbone of **T** (0.8 nm). Thus, **T** presumably arranges as dimers through the formation of hydrogen-bonds between two diaminotriazine groups. All dodecyloxy chains are resolved and interdigitate with chains of neighboring molecules. The unit cell contains two molecules ($a_1 = 2.3$ nm, $a_2 = 2.9$ nm, $\alpha = 66^\circ$ for **T**) and a tentative molecular model is presented in Figure 3.1a3. As expected for achiral compounds, both mirror image structures are formed (see Chapter 2) and the angle between a main symmetry axis of graphite and unit cell vector a measures $+12^\circ$ and -11° .

Unexpectedly, the STM images for OPV_xT ($x = 3,4$; Figure 3.1b,c) showed molecules arranged in hexameric rosette structures. These resemble a six-bladed windmill lying flat on the surface with six diaminotriazine units associated through hydrogen-bonding forming the center of the rosette.³³⁶ The blades appear as bright rods corresponding to the conjugated backbones of the OPVs in which individual phenyl rings are sometimes resolved. The rosettes are ordered in rows and form a hexagonal 2D crystal lattice with alkyl chains interdigitating with adjacent rosettes. The cavity of the rosettes has an estimated diameter of 0.7 nm. Unit cells contain six molecules ($a_1 = 5.5$ nm, $a_2 = 5.6$ nm, $\alpha = 60^\circ$ for OPV_3T , and $a_1 = 6.1$ nm, $a_2 = 6.2$ nm, $\alpha = 60^\circ$ for OPV_4T) and a tentative molecular model is presented in Figure 3.1b3 (OPV_3T) and Figure 3.1c3 (OPV_4T).

Although OPV_3T and OPV_4T appear to order in a similar way; namely, with oblique unit cells, rosette structure, specific orientation of alkyl chains and OPV backbone with respect to the graphite symmetry axes, a comparable angle between the OPV backbone and the

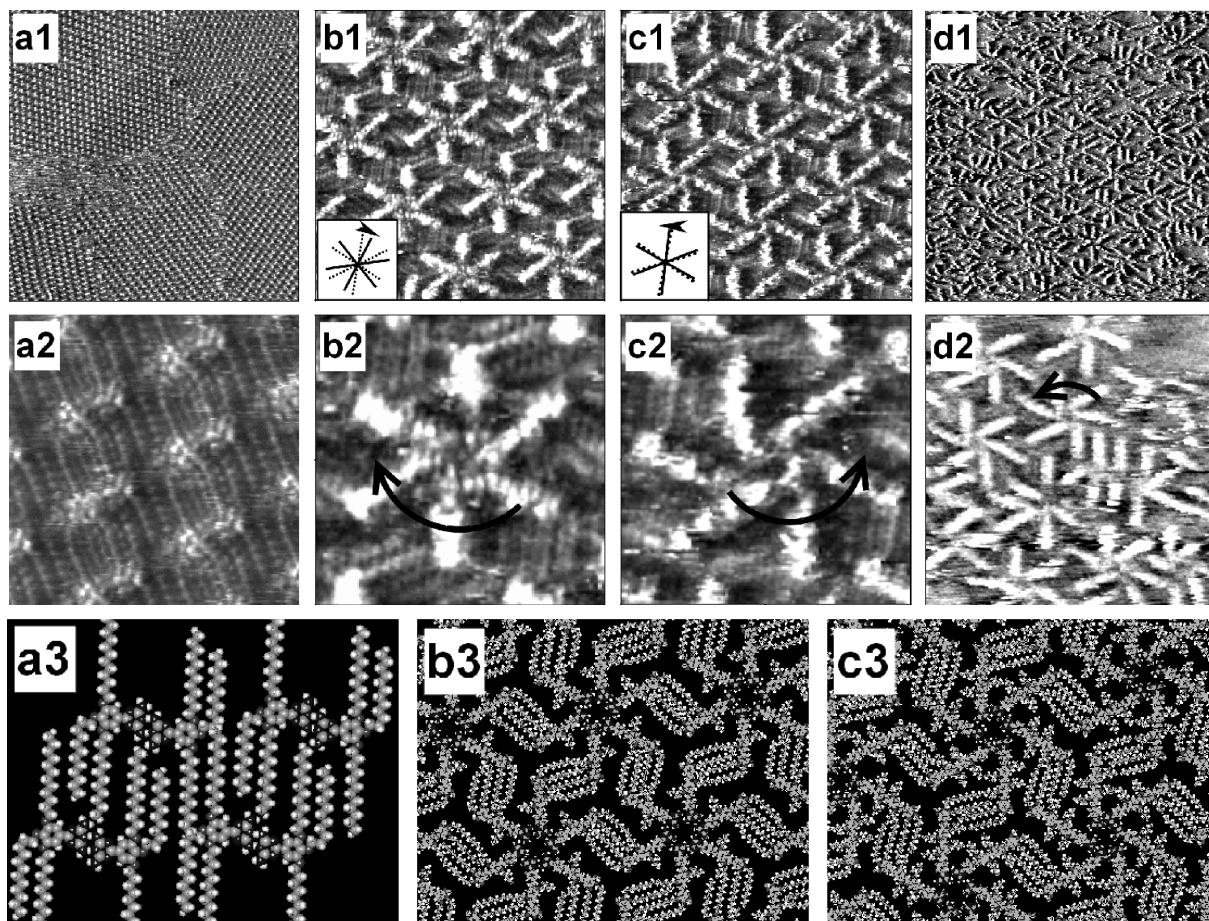


Figure 3.1: STM images of monolayers physisorbed at the liquid/solid interface. (a) T: (a1) $100 \times 100 \text{ nm}^2$. (a2) $7.2 \times 7.2 \text{ nm}^2$. (a3) tentative molecular model. (b) OPV_3T : (b1) $14.4 \times 14.4 \text{ nm}^2$. (b2) zoom in on b1. (b3) tentative molecular model. (c) OPV_4T : (c1) $18.4 \times 18.4 \text{ nm}^2$. (c2) zoom of c1. (c3) tentative molecular model. (d) OPV_5T : (d1) $54 \times 54 \text{ nm}^2$. (d2) $22 \times 22 \text{ nm}^2$. Inset in b1 and c1 shows the propagation direction of rosette rows (solid line) and the main symmetry axes of graphite (dashed line). The red arrow in b2 and c2 indicates the 'rotation direction' of the rosette.

dodecyloxy chain, unidirectional orientation of the molecules in individual rosettes, nevertheless the organization of the molecules within a single rosette surprisingly differs. The rosettes of OPV_3T and OPV_4T have different 'rotation directions', as shown by the orientation of the OPV backbones; OPV_3T exclusively rotates clockwise (CW, see arrow Figure 3.1b2) while in OPV_4T rosettes, the molecules are exclusively arranged in a counterclockwise (CCW, see arrow Figure 3.1c2) fashion. No rosettes of opposite chirality were found. Also the relative orientation of rows of rosettes with respect to the main crystallographic axes of graphite shows opposite 2D chirality ($+18^\circ$ and -3° for OPV_3T and OPV_4T , respectively). This is the first observation of simultaneous point and organization chirality in a monolayer. OPV_5T does not form arrays of rosettes extending into a well-ordered 2D crystal lattice (Figure 3.1d), but gives a disordered phase with the local formation of rosettes rotating counterclockwise.

In all cases, hydrogen-bond interactions between the diaminotriazine headgroups specifically positions the molecules in monolayers in addition to interactions between alkyl chains, molecule-substrate interactions and the formation of a dense molecular packing with a minimum of steric interactions. Figure 3.2 illustrates three types of hydrogen-bonding patterns.³³⁷⁻³³⁹ Type 1 leads to dimer formation (a,b), type 2 can result in rosette formation (c,d) and type 3 can lead to tape formation (e,f). Although the binding constants are expected to be

rather low and of equal strength for all conformations, extended structures would prevail by the additional enthalpic gain.

However, tapes (e and f) are not observed, only for **OPV₅T** some parts of the monolayer show aligned OPVs that may be assigned to tape formation. Tape formation on a large scale is probably excluded by steric interactions between (*S*)-2-methylbutoxy groups; tape formation would reduce the distance between OPV units from about 1.7 nm (see Chapter 2) to 1.2 (e) and 0.9 nm (f). Exclusive dimer formation (a,b) by **T** seems to be enforced by maximized interaction of the alkyl chains with graphite; all alkyl chains are adsorbed while modeling shows that tape formation would require that not all alkyl chains are adsorbed on the surface.

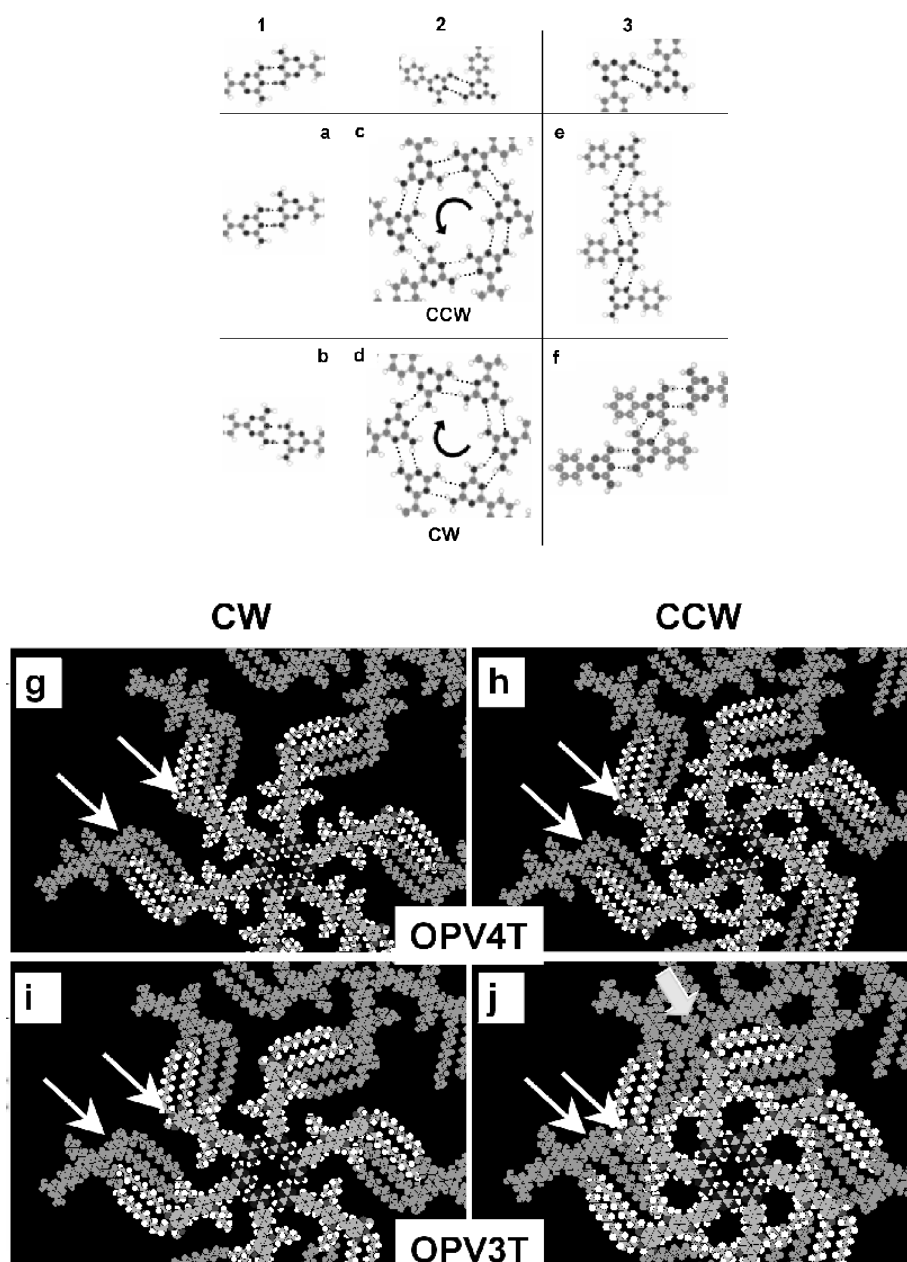


Figure 3.2: Schematic representation of possible interaction types (1,2,3) between two diaminotriazine units. Type 1 leads to dimer formation (a, b) being mirror-image structures. Type 2 leads to CCW (c) and CW (d) rosette formation being mirror-image structures. Type 3 leads to tape formation (e, f). Possible (g, i) CW and (h, j) CCW rosettes of **OPV₃T** and **OPV₄T**, respectively. Arrows indicate nearest phenyl rings from adjacent rosettes.

Rosette formation by **OPV₃T** and **OPV₄T** is apparently a balance of both type 1 (minimizing the steric interactions and maximizing alkyl-graphite interaction) and type 3 (maximize the hydrogen-bond interactions) allowing for a minimum free surface. Nonetheless, longer OPVs lead to rosette structures with increased empty surface in the periphery of the rosette; experimentally evidenced by restricted rosette formation by **OPV₅T**. Intuitively, one would expect that the 'rotation direction' is independent of the number of stereocenters, *i.e.* conjugated oligomer length, this is apparently not the case. The molecular models in Figure 3.2 show that CW and CCW structures are not mirror images; *i.e.* diastereoisomers, and as a result, they will differ in energy. The free volume of the **OPV₄T** rosettes is the least in the case of CCW rosettes and therefore expected to be more stable, which corresponds with the experimental observation. However, a CCW rosette of **OPV₃T** would be destabilized by the steric interactions of the OPV and dodecyloxy chains; hence the observed CW rosette structure can be explained.

3.4 SELF-ASSEMBLY IN SOLUTION

3.4.1 Optical Properties

With the STM results in hand, it is intriguing to study the behavior of the molecules in solution and to search for the self-assembly of the rosettes into space-filling tubules. The UV/vis absorption spectra of **OPV₃T** and **OPV₄T** in chloroform show structureless bands at $\lambda_{\text{max}} = 408$ and 430 nm, respectively. The fluorescence maxima are positioned at $\lambda_{\text{em,max}} = 470$ and 501 nm, respectively. The absorption and fluorescence data are characteristic of

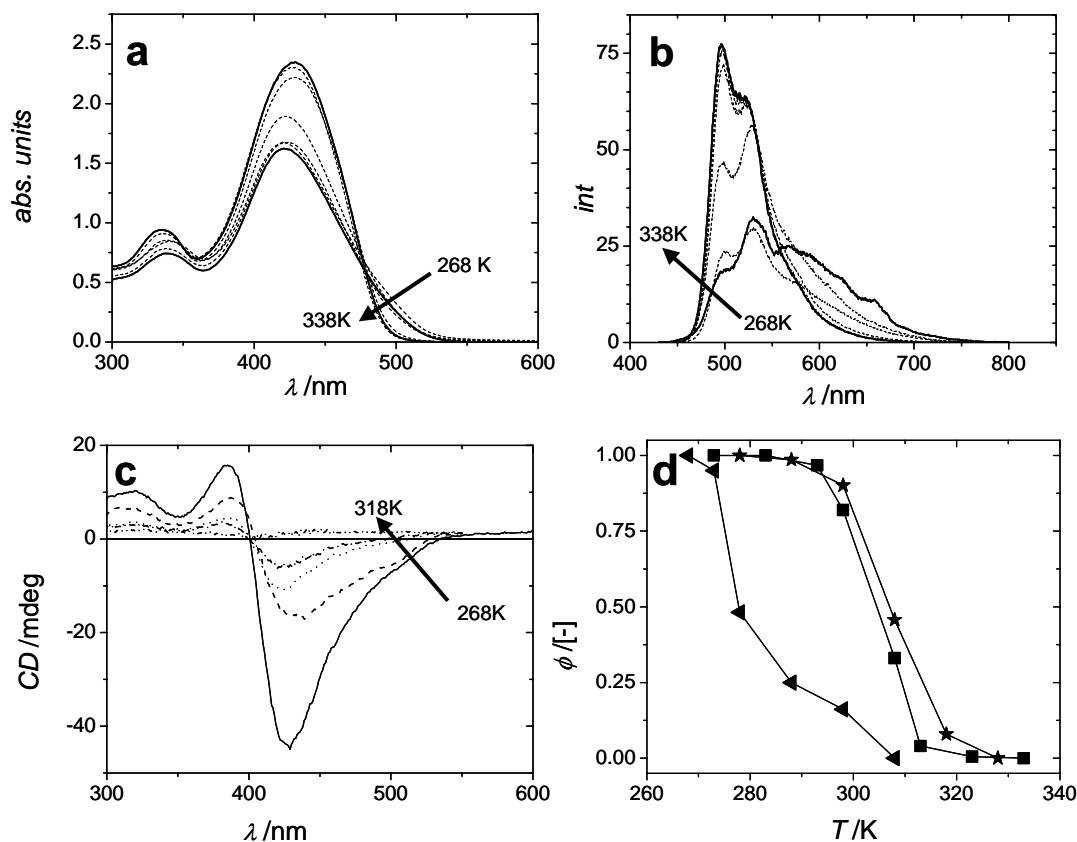


Figure 3.3: Temperature variable (a) UV/vis, (b) fluorescence and (c) CD spectra of **OPV₄T** in heptane solution (5×10^{-5} M). (d) Phase transition curves with changes (ϕ) in CD (triangle), fluorescence (star) and UV/vis (square) data versus temperature on a normalized scale for **OPV₄T**.

molecularly dissolved oligomers and the maxima shift to the red when the conjugation length increases.³⁴⁰ The UV/vis absorption spectrum of **OPV₄T** in heptane (5×10^{-5} M) shows a blue shift of the main band to $\lambda_{\text{max}} = 421$ nm (Figure 3.3a) and a red shift in the onset of the absorption. Similar spectral changes were observed in other apolar alkanes like pentane and dodecane. For **OPV₃T**, a similar shift in the onset of the absorption band is observed only at higher concentrations, while the absorption maximum remains unchanged.³⁴¹ The fluorescence intensity of **OPV₃T** (not shown) and **OPV₄T** in heptane (Figure 3.3b) are reduced and strongly red shifted to $\lambda_{\text{max}} = 510$ and 530 nm, respectively.

A bisignated CD effect for **OPV₄T** (Figure 3.3c) is observed exhibiting a positive Cotton effect [+] at higher energy ($\lambda_{\text{max},[+]} = 387$ nm) and a negative Cotton effect [-] at lower energy ($\lambda_{\text{max},[-]} = 428$ nm). The zero-crossing lies at $\lambda = 400$ nm, which is not related to a maximum in absorption for **OPV₄T** in heptane. Surprisingly, the bisignated CD spectrum of **OPV₃T** (Figure 3.4a) is opposite to that of **OPV₄T** ($\lambda_{\text{max},[-]} = 380$ nm and $\lambda_{\text{max},[+]} = 428$ nm). The zero-crossing of the Cotton effect of **OPV₃T** is positioned at $\lambda = 405$ nm which is close to the absorption maximum of the chromophore indicating strong exciton coupling. It is tempting to compare the opposite CD effects for the two molecules with the opposite chirality of the two molecules at the graphite surface (Section 3.3). However, for **OPV₄T**, an inversion of the Cotton effect with time was observed (Figure 3.4c). At 288 K, within 80 minutes an almost complete conversion was obtained ($\lambda_{\text{max},[-]} = 410$ nm and $\lambda_{\text{max},[+]} = 448$ nm) accompanied by a shifted zero-crossing to 422 nm which is in close proximity of the absorption maximum. Annealing of **OPV₃T** did not lead to sign reversal, only an increase of the Cotton effect was observed, while the zero-crossing is even closer to the absorption maximum. The sign reversal of **OPV₄T** shows first order kinetics with a rate constant of $k = 5.6 \times 10^{-4}$ s⁻¹ (Figure 3.4c, inset). The helix that is initially present is presumably the kinetically controlled aggregate while the helix that is finally formed is the thermodynamically stable one.³⁴² Hence, the exciton coupled CD spectra for **OPV₃T** and **OPV₄T** are the same for the thermodynamically stable structures.

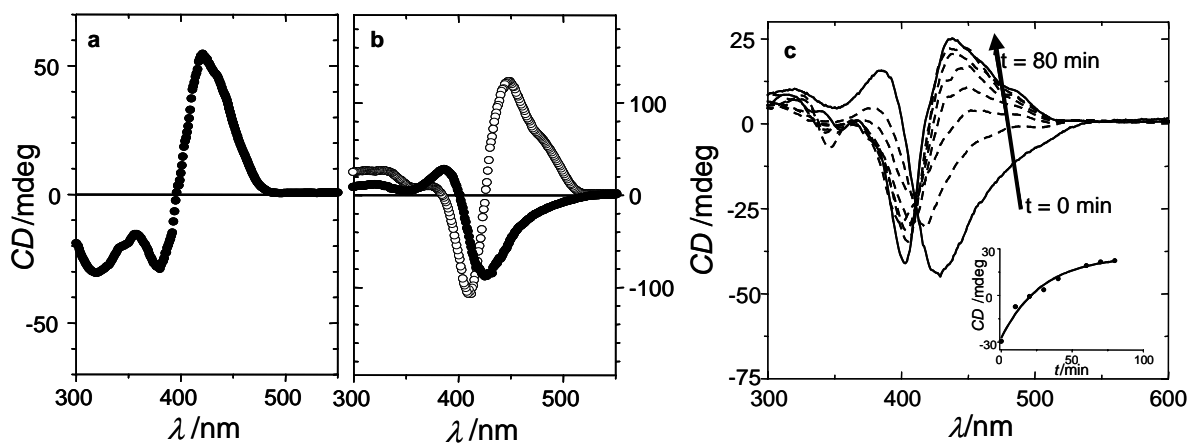


Figure 3.4: CD spectra of (a) **OPV₃T** (2.5×10^{-4} M) and (b) **OPV₄T** (5×10^{-5} M) of annealed heptane solutions recorded after waiting at 293 K for 10 min (filled circles) and for 24 hr (open circles). (c) Time dependent CD spectra of **OPV₄T** in steps of 10 min at 288 K. Inset shows the change of the CD intensity at $\lambda = 450$ nm versus time fitted to first order kinetics.

The aggregation process of **OPV₄T** was further studied by temperature dependent measurements (Figure 3.3). In heptane, the fluorescence maximum shifts from $\lambda_{\text{max}} = 530$ nm to 495 nm upon heating while the absorption maximum shifts from $\lambda_{\text{max}} = 420$ nm to 430 nm. The values at high temperature are close to those found in chloroform indicating molecularly

dissolved species. The phase transition temperature from the aggregated state to molecularly dissolved species lies at $T_m = 305$ K (Figure 3.3d). Remarkably, the Cotton effect disappears earlier ($T_m = 280$ K, Figure 3.3d) than the disassembly. This behavior indicates that an aggregation process occurs with first a transition from molecularly dissolved species into achiral H-type stacked structures that further develop into helical stacks. Hence, it is proposed that several secondary interactions independently act in the self-assembly process.³⁴³

3.4.2 Structure Properties

Small angle neutron scattering (SANS) and TM-AFM measurements on **OPV₄T** assemblies were used to study the shape of the supramolecular aggregates in solution and on graphite. SANS data (for more details see Section 4.4.3) of **OPV₄T** (5×10^{-4} M in dodecane, $T = 288$ K) showed a linear slope of -1 with a side maximum in the plot of the scattering vector vs the scattering intensity (Figure 3.5a) which is representative of cylindrical aggregates. The scattering data at low angles do not show a change in slope indicating that the persistence length of the aggregates reached at minimum experimental Q at least 185 nm. From the position of the side maximum at high angles, the radius of the cross section can be estimated as 7 nm.

TM-AFM of **OPV₄T** assemblies was performed on small deposits from heptane solutions (5×10^{-5} M) on graphite.³⁴⁴ Cylindrical aggregates were revealed with lengths of several tens of micrometers (Figure 3.5b). Presumably, during the transfer process the stacks present in solution further self-assemble end-to-end yielding longer aggregates in the solid state. Crossings of separate fibers are often observed. The width of the stacks is about 40 nm. Corrected for broadening of the lateral dimensions due to tip-convolution effects the actual width is about 10 nm.³⁴⁵ The heights of the stacks were determined to be uniformly 7.2 nm from the height profile (Figure 3.5c) which is more reliable since soft tapping conditions were applied. This thickness is in agreement with the SANS data and corresponds well to the diameter of the hydrogen-bonded hexamers found by STM pointing to fibers consisting of stacked rosettes. The measured length and diameter show that the aspect ratio of the aggregates can be as high as 1500. We did not observe helicity in the stacks however, helicity might still be present but not imaged due to a pitch length that is too small to be detected.

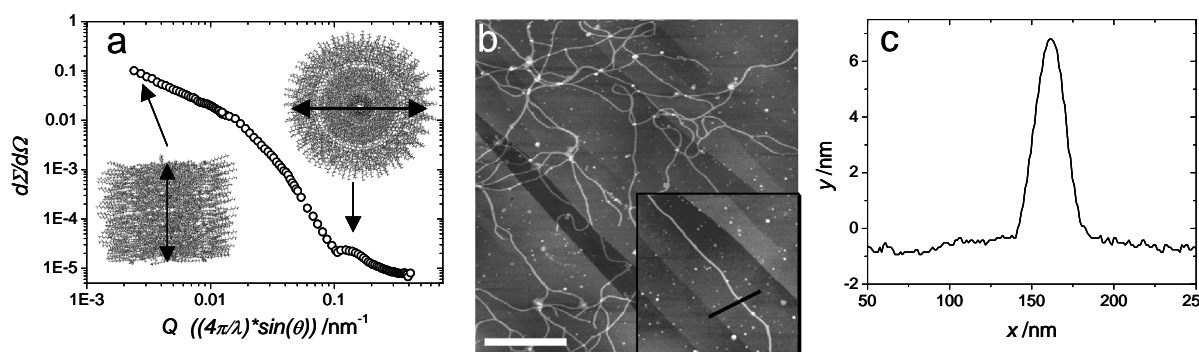


Figure 3.5: (a) SANS data revealing columnar structures in dodecane solutions of **OPV₄T**. (b) TM-AFM image of drop cast **OPV₄T** solutions in heptane (5×10^{-5} M) on graphite (z-scale 20 nm; bar represents 1 μm ; inset 800 x 800 nm^2 ; z-scale 20 nm). (c) Height profile as indicated by the black bar in the inset in b.

Notwithstanding it is tempting to relate the 'rotation direction' or supramolecular chirality of the chiral rosettes as detected by STM with the observed supramolecular chiral structures as detected by CD, it is practically impossible to do this at the present time. CD spectroscopy probes primarily rosette–rosette interactions, whereas in STM the packing of rosettes is predominantly determined by rosette–graphite interactions. The formation of the tubules, however, can be proposed based on earlier work on other supramolecular aggregates.²⁵³ The OPVs with diaminotriazine motifs self-assemble hierarchically; first forming hexameric rosettes by hydrogen–bond formation, which subsequently develops into stacks aided by π – π interactions of the phenylenevinylenes. Once organized in stacks that are highly space–filled as compared to self-assembled rods, the chiral side chains induce supramolecular helicity. It is proposed that the cyclic hexameric rosettes are not fully planar at the triazine end, resulting in a propeller arrangement allowing interplanar hydrogen–bond interactions from rosette to rosette, hereby locking the rosettes within the tubules (Figure 3.6). Upon heating, these hydrogen–bonds break, resulting in a loss of the Cotton effect. Time–variable CD spectra show that the locking of rosettes is a very delicate process.

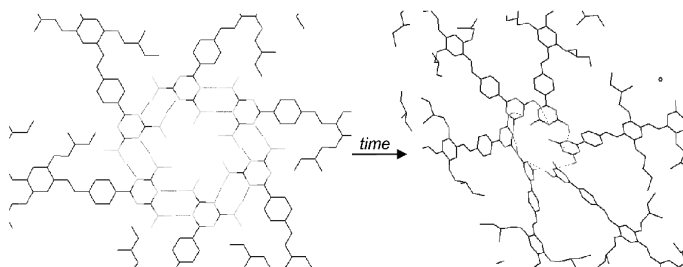


Figure 3.6: Transition from a planar rosette formation to a propeller arrangement as a result from energy minimization at room temperature of three face–to–face stacked rosettes. The molecular structures are calculated by molecular dynamics in HyperChem V7.04, Molecular Modeling System, Hypercube, Inc., using MM+ force fields. For reasons of clarity, only one rosette is shown.

3.5 CONCLUSIONS

We have synthesized various chiral oligo(p–phenylenevinylene)s equipped with a hydrogen–bonding diaminotriazine unit and have examined the self–assembly at the liquid/solid interface and in solution. At the liquid/graphite interface dimers or cyclic hexameric structures are formed depending on the length of the molecule. The shape of the assemblies is the result of a delicate balance between weak hydrogen–bonding, van der Waals interactions and the stereocenter present in the molecule. In apolar solvents, the hexamers stack into chiral tubules of 7.2 nm diameter in which the helicity depends on the oligomer length. These tubules display a perfect space filling and are still soluble due to the apolar shell that surrounds the stacks. Time–variable CD measurements reveal that the final self–assembly of the tubules involves a delicate process. In the next chapter, work will be described in which the strength of the hydrogen–bonding interactions will be increased in the same set of π –conjugated oligomers and the effect of this on the self–assembly process evaluated.

The self–assembly of oligo(p–phenylenevinylene)s into tubular aggregates in solution and at surfaces is determined by the same weak interactions that determines the packing of molecules in a crystal, showing that such interactions are useful to construct well–organized π –conjugated assemblies.

4 COLUMNAR SELF-ASSEMBLY OF OLIGO(P-PHENYLENEVINYLENE)S HAVING QUADRUPLE HYDROGEN-BONDS

ABSTRACT

Oligo(p-phenylenevinylene)s of different conjugation length have been synthesized having a self-complementary hydrogen-bonding motif. All oligomers contain chiral side chains and a tridodecyloxy unit. Dimers are formed as studied with scanning tunneling microscopy and ¹H-NMR spectroscopy. Neutron scattering data show that rigid cylindrical objects are formed. Stacks of the tetramer have a persistence length of 150 nm and a diameter of 6 nm. The trimer shows rigid columnar domains of 90 nm with a diameter of 5 nm. Temperature and concentration variable measurements show that the stability of the stacks increases with the conjugation length as a result of more favorable π - π interactions. At the surface single isolated cylinders are visualized by atomic force microscopy having similar diameters and persistence lengths as in solution. Further detailed photophysical measurements revealed different phases in the self-assembly of the OPV oligomers. It is shown that the the initial formation of small pre-aggregates is essential for the growth into long helical stacks. The self-assembly could be described by a nucleation-elongation assembly model. At higher concentrations significant side-by-side aggregation effects are prone to occur.

The presence of an aliphatic linker, covalently linking two OPV units, results in disordered stacks. This behavior is presumably the outcome of a competition between favorable π - π interactions and restricted conformational freedom due to the linker. The length of these polymers as well as the chiral order in the assemblies can be controlled by the addition of chain-stoppers.

CONTENTS

	<i>page</i>
4.1 Introduction	52
4.2 Synthesis	52
4.3 Self-Assembly at the Liquid/Solid Interface	54
4.4 Self-Assembly in Solution	56
4.4.1 Assemblies of OPV _x UTs	56
4.4.2 Assemblies of (OPV ₄ UT) ₂	59
4.4.3 Structure Properties in Solution	61
4.4.4 Structure Properties at the Surface	62
4.5 A Closer Look at the Self-Assembly of OPV _x UTs	64
4.5.1 Monitoring the Self-Assembly	64
4.5.2 General Theory of Isodesmic and Non-Isodesmic Self-Assembly	64
4.5.3 Modeling the Self-Assembly Process	67
4.5.4 Self-Assembly monitored by UV/vis and Fluorescence	70
4.5.5 Mechanism of the Self-Assembly Process	71
4.6 Conclusions	72
4.7 Towards Electrically Aligned OPV-gels	72

4.1 INTRODUCTION

Supramolecular organization of π -conjugated building blocks has been achieved by using solvent/non-solvent mixtures, block-copolymers or liquid crystallinity.³⁴⁶⁻³⁴⁸ Only a few examples have been reported of the use of hydrogen-bonding motifs to organize π -conjugated systems.³⁴⁹ Hydrogen-bonds are attractive since they are directional and selective. In the work described in the previous Chapter, relative weak two-fold hydrogen-bonds were used to position π -conjugated oligomers giving rise to different hydrogen-bonded motifs. This Chapter will describe the programmed self-assembly of π -conjugated oligomers in solution in which the hydrogen-bond strength, and thereby the directionality, is increased by using the self-complementary quadruple hydrogen-bonding ureido-s-triazine (UT) motif. Previously, the formation of helical columnar polymers in alkane solvents by both stacking and hydrogen-bonding has been demonstrated for self-complementary molecules functionalized with ureido-s-triazines units (Chart 4.1).³³³

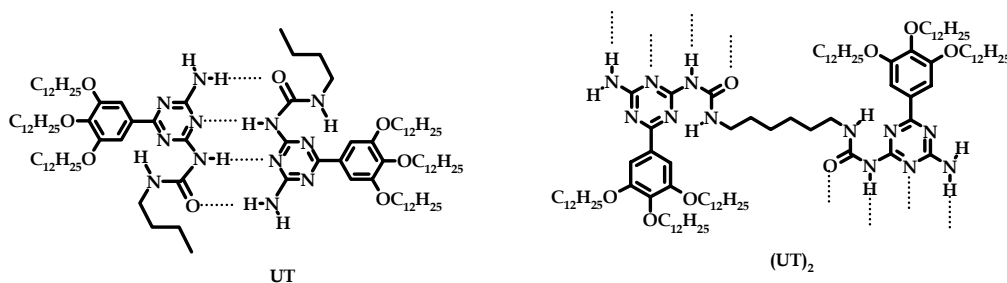
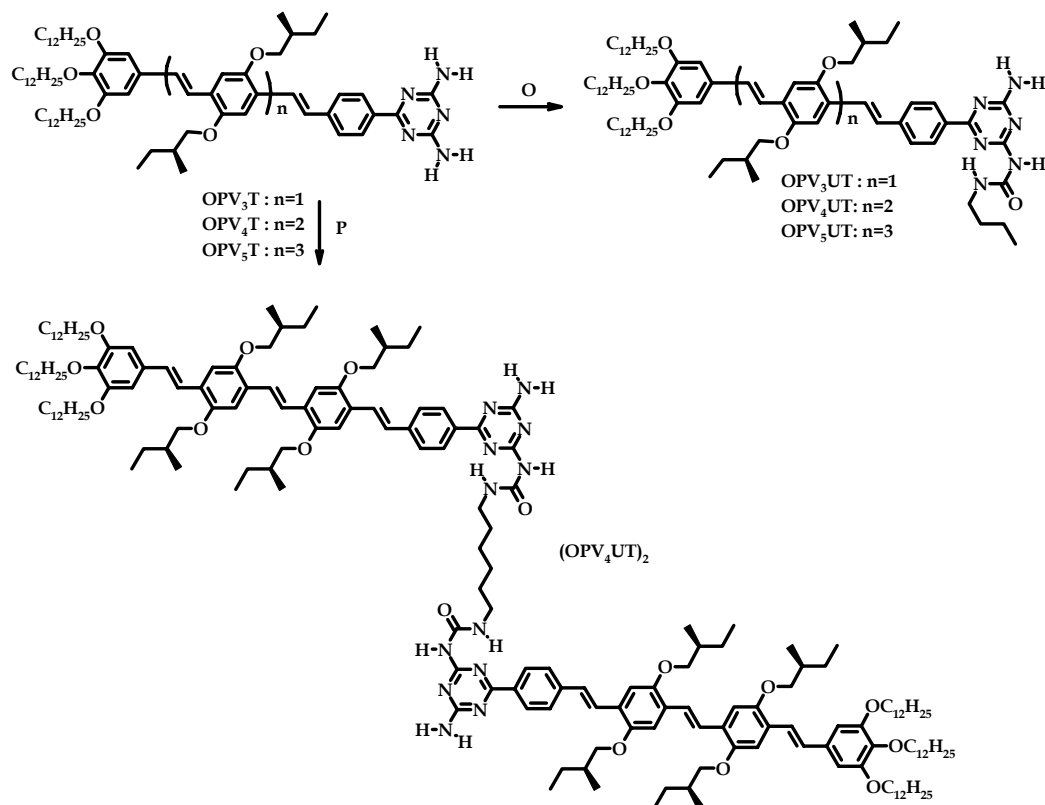


Chart 4.1

Association via strong quadruple hydrogen-bonding (ADAD motif) leads to dimerization; giving dimers for **UT** and a random coil polymer for **(UT)₂**. In apolar solvents, additional π - π stacking occurs yielding columnar architectures. Columnar architectures could be interesting as they provide a one-dimensional pathway for charge transport; however, the incorporation of a semiconducting part is required. It was anticipated that extended π -conjugated dimeric cores would allow for the creation of such supramolecular columns. This Chapter reports work on the synthesis and supramolecular organization in apolar solutions of chiral π -conjugated oligo(*p*-phenylenevinylene) (OPV) molecules containing quadruple hydrogen-bonding units.

4.2 SYNTHESIS

The OPVs containing the triazine hydrogen-bonding unit (**OPV_xT**, described in Chapter 3) were reacted with butylisocyanate in dry refluxing pyridine to obtain **OPV₄UT** and **OPV₅UT** in good yields of 58% and 53%, respectively (Scheme 4.1). The synthesis of **OPV₃UT** is described elsewhere.³³⁴ Reaction of **OPV₄T** with hexamethylenediisocyanate in dry refluxing pyridine, gave **(OPV₄UT)₂** (Scheme 4.1). In this case, the yield was considerably lower (14%) due to the large excess of **OPV₄T** used to prevent the formation of mono-acylated triazine, *i.e.* triazine that is acylated by one hexamethylenediisocyanate, and the formation of diacylated triazine, *i.e.* triazine that has both amino groups acylated by the isocyanate. The excess of **OPV₄T** could be recovered. The OPV compounds were fully characterized. IR measurements in chloroform revealed the different NH stretch-vibrations corresponding hydrogen-bonded **OPV_nUT**.



Scheme 4.1: **UT** and **(UT)₂** and synthetic route to **OPV_nUT** and **(OPV_nUT)₂** equipped with quadruple hydrogen-bonding motifs. O) *n*-butylisocyanate, refluxing pyridine, 8h. P) hexamethylenediisocyanate, refluxing pyridine, 8h.

The ¹H-NMR spectra of **OPV_xUT** in chloroform showed the appearance of the NH signals at δ 5.46, 9.28, 9.9 and 10.24, typical for dimeric hydrogen-bonded ureido-s-triazine species. Analysis of the downfield shift of these hydrogens as a function of the **OPV_xUT** concentration yielded an association constant of $K_{\text{dim}} = 2.1 (\pm 0.3) \cdot 10^4 \text{ M}^{-1}$. This binding constant is similar to **UT**, indicating that the π-conjugated part has no influence on the hydrogen-bonding strength. The ¹H-NMR spectrum of compound **(OPV₄UT)₂** showed the NH resonances to be located at the same positions as found for **OPV_xUT**. However, now broadening of the specific hydrogen-bonded signals was observed and also the OPV-hydrogens displayed a significant broadening which is presumably due to intermolecular interactions and restricted rotational freedom of the OPV units in the supramolecular polymer. Due to this broadening no association constants could be determined. UV/vis and fluorescence spectroscopy were performed on chloroform solutions of **OPV_xUT** showing clearly the effect of conjugation length. A red shift of the absorption maximum ($\lambda = 412, 437$ and 444 nm respectively) and emission maximum ($\lambda = 470, 501$ and 515 nm , respectively) was observed upon going from the trimer to the pentamer (Figure 4.1). The absorption and emission maxima for **(OPV₄UT)₂** are similar as for **OPV₄UT**. The observed π-π* transitions are similar to related oligo(*p*-phenylenevinylene)s having the same conjugation length.³⁴⁰

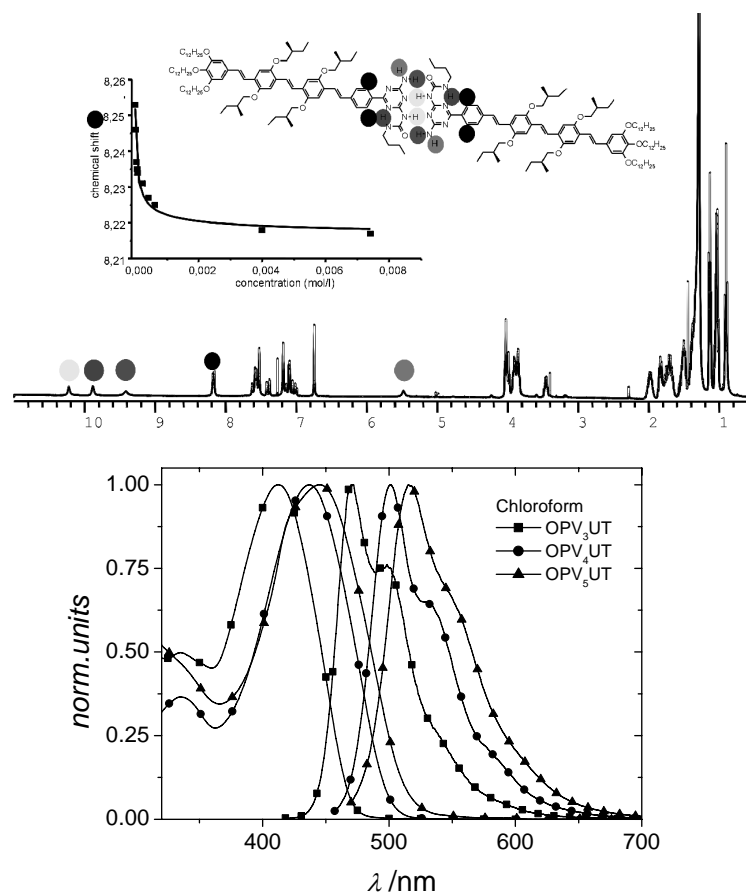


Figure 4.1: UV/vis and emission spectra of OPV_nUT in chloroform solutions (left). NMR spectrum of OPV_4UT with NH signals indicated (right). Inset shows the fit to the dilution curve representing the equilibrium between monomeric and dimeric species.

4.3 SELF-ASSEMBLY AT THE LIQUID/SOLID INTERFACE

The self-assembly of the OPV_xUT was first studied at the liquid/solid interface. Figure 4.2 shows current STM images of the different oligomers obtained at the 1,2,4-trichlorobenzene/graphite interface. Similar contrast characteristics as presented for OPV_xT (see Chapter 3) are visible; the π -conjugated segments appear as the brightest areas while the alkyl tails will lie in the dark parts.²⁹⁷ The long bright rods as observed in Figure 4.2 correspond to the length of the π -conjugated parts of the hydrogen-bonded dimers (Table 4.1 p. 63). The adsorbed dimers further assemble into lamellae over hundreds of nanometers. The distance between two dimers in a lamella is sufficient to accommodate a face-on orientation of the π -conjugated parts and fully extended chiral (*S*)-2-methylbutoxy side chains. For OPV_4UT (Figure 4.2a) and OPV_5UT (Figure 4.2b) this leads exclusively to counterclockwise (CCW) oriented dimers in lamellae with an exclusive symmetry-equivalent propagation direction with respect to the substrate. In the spacing between consecutive lamellae two out of three dodecyloxy side chains per molecule could be detected in an interdigitating fashion following the six-fold symmetry of the graphite. The location of the third chain was not revealed.

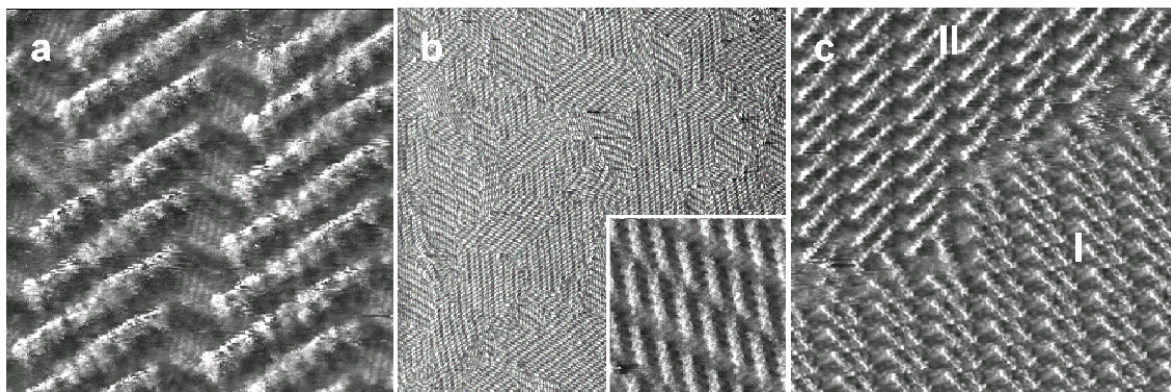


Figure 4.2: STM images of dimeric OPV_nUT monolayers on HOPG. (a) OPV_4UT , $12.1 \times 12.1 \text{ nm}^2$, $I_{set} = 0.8 \text{ nA}$, $V_{bias} = -0.68 \text{ V}$. (b) OPV_5UT , multiple domains covering a large area, $180 \times 180 \text{ nm}^2$, $I_{set} = 1.0 \text{ nA}$, $V_{bias} = -0.80 \text{ V}$. All molecules adopt the same counterclockwise orientation. Inset: zoom of a domain, $10.7 \times 10.7 \text{ nm}^2$, $I_{set} = 1.0 \text{ nA}$, $V_{bias} = -0.75 \text{ V}$. (c) OPV_3UT , two lamellar domains (I and II) with opposite handedness of the OPV backbone, $32.0 \times 32.0 \text{ nm}^2$, $I_{set} = 0.9 \text{ nA}$, $V_{bias} = -1.06 \text{ V}$.

On the contrary, a decrease in π - π interactions with the substrate seemingly prevents such an exclusive propagation direction of the lamellae build from OPV_3UT (Figure 4.2c). Here, two different enantiomorphic phases are observed with slightly more densely packed dimers. The minority of the domains (packing II, Figure 4.2c) display a CCW phase similar to that of OPV_4UT and OPV_5UT whereas the majority (packing I, Figure 4.2c) of the domains display the clockwise (CW) phase having lamellae with an offset of -14° with respect to the graphite symmetry axis.³⁵⁰ Note that the packing I and II are polymorphous; they are not mirror images of each other.

Clearly, the geometrical arrangement OPV_xUT in the monolayer is a compromise between the lateral intermolecular interaction and the bonding to the substrate. 2D assemblies show lamellae in which molecules are face-on oriented, in this way maximizing the overlap of their orbitals with those of graphite resulting in a maximum enthalpic gain.²⁸⁴ The internal arrangement of the lamellae can provide extra gain in absorption energy. The enantiomeric resolution is determined by the molecular conformation, which is mainly governed by the balance between the preferred adsorption of chiral methyl groups in the side chains and the π - π stacking in the central core of the dimers.²⁹⁷ Apparently, a certain number of chiral groups is needed to steer the internal arrangement to one unique preferred crystallite. The lateral aliphatic dodecyloxy chains stabilize the lamellae in 2D assemblies.

Another conformational difference is observed on the level of the individual dimers. Dimers can be detected as one bright rod (Figure 4.2a,c) but also as two bands with a clear offset between the OPV units (inset Figure 4.2b and Figure 4.3). Presumably, the orientation of the vinylene bonds determines what happens. An offset will follow if (all) vinylene bonds point toward the butyl chain of ureido-*s*-triazine (conformation 1, Figure 4.3), whereas the linear dimer will result from an orientation in which (all) vinylene bonds point away from the butyl chain of ureido-*s*-triazine (conformation 2, Figure 4.3). Interestingly, the direction of the offset remains the same for one polymorph. For the CCW phase, the π -conjugated segments in the right half of a lamella are always shifted upwards with respect to the π -conjugated segments in the left half of a lamella. For the CW phase, only observed for OPV_3UT , the π -conjugated segments in the right half of a lamella are always shifted downwards with respect to the π -conjugated segments in the left half of a lamella. Apparently, the chirality of

the molecular building blocks is, in addition to the ‘rotation direction’ of a dimer within a lamella, CW or CCW, also determining the offset between the two hydrogen-bonded OPVs.

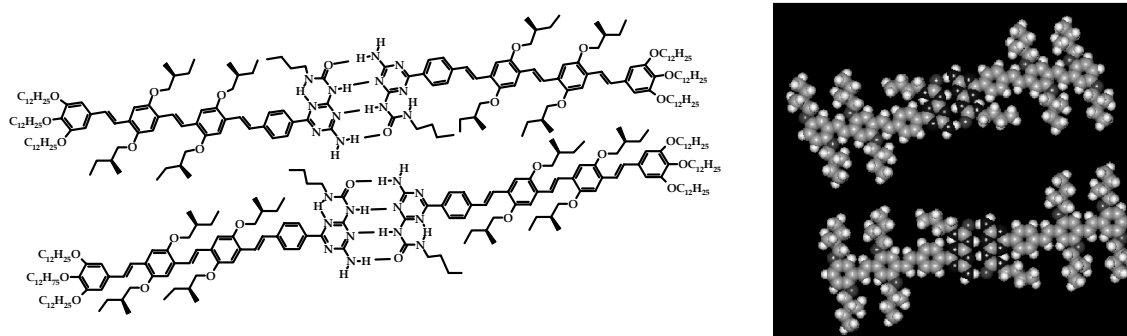


Figure 4.3: Chemical structures (left) and space-filled molecular models (right) illustrating two possible dimer conformations. The upper one shows a pronounced shift between the OPV-rods (conformation 1). The lower one shows the dimer as a linear rod (conformation 2).

4.4 SELF-ASSEMBLY IN SOLUTION

4.4.1 Assemblies of OPV_xUTs

The $^1\text{H-NMR}$ spectra of OPV_4UT in d_{26} - n -dodecane in the temperature range of 388 K - 358 K (Figure 4.4) revealed similar features as in d -chloroform at room temperature, indicating the presence of dimeric species. We have not determined the dimerization constant but we expect this to be higher than the value measured in chloroform based on literature examples.²⁵⁹ Cooling to 343 K gave rise to broadening of the signals of the aromatic hydrogens indicating aggregation. At room temperature extreme line broadening was observed.

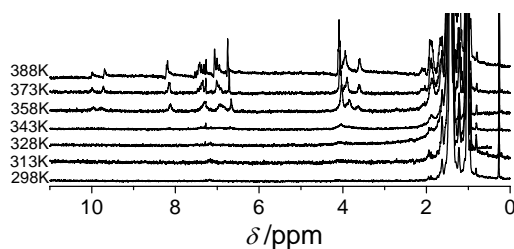


Figure 4.4: Variable temperature $^1\text{H-NMR}$ spectra of a d_{26} - n -dodecane solution of OPV_4UT (2×10^{-4} M).

The optical properties of the self-assembly of the OPV_4UT were also studied in dodecane. The UV/vis ($\lambda_{\text{max}} = 438$ nm) and fluorescence spectra ($\lambda_{\text{max}} = 500$ nm) of a heated (343 K) apolar dodecane solution of OPV_4UT were comparable to those in chloroform indicating molecularly dissolved monomeric and hydrogen-bonded dimeric species. At low temperatures (283 K) a shoulder at the red side of the absorption maximum (Figure 4.5a) is observed and the fluorescence intensity is decreased and shifted to the red ($\lambda_{\text{max}} = 552$ nm) indicating aggregation (Figure 4.5b). Further proof for the existence of two different phases of OPV_4UT in solution comes from the circular dichroism spectra (Figure 4.5c). The π - π^* transition is optically silent above 343 K whereas at 283 K, a bisignated Cotton effect developed, having a negative exciton coupling. This negative coupling suggests the presence of a left-handed helical arrangement of the transition dipoles of the OPV molecules.^{351a}

Change of solvent has no systematic influence on the g_{abs} (7.2×10^{-3} (pentane), 7.3×10^{-3} (heptane) and 5.2×10^{-3} (dodecane)) at 6×10^{-6} M for **OPV₄UT** at 283 K, suggesting similar types of aggregates in these solvents.

Upon increasing the temperature in steps of 10 K and allowing 10 min equilibration, at a first glance, the spectral changes in the CD spectra for **OPV₄UT** occurred simultaneously with changes recorded in the fluorescence and UV/vis spectra. In Figure 4.5d are plotted these changes in the optical spectra (θ), at a wavelength where they are the most pronounced (CD: $\lambda = 460$ nm; fluorescence: $\lambda = 500$ nm and UV/vis: $\lambda = 335$ nm), versus temperature (T). The curves constructed from the three photophysical techniques show fairly equivalent transition curves after normalization. Remarkably, the position of the temperature induced spectral changes depends only in the UV/vis spectra on the chosen wavelength. Monitoring the changes at $\lambda = 335$ nm yielded a transition curve coinciding with curves constructed from the fluorescence and CD data, whereas monitoring at $\lambda = 490$ nm showed a shifted transition curve to a higher temperature (inset Figure 4.5d). The 0–0 vibronic of the S_1 – S_0 transition at $\lambda = 490$ nm changes more gradually while for the S_2 – S_0 transition at $\lambda = 335$ nm a more abrupt change is visible.^{351b} Temperature dependent changes in the absorption spectra can not only be related to aggregation but also to conformational effects. The transition dipole moments of the S_1 – S_0 transition, oriented along the long molecular axis, and the S_2 – S_0 transition, a more localized state, will respond to a different extent to such conformational effects. Apparently, monitoring the changes in the absorption at the S_2 – S_0 transition coincides more with the changes in the fluorescence and CD data.

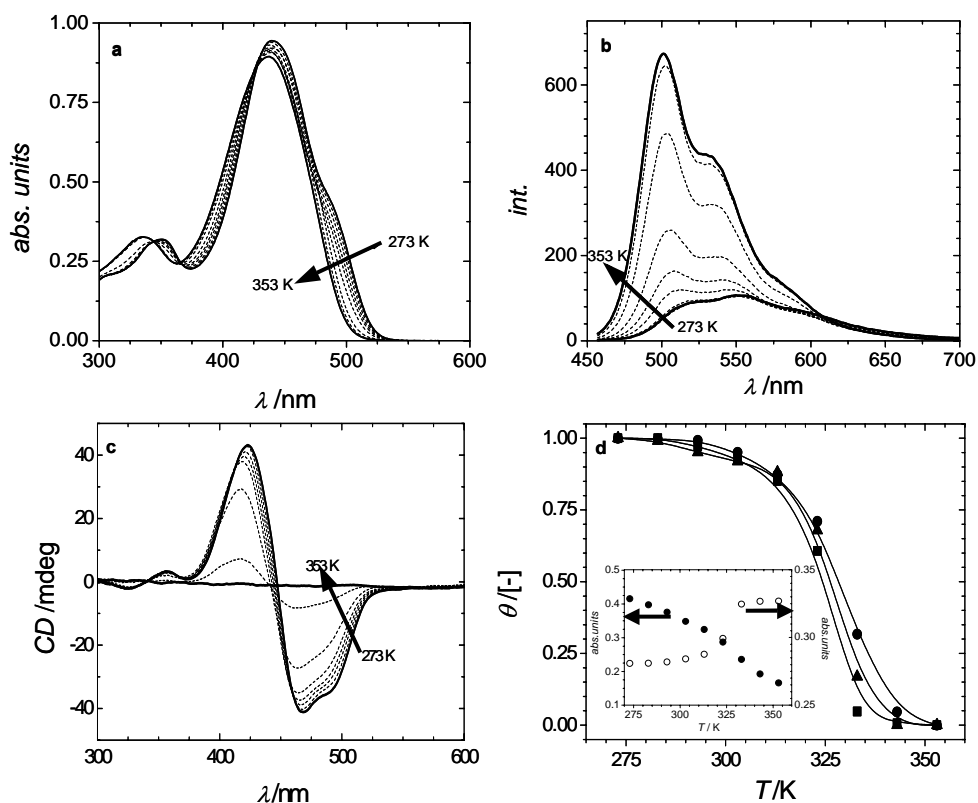


Figure 4.5: Variable temperature (heating ramp) (a) UV/vis, (b) fluorescence and (c) CD spectra for **OPV₄UT** in dodecane solution (1.4×10^{-5} M). (d) Coinciding phase transition curves are plotted as changes (θ) in the UV/vis ($\lambda = 335$ nm, squares), fluorescence ($\lambda = 500$ nm, circles) and CD ($\lambda = 460$ nm, triangles) spectra versus temperature (normalized scale). Inset in d shows temperature induced change in absorption at $\lambda = 335$ (open) and 490 nm (closed).

Analogous temperature dependent spectral transformations were observed for **OPV₃UT** (data not shown) and **OPV₅UT** (Figure 4.6). The spectral characteristics of the trimer are blue shifted compared to **OPV₄UT** while those of the pentamer are red shifted, because of the difference in conjugation length. This behavior is demonstrated in Figure 4.7. Red shifted CD spectra are observed going from **OPV₃UT** to **OPV₅UT** that increase in intensity but have in all cases a negative exciton coupling.

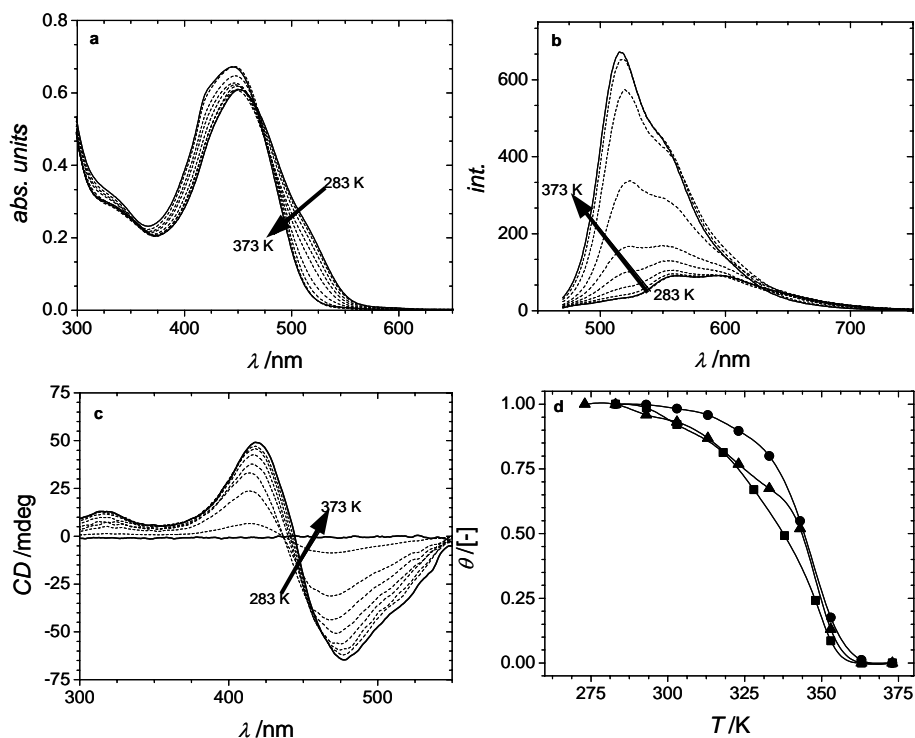


Figure 4.6: Variable temperature (heating ramp) (a) UV/vis, (b) fluorescence and (c) CD spectra for **OPV₅UT** in dodecane solution (1×10^{-4} M). (d) Coinciding phase transition curves are plotted as changes (θ) in the UV/vis ($\lambda = 350$ nm, squares), fluorescence ($\lambda = 525$ nm, circles) and CD ($\lambda = 475$ nm, triangles) spectra versus temperature (normalized scale).

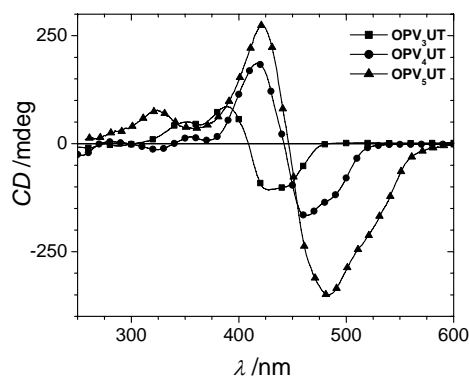


Figure 4.7: CD spectra of **OPV_nUT** (4×10^{-4} M, dodecane, $x = 3, 4, 5$) plotted in one graph.

When temperature variable measurements (heating ramps) in dodecane were performed with the same concentrations of **OPV₃UT**, **OPV₄UT** and **OPV₅UT**, the phase transition curves shifted to higher temperatures, obviously due to additional π - π interactions provided by the increase in conjugation length. The transition curves have similar shapes as found for short oligonucleotides, in which the midpoint of such type of transition curves is called the melting temperature, T_m . The T_m of the OPV helices increases not only with their

conjugation length, but also with the concentration of the OPVs (Figure 4.8). The phase transition curves show a shift of approximately 15 K for all OPV oligomers per decade of concentration.

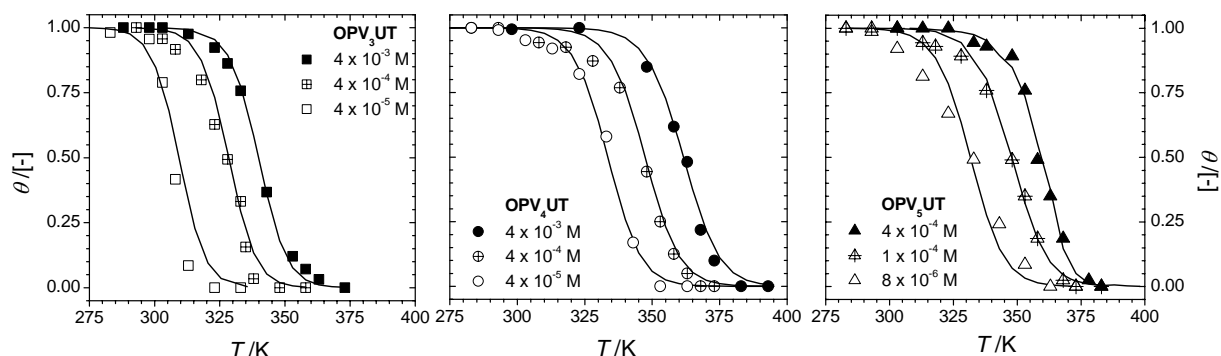


Figure 4.8: Plots of normalized spectral changes (θ) versus temperature for **OPV₃UT**, **OPV₄UT** and **OPV₅UT**. Data points originate from variable temperature CD spectra for concentrations as indicated. Lines are drawn to guide the eye.

A linear dependence of T_m with the logarithm of the concentration was found (Figure 4.9). The thermodynamic parameters of the melting transition were evaluated from the Van 't Hoff plot (Figure 4.9a). The enthalpy decreased from $\Delta H = -130$ to -170 kJ/mol while the entropy decreased from $\Delta S = -335$ to -410 J/molK upon elongating the conjugation length from **OPV₃UT** to **OPV₅UT**. The negative enthalpy and entropy values illustrate that the aggregation is an enthalpy-driven process.

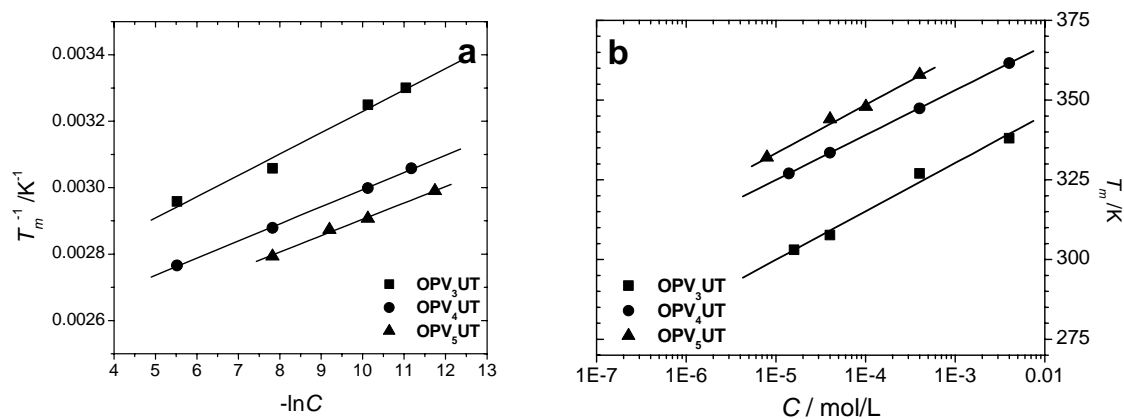


Figure 4.9: Van 't Hoff plot (left) and a graph in which the T_m is plotted versus concentration (right).

4.4.2 Assemblies of **(OPV₄UT)₂**

UV/Vis, fluorescence and CD spectra were also recorded for **(OPV₄UT)₂** in chloroform and dodecane (Figure 4.10a). In chloroform, an absorption maximum at $\lambda_{\max} = 445$ nm is found which is at the same position as observed for **OPV₄UT**. No CD effect in this solvent was observed. The absorption maximum for **(OPV₄UT)₂** in dodecane is red shifted ($\lambda_{\max} = 453$ nm) while a weak shoulder appears at $\lambda = 485$ nm. Furthermore, in contrast to the strong bisignate CD spectrum of **OPV₄UT**, a weak Cotton effect was found for only concentrated solutions of **(OPV₄UT)₂**. The emission spectrum of **(OPV₄UT)₂** in chloroform ($\lambda_{\text{ex}} = 445$ nm, $\lambda_{\text{em,max}} = 528$ and 567 nm) and dodecane ($\lambda_{\text{ex}} = 453$ nm, $\lambda_{\text{em,max}} = 540$ and 576 nm) are more or less the same

which is in contrast with the behavior of OPV_4UT . The weak CD effect found for $(\text{OPV}_4\text{UT})_2$ in dodecane indicates that the aggregates are not helical, or are of a different type to that formed by OPV_4UT .

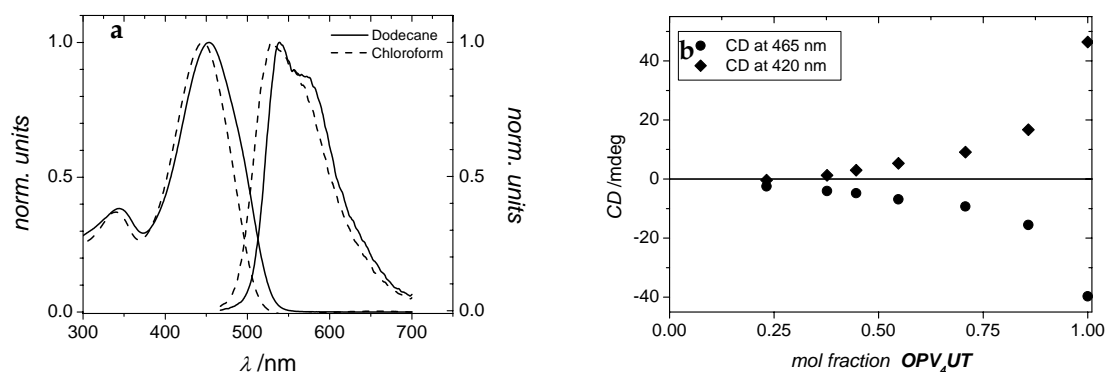


Figure 4.10: (a) Normalized UV/vis and fluorescence spectra of $(\text{OPV}_4\text{UT})_2$ in dodecane (0.05 g/L), chloroform (0.05 g/L). (b) Change of the CD intensity of OPV_4UT in dodecane for different mixtures of OPV_4UT and $(\text{OPV}_4\text{UT})_2$.

It was found earlier that **UT** with chiral side chains showed no Cotton effect in dodecane while in the case of the analogous $(\text{UT})_2$ a CD effect was observed and it was concluded that the presence of a covalent linker between the triazine units was important in maintaining supramolecular chirality. Dimers of **UT** are also stacked, however, the dimerized molecules are not interacting in a helical fashion. In the case of OPV_4UT , the dimers interact stronger due to more π - π interactions resulting in a helical aggregate. In the case of $(\text{OPV}_4\text{UT})_2$, a competition exist between the ideal stacking of the OPV units and the restricted conformation due to the alkyl linker, resulting in less ordered aggregates. Presumably, $(\text{OPV}_4\text{UT})_2$ is present as a random coil polymer in chloroform that self-assembles in dodecane into so-called frustrated stacks. The observation of a competition of multiple interactions in the supramolecular structures described in this Section reflect a very interesting and challenging problem in supramolecular chemistry.

Monomers possessing two strong quadruple hydrogen-bonding self-complementary ureido-pyrimidone units can form supramolecular polymers that display almost all properties of macroscopic polymers.³⁵² The chain length of such polymers can easily be adjusted with the addition of monomers possessing only one ureido-pyrimidone unit, which acts as a chain stopper. In order to tune the virtual length of our supramolecular aggregates, OPV_4UT was used as a chain stopper in supramoleculer polymeric stacks formed by $(\text{OPV}_4\text{UT})_2$. In order to promote the exchange of the molecules, the solutions were heated up to 343 K for five minutes and after cooling to 293 K the CD spectra were recorded. A nonlinear behavior of the CD effect as function of the mol fraction OPV_4UT was observed, indicating exchange of the compounds (Figure 4.10b). The CD effect is already dropped by a factor 5 at a 0.7 mol fraction of OPV_4UT . This behavior illustrates the possibility to of incorporating OPV_4UT as a chain stopper into the supramolecular aggregates formed by $(\text{OPV}_4\text{UT})_2$ and that the virtual length of these polymers can probably be tuned.

4.4.3 Structure Properties in Solution

SANS experiments were performed to elucidate the shape of the supramolecular aggregates in solutions. Experiments were performed in d_{26} -dodecane with concentrations below 0.7 vol% for **OPV₃UT** and **OPV₄UT**, covering a range of scattering vectors (Q) from $0.03 \text{ nm}^{-1} < Q < 3 \text{ nm}^{-1}$. In all cases, the variation of the scattering intensity ($d\Sigma/d\Omega$) as function of Q (normalized by the volume fraction) clearly indicated the presence of supramolecular assemblies. The scattering intensity is described by $I(Q) = \phi V_p P(Q) S(Q)$ where $P(Q)$ represents the form factor of the aggregates and $S(Q)$ is the contribution for interparticle correlations. For dilute solutions, it is assumed that $S(Q) \sim 1$ (indicating negligible correlation effects) while $P(Q)$ was approximated by assuming an isotropic arrangement of cylindrical particles. Provided that the aspect ratio of the cylinders is large, *i.e.* $L \gg R$, the form factor contribution for cylinders should reveal a broad region in which $I(Q) \sim Q^{-1}$ from low Q to moderate Q . At high Q , the observed Q^{-4} dependence indicates a sharp interface of the cylinders modulated by the oscillations of a well-defined cross section appearing as a secondary maximum at $Q \sim 4.49/R$.

Indeed, the Holtzer plot representation of the scattering data clearly revealed an intensity decay $\sim Q^{-1}$, thus revealing the presence of cylindrical structures. The cylinders have a well-defined interface as can be seen from the Q^{-4} -dependence in the region $L < Q < R$. Excellent fits based on a model assuming homogeneous rigid cylindrical structures, yielded columns with length $L \sim 150 \text{ nm}$ and a diameter $D \sim 5.8 \text{ nm}$ for **OPV₄UT** at $Q < 10 \text{ nm}^{-1}$ (Figure 4.11a). The **OPV₃UT** SANS pattern can be interpreted by similar cylindrical structures. However, in this case the deviation from the Q^{-1} behavior of the data at very low Q indicates intercolumnar interactions, *i.e.* entanglements of the columns resulting in a transient network in which the crossing points are $\sim 90 \text{ nm}$ apart.³⁵³ It is evident from the shifted side maximum of the form factor (Figure 4.11b) that the diameter of the columns formed by **OPV₃UT** ($D \sim 5.0 \text{ nm}$) is smaller than those of **OPV₄UT**, which is in agreement with its shorter oligomer length. Molecular dynamics calculations reveal that the overall length of **OPV₄UT** hydrogen-bonded dimer omitting the dodecyloxy tails is 5.7 nm and that of **OPV₃UT** is 4.7 nm (Table 4.1, p. 63) which matches well with the SANS data. This shows that the hydrogen-bonded dimers stack on top of each other forming cylindrical structures. A similar scattering behavior was observed upon increasing the temperature indicating that length and diameter of the cylinders remain

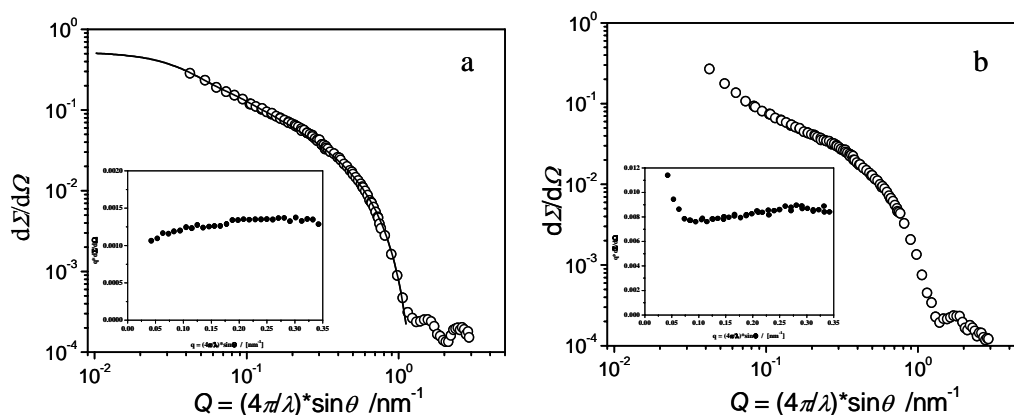


Figure 4.11: SANS intensity decay data versus Q from d_{26} - n -dodecane solutions containing (a) **OPV₄UT** and (b) **OPV₃UT** indicating the same type of structures. Curve in a was fitted according to a model assuming homogeneous cylindrical structures and reveals $L \sim 150 \text{ nm}$ and $R \sim 2.9 \text{ nm}$. Holtzer plot (inset) shows a clear intensity decay $\sim Q^{-1}$ for **OPV₄UT**, for **OPV₃UT** the deviation of the data from the Q^{-1} behavior at very low Q indicates intercolumnar interactions.

unchanged until 343 K when the scattered intensity for **OPV₃UT** started to decrease strongly, signifying dissociation of the aggregates.

SANS experiments were also performed for the supramolecular assemblies formed by **(OPV₄UT)₂** in dodecane, (Figure 4.12). The results showed a broad region in which the intensity $I(Q)$ correlates with Q^{-1} , representative for cylindrical aggregates. The fits to the data yielded columns with lengths of approximately 180 nm and a diameter of about 4 nm. Remarkably, the diameter for columns of **(OPV₄UT)₂** is reduced compared to **OPV₄UT** indicating that the OPVs presumably adopt a tilted orientation.

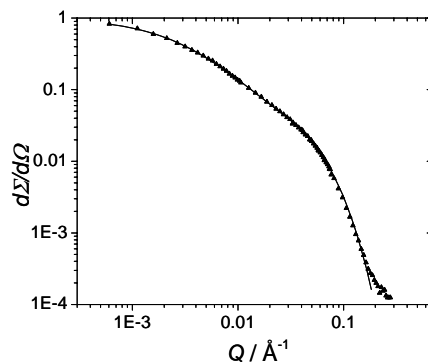


Figure 4.12: SANS data intensity decay data versus Q for **(OPV₄UT)₂** in d_{26} -dodecane and fit according to cylindrical form factor.

4.4.4 Structure Properties at the Surface

The self-assembled stacks of **OPV₄UT** in heptane were transferred to a solid support, graphite, and investigated with TM-AFM. In deposits from solution in heptane (7×10^{-4} M), the stacks are seen as side-by-side associated fibers (Figure 4.13a). Broad bundles having a height of 5.5 nm, merge and separate continually thereby changing the number of side-by-side lying fibers. Numerous single fibers are found in deposits from lower concentrations, 6.7×10^{-6} M (Figure 4.13b). Although a constant width of about 40 nm for the fibers was found, tiny surface features are easily smeared out by a few tens of nanometers due to geometrical effects caused by the tip size. Therefore, the values of the measured heights of the fibers are a more accurate way to determine the diameter of the fibers. This is only the case if the interaction forces between tip and surface are minimized to limit deformation and/or destruction. Images were compared of the same fiber in which the tapping conditions were varied. The use of high forces (high amplitudes and low set-point ratios) result in destruction of the fibers. Low force imaging conditions (high set-point ratios and low amplitudes) provide stable imaging without deformatting the fibers. These single cylindrical fibers of **OPV₄UT** have a uniform height of 5.5 nm (Figure 4.13d), which corresponds very well with the STM, SANS and MD calculations (Table 4.1). In a few cases, two fibrils cross each other and the heights of these crossovers were about 9.9 nm as indicated from the line scan in Figure 4.13b. The helicity of the stacks could not be observed. Helicity might still be present, but not visible with AFM due to a pitch length that is too small or due to the achiral organization of the long aliphatic tails at the periphery of the stacks that mask the helicity of the interior of the stacks. The length of the **OPV₄UT** fibers varies from 50 nm to 1 micrometer. Figure 4.13c shows a detailed analysis of the straight segments in the fibers having an average length of 125 nm ($\Delta = 25$ nm). This persistence length fits very well with the length obtained by the SANS measurements

(150 nm). Presumably during the transfer process from solution to the solid support, the stacks present in solution self-assemble further in the stack direction to cylinders as long as 1 micrometer. This process is less defined resulting in kinks and a broad distribution of the length of the fibers. Similar observations were obtained for **OPV₃UT** and **OPV₅UT** having fibers of a height of 4.7 and 6.1 nm, respectively.

Table 4.1: Comparison of the dimensions for **OPV_nUT** determined by Molecular Dynamics, SANS, TM-AFM and CD.

	MD [nm]	STM [nm]	SANS [nm]	TM-AFM	CD		
length	dimer ^a	dimer ^b	dimer ^c	stack ^d	dimer ^e	stack ^f	stack ^g
OPV₃UT	4.7	4.8 (4.6)	5.0	90	4.7	n.d.	125
OPV₄UT	5.8	5.4	5.8	150	5.5	125	155
OPV₅UT	6.9	6.5	n.d.	n.d.	6.1	n.d.	175

^alength omits the dodecyloxy tails. ^bfrom unit cell, ^cfrom the side maximum of the Bessel function ^dfrom fit, ^efrom height profiles ^ffrom histogram in Figure 4.13d and ^gfrom Figure 4.17 (vide infra).

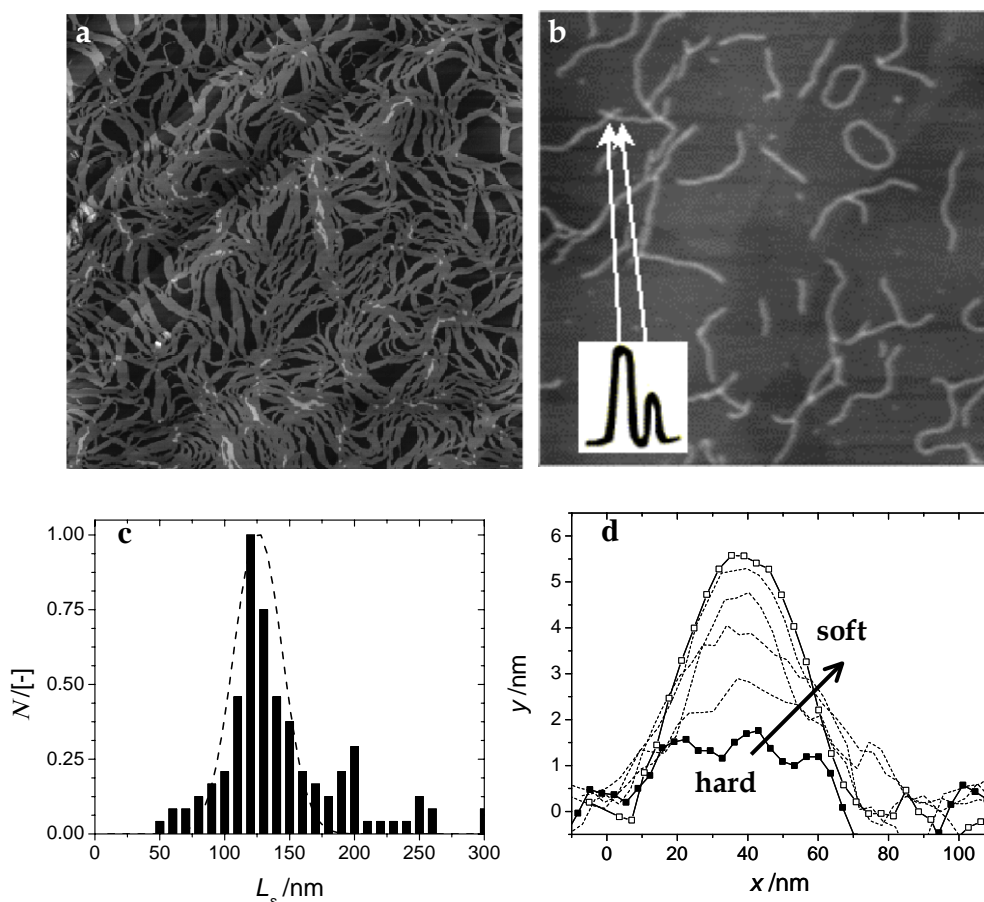


Figure 4.13: TM-AFM images of **OPV₄UT** on graphite from heptane solutions (a) 7×10^{-4} M, $7 \times 7 \mu\text{m}^2$, z-scale 25 nm, (b) 6.7×10^{-6} M, $5 \times 5 \mu\text{m}^2$, z-scale 25 nm. Inset shows two line scans over a crossing of two fibers and a single fiber for comparison, clearly the former (9.9 nm) being approximately the double of the latter (5.5 nm). (c) Histogram of straight segments present on the surface with the dashed line a gaussian fit to this data. (d) Height profiles of a single fiber with varying tapping conditions from soft (open squares) to hard (filled squares) as follows: A_{sp}/A_0 (A_0) = 0.90 (1.5 V), 0.95 (2 V), 0.80 (2 V), 0.70 (2 V), 0.50 (2 V), 0.25 (2 V).

4.5 A CLOSER LOOK AT THE SELF-ASSEMBLY OF OPV_xUTs

4.5.1 Monitoring the Self-Assembly

To get a better insight into the mechanism of the self-assembly process (*vide infra*), it is important to improve the resolution of the experimental data that probes the process. The self-assembly can be probed by temperature dependent UV/vis, fluorescence and CD measurements (see Section 4.4.1). The resolution of these measurements can be improved by monitoring at one wavelength the crossover from the monomeric state (actually hydrogen-bonded dimers, see Section 4.4.1) to the aggregated, *i.e.* polymeric, state in small steps of 0.01 K upon cooling from 375 K to 275 K (Section 4.4.1) using a peltier temperature programmer for thermostating the samples. In addition, a slow cooling rate of 0.5 K/min is applied to suppress kinetic (non-equilibrium) effects on the self-assembly. When monitoring the growth of the intensity of the CD band at $\lambda = 466$ nm, a sharp increase at a specific temperature is observed (see arrow, Figure 4.14) indicative for the transition from monomers into helical aggregates. For comparison, the CD intensity taken from the spectra measured upon heating in steps of 10 K are plotted in the same curve. Having the extensive set of datapoints, it will be possible to describe the self-assembly process with an isodesmic and non-isodesmic (cooperative) growth mechanism.

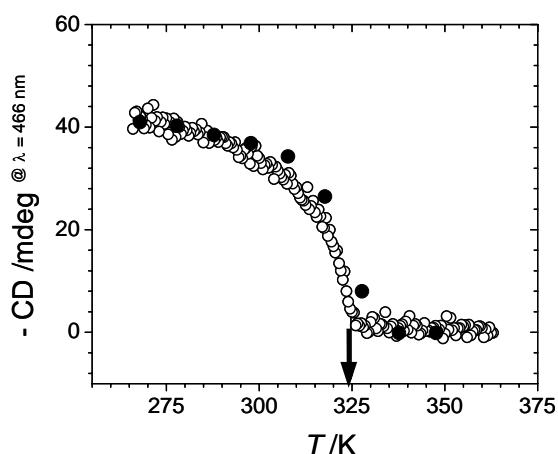


Figure 4.14: Temperature dependent CD data monitored at $\lambda = 466$ nm upon cooling the solution of **OPV₄UT** (1.1×10^{-5} M, dodecane) represented as open circles. For reasons of clarity not all data points are shown. Arrow indicate change of the signal at a specific temperature. The filled circles represent the change in CD intensity at $\lambda = 466$ nm taken from the spectra measured upon heating in steps of 10 K and allowing 10 min equilibration.

4.5.2 General Theory of Isodesmic and Non-Isodesmic Self-Assembly

Referring to the schematic phase diagram in Figure 4.15 that represents the current understanding of helical assembly, this would imply that the self-assembly of **OPV₄UT** is close to a direct transition from monomers (hydrogen-bonded dimers) to helical aggregates (see the arrow in Figure 4.15). Transitions in this part of the phase diagram have been described by Oosawa and Kasai for f-actin assembly^{354a} and also recently by Semenov *et al.*^{354b} for the helical assembly of oligopeptides through the formation of small β -sheet "pre-aggregates". The full theory on which the scheme shown in Figure 4.15 is based,

combines the classical Zimm–Bragg theory for the helix–coil transition in biopolymers and the theory of equilibrium polymerization. This model is in good agreement with experimental data on the helical assembly of discotic molecules.^{355,356} Here, we opt for a simplified version of the Oosawa–Kasai model to describe the self-assembly of OPV₄UT, by treating the non–isodesmic helical assembly (characterized by an activation step and subsequent propagation steps) independently from the isodesmic assembly of non–helical structures (*i.e.* pre–aggregates). The two kinds of assemblies are then linked via an equilibrium between non–helical and helical assemblies of a certain critical size.³⁵⁷ We will show in the next Section that the transition we find in the CD data indeed follows such cooperative mechanism.

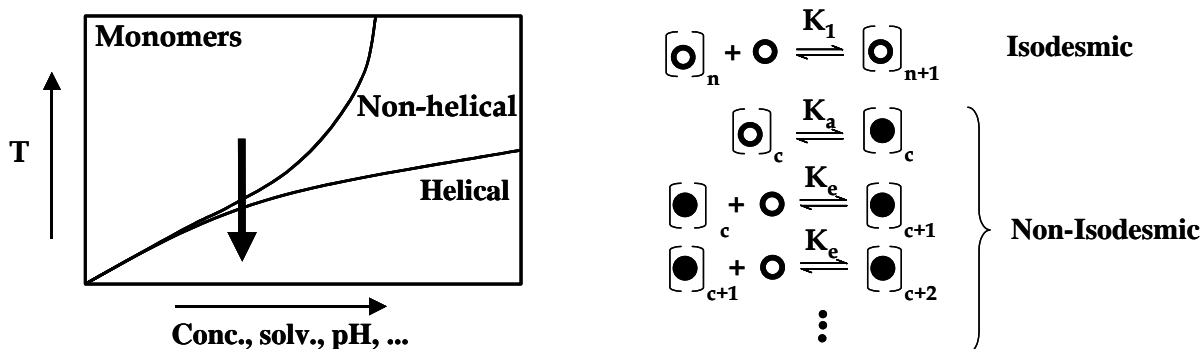


Figure 4.15: Phase diagram showing the direct transition of monomers into helical assemblies or via the formation of non–helical assemblies. In the case when the assembly follows the thick arrow as indicated in the diagram, non–helical assemblies can serve as pre–aggregates having c monomers associated. Equilibria that describe the isodesmic and the non–isodesmic or cooperative aggregation are given. Symbols indicate chirally (filled) and non–chirally (open) stacked monomers. c and n indicate the mean aggregation number N .

The simplified model (Figure 4.15) considers a helical aggregation starting from several successive monomer additions into a pre–aggregate. If the equilibrium constants (K_1) of all sequential back and forward reaction steps are presumed to be equal, this case is referred to as the isodesmic equilibrium aggregation. In the case of non–isodesmic or cooperative assembly, at a critical value of c , an equilibrium (K_a) between the concentration of helical and non–helical pre–aggregates can occur. Further growth by attaching monomers to the helical state is assumed to have the same equilibrium constant (K_e). Helical aggregation can occur via thermal activation. If K_a is sufficiently small, disfavoring the helical pre–assembly, this will result in a highly cooperative process. In this cooperative process, aggregates only become stable and long after the very first association steps forming a pre–aggregate or nucleus, and therefore, cooperative aggregation is also called nucleation–elongation aggregation.³⁵⁸

For the derivation of the formulae that describe such thermally activated self–assembly, the reader is referred to the review of Van der Schoot.³⁵⁷ It turns out that the mean aggregation number (N) of the non–helical supramolecular chains can be described by one single parameter G , the free energy of association. The associated equilibrium constant for the isodesmic aggregation can be expressed as:

$$K_1 = \exp(-G_m/RT) = \exp[h_m(T - T_m)/RT_m^2] \quad \text{eq. 1}$$

where, h_m is the enthalpy of a single non-covalent bond in J/mol at the temperature $T = T_m$ in K, the transition temperature from monomers to polymers. The fraction of aggregated molecules, ϕ_n , is related to N by:

$$\phi_n = 1 - N^{-2} \quad \text{eq. 2.}$$

Note that ϕ_n is a dimensionless parameter and that the dimensionless constant K_1 is related to the dimension-bearing one via vK with K the equilibrium constant in L/mol and v the molar density of monomers in solution. It is important to note that for the isodesmic equilibrium assembly the crossover from the monomer-dominated regime to the aggregate-dominated regime is gradual, with $\phi_n = 0.5$ formally defined as T_m , *i.e.*, where half the material is aggregated. Remarkably, if $\phi_n = 0.5$, $N = 1.4$, showing that in the middle of the transition from monomers to aggregates, the solution mainly consists of monomers and dimers.

In the case of the nucleation-elongation aggregation, we have two (dimensionless) equilibrium constants: K_a for the association of OPV-dimers into nuclei, and K_e for the further association of dimers and nuclei into stacks. The elongation process can be described through:

$$K_e = \exp(-G_e/RT) = \exp[h_e(T - T_e)/RT_e^2] \quad \text{eq. 3}$$

where, h_e is the excess enthalpy of a single helical (non-covalent) bond in J/mol at $T = T_e$, the temperature at which the elongation starts. The mean aggregation number, given by:

$$\exp(-G_e/RT) = 1 - N^{-1} + K_a N(N - 1) \quad \text{eq. 4,}$$

can be estimated in the pre-nucleation regime as:

$$N \sim 1 + \exp(-G_e/RT) \quad \text{eq. 5,}$$

and at $T = T_e$ eq. 4 gives:

$$N \sim K_a^{-1/3} \quad \text{eq. 6,}$$

while in the elongation regime ($K_a N \gg 1$) eq. 4 gives:

$$N \sim [\exp(-G_e/RT)/K_a]^{1/2} \quad \text{eq. 7.}$$

Interestingly, the value of K_a determines the final aggregate size. If K_a reaches zero, nucleation is highly unfavorable leading to very sharp transition between monomers and aggregates, *i.e.* a highly cooperative process. If K_a reaches zero, the fraction aggregated molecules in the pre-nucleation regime relates as:

$$\phi_n \sim 1 - \exp[h_e(T - T_e)/RT_e^2] \quad \text{eq. 8,}$$

at $T = T_e$ we have:

$$\phi_n \sim K_a^{1/3} \quad \text{eq. 9.}$$

It is possible to show that near T_e the fraction relates as:

$$\phi_n \sim K_a^{1/3} \exp[(2/3K_a^{-1/3} - 1)h_e/RT_e^2(T - T_e)] \quad \text{eq. 10.}$$

By means of spectroscopic techniques, the temperature dependence of ϕ_n is accessible. After normalizing the CD data, the curves represent the fraction of aggregated OPVs (ϕ_n).³⁵⁹ In the case of nucleation–elongation aggregation, a one–parameter fit (ϕ_{sat}) of the data can be provided by:

$$\phi_n = \phi_{\text{sat}}[1 - \exp[-r/\phi_{\text{sat}}(T - T_e)]] + \phi_o \quad \text{eq. 11}$$

based on eq. 8 with ϕ_{sat} is the saturation level of the data, ϕ_o is the baseline level of the data and $r = -\phi_{\text{sat}}h_e/RT_e^2$. To determine the mean aggregation number, eq. 7 can be used to derive:

$$N = K_a^{-1/2}[(\phi - \phi_o)/(\phi_{\text{sat}} + \phi_o - \phi)] \quad \text{eq. 12.}$$

In the case of isodesmic aggregation, the one–parameter fit (ϕ_{sat}) for the data is given by:

$$\phi_n = \phi_{\text{sat}}[1 - \exp[-r/\phi_{\text{sat}}(T - T_m)]] + \phi_o \quad \text{eq. 13}$$

based on eq. 1 with $r = -\phi_{\text{sat}}h_m/RT_m^2$ while

$$N = [(\phi - \phi_o)/(\phi_{\text{sat}} + \phi_o - \phi)] \quad \text{eq. 14}$$

based on eq. 2.

4.5.3 Modeling the Self–Assembly Process

We consider the CD transition curves probing the helical assembly, measured for four different concentrations of **OPV₄UT**. The normalized curves are displayed in Figure 4.16. These curves could be modeled by eq. 11 showing unambiguously that the self–assembly of **OPV₄UT** is a highly cooperative process based on the appearance of a sharp transition during aggregation. This indicates that large aggregates are not present above the characteristic temperature T_e (the region above $T/T_e = 1$). Large aggregates are only formed after an oligomeric nucleation step (see the enlarged regions in Figure 4.16). The temperature T_e decreases upon diluting, revealing a linear relationship in the Van 't Hoff plot (Figure 4.16), similar to that observed in Figure 4.9, with $\Delta H = -100$ kJ/mol OPV dimer in aggregates while the $\Delta S = -215$ J/K per mol OPV dimer in aggregates. At $T = T_e$, the theory allows the calculation of the value of K_a , about 2×10^{-4} to 2×10^{-5} according to eq. 9 (Figure 4.16). The early stage of the helical self–assembly, *i.e.* the formation of pre–aggregates, was perfectly fitted in all cases by eq. 10 with the same values for K_a and T_e (see the Figure 4.16.). The initial stacking of the OPV dimers into pre–aggregates is a prerequisite for spontaneous growth of the helix at temperatures below T_e (below $T/T_e = 1$, Figure 4.16); this is called the cooperative effect. The growth in the elongation regime by the many reinforcing non–covalent interactions is enthalpy–driven with an excess bond formation enthalpy of about -56 kJ/mol estimated from the slope at T_e . Although there is good overlap between experiment and theory in the case of the most dilute solution (5.4 μM), interestingly, for the higher **OPV₄UT** concentrations used,

the theory underestimates the CD data at low temperatures (low T/T_e). The fits for the higher concentrations show $\phi_{\text{sat}} = 0.91$ for 11 μM , $\phi_{\text{sat}} = 0.85$ for 48 μM and $\phi_{\text{sat}} = 0.75$ for 240 μM . Moreover, the temperature at which the deviation between theory and experiment occurs shift to higher temperatures upon increasing the concentration, for 11 μM at $T = 293$ K, for 48 μM at $T = 305$ K and for 240 μM at $T = 323$ K.

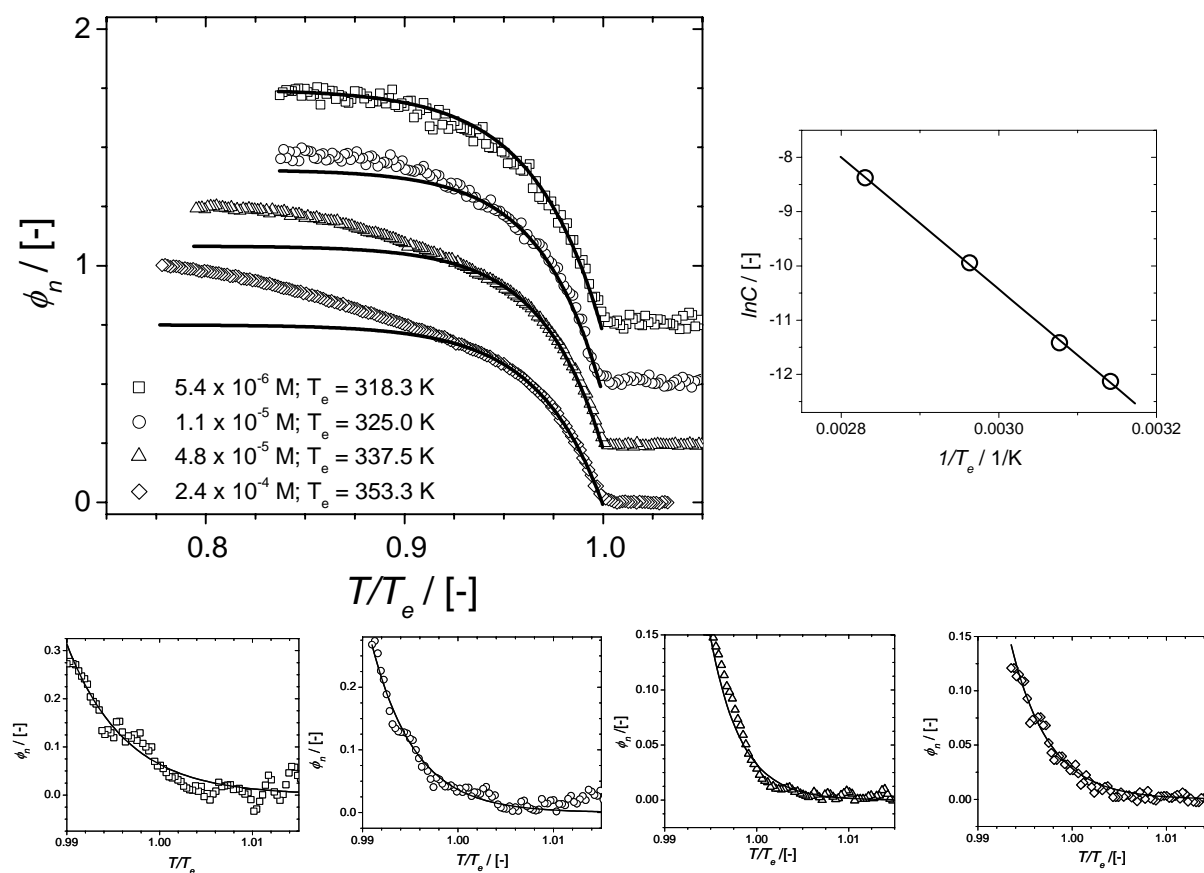


Figure 4.16: Temperature dependencies of the self-assembly in dodecane for the normalized fraction (ϕ_n) at various **OPV₄UT** concentrations. Data points were obtained by monitoring the CD band at $\lambda = 466$ nm. One-parameter fits according to equation 11 are displayed. A vertical offset of the curves of 0.25 is chosen for reasons of clarity. At the right is the Van 't Hoff plot constructed for T_e versus concentration. At the bottom are the immediate regime around T/T_e enlarged and fitted by equation 10.

This behavior is also visible in the plot of N vs T (Figure 4.17) based on eq. 7 and 12. Also here is the cooperativity of the self-assembly apparent; close to a critical T_e grows rapidly the size of the aggregates after the formation of pre-aggregates. At lower temperatures, the average columnar length at the point of deviation between experiment and prediction is remarkably constant, $N = 410 - 470$, which we assign to the cooperative stack length. In the case of the dilute solution, the extrapolated value to low temperature reaches the same cooperative length. Assuming a π - π stacking distance of 0.35 nm, this corresponds to a columnar length of ca. 145 – 165 nm. With the data from the SANS (Figure 4.11) and AFM (Figure 4.13) in hand, the deviation from one-dimensional growth can be interpreted as the clustering of stacks. The persistence lengths found by SANS and AFM of about 150 and 125 nm, respectively (Table 4.1, p. 63), are in excellent agreement with the cooperative length of 145 – 165 nm, predicted from the CD data. Similar CD measurements on **OPV₃UT** (46 μM ; $T_e = 317.5$ K) reveal a shorter cooperative length of ca. 125 nm while for the **OPV₅UT** (35 μM ; $T_e =$

356.5 K) a longer cooperative length of ca. 175 nm is found (Figure 4.17b). This trend is also in agreement with the SANS results. Note that the CD–shape of supramolecular aggregates of, *e.g.*, chlorosomes, cyanine dyes or π –conjugated polymers possibly reveal a pronounced rod–length dependence resulting from macroscopic chirality.^{360–364} Such contribution to the CD–shape is additional to the microscopic chirality, *i.e.*, the spatial arrangement of the transition dipole vectors of the interacting molecules.³⁶⁵

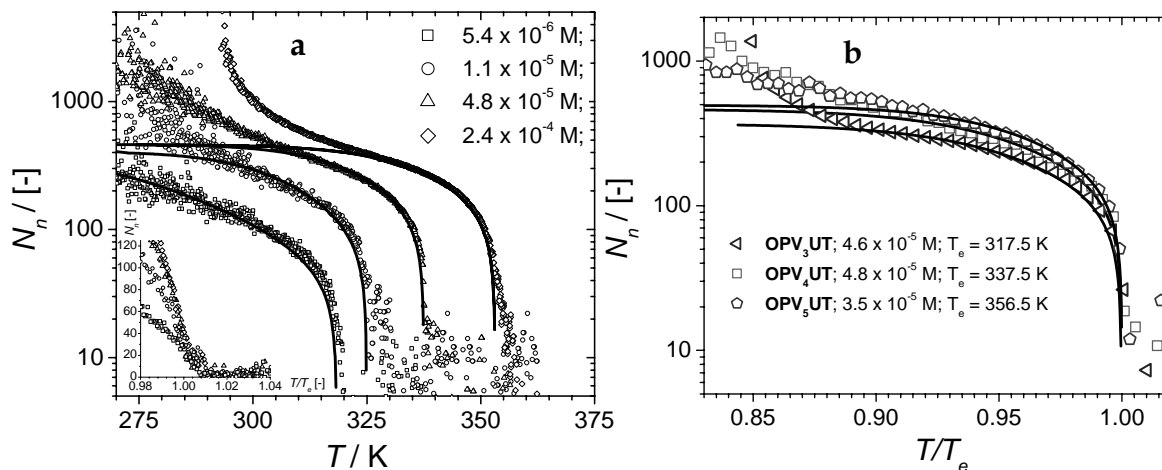


Figure 4.17: Prediction of the average number of molecules participating in the aggregation process (N) versus temperature at four different concentrations for **OPV₄UT** in dodecane according to equation 12 (a). Inset shows enlarged region around $T/T_e = 1$. Similar plot (b) shows the comparison between **OPV₃UT**, **OPV₄UT** and **OPV₅UT**.

The plot in Figure 4.17 also allows the size of the pre–aggregates, at $T = T_e$ to be calculated. Remarkably, the size of these aggregates varies only little over the concentration range, between 20 and 40 hydrogen–bonded dimers, indicating a similar type of aggregation in the nucleation regime. The values are in agreement with eq. 6 giving 17 to 37 hydrogen–bonded dimers. Computer simulations of the photophysical properties of the **OPV₄UT** stacks, reported elsewhere^{366a}, are in agreement with the experimental CD spectra with enforced rotation angles between adjacent stacked dimers in the range of 6 to 12°. Intriguingly, to make one helical pitch (180°) this would involve 15 to 30 stacked hydrogen–bonded dimers.

At 168 μM , a melting endotherm could be detected, using a sensitive differential scanning calorimeter corresponding to a melting point of 352.3 K (Figure 4.18). The strong endotherm in this solution confirms the high cooperativity of the transition. The enthalpy of

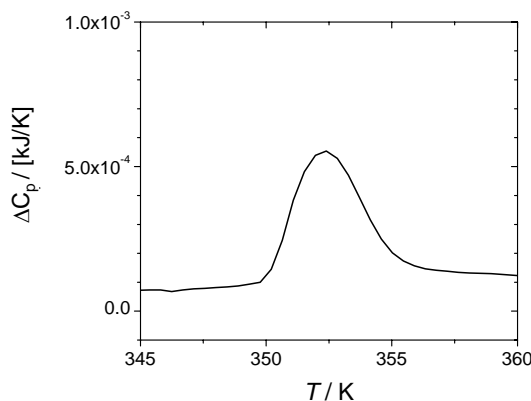


Figure 4.18: DSC thermodiagram of 0.5 mL of 1.7×10^{-4} M of **OPV₄UT** in dodecane.

bond formation, h_e , can be derived from the relation $\Delta C_p \sim h_e^2/RT_e^2$ to be about -48 kJ/mol, in good agreement with the value found from the CD melting curves.

4.5.4 Self-Assembly monitored by UV/vis and Fluorescence

To gain more insight into the assembly process similar detailed measurements were carried out by monitoring the change in the absorption and fluorescence for solutions of **OPV₄UT** (1.1×10^{-5} M). When monitoring at $\lambda = 490$ nm (Figure 4.19a) the change in the UV/vis transition curve is gradual and occurs at a higher temperature than the transition in the CD curve (Figure 4.20) in agreement with the observations reported in Section 4.4.1. Upon normalizing³⁶⁷ the UV/vis data (Figure 4.20), the shape of curve is typical for isodesmic self-assembly with T_m is 342.2 K and $h_m = -44$ kJ/mol. The discrepancy between the UV/vis and the CD curves can possibly attributed to the fact that UV/vis probes primarily the formation of pre-aggregates whereas the CD monitors the transition from pre-aggregates into long helical stacks.

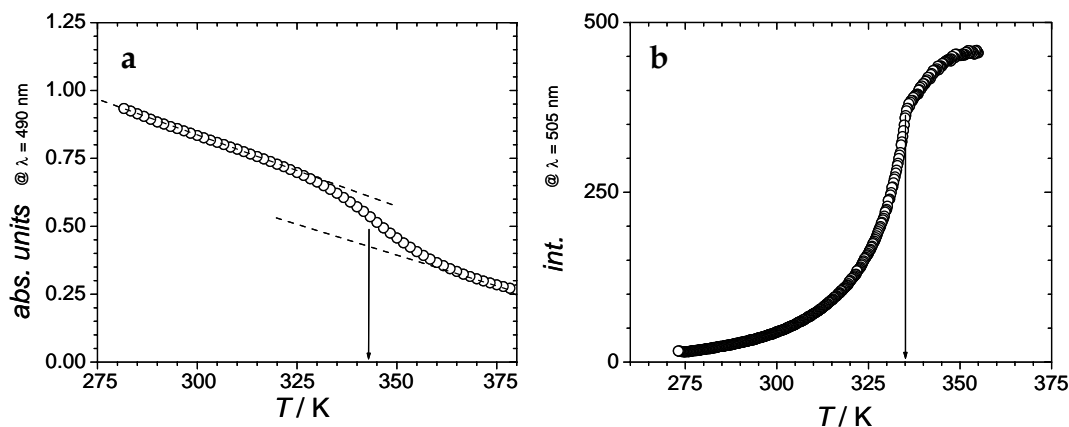


Figure 4.19 (a) Aggregation data for **OPV₄UT** ($11 \mu\text{M}$ in dodecane) following the absorbance at $\lambda = 490$ nm and (b) the emission at $\lambda = 500$ nm. Not all data points are shown. Arrows indicate changes of the signal at specific temperatures.

The change in the emission was followed at $\lambda = 500$ nm, characteristic for free **OPV₄UT** dimers. In this transition curve (Figure 4.19b), a transition point is found that is located in the region in-between the specific temperatures in the CD and UV/vis transition curves (Figure 4.20). The shape of the fluorescence transition curve is typical for a cooperative self-assembly process and could be fitted by eq. **10** and **11** yielding $T_e = 335.5$ K at $\phi_n = 0.19$ and $K_a = 7 \times 10^{-3}$ (inset Figure 4.21). This process is far less cooperative contrasting with the transition observed in the CD data ($K_a = 2 \times 10^{-4}$). The pre-aggregate contains about 5 stacked **OPV₄UT**-dimers whereas the assembly at $T = 325$ K contains about 18 OPV dimers (inset Figure 4.20). This value is well in agreement with the mean aggregation numbers of the pre-aggregates probed by CD. At lower temperatures (higher aggregated fractions) the fit deviates from the data (inset Figure 4.21) and, interestingly, the deviation point coincides with the point where the CD effect arises. It is appealing to relate this extra quenching of the fluorescence in the stacks to this coincident induction of the helicity. It is known that improved ordering could lead to a faster diffusion of excitons to trap sites.^{366b} When comparing the transition curve of the fluorescence with the absorption curve, apparently the formation of a pre-aggregate of about 5 OPV-dimers gives rise to the most pronounced changes in the absorption spectrum.

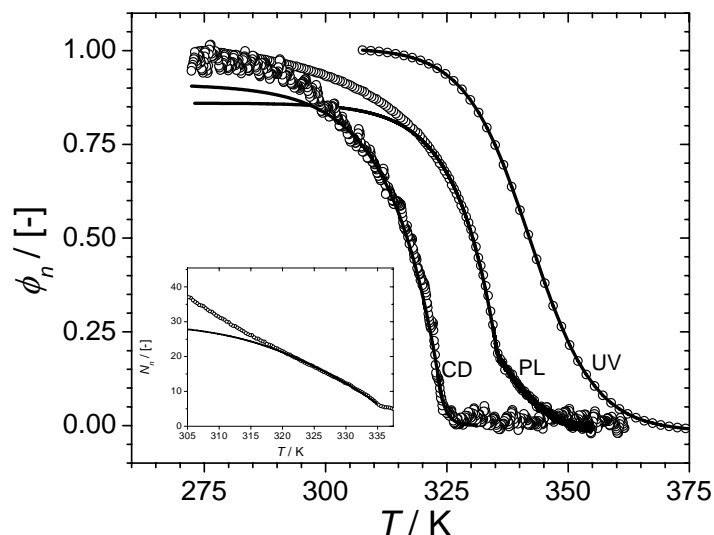


Figure 4.20: Detailed transition curves based on UV/vis, fluorescence (PL) and CD data for OPV_4UT ($11 \mu\text{M}$, dodecane). Fits to the data are shown based on the equations for nucleation–propagation assembly (CD, PL) and for isodesmic assembly (UV/vis). Inset shows mean aggregation number vs temperature based on fluorescence data.

4.5.5 Mechanism of the Self-Assembly Process

The mechanism of OPV_4UT self-assembly in solution can be proposed to occur as follows based on the data presented in this Chapter. First, the OPV_4UT monomers dimerize via hydrogen-bond formation. Upon cooling, about 5 of such dimers associate into small disordered pre-aggregates via an isodesmic process. Such pre-aggregates grow cooperatively further to about 20 stacked dimers. At this stage, the pre-aggregates become helical. After the helical transition, strong cooperative growth is observed. Upon further cooling, the cooperative stack length is reached when 410 to 470 dimers are assembled and finally clustering of the assemblies occurs. Figure 4.21 provides a cartoon summary of these processes and shows that the self-assembly of π -conjugated oligomers using several secondary interactions simultaneously follows nature's paradigm.

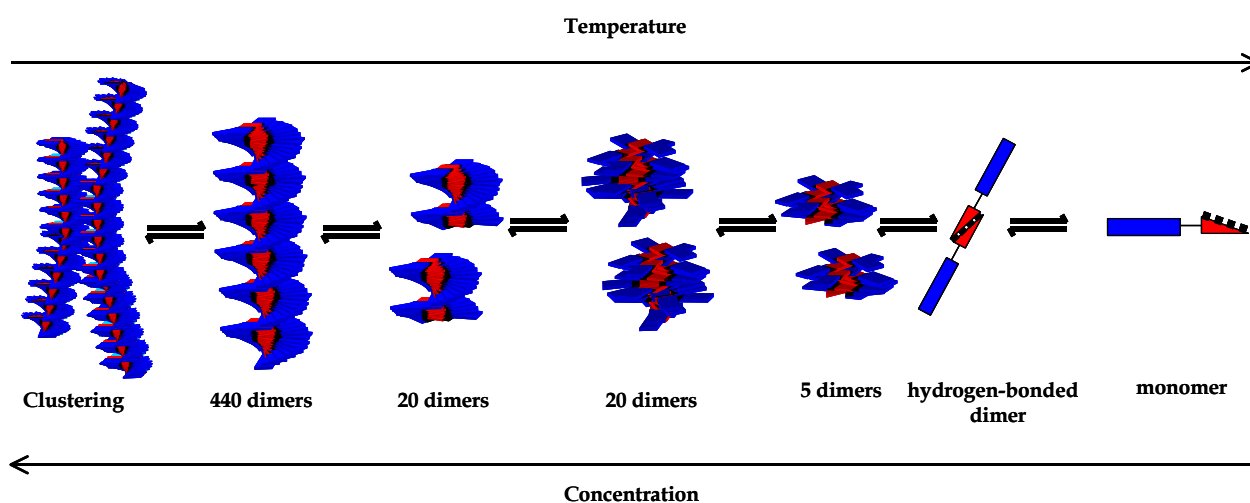


Figure 4.21: Schematic representation of the self-assembly in solution of OPV_4UT as function of concentration and temperature.

4.6 CONCLUSIONS

Optical measurements show that it is possible to self-assemble π -conjugated molecules into helical columnar polymers in apolar solution similar to processes found in nature. SANS measurements reveal rigid cylindrical objects having persistence lengths of 150 nm with a diameter of 6 nm for **OPV₄UT**. The stability and the persistence length of the stacks in solution increases with the conjugation length as a result of increased π - π interaction. Detailed optical measurements, that monitor the self-assembly processes of the OPVs, lead to a description in terms of a nucleation-elongation model that accounts for the high cooperativity of the self-assembly. The initial association of the OPV dimers into small pre-aggregates is essential to the formation of long helical stacks. The helix formation is enthalpy-driven and a cooperative length of about 440 dimers is found. At high concentration, evidence of network formation is found in agreement with the SANS and AFM results.

The transfer to a solid support of these self-assembled fibers is one of the first examples of single organic fibers consisting of self-assembled chromophores. These individual nano-sized fibrils might be interesting in the field of supramolecular electronics (Chapter 5).

Introduction of a covalent spacer between adjacent dimers resulted in frustrated stacks. Therefore, it is interesting to introduce hydrogen-bonds in the stack direction. Doing so, a large electric dipole along the stack is created; an interesting tool for nano-manipulation of fibrils by electric fields (Section 4.7).

4.7 Towards Electrically Aligned OPV-gels

Liquid crystals can organize into columnar stacks that can be aligned with an electric field.³⁶⁸ This would be an attractive approach to obtain homogeneous films. An interesting class of liquid crystals is based on C_3 -symmetrical discotics containing a 1,3,5-benzenetricarboxamide unit.³⁶⁹ Solvophobic effects, hydrogen-bonding and π - π stacking interactions, have been used to organize the building blocks into cylindrical fibers in solution and in the solid state. Introducing chiral side chains leads to helical fibers.³⁷⁰ Some of these aggregates form organogels: entangled, three-dimensional, continuous networks of fibers in which the solvent is encapsulated.³⁷¹ However, so far, discs containing 1,3,5-benzenetricarboxamide units have not been substituted with semi-conducting units. Therefore, **C₃-OPV₄** (Figure 4.22) was synthesized by reacting trimesic chloride with an OPV amine derivative according to literature procedures.³⁷⁰ In methylcyclohexane (MCH) at high concentrations (10^{-3} M) a gel was obtained visualized by TM-AFM, showing a dense fibrillar network at the substrate. Hydrogen-bond formation was confirmed by IR; in MCH the N-H and C=O stretch vibrations are at 3225 cm^{-1} and 1648 cm^{-1} similar to those found earlier for the C_3 -analogues lacking the OPV indicating hydrogen-bonded species,³⁷² whereas in tetrahydrofuran (THF) solution, these vibrations are at 3422 cm^{-1} and 1671 cm^{-1} indicative of absence of hydrogen-bonding. A two-step assembly process was observed; UV/vis and PL data show a transition from molecular dissolved species to non-helical stacks at $80\text{ }^\circ\text{C}$. At $54\text{ }^\circ\text{C}$, a small non-bisignated Cotton effect develops. This indicates helical induction in the stacks of **C₃-OPV**, however we propose that frustrated stacks are formed in which the π - π stacking interactions compete with the hydrogen-bond interactions. Preliminary experiments show that it is not possible to align these stacks in an electric field.

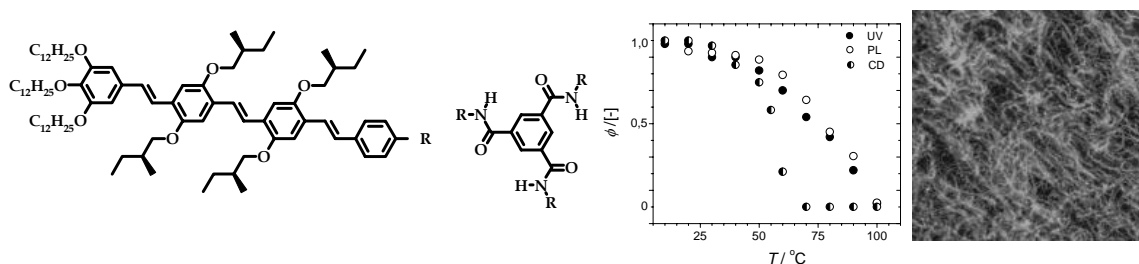


Figure 4.22: C_3 -symmetrical discotic molecule (**C₃-OPV₄**) bearing three tetrameric OPVs (**18** is $R = \text{NH}_2$) Transition curves in methylcyclohexane show two-step assembly. AFM shows densified fibrillar network.

5 CONTROLLED DEPOSITION AT DEVICE SURFACES OF SELF-ASSEMBLED OLIGO(P-PHENYLENEVINYLENE)S

ABSTRACT

Chiral columnar stacks of oligo(*p*-phenylenevinylene) (OPV₄UT) have been self-assembled in heptane and the transfer of single stacks to a solid support has been studied by atomic force microscopy. The transfer of the single cylinders as isolated objects from solution to a solid support was only possible when specific concentrations and specific solid supports were used. At higher concentrations, an intertwined network is formed, while, at low concentration, ill-defined globular objects are observed. Only inert substrates (graphite and silicon oxide) tolerate single fibers. In the case of repulsive surfaces (mica and glass) clustering of stacks occurs while at an attractive surface (gold) the stacks are destroyed. The stacks on graphite have been studied by fluorescence imaging. The polarized optical response shows a high degree of internal order in the self-assembled chiral fibrils. By spin coating films with thicknesses of the order of 75 nm are made having a supramolecular organization that resembles the organization present in solution. The uniform rod-like morphological domains range over several hundreds of nanometers as shown by atomic force microscopy. Based on time-resolved emission spectra, this rod-like morphology causes a fast migration of excitations to trap sites. The films could be applied in a field effect transistor showing mobilities of the order of 10⁻⁶ cm²/Vs. Surprisingly, no currents could be detected in the course of the current work when isolated fibers are used as the conducting pathway in nanosized field effect transistors. Uniform rod-like domains of the OPVs were preserved when blended with a C₆₀ derivative producing stable photovoltaic devices.

CONTENTS

	<i>page</i>
5.1 Introduction	74
5.2 Single Fibers	74
5.2.1 Atomic Force Microscopy	74
5.2.2 Fluorescence Imaging of Fibrils	78
5.2.3 Fibrils in Nanoscopic Field Effect Transistors	80
5.3. Fibrils in Films	81
5.3.1 Atomic Force Microscopy	81
5.3.2 Fluorescence Spectroscopy	82
5.3.3 Field Effect Transistor	83
5.3.4 Photovoltaic Cell	83
5.4 Conclusions	85

5.1 INTRODUCTION

Many examples are reported in which molecules are directed into well-organized self-assembled structures with a specific function through use of molecular recognition.^{43,253,309,373-375} Different types of non-covalent interactions have been applied creating architectures that have a specific function and are relatively stable.^{329,333,376-380} An emerging challenge for applying these supramolecular architectures in the field of materials science is the transfer of such objects to a solid support and a restricted number of studies show the opportunities and limitations of this process.^{328,332,372,381,382}

An effective strategy for the construction of individual nano-sized columns having π -conjugated oligomeric building blocks is essential for the development of the field of supramolecular electronics. Such organic assemblies could represent an alternative to (hybrid) inorganic wires,⁵⁻⁷ carbon nanotubes^{8,9} and (single) organic molecules.²⁻⁴ Various examples of self-assembled semiconducting organic rods in solution have already been presented in the recent literature³⁴⁶ and in the previous Chapters; however, examples of directed transfer of such nanowires to solid supports and investigation of their behavior are scarce and there are no examples of practical exploitation of these possibilities. Alternatively, many literature examples^{242,291,346,383} construct nano-sized rods at the surface relying on the simultaneous events of transferring and self-assembling π -conjugated molecules at the surface (see also Section 2.4). Both approaches will benefit from understanding the parameters that play a role in the transfer process of self-assembled molecules from solution to solid supports that are relevant for devices and that is the subject of this Chapter.

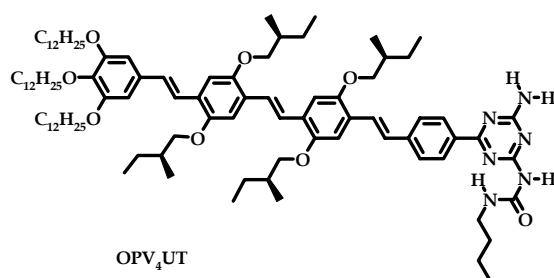


Chart 5.1

5.2 SINGLE FIBRILS

5.2.1 Atomic Force Microscopy

Chapter 4 reports the transfer of self-assembled fibers of **OPV₄UT** (Chart 5.1) from heptane to graphite yielding fibers that have similar dimensions, *i.e.* persistence length and diameter, to those found in solution. The starting concentration of the solution used for drop casting is, however, crucial for the observation of single fibers of **OPV₄UT** on graphite (HOPG). When the solution was diluted to 1.3 μM , at which stacks of **OPV₄UT** are partly dissolved, many globular structures were visible next to the self-assembled single fibrils (Figure 5.1d). The formation of globular structures is probably the outcome of uncontrolled self-assembly during the casting procedure of the molecularly dissolved OPV fractions (Figure 4.8). Further dilution to 0.13 μM showed only globular structures (Figure 5.1e). At this

concentration, optical spectroscopy showed that only molecularly dissolved species are present in solution at room temperature (Figure 4.8).

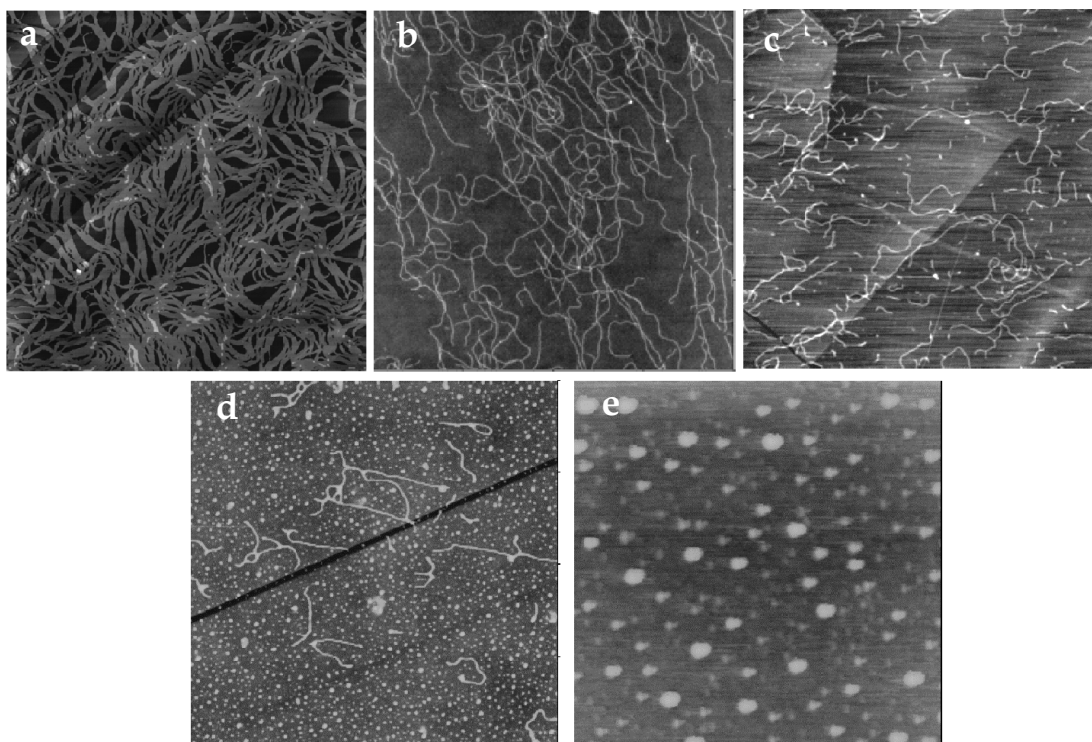


Figure 5.1: TM-AFM images of **OPV₄UT** on graphite showing different types of aggregation depending on the concentration of the drop cast solution; (a) 7×10^{-4} M, $7 \times 7 \mu\text{m}^2$, z-scale 25 nm, (b) 1.3×10^{-4} M, $10 \times 10 \mu\text{m}^2$, z-scale 10 nm, (c) 1.3×10^{-5} M, $7 \times 7 \mu\text{m}^2$, z-scale 10 nm, (d) 1.3×10^{-6} M, $7 \times 7 \mu\text{m}^2$, z-scale 10 nm and (e) 1.3×10^{-7} M, $5 \times 5 \mu\text{m}^2$, z-scale 40 nm.

Applying a more concentrated solution of 130 μM resulted in joining together of individual strands predominantly in an end-to-end fashion (Figure 5.1b). At 700 μM , side-by-side association of the fibers was observed as an additional assembly process (Figure 5.1a). Broad bundles having a height of 5.5 nm, merge and separate continually thereby changing the number of side-by-side lying fibers. Clearly, not only the concentration but also the temperature of the cast solutions will determine the quality of the fibrils on the surface. Whereas a fibrillar network was observed up to 313 K (Figure 5.2a), in the range of 328 – 343

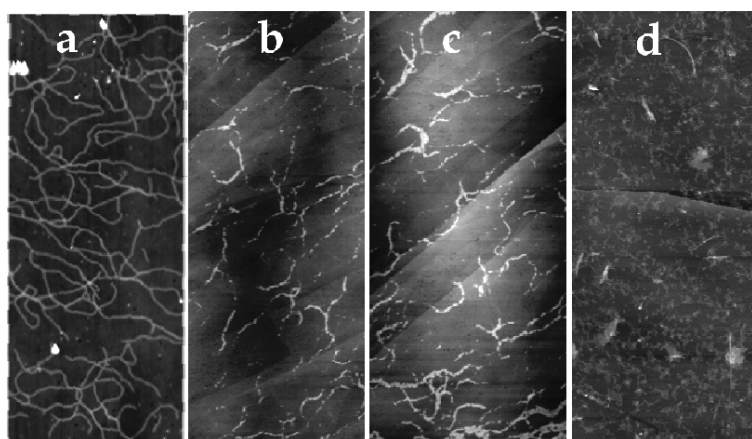


Figure 5.2: TM-AFM images ($2.5 \times 7.5 \mu\text{m}^2$, z-scale 10 nm) of **OPV₄UT** on graphite showing different types of aggregation depending on the temperature of the drop cast solution (1.3×10^{-4} M) (a) 313 K, (b) 328 K, (c) 343 K and (d) 358 K.

K, the network was lost and small fibrils were observed (Figure 5.2b,c). At high temperatures, well above 340 K, no fibrils are observed (Figure 5.2d). Apparently, and strikingly at first glance, to observe fibers at graphite it is required first to form stacks in solution before casting this solution onto a surface. Although *e.g.* evaporation of the solvent leads to an increase of the concentration, molecule–graphite interactions can be dominant over the formation of stacks starting off from too diluted or too hot solutions. The results show the subtleties of transferring supramolecular assemblies to surfaces. Similar observations were carried out for **OPV₃UT** and **OPV₅UT**. In the case of **OPV₃UT**, however, all concentrations at which the objects on the surface change from a globular shape to isolated fibrils and fibrillar networks were higher, while in the case of **OPV₅UT** these concentrations were lower. This behavior corresponds very well with the behavior in solution (Chapter 4) where the stability of the stacks increases with the conjugation length.

Single fibers were observed on graphite only when specific concentrations or temperatures were used. However, solid supports used in devices are different and consist of several components. Therefore, we have also investigated the deposition of the stacks in heptane on different types of solid supports (Figure 5.3). On silicon oxide wafers (Figure 5.3b) fibers were obtained similar to those found on graphite (Figure 5.3a), side-by-side lying stacks of **OPV₄UT** were formed on glass slides (Figure 5.3c) and the width of the fibers varies while the height is in all the cases approximately 5 nm. On mica (Figure 5.3d) the same results were found as on glass. Average contact angles confirmed that graphite (80°) and silicon oxide wafers (70°) are more hydrophobic surfaces yielding single fibers while on glass (30°) and mica (20°), which are more hydrophilic, a lamellar structure exists. The latter can probably be ascribed to more favorable interactions between the stacks rather than between the stacks and

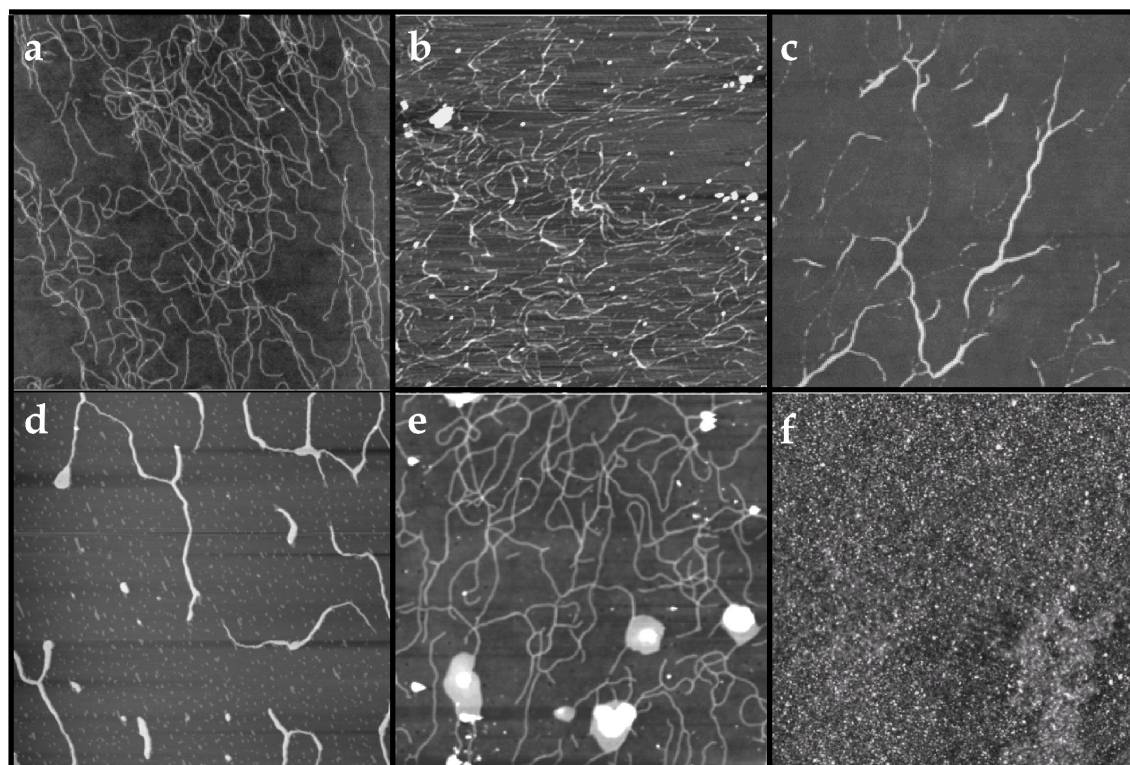


Figure 5.3: TM–AFM images of **OPV₄UT** drop cast from heptane on (a) graphite (1.3×10^{-4} M, $10 \times 10 \mu\text{m}^2$, z–scale 10 nm), (b) silicon oxide wafer (6.7×10^{-5} M, $10 \times 10 \mu\text{m}^2$, z–scale 10 nm) (c) glass slide, (d) mica, (e) carbon coated glass (6.7×10^{-5} M, $5 \times 5 \mu\text{m}^2$, z–scale 10 nm) and (f) gold. (c, d and f: 6.7×10^{-5} M, $7 \times 7 \mu\text{m}^2$, z–scale 10 nm).

the surface. When the polar glass substrate was coated with a thin layer of carbon (50 nm), a contact angle of 78° was measured indicating that the surface is hydrophobic. On this surface similar results to those seen on graphite were obtained, illustrating that it is possible to suppress repulsive surface interactions towards the stacks (Figure 5.3e). Applying a droplet of the same solution to gold surfaces resulted in complete destruction of the stacks (Figure 5.3f). Presumably, the molecule–gold interactions are so strong that they overrule the molecule–molecule interactions within the stacks, resulting in ill-defined globular objects despite the hydrophobic nature of gold (contact angle is 90°).

The observations described, stunningly illustrate the importance of molecule–surface interactions for the successful transfer of the supramolecular stacks that are present in solution to a solid support (inert surfaces, Figure 5.4). When the molecule–molecule interactions present in the supramolecular stacks in solution are perturbed by stronger molecule–surface interactions (attractive surfaces, Figure 5.4), the stacks can not be transferred to the surface. Repulsive surfaces (Figure 5.4) give rise to clustering of stacks due to the minimization of the contact area between the stack and the support resulting in lamellar arrays of stacks. Together with the fact that the concentration and the temperature of the cast solution determines the equilibrium between individual molecules and the supramolecular stack, it is obvious that many variables control the successful transfer of stacks from solution to surfaces.

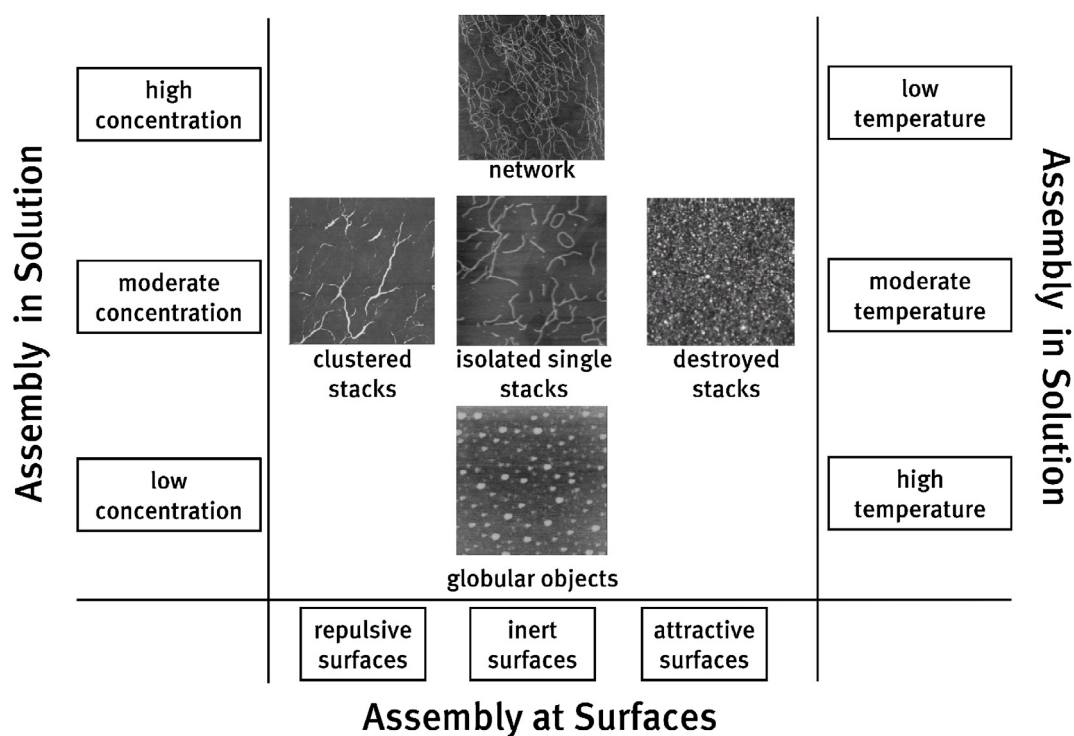


Figure 5.4: Plot representing the role of the interaction of the surface towards the stacks versus the concentration and temperature in the transfer process to the solid state of the supramolecular stacks formed in solution. TM–AFM images of glass (repulsive surface), graphite (inert surface, three concentrations) and gold (attractive surface).

5.2.2 Fluorescence Imaging of Fibrils

Methods to investigate the structural order of organic assemblies at the surface are tedious and have not been addressed before when it concerns π -conjugated structures. It is evident that the performance of potential nano-sized electronics will highly benefit from self-assembled fibrils having a uniform internal organization of the molecular building blocks. Therefore, we have employed polarized fluorescence microscopy (FM) to characterize the order in the fibrils at the surface. The dominant optical dipole moments for absorption and emission of **OPV₄UT** are directed along the long axis of the tetra(p-phenylenevinylene) unit. The regular molecular arrangement in the stack (see Chapter 4) is expected to result in a pronounced polarization of the fluorescence emission perpendicular to fiber axis.³⁸⁴

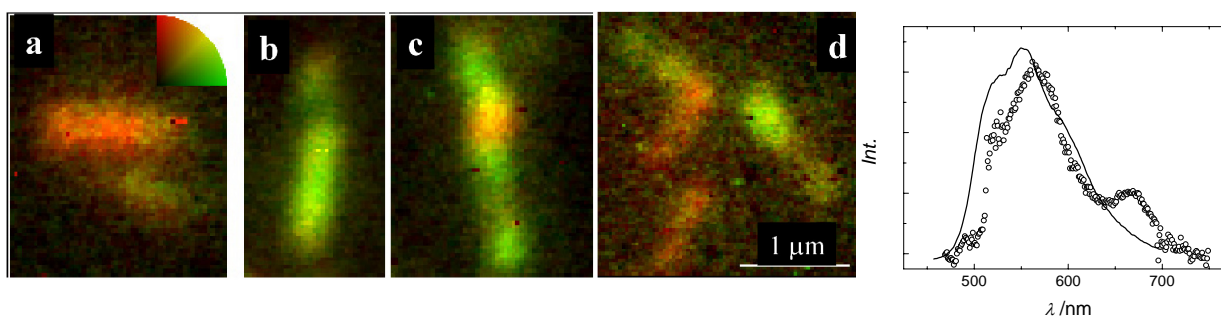


Figure 5.5: FM images ($\lambda_{exc} = 458$ nm, capture time = 300 s) of fibers of **OPV₄UT** on graphite with both excitation and detection polarizations having either a horizontal (0°) or vertical (90°) orientation with respect to the image. The color coding corresponds (see inset upper right corner in a) to the intensity ratio of the two polarization orientations: $R = I_{ver}/I_{hor}$ ranging from green ($R < 1$) to red ($R > 1$) through yellow ($R = 1$). Emission spectra of a single fiber (open symbols) and of a solution consisting of stacks used for drop casting (solid line).

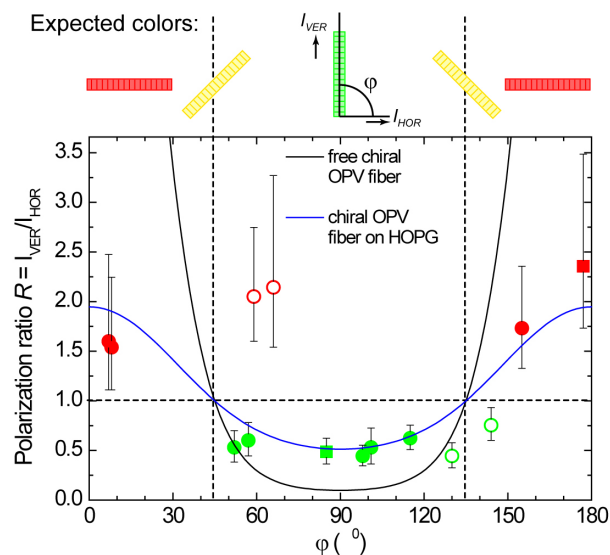


Figure 5.6: The symbols show the average polarization ratio R of all fourteen measured fibers as a function of the angle φ of the angle between the direction of the fiber and the horizontal axis. For clarity, the data points are given the same color as the color-code used in Figure 5.5, i.e. $45^\circ < \varphi < 135^\circ$ are green ($R < 1$) in this graph, whereas the others $0^\circ < \varphi < 45^\circ$ or $135^\circ < \varphi < 180^\circ$ are red ($R > 1$). The solid lines are calculations of R considering chiral **OPV₄UT** fibers in vacuum (black line) or on graphite (blue line). Top panel: the expected polarization degree and color coding for chiral **OPV₄UT** fibrils.

Figure 5.5 shows typical polarized FM pictures of individual fibers by imaging the emission. The emission spectrum of a single fiber (Figure 5.5) is very similar to the emission of a solution of fibers. The FM images reveal that the fluorescence of each fibril is polarized and that the direction of the polarization is strongly correlated to the direction of the fiber.^{385a} Figure 5.5a shows a fibril of about 1 μm in length, oriented horizontally, having a uniform red colour which indicates a vertically polarized emission from the entire fiber. The emission profile of this fibril shows that the vertically polarized emission is more intense than that of the horizontally polarized emission, yielding a polarization ratio $R = 2.4$. In contrast, the vertically oriented fibril in Figure 5.5b, exhibits an overall green colour, *i.e.*, a horizontally polarized emission.^{385b} The relationship between the light polarization and fiber orientation is apparent from Figure 5.5d, which shows three fibrils, one of them having a 90° bend, leading to a change in the colour-code at the bend. Most of the self-assembled fibrils reveal a uniform polarization over micrometer ranges, due to effective head-to-tail positioning of the smaller stacks in solution, and only some of them are not uniformly polarized. For instance, the colour-coded FM image of the long vertical fibril in Figure 5.5c displays a red-yellow defect in the overall green fibril, which indicates the mispositioning of one stack with respect to the others. From the fourteen measured fibrils, it appears that ten of the fibers show polarization in line with a dominant dipole moment perpendicular to the axis of the fibers. This is in agreement with stacked dimers of **OPV₄UT** perpendicular to the stack direction. Nanofibrils with $45^\circ < \varphi < 135^\circ$ appear green in the graph in Figure 5.6, whereas the others ($0^\circ < \varphi < 45^\circ$ or $135^\circ < \varphi < 180^\circ$) are red. Only four of the measured fibrils reveal an unexpected color-coding which differs from the fibrils in other areas (open circles in Figure 5.6). It is striking that all these four fibrils were situated in one region of the substrate having the same tilted orientation of the **OPV₄UT** molecules in a fiber (Figure 5.5d).

Although all fibrils exhibit a profound polarization, the maximum polarization ratio is rather low ($R \approx 2$). To explain this observation we have calculated R as a function of fiber orientation, using a model that calculates the polarized optical response of a chiral fibril by summing up the optical dipoles.^{386,387} The model takes into account the depolarizing effects of both the FM set-up and the HOPG substrate.³⁸⁶ The result of this calculation (blue line in Figure 5.6) describes the observed data remarkably well. The model provides two main reasons for the rather low polarization degree. First, the chiral composition of the stacks implies that the emission is the sum of polarized and *unpolarized* contributions of dipoles that are parallelly and perpendicularly oriented to the substrate, respectively. However the unpolarizing effect of the perpendicular dipoles alone can not explain our data, as is clear from the black curve in Figure 5.6, calculated for free chiral OPV stacks. Second, the dielectric constant of the underlying HOPG results in a lower intensity of the polarized horizontal dipoles as compared to the unpolarized vertical dipoles, causing a drastic reduction of R .

The control of the internal order within self-assembled fibrils, and the ability to measure it, is a crucial step for obtaining uniform organic fibrils that can be applied in nano-sized electronics at room temperature.

5.2.3 Fibrils in Nanoscopic Field Effect Transistors

Fibrils of **OPV₄UT** were investigated to see if they could be applied as conductive fibrils in a nano-sized field effect transistor. To demonstrate the importance that all components of such devices must act inertly to supramolecular stacks, two electrode patterns were used. A classical pattern was applied, (Figure 5.7a, usually used to measure charge transport properties of carbon nanotubes⁸), consisting of a gate electrode of aluminum oxide and a source-drain electrode of gold (gap-size 50 nm), attached to a silicon oxide wafer. After transfer of the stacks to this electrode pattern it can be clearly seen that gold destroys the stacks of **OPV₄UT** while they are intact at the silicon oxide surface and aluminum oxide gate (Figure 5.7b). Surprisingly, when a second electrode pattern was used in which an alloy of gold-palladium was applied as source-drain electrodes (gap-size 200 nm) on a silicon oxide wafer, fibrils were also observed at the gold-palladium surface. Contact angle measurements confirm that the gold-palladium surface is also hydrophobic in nature (88°) as is graphite (80°), gold (84°), palladium (94°) and silicon oxide wafers (70°), however, the surface characteristics have changed compared to pure gold surfaces since on that surface no fibrils could be observed. X-ray photoelectron spectroscopy showed that the electrode surface composition changed having an Au:Pd elemental ratio of 3:2.

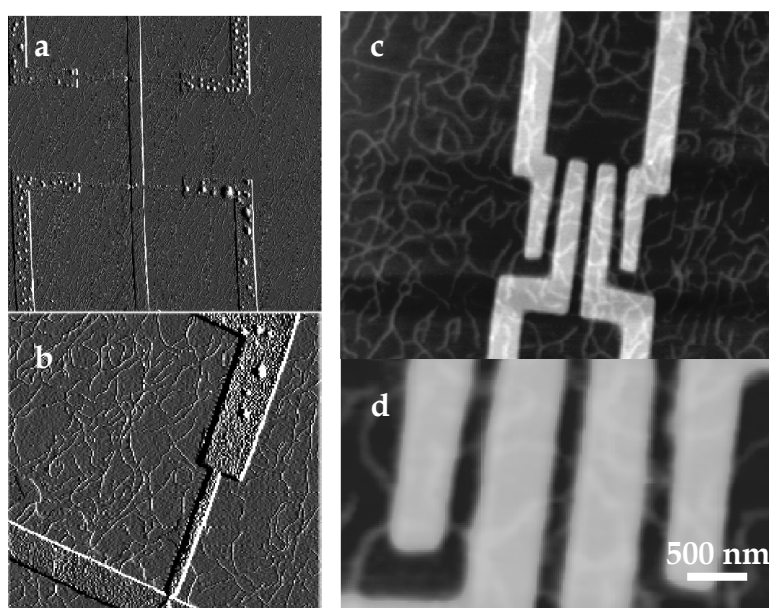


Figure 5.7: TM-AFM images of two different FET devices with nanoscopic dimensions. (a) aluminum oxide gate, gold source-drain contacts attached to a silicon oxide wafer (height, $20 \times 20 \mu\text{m}^2$, z-scale 65 nm). (b) close-up amplitude image. (c) gold-palladium source-drain contacts on silicon oxide wafer (height, $6.3 \times 6.3 \text{ mm}^2$, z-scale 35 nm). (d) close-up of several fibers of **OPV₄UT** bridging the source-drain electrodes.

Figure 5.7d shows a few single fibers spanning the 200 nm gap of the electrode fingers allowing for the measurement of the mobility of the charge carriers through the fibers. However, no electrical conductivity through the single fibers (20 samples) could be detected with the electronic measurement system having an upper limit of 1 T Ω and without destroying the devices. Many reasons can be thought of that hamper any traceable charge flow through the fibrils. It is known, for example, that chemical defects can influence dramatically the performance of devices.^{388a} Contact problems between electrodes and the core of the fiber can hamper injection of charges as the fibers have an aliphatic jacket. Alkyl chains are known to be poor conductors, however, separate measurements by others show that if most of the

applied voltage drop occurs over the alkyl chain domain, much higher currents should have been observed.³⁸⁹ Of course, the edge-on orientation to the surface of the dimers in the fibrils is not favorable, but similar measurements by others show the possibility of injecting charges in such geometry. Structural defects in the fibers, as observed by fluorescence microscopy, may limit the charge carrier transport. Charge transport is also influenced by the nature of the side chains, *i.e.* linear or branched. Recently it is shown that the mobility in PPVs can be improved significantly up to values of 10^{-3} cm²/Vs by symmetrically substituting the PPVs with linear alkyl chains.^{388b} To estimate what currents can be expected through fibers of **OPV₄UT** the next Section addresses the charge carrier mobility in thick films in field effect (bulk) transistors.

5.3 FIBRILS IN FILMS

5.3.1 Atomic Force Microscopy

To achieve homogeneous films, required for most plastic electronic devices, a spin coating procedure using more concentrated solutions was adopted. The films were studied with TM-AFM and fluorescence spectroscopy. After spin coating heptane solutions of **OPV₄UT** (7 g/L) onto an HDMS-treated silicon oxide surface covering interdigitated gold electrodes (source-drain), the TM-AFM height image showed smooth films with a thickness of 75 nm and a root-mean-square (rms) roughness of 5 nm. High-resolution AFM images of such films can be obtained using metal-coated tips on good quality cantilevers (*Q*-factor > 200) with a small spring constant in resonant mode.²⁴ Phase imaging with such metal-coated tips revealed individual elongated rod-like textures (Figure 5.8b) for films of **OPV₄UT**, which are not resolved on the simultaneously recorded height image (Figure 5.8c). The width of the rods is constant (about 5 nm) as deduced from the line scan. Their lengths are spanning hundreds of nanometers which is in agreement with the SANS data (Chapter 4). Mesoscopic domains in which columns lie straight next to each other are clearly visible (Figure 5.8d) probably as a result of side-to-side aggregation of the rods. The orientation of the domains is isotropic, creating series of domain boundaries.

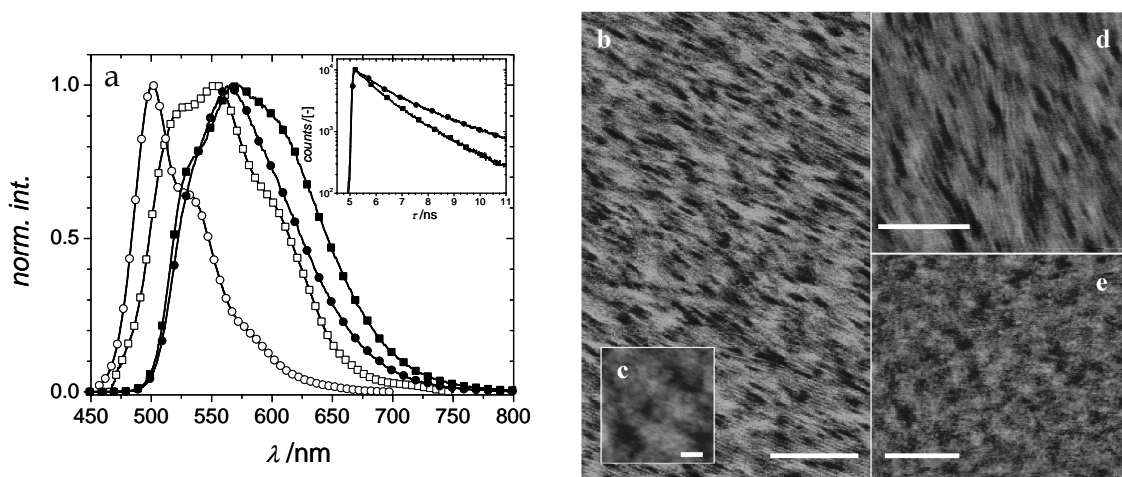


Figure 5.8: (a) Emission spectra of **OPV₄UT** in solution (open symbols) and of films (filled symbols). Solvents used are heptane (squares) and chloroform (circles). Films were spin coated from these solutions onto device substrates. Inset shows decay traces of the emission at $\lambda = 650$ nm for films spun from heptane and chloroform. (b) TM-AFM phase image (z -scale 35°) of a film spun from heptane with the simultaneously recorded topography (z -scale 15 nm) in (c) and a recorded close-up phase image (z -scale 35°) in (d). (e) TM-AFM phase image (z -scale 5°) of a film spun from chloroform. All bars represent 100 nm. Images were measured after device operation (see Section 5.3.3).

In contrast, films spun from a chloroform solution (7 g/L, Figure 5.8e), completely lack the rod-like morphology and assemblies that range from 5 to 50 nm in size were seen. Since **OPV₄UT** is molecularly dissolved in chloroform, the solid-state morphology is probably the result of ill-defined aggregates that are formed during the spin coating process. The smoothness of the films spun from heptane, together with the uniform domain sizes of several hundreds of nanometers is an improvement compared to those reported for related poly(p-phenylenevinylene)s, PPVs.⁴²

5.3.2 Fluorescence Spectroscopy

The solid state fluorescence spectra of **OPV₄UT** depend on the solvent used for spin coating. The steady-state emission spectrum of films spun from heptane show a maximum at $\lambda_{em,max} = 573$ nm (Figure 5.8a) while films spun from chloroform have a maximum at $\lambda_{em,max} = 563$ nm. The lifetime of the emission at $\lambda_{em} = 570$ nm of **OPV₄UT** in the films is considerably shorter than of **OPV₄UT** in solutions (Figure 5.8a) whereas the decay of the emission at $\lambda_{em} = 650$ nm in the films is comparable to that in solutions. The decay times of the emission at $\lambda_{em} = 570$ and 650 nm for films spun from heptane (chloroform) are $\tau = 0.30$ ns ($\tau = 0.65$ ns) and $\tau = 1.1$ ns ($\tau = 1.7$ ns), respectively. These differences indicate that the excitations reach trap sites earlier when heptane is used.³⁹⁰ To get more insight into this behavior, time-resolved emission spectra of both films were measured. Figure 5.9 shows that the fluorescence of the film spun from chloroform gradually red shifts after excitation at $\lambda = 400$ nm. In addition, in the case of films from chloroform, the first time traces show typical spectra for molecularly dissolved species which could not be observed in the films spun from heptane. The band shape of the emission spectrum changes in both films giving similar spectra for the traces at later times. This red shift is possibly the result of excitation migration to traps, which exist in the low energy tail of the emission spectrum and are presumably very similar of nature for both films.³⁹¹ The red shift to $\lambda = 600$ nm occurs, however, much faster (< 1 ns) in the films spun from heptane than observed for films spun from chloroform (> 3 ns). Apparently, the films spun from heptane are more ordered making them advantageous for device applications. These observations are in agreement with the research on π -conjugated polymers.⁴⁰⁷ Film morphology favoring energy migration show that the blue portion of the emission has a shorter lifetime due to competitive energy transfer trap states with spontaneous emission.

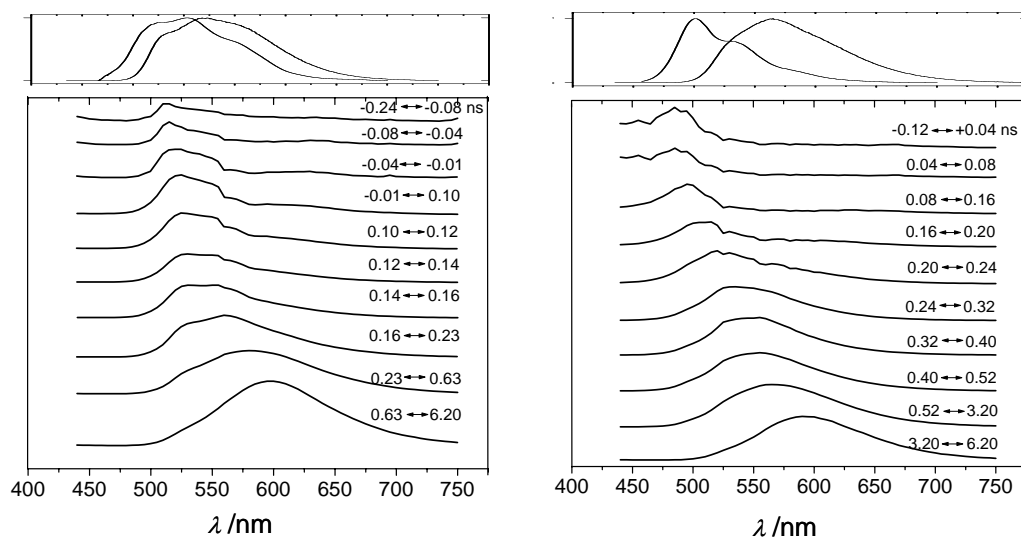


Figure 5.9: Time-resolved emission spectra of films spun from heptane (left) and chloroform (right). Spectra are accumulated in the indicated time windows and smoothed. At the top is shown the steady-state emission spectra of solution and films (red-shifted) for comparison.

5.3.3 Field Effect Transistor

As shown in the previous Sections on the basis of AFM and fluorescence data, the rigid columnar stacks present in heptane solutions of **OPV₄UT**, could be transferred to a FET device by spin coating. The film morphology could be controlled by the applied solvent. To discriminate between the performances of the rod-like (cast from heptane) and the amorphous morphology (cast from chloroform), FET characteristics of both films were compared. Representative output ($I_{SD}-V_D$) and transfer ($I_{SD}-V_G$) curves were measured in the dark and under vacuum (10^{-4} mbar) at 40 °C (Figure 5.10). All devices are FET active and stable and exhibit p-type conduction evident from the negative gate voltages that turn the devices on. Typical on-to-off current ratio (I_{ON}/I_{OFF}) are $\sim 10^3-10^4$. Films spun from heptane show a saturation electron mobility³⁹² of 1×10^{-6} cm²/Vs deduced from the slope of the linear part of an I_D vs V_G plot (left inset Figure 5.10). The threshold voltage (V_T) of -15V lies closely to the onset voltage. The output curves show ohmic contacts and the hysteresis is negligible. The FET performances found for films spun from chloroform show that the I_D saturates at lower V_G , which indicates a lower resistance in these films. The mobility decreased to lower than 10^{-7} cm²/Vs and has an I_{ON}/I_{OFF} ratio of only 10^2 . The poor FET activity is probably due to the disorder in the film morphology. The highest mobility observed for the rod-like film morphology is lower than earlier reported for OPVs⁵⁰ (10^{-4} cm²/Vs), however, these values were measured on vacuum deposited films.

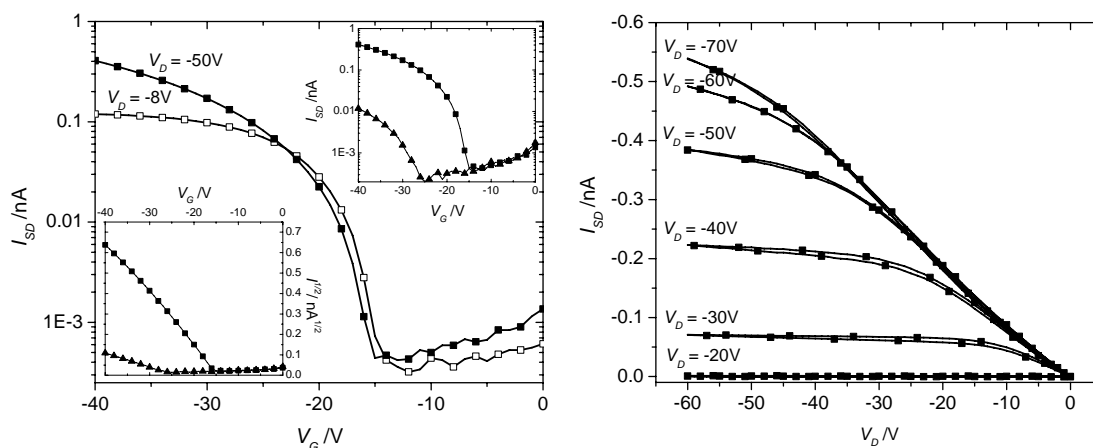


Figure 5.10: Left are the transfer ($I_{SD}-V_G$) curves plotted on semilogarithmic axes for devices spun from heptane (squares) at $V_D = 8V$ and $50V$. Inset (left) shows the $I^{1/2}$ vs V_G curves for $V_D = 50V$ for devices spun from heptane (squares) and chloroform (triangles). Inset (right) shows transfer curves for $V_D = 50V$ for both solvents. Right are the output ($I_{SD}-V_D$) curves (with hysteresis) plotted for various values of V_G for device spun from heptane.

5.3.4 Photovoltaic Cell

The self-assembled OPVs in combination with the C₆₀ derivative, PCBM, (Chart 5.2, next page), have also been applied in photovoltaic cells with controlled film morphology. It is known that OPVs are p-type and PCBM is n-type. Since PCBM is poorly soluble in chloroform and apolar solvents such as dodecane or heptane, toluene was chosen as the solvent. Furthermore, (**OPV₄UT**)₂ was used as donor since it forms a supramolecular polymer in this solvent while **OPV₄UT** is only present as molecularly dissolved species in toluene. First we have spun a film of only (**OPV₄UT**)₂ from toluene. Smooth films were obtained with no pinholes or defects as seen from the TM-AFM images (Figure 5.11a). The supramolecular

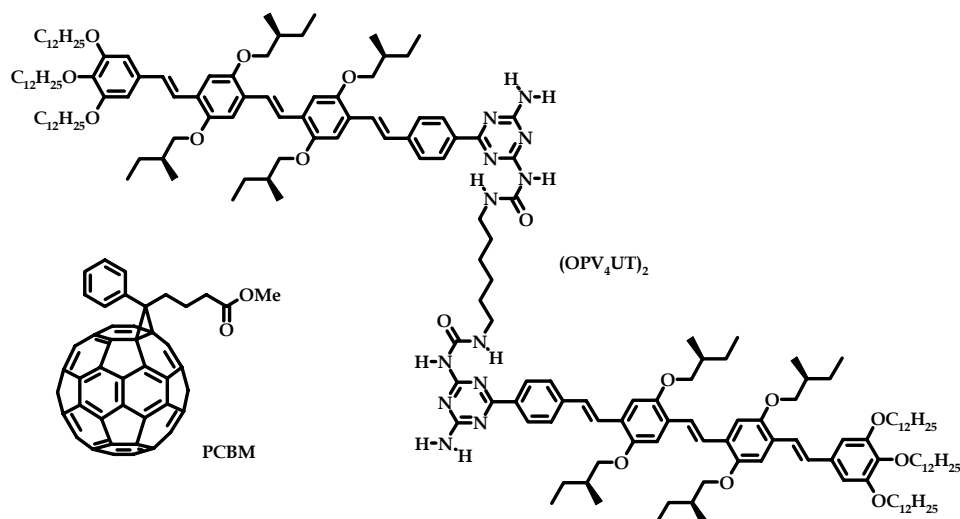


Chart 5.2

polymeric films had a rms-roughness of 1.4 nm and peak-to-peak variations of less than 10 nm. Phase imaging²⁴ (Figure 5.11b) reveals elongated rod-like textures having constant widths of about 4–5 nm as deduced from the line scan. The lengths of the rods are in agreement with the SANS data that was reported in Chapter 4 for dodecane. This behavior shows that in concentrated toluene presumably the same type of rods are formed as in dodecane. The rods form domains of on average 200 nm in size, thereby creating series of domain boundaries similar to those found for **OPV₄UT** spun from heptane indicating that the films consist of well-organized material. The spin cast films are still fluorescent with an emission maximum at about $\lambda_{em,max} = 572$ nm which is red shifted compared to toluene solution.

Surprisingly, the composite films **(OPV₄UT)₂** with PCBM spun from toluene gave a very rough surface with rms-roughness of 24 nm and a peak-to-peak distance of 88 nm (Figure 5.11c).³⁹³ Globular structures ranging from tens to several hundreds of nanometers in diameter are spread over the surface.^{394–396} The phase shift (Figure 5.11e) showed brighter and darker regions which can be attributed to regions with different compositions. The semicontinuous network that is observed, throughout the surface, resembles the elongated textures as seen in Figure 5.11b. However, areas that lead to a phase shift appear less on the globules, whereas a more homogeneous closed network is observed in the areas between the globules. Apparently, the areas between the globules are **(OPV₄UT)₂**-rich, while the globules contain more PCBM. It should be noted, however, that these nanoscale structures, although of the same dimensions in both diameter and length, are qualitatively different from the

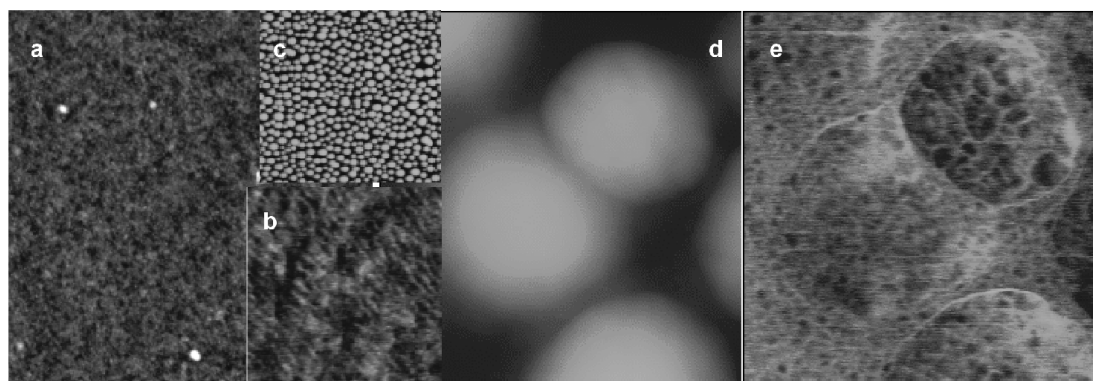


Figure 5.11: Height images (a) $10 \times 10 \mu\text{m}^2$, z-scale 10 nm and (b) zoom, $200 \times 200 \text{ nm}^2$ of spin coated films of **(OPV₄UT)₂** from toluene. Height images (c) $10 \times 10 \mu\text{m}^2$, z-scale 90 nm and (d) zoom $760 \times 760 \text{ nm}^2$ with (e) simultaneously recorded phase image (z-scale 1V) on composite films of **(OPV₄UT)₂/PCBM** from toluene.

structures observed in pure films of $(\text{OPV}_4\text{UT})_2$; they are further apart and less aligned in domains.³⁹⁷ The existence of the supramolecular network on films spun from toluene is supported by OPV fluorescence quenching of the blends despite the very coarse demixing.

Photovoltaic devices were constructed by evaporating aluminum top electrodes on the films and characterized in the dark and under white-light illumination of a halogen lamp (100 mW/cm², 400–800 nm). Figure 5.12a shows the semilogarithmic plot of the J/V curves of a typical device. The curves are completely reversible and stable, and the device shows excellent diode behavior with a rectification ratio between -2 V and 2 V of approximately 10³ revealing little or no shunts. Under white-light illumination, a short circuit current of 0.64 mA/cm and an open circuit voltage 0.79 V was measured. The fill factor is 0.48.^{398a} The incident photon-to-current conversion efficiency (IPCE, Figure 5.12b) reached a maximum of 12% at $\lambda = 430$ nm which is lower when compared to blends (1:4) of poly(p-phenylenevinylene) and PCBM that show 50% at $\lambda = 500$ nm.^{398b} The reduced performance of the $(\text{OPV}_4\text{UT})_2$ based device is a consequence of both the reduced conjugation length and the diluting effect of the aliphatic substituents. The overall power-conversion efficiency (η) is 0.25%. The device characteristics are, however, one of the best reported for oligo(p-phenylenevinylene)s based photovoltaics.

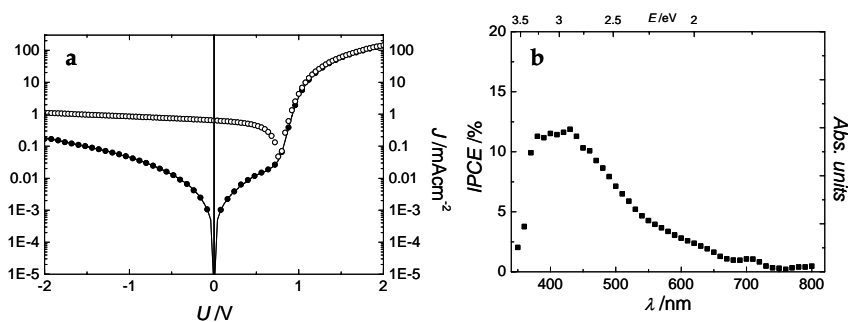


Figure 5.12: Photovoltaic properties of an ITO/PEDOT-PSS/PCBM: $(\text{OPV}_4\text{UT})_2$ /LiF/Al device with an active area of 1 cm² spin coated from toluene (a) Semi-logarithmic plot of current versus voltage in the dark (closed) and under illumination (open) (b) corresponding IPCE curve.

5.4 CONCLUSIONS

The controlled transfer of supramolecular stacks from solution to solid supports appears to be a delicate process. Not only a specific concentration and temperature has to be chosen, but also specific inert substrates need to be selected. Fluorescence microscopy measurements on OPV fibrils on a surface show a polarized optical emission providing evidence that the internal organization of the fibrils is preserved during the deposition process. The control of the internal order of self-assembled fibrils, and the ability to measure it, is a crucial step forward in the construction of uniform organic fibers that can be applied in nanosized electronics. The design of such nanoscopic devices must be such that all components behave as inert surfaces towards self-assembled structures. The fibrils are deposited on nanosized FET electrode patterns, however, no current was measured through the fibrils. This is presumably the result of bad contact between the fibers and the electrodes or a low intrinsic charge carrier mobility.

The film morphology of bulk FET devices has been controlled by the solvent. Thick films of self-assembled fibers that form highly ordered domains were made. Such films from

self-assembled molecules show a better charge carrier mobility in comparison with non-assembled oligomers. The uniform rod-like domains of the OPVs were preserved when blended with a C_{60} derivative producing stable photovoltaic devices despite considerable phase separation.

The concept of controlling the morphology in the solid state by programmed self-assembly in solution, in principle applicable to all kinds of π -conjugated oligomers, is an attractive approach to improve the performance of devices. Successful implementation of self-assembled π -conjugated systems in electronics depends largely on the other layers and electrodes present in the devices. To increase the compatibility and simplify processability, it is a dream to self-assemble all components at once like nature does. A step forward in this direction will be presented in the next Chapter reporting the collective assembly of p- and n-type molecules.

6 HYDROGEN-BONDED SELF-ASSEMBLY OF DONOR AND ACCEPTOR MOLECULES

ABSTRACT

Hydrogen-bonded donor-acceptor chromophoric dyads and triads were obtained using diaminotriazine-oligo(*p*-phenylenevinylene)s as donor and bay-(1,6,7,12)-substituted perylene-imides as acceptor. Temperature dependent optical studies show that in apolar solvents the hydrogen-bonded complexes form well-ordered aggregates. Circular dichroism and atomic force microscopy reveal assembled chiral OPV-*pery*lene superstructures consisting of left-handed helical co-assembled chromophores that further develop into right-handed supercoils. Aggregation of the hydrogen-bonded triads is more enthalpy-driven than in the dyad generating longer aggregates. The aggregates show photo-induced electron transfer on a sub-picosecond timescale, while electron recombination occurs within 1 nanosecond.

The morphology of the active layer on device-relevant substrates could be controlled by programmed self-assembly of the two components in solution resulting in supramolecularly positioned π -conjugated donor and acceptor building blocks. In such a way, ideal pathways for charge transport are created and ambipolar charge transport was demonstrated by the construction of field effect transistors.

CONTENTS	page
6.1 Introduction	88
6.2 Synthesis	88
6.3 Self-Assembly at the Liquid/Solid Interface	89
6.4 Self-Assembly in Solution	90
6.4.1 Optical Properties	90
6.4.2 Structure Properties	94
6.5 Devices constructed from Supramolecular Hydrogen-bonded Architectures	97
6.5.1 Photovoltaic Cells	97
6.5.2 Field Effect Transistors	97
6.6 Conclusions	99

6.1 INTRODUCTION

Recently, ambipolar organic field effect transistors (FETs) have been reported with promising performances based on blends, bilayers and single components. Nevertheless, these devices require processing conditions that are often tedious and not readily optimized.³⁹⁹⁻⁴⁰⁶ Ideally, highly defined nanostructured p-n junctions will realize optimal device performance. Such well-defined junctions could also improve electron-transfer processes and charge transport of both p- (holes) and n-type (electrons) charge carriers, not only in FETs, but also in photovoltaic devices. So far, controlled morphologies of p-n junctions based on π -conjugated molecules have been established by thermotropic and lyotropic liquid crystallinity.⁴⁰⁷ In contrast, the use of hydrogen-bonding may provide another pathway, however, this has been restricted to a large number of studies of photo-induced electron-transfer reactions wherein donor (D) molecules and acceptors (A) are assembled by hydrogen-bonding interactions. Nonetheless, until now, such hydrogen-bonded assemblies have never been brought to the next level of organization by further self-assembly into superstructures required for device fabrication.⁴⁰⁸ This self-assembly principle is not only of great interest in the area of opto-electronic materials research but also important for addressing fundamental questions in biology where hydrogen-bonding plays an important role in electron-transfer processes.

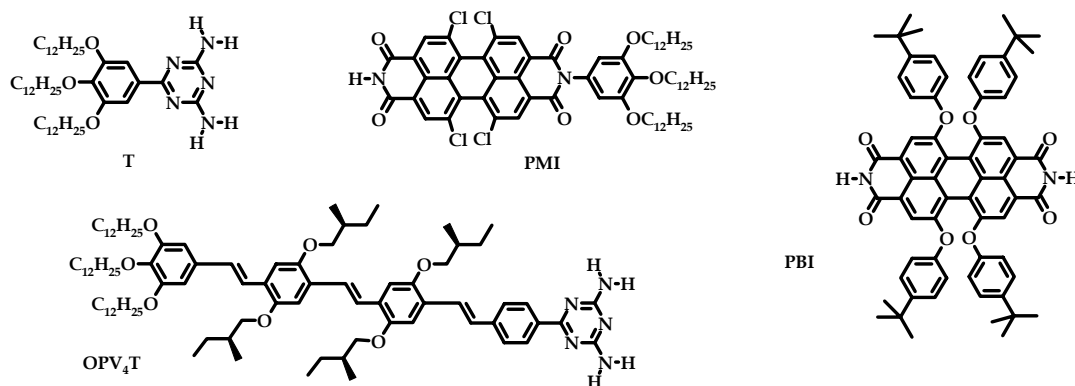
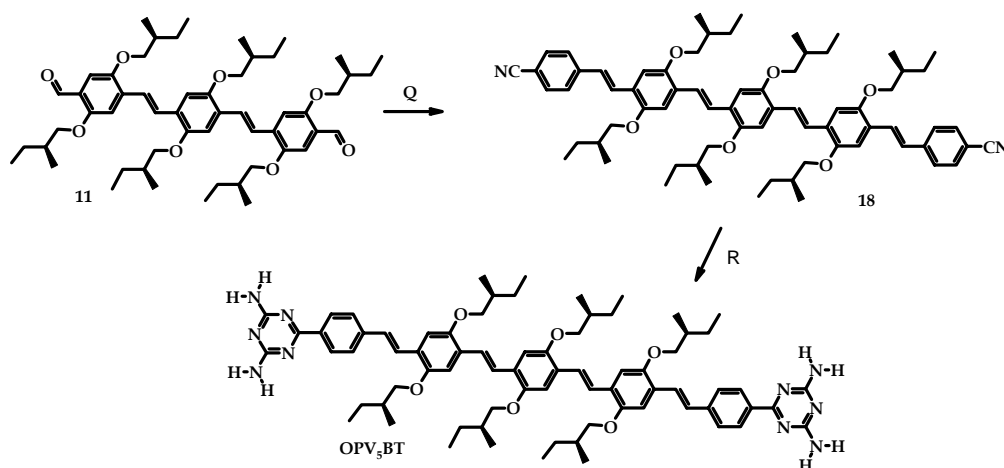


Chart 6.1

This Chapter reports studies of the hydrogen-bonded self-assembly of two different π -conjugated molecules, oligo(p-phenylenevinylene)s (OPVs) (donor) and perylenes (acceptor) (Chart 6.1) in solution. The perylene-imides have either one or two complementary binding sites for the diaminotriazine OPV. Alternatively, an OPV derivative bearing two complementary binding sites for the imide unit of the perylene was synthesized (Scheme 6.1). The programmed self-assembly of the two components led to supramolecular structures in solution which could be transferred to solid supports resulting in highly organized films. Ambipolar charge transport was demonstrated by the construction of field effect transistors.

6.2 SYNTHESIS

The perylene derivatives **PBI** and **PMI** were synthesized in the group of prof.dr. F. Würthner.⁴⁰⁹ Compounds **T** and **OPV₄T** were reported in Chapter 3. **OPV₅BT** was synthesized starting from the bisaldehyde derivative **11** (Scheme 6.1). Converting dialdehyde **11** into



Scheme 6.1: Q) DMF/THF, diethyl(4-cyanobenzyl)phosphonate, $\text{KOC}(\text{CH}_3)_3$, 4h, 84%. R) dicyandiamide, 2-methoxyethanol, KOH, 8h, reflux, 8%.

dicyano OPV derivative **18** proceeded smoothly in good yield (84%). Much to our surprise, the reaction mixture became turbid in the course of the reaction of **18** with dicyandiamide. The polar diaminotriazine groups on **OPV₅BT** hamper the solubility in common organic solvents, making the purification difficult resulting in very low yield (8%). The addition of the perylene derivatives did not improve the solubility.

To investigate the p- and n-type character of the OPV and perylenes, electrochemical measurements were carried out. A cyclic voltammogram in CH_2Cl_2 revealed one oxidation process for **OPV₄T** ($E_{1/2} = 0.3$ V vs Fc/Fc⁺) showing its p-type character while two reduction processes were observed for **PBI** ($E_{1/2} = -1.2$ and -1.4 V) and **PMI** ($E_{1/2} = -0.8$ and -1.2 V) reflecting the difference in the electron donating and accepting character of the substituents on the n-type perylene derivatives.

6.3 SELF-ASSEMBLY AT THE LIQUID/SOLID INTERFACE

The formation of hetero-complexes was first investigated at the liquid/solid interface by STM. The expected trimeric complex between **OPV₄T** and **PBI** and **PMI** was not observed; the physisorption of **OPV₄T** from 1-phenyloctane into rosettes was exclusively observed. In the case of mixing **T** with **PBI**, **T-PBI-T** complexes (solid arrows in Figure 6.1a) were frequently observed. The hetero-complexes are, however, only locally assembled in rows, nicely embedded in a **T** dimer matrix (dashed arrows, compare Figure 6.1b). Figure 6.1b clearly reveals the linear geometry of the components indicating hydrogen-bond interactions between **PBI** and **T**, in line with the prediction. The very high ratio (1:9) of **T**:**PBI** required to induce hetero-complex absorption, and the gradually co-absorbing **PBI** with **T** in time, leads to the conclusion that the formation of a **T** monolayer is at least kinetically favored compared to **PBI** and hetero-complex absorption. This manifests in the initial coverage of the **T** dimers being gradually modified by the formation of **T-PBI-T** structures. Apparently, **PBI** has a lower affinity for graphite than the triazine derivatives, probably due to the absence of extended alkyl chains and the significant twisting of the π -system.⁴¹⁰ If the intermolecular interaction strength of the two building blocks exceeded those for the pure components, it would presumably be possible to observe the hetero-complexes and obtain a more uniform surface coverage.

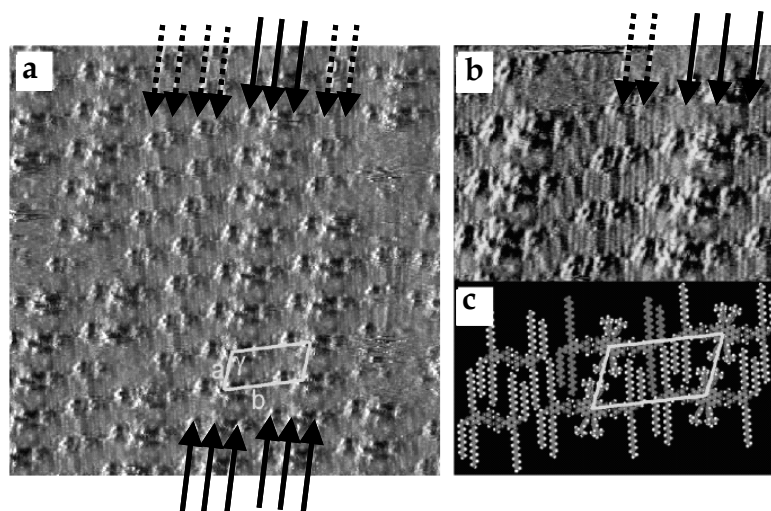


Figure 6.1: STM images of monolayers **T/PBI**. (a) $23.5 \times 23.5 \text{ nm}^2$, unit cell is indicated. (b) $12.3 \times 8.8 \text{ nm}^2$. The hetero-complexes are indicated by filled arrows. Dashed arrows refer to dimers of **T**. (c) Tentative model, unit cell is indicated.

6.4 SELF-ASSEMBLY IN SOLUTION

6.4.1 Optical Properties

Although the binding constant of the hetero-complexes is expected to be rather low in chloroform, a significant increase will be found in more apolar solvents, like methylcyclohexane (MCH).⁴¹¹ Moreover, the binding strength will further increase when additional π - π stacking interactions take place during the process of superstructure formation.⁴¹² At 10^{-7} M in MCH, the UV/vis and emission maxima are located at $\lambda_{\text{abs}} = 426$ and $\lambda_{\text{em}} = 495 \text{ nm}$ for **OPV₄T**, at $\lambda_{\text{abs}} = 512$ and $\lambda_{\text{em}} = 540 \text{ nm}$ for **PMI** and for **PBI** at $\lambda_{\text{abs}} = 563$ and $\lambda_{\text{em}} = 590 \text{ nm}$ (Figure 6.2, only UV/vis spectra are shown). The position and the shape of the spectra are similar to those found in chloroform indicating molecularly dissolved species.

UV/vis, fluorescence and CD titration experiments in MCH were performed to study the interactions of **OPV₄T** with **PMI** and **PBI**. A red shift from $\lambda_{\text{max}} = 560 \text{ nm}$ to $\lambda_{\text{max}} = 610 \text{ nm}$ was observed for the perylene absorption maximum upon adding aliquots of **OPV₄T** to **PBI** (Figure 6.3a). This shift is much larger than for all perylene aggregates studied so far⁴⁰⁹ and it suggests that the perylenes pack tightly in a J-type aggregate. If the concentration of **OPV₄T**

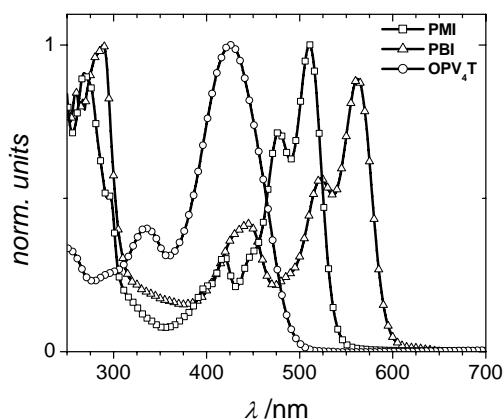


Figure 6.2: Normalized UV/vis spectra of compounds **OPV₄T**, **PMI** and **PBI** in MCH (10^{-7} mol/L).

was taken as constant and **PBI** was added, a red shift was observed for the OPV absorption maximum, from $\lambda_{\max} = 426 \text{ nm}$ to $\lambda_{\max} = 443 \text{ nm}$ (data not shown). Ordinary J-aggregated chromophores show intense fluorescence but here the fluorescence of the perylene was drastically quenched which could be rationalized by an electron-transfer process from the OPV-donor to the perylene-acceptor chromophore. Optimal quenching of fluorescence was obtained when all imide binding sites of **PBI** were hydrogen-bonded to the triazines of **OPV₄T** (Figure 6.3b).

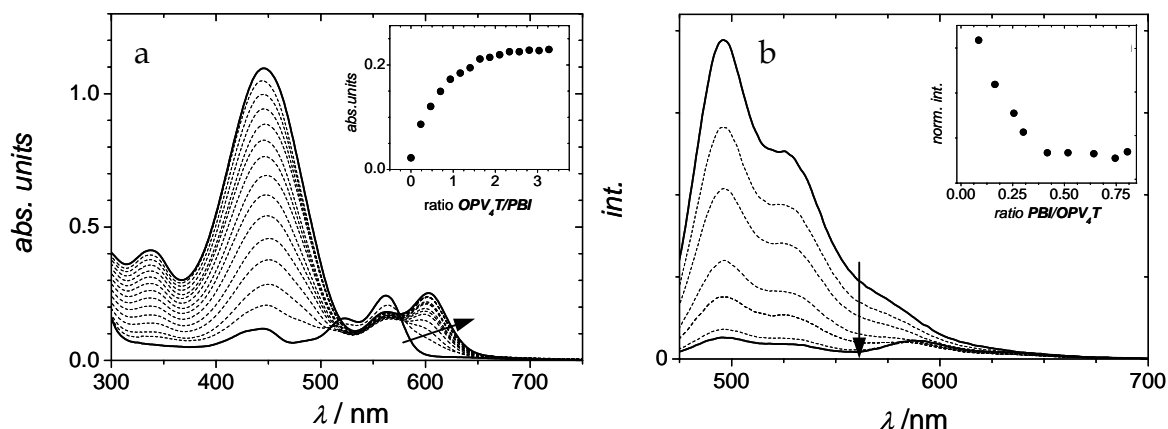


Figure 6.3: Titration experiments for (a) **PBI** ($1.1 \times 10^{-5} \text{ M}$) with **OPV₄T** (0 to $3.6 \times 10^{-5} \text{ M}$) monitoring UV/vis absorption (Inset shows absorbance change at $\lambda = 600 \text{ nm}$ as function of **OPV₄T**/**PBI** ratio) and (b) **OPV₄T** ($3.7 \times 10^{-6} \text{ mol/L}$) with **PBI** (0 to $3 \times 10^{-6} \text{ mol/L}$) monitoring the emission ($\lambda_{\text{exc}} = 450 \text{ nm}$) (Inset shows the changes of the fluorescence intensity at $\lambda = 500 \text{ nm}$ as function of **PBI**/**OPV₄T** ratio).

Similar titration experiments for **OPV₄T**:**PMI** were performed (Figure 6.4). Due to the large overlap of the two chromophores, it is more difficult to follow exclusively the change of the absorption of one of both components upon titration. However, when following the changes in absorption at $\lambda = 525 \text{ nm}$ upon adding **OPV₄T** to **PMI** and at $\lambda = 550 \text{ nm}$ upon adding **PMI** to **OPV₄T**, the formation of a 1:1 complex is apparent. Also it can be seen that the maximum of the **OPV₄T** shifts to the red indicating that a similar type of J-aggregate is formed.

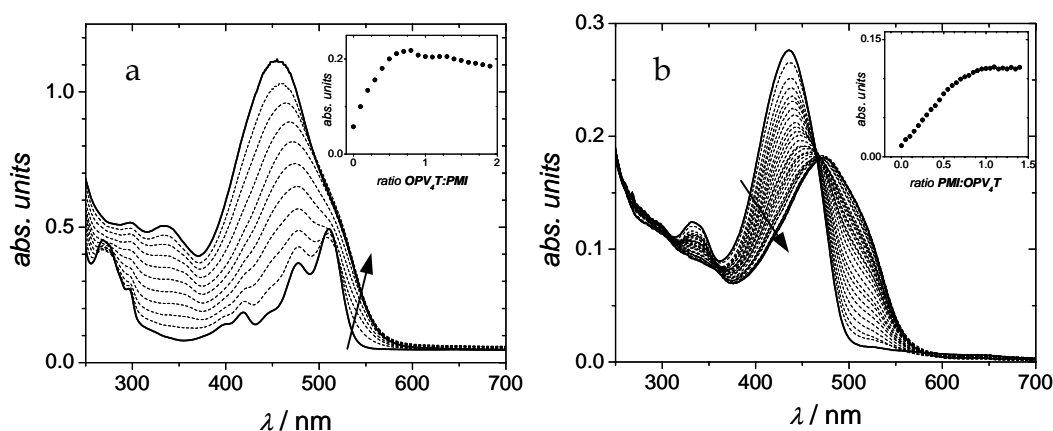


Figure 6.4: Titration experiments for (a) **PMI** ($1.1 \times 10^{-5} \text{ M}$) with **OPV₄T** (0 to $1.8 \times 10^{-5} \text{ M}$) monitoring UV/vis absorption. Inset shows absorbance change at $\lambda = 550 \text{ nm}$ as function of **OPV₄T**/**PMI** (b) **OPV₄T** ($3.6 \times 10^{-6} \text{ mol/L}$) with **PMI** (0 to $4.2 \times 10^{-6} \text{ mol/L}$) monitoring the UV/vis absorption. Inset shows the absorbance change at $\lambda = 525 \text{ nm}$ as function of **PMI**/**OPV₄T**.

The self-assembly process between the different chromophoric building blocks was further investigated by temperature dependent optical spectroscopy. In the case of **OPV₄T-PBI-OPV₄T**, at temperatures higher than 368 K, the absorption spectrum was similar to those of the individual compounds in chloroform at room temperature (Figure 6.5a). In addition to the changes in the absorption and emission spectra, a bisignated Cotton effect at the position of the OPV absorption develops upon cooling the solution. Interestingly, simultaneously a negative Cotton effect at the position of the perylene absorption ($\lambda_{[-]}$ = 610 nm) developed indicating that the chirality of the OPV side chains is expressed in the perylene-core. The optical activity found in all absorptions clearly evidences that the complexes stack into aggregates with a left-handed helical screw sense, similar to other π -conjugated oligomers described in previous Chapters.⁴¹³ The CD intensity of **OPV₄T** and **PBI** was completely lost at 368 K (Figure 6.5b). Upon cooling, the CD spectrum was fully recovered, indicating full reversibility. A sharp increase of the emission of **PBI** at λ = 591 nm (λ_{exc} = 575 nm) at elevated temperature indicates loss of complexation. The three optical techniques prove the existence of two phases for the **OPV₄T-PBI-OPV₄T** complex in solution having a melting temperature of 331 K, *i.e.* aggregates at low temperatures and molecularly dissolved species at high temperatures (Figure 6.6).

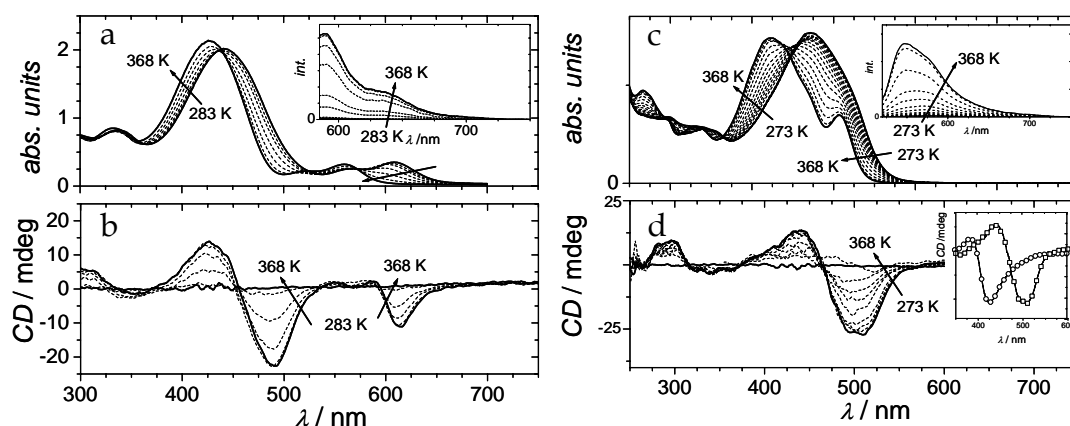


Figure 6.5: Spectra from variable temperature measurements (a) UV/vis (inset show emission) and (b) CD for **OPV₄T-PBI-OPV₄T** (MCH, 3.7×10^{-5} mol/L). Idem for **OPV₄T-PMI** (MCH, 3.1×10^{-5} mol/L) (c) UV/vis (inset shows emission) and (d) CD (inset shows Cotton effect of pure **OPV₄T** (1×10^{-4} M, MCH) and **OPV₄T-PMI** at 298 K).

In the case of **OPV₄T-PMI**, the spectral changes upon cooling are also indicative of the collective assembly of both components into aggregates (Figure 6.5c,d). When comparing the Cotton effects of the complex **OPV₄T:PMI** with pure **OPV₄T** (Chapter 3), the minimum is shifted from $\lambda_{[-]}$ = 427 nm in the case of **OPV₄T** to $\lambda_{[-]}$ = 507 nm in the case of the complex **OPV₄T:PMI**, indicating that both chromophores are co-assembled in one stack with the chirality of the OPV side chains expressed in the perylene-core (inset Figure 6.5d).

Remarkably, the melting temperature for aggregates of **OPV₄T:PMI** is almost the same (at the same concentration of perylene), T_m = 334 K. From the melting curves (Figure 6.6), it is clear that the melting of the dyad is much more gradual compared to the triad. From Section 4.5 it follows that the slope of the melting curve can be related to the enthalpy of bond formation and to the length of the aggregate. A steep melting curve is associated with a larger enthalpy in comparison to less steep melting curves. The former melting behavior will generate considerably longer aggregates.

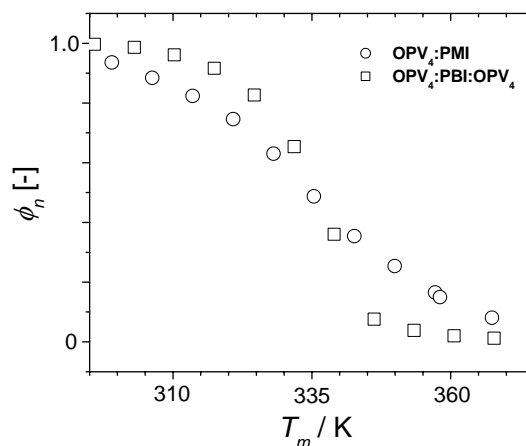


Figure 6.6: Melting curves for assemblies of the diad and triad complexes based on UV/vis data.

Based on the electrochemical studies, it is likely that the fluorescence quenching can be explained by a photo-induced electron-transfer process between the OPV donor and perylene bisimide acceptor. Femtosecond pump-pulse spectroscopic measurements were performed in MCH to determine the rate of charge separation in the aggregates of **OPV₄T-PBI-OPV₄T** and **OPV₄T-PMI**. When excited at $\lambda = 455$ nm, the low-energy absorption of the OPV radical cation at 1450 nm can be detected, indicating photo-induced electron-transfer. The rates of charge separation (k_{CS}) and charge recombination (k_{CR}) were determined by monitoring the temporal evolution of the absorption at $\lambda = 1450$ nm (Figure 6.7). The rise of the signal occurred within 1 ps for both complexes, indicative of a very efficient and fast charge formation ($k_{CS} > 10^{12}$ s⁻¹). Charge recombination was much slower for **OPV₄T-PBI-OPV₄T** ($k_{CR} = 6.3 \times 10^{10}$ s⁻¹ corresponding to a time constant of 16 ps) and for **OPV₄T-PMI** ($k_{CR} = 5.0 \times 10^{11}$ s⁻¹, time constant of 2 ps).

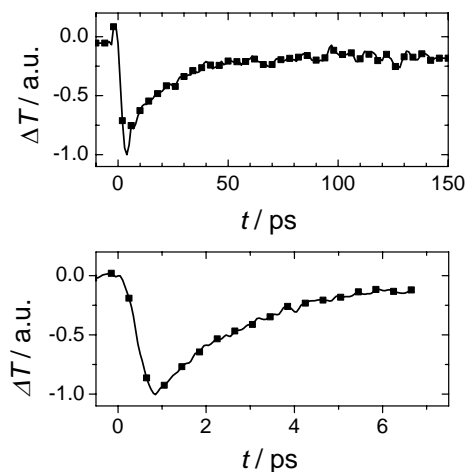


Figure 6.7: Differential transmission dynamics of **OPV₄T-PBI-OPV₄T** (top, 5×10^{-5} mol/L in MCH) and **OPV₄T-PMI** (bottom, 3.1×10^{-5} mol/L in MCH) recorded at $\lambda = 1450$ nm (low-energy absorption of OPV radical cations) after excitation at $\lambda = 455$ nm at 298 K.

6.4.2 Structure Properties

TM-AFM measurements (Figure 6.8) were done to study the shape of the supramolecular aggregates after transferring them from solution to a graphite surface. The images in Figure 6.8b show cylindrical aggregates for **OPV₄T-PBI-OPV₄T**. When a solution of **OPV₄T-PBI-OPV₄T** (3.7×10^{-5} M in MCH) was deposited on graphite, the length of the individual rods varies between 170 and 420 nm (inset Figure 6.8a). Corrected for tip-convolution effects,³⁰⁵ the actual width of the rods is about 10 nm while the height of the rods can be estimated as 4.1 nm. This height is a more accurate measure of the diameter of the rods and is in agreement with the molecular modeling studies that reveal columnar stacks of about 3.5 nm (7.2 nm in length when omitting dodecyloxy chains) consisting of stacked triads assembled in a J-type fashion (Figure 6.10) which requires the aromatic cores to be tilted. An entangled network is formed when more concentrated solutions are used as a result of side-by-side and end-to-end aggregation of the rods.

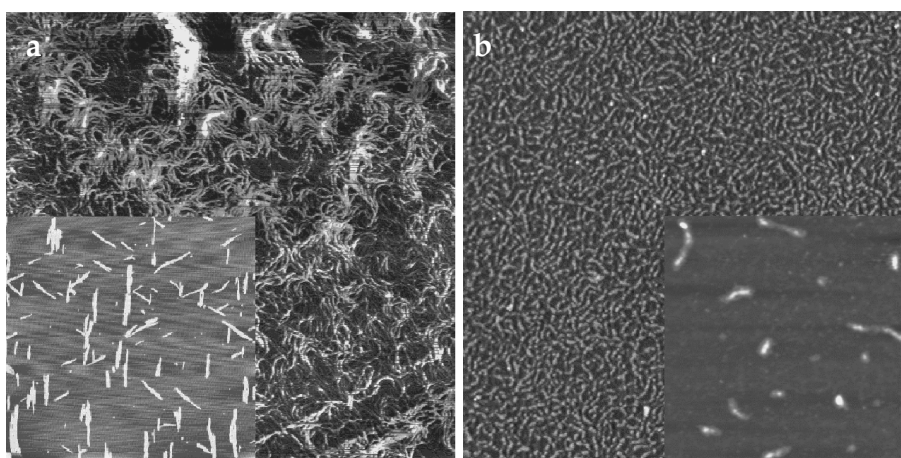


Figure 6.8: TM-AFM images of **OPV₄T-PBI-OPV₄T** for two concentrations (a) 7.4×10^{-5} M, $10 \times 10 \mu\text{m}^2$, z -scale 10 nm, inset: 3.7×10^{-5} M, $3.1 \times 3.1 \mu\text{m}^2$, z -scale 10 nm and of **OPV₄T-PMI** for two concentrations (b) 6.2×10^{-5} M, $5 \times 5 \mu\text{m}^2$, scale 10 nm, inset: 3.1×10^{-5} M, $1.25 \times 1.25 \mu\text{m}^2$, z -scale 10 nm.

In the case of drop casting solutions of **OPV₄T-PMI** onto graphite, much shorter rods are present (inset Figure 6.8b). This observation is in agreement with the characteristics of the melting curves of the aggregates in Figure 6.6. The lengths of the rods vary between 35 and 175 nm while the height is about 3.3 nm. The length of a dyad as revealed by molecular modeling is 4.1 nm (omitting the dodecyloxy chains) indicating that the dyads are aggregated in a J-type fashion, *i.e.* a tilted stack. When a more concentrated solution of **OPV₄T-PMI** was used an interconnected network was formed (Figure 6.8b).

Thick films could be constructed when an even more concentrated solution (7 g/L, MCH) of **OPV₄T-PBI-OPV₄T** and **OPV₄T-PMI** assemblies were spun cast onto a conducting layer of poly(ethylene dioxythiophene) polystyrenesulfonate (PEDOT:PSS), a relevant support for construction of photovoltaic cells, and onto a silicon oxide substrate covered with gold electrodes, a relevant surface for construction of field effect transistors. On both substrates similar morphologies were obtained for the **OPV₄T-PBI-OPV₄T** and **OPV₄T-PMI** systems. The thicknesses of the films range from 75 to 85 nm for both substrates.

TM-AFM revealed helical fibers of **OPV₄T-PBI-OPV₄T** lying on top of the bulk film with PEDOT:PSS as the substrate (Figure 6.9a,b). The width of the smallest fiber is close to 4 nm (upper arrow, Figure 6.9c shows 5 parallel fibers, this region is expanded in Figure 6.9d).

Thicker and right-handed helical rod-like fibers were observed with a length of several micrometers and a width of about 13 nm (bottom arrow, the distance has been corrected for tip dimensions).³⁰⁵ It is assumed that multiple small fibers are coiled around each other to afford those thicker supercoils due to Van der Waals interactions between the smallest fibers. Further self-assembly to double-helical or even larger intertwined assemblies takes place as can be seen in Figure 6.9c (arrow at the center). The composition of the bulk of the film itself remains elusive; however, the higher magnification images of the surface show domains consisting of multiple rods lying side-by-side (Figure 6.9e).

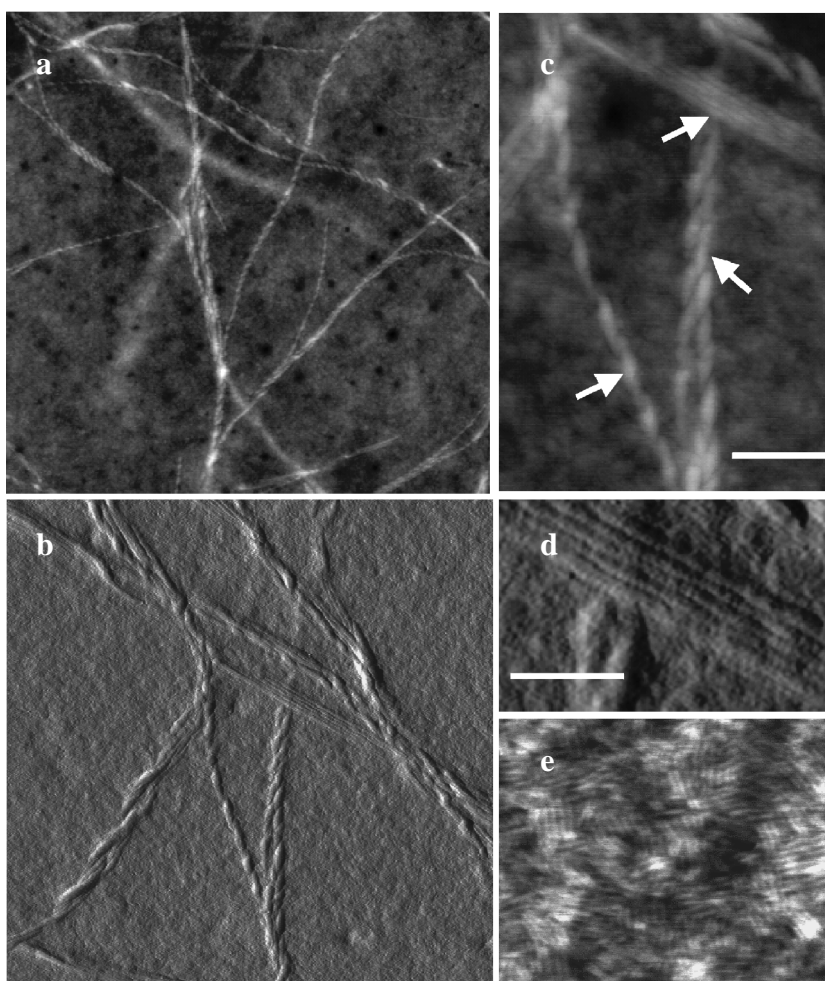


Figure 6.9: TM-AFM images of the **OPV₄T-PBI-OPV₄T** complex after spin coating from MCH (7 g/L) on a glass/ITO/PEDOT:PSS slide; a) height, 3.5 x 3.5 μm^2 , z-scale 20 nm b) phase, 1 x 1 μm^2 , z-scale 45°, c) locally recorded enlarged area of b (height, z-scale 15 nm, bar is 100 nm) d) electronic zoom of the location around the upper arrow (phase, z-scale 35°, bar is 50 nm) e) locally recorded zoom on areas between coiled fibers (phase, 400 x 300 nm, z-scale 55°).

For the **OPV₄T-PBI-OPV₄T** aggregates, the transfer of chiral information is over several hierarchical levels: first the chiral information of the side chain is transferred to the OPV backbone and simultaneously through hydrogen-bonding to the perylene core, leading to left-handed helical stacking of the two dyes, as demonstrated by the CD results (Figure 6.5). To explain the large red shift of the perylene absorption, winding of the complex in a chiral screw sense as shown in Figure 6.10 seems to be a reasonable possibility. For such an assembly each molecule of **PBI** is coordinated by hydrogen-bonding to two molecules of **OPV₄T** and all polar parts (*e.g.* the hydrogen-bonding sites and the π -surfaces) are overlapped in the interior

whilst the alkyl parts are directed into the aliphatic solvent or interpenetrate with neighboring fibers at the surface. Finally, those left-handed fibers intertwine to give right-handed supercoils (Figure 6.9). Such a change of handedness is not surprising and has already been observed for many supramolecular aggregates, and could be rationalized in terms of a screw packing model.⁴¹⁴

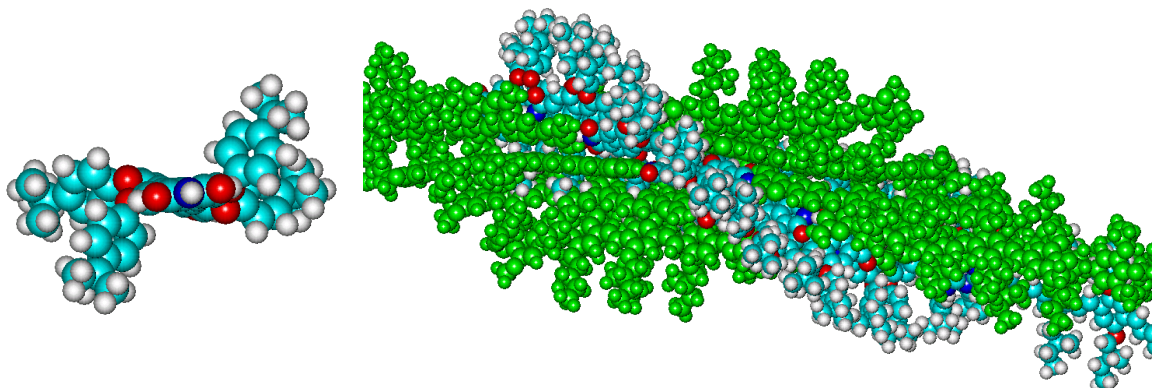


Figure 6.10: **PBI** is shown with a 30° twist of two naphthalene parts (left). Eight head-to-tail stacked perylene bisimides hydrogen-bonded to OPVs (green) are shown (right). The dodecyloxy tails have been replaced by methoxy for clarity. The assembly should have a diameter of only about 3 nm but the hydrophobic C_{12} alkyl part is considered to wrap around the aromatic core which will increase the diameter. There is a shift of ca. half a unit to account for the J-type packing).

Films spun from solutions of **OPV₄T-PMI** showed a fibrillar morphology throughout the surface of the film on the FET substrate, however, no helical structures were observed (Figure 6.11a). It seems that head-to-tail packing of the stacks is limited to a length of about 110 nm whereas side-by-side stacking of rods is dominant, evident from the lamella-width of multiples of about 3.3 nm, being the diameter of a single rod (Figure 6.11b). Both systems were also spun cast from chloroform solutions revealing dotted textures throughout the surface (data not shown). The behavior is similar to that described in the previous Chapter for the **OPV₄UT** system.

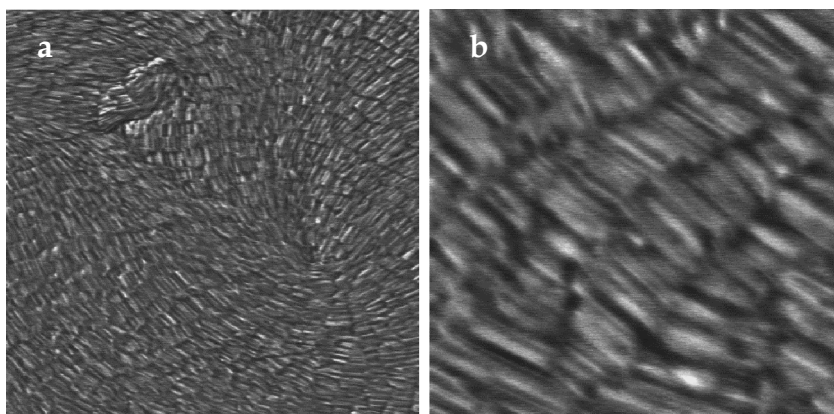


Figure 6.11: TM-AFM images of the **OPV₄T-PMI** complex after spin casting from MCH (10 g/L) on a field effect transistor substrate a) phase, $3.35 \times 3.35 \mu\text{m}^2$, z-scale 25° . b) locally recorded enlarged area of a. (phase, $415 \times 415 \text{ nm}^2$, z-scale 25°).

6.5 DEVICES CONSTRUCTED FROM SUPRAMOLECULAR HYDROGEN-BONDED ARCHITECTURES

The morphology of the active layer on device-relevant substrates is controlled by programmed self-assembly of two different components in solution. The self-assembled structures in MCH contain hydrogen-bonded junctions between π -conjugated donor (**OPV₄T**) and acceptor (**PBI** or **PMI**) components and show photo-induced electron-transfer. These structures could be deposited at device relevant surfaces (see Section 6.4.2). The films reveal rods creating ideal pathways for charge transport of both p- and n-type charge carriers either in a photovoltaic cell or in an ambipolar field effect transistor.

6.5.1 Photovoltaic Cells

Photovoltaic cells were constructed from the **OPV₄T-PBI-OPV₄T** triad using MCH as the solvent. The counter electrode (LiF:Al) was evaporated on top of the glass/ITO/PEDOT:PSS/**OPV₄T-PBI-OPV₄T** layers. The J/V characteristics revealed poor diode behavior with an open circuit voltage of 0.74 V and a low current density (2.6 $\mu\text{A}/\text{cm}$). As shown in our AFM study, the co-aggregated dyes tend to organize themselves laterally on the surface, which is not favorable for the charge transport to the metal electrodes. The lateral organization, however, might be advantageous for use in field effect transistors.

6.5.2 Field Effect Transistors

FET devices were fabricated as reported in Section 5.3.3. Briefly, stacks of **OPV₄T-PBI-OPV₄T** and **OPV₄T-PMI** were spun cast (10 g/L, 50 nm thick) on HDMS-treated Si/SiO₂ substrates having source-drain gold contacts. Measurements were performed in air and vacuum (10^{-4} mbar) and the devices could be cycled more than 20 times in air and light without degradation. The standard saturation FET equation (Section 5.3.3) was employed to calculate the carrier mobility ($W = 2 \mu\text{m}$ and $L = 20 \mu\text{m}$).

Figure 6.12 shows typical electronic performance of FET devices based on **OPV₄T-PMI** films of rod-like morphology, spun from MCH, measured under various conditions. The behavior is characteristic of ambipolar devices. On the one hand, transfer characteristics of the transistor in the p-channel mode (the gate and drain electrodes are biased negatively with respect to the source electrode, Figure 6.12a) show that for high V_G the transistor operates in hole enhancement mode and its performance is similar to a unipolar p-type transistor (Section 5.3.3) with a saturated hole mobility about $2 \times 10^{-7} \text{ cm}^2/\text{Vs}$. This value is lower than measured for pure **OPV₄T** devices (Section 5.3.3), presumably due to the smaller rods. On the other hand, operating the transistors in electron-accumulating mode (Figure 6.12c) reveals an increase in I_D for $V_D < -30\text{V}$ at $V_G = -10\text{V} - -30\text{V}$. This increase in I_D is a result of an electron-accumulation region induced near the drain contact when $V_D \ll V_G + V_{SO}$ where V_{SO} is the switch-on voltage for the p-channel mode of operation.

To investigate this behavior further, we measured the transfer characteristics of a film of **OPV₄T-PMI** in the electron-accumulation mode (Figure 6.12b). For this purpose, the gate and drain electrode are biased positively with respect to the grounded source electrode. The transfer curves exhibit typical n-channel behavior with the creation of an electron enhancement current having an electron mobility of about $1.5 \times 10^{-7} \text{ cm}^2/\text{Vs}$. The electron-drain current increases significantly as the gate electrode is biased even more negatively, and reaches 10 nA for $V_G = 80 \text{ V}$. In all measurements, the drain currents are more

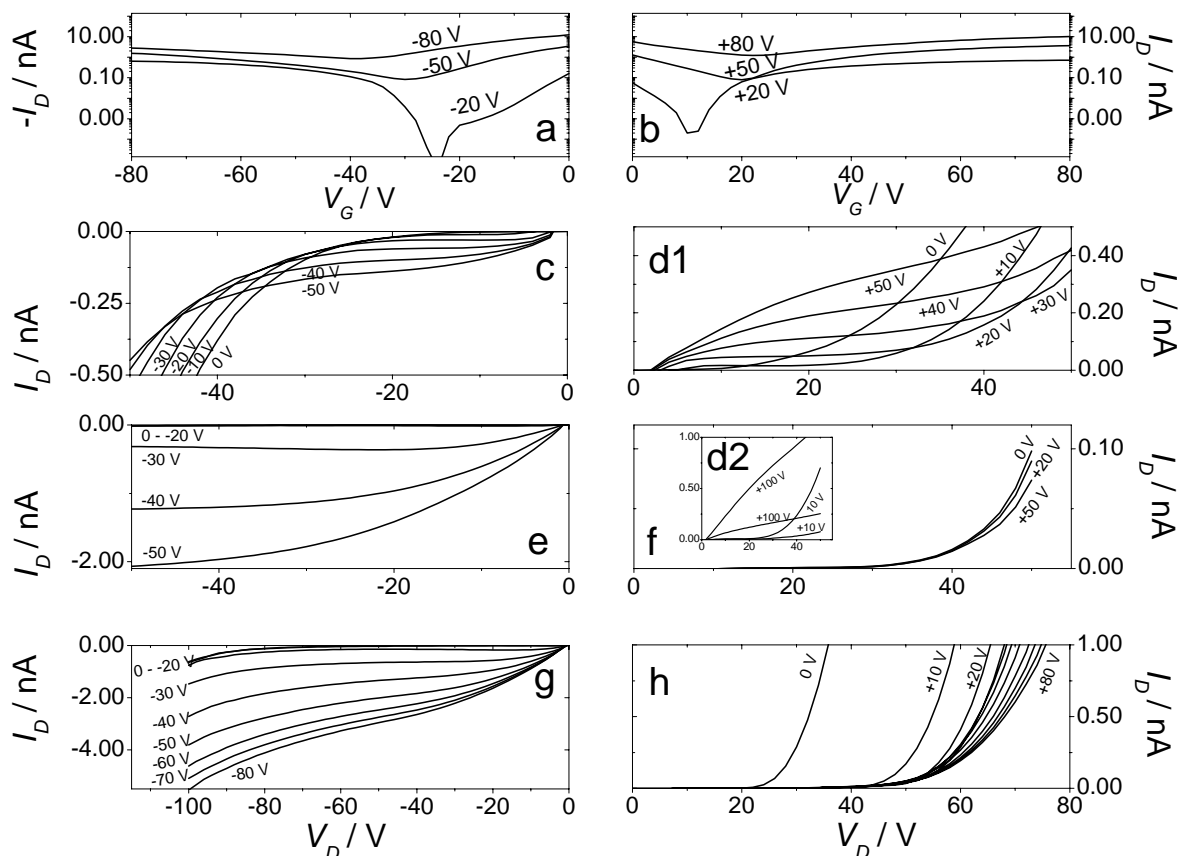


Figure 6.12: Transfer (I_D - V_G) curves at various V_D and output (I_D - V_D) curves at various V_G of FETs of **OPV₄T:PMI** (a, b, c, d1, d2) and **OPV₄T:PBI:OPV₄T** (e, f, g, h). Hole-enhancement mode or p-type is operating in a, c, e and g. Electron-enhancement or n-type is operating in b, d1, d2, f and h.

than a factor of ten higher than the corresponding gate currents, emphasizing the real n-channel operation of the films. (Figure 6.12d1) The output characteristics of the film of **OPV₄T-PMI** show, for $V_G > 40$ V, a characteristic n-channel transistor operation.

Devices based on **OPV₄T-PBI-OPV₄T** also operate well in air, however, the electron enhancement is much less pronounced, probably due to a lower electron affinity of the perylene derivative consistent with the CV measurements discussed earlier (Section 6.2). When sweeping the gate and drain voltage between +50/-50V only the contribution of **OPV₄T** is observed when operating either in hole and electron enhancement mode (Figure 6.12e,f) while a signature of ambipolarity is observed at much higher drain voltages in the hole enhancement mode (Figure 6.12g, h).

The film of **OPV₄T-PMI** clearly shows both n- and p-type behaviors in a FET configuration. Ambipolar transport has been observed previously in blends and bilayers and single component FETs, however, in our case the morphology is controlled by a simple self-assembly step in the solution before spin coating.³⁹⁹⁻⁴⁰⁴ Films spun from chloroform do not show any ambipolar charge transport because they lack a favorable interpenetrating network of electron donors and electron acceptors (Figure 6.12d2).

6.6 CONCLUSIONS

The work discussed in this chapter showed that supramolecular p–n–heterojunctions can be formed by the co–assembly of OPV donor and perylene acceptor chromophores. Supramolecular triads and dyads that are formed via hydrogen–bonding, self–assemble into chiral stacks by π – π interactions. The triads generate longer aggregates than the dyad. Based on cyclic voltammetry and transient absorption spectroscopy, fluorescence quenching of OPV and perylene in the assembly can be related to photo–induced electron–transfer that takes place even in apolar solvents. Such supramolecular assemblies could serve as model systems to link the well established electron–transfer reactions observed in isolated donor–acceptor molecules or their complexes in solutions with those observed in the solid state. We expect that unraveling the effects of electron–transfer dynamics in supramolecular assemblies will aid the future design of multifunctional architectures and nanostructured materials.

The well–defined p–n stacks could be transferred from solution to the solid state and stable ambipolar field effect transistors were constructed. To the best of our knowledge, this is the first example of ambipolar charge transport in a FET based on defined supramolecularly nanostructured p–n junctions.

7 CHIROPTICAL STUDIES AND MANIPULATION OF SELF-ASSEMBLED OLIGOTHIOPHENE CAPSULES

ABSTRACT

This chapter reports the formation of aggregates in alcohols of a series of α - α' penta(ethyleneoxide) functionalized oligothiophenes that vary in the number of thiophene rings, ranging from five to seven, and in the location of a stereocenter in the ethyleneoxide side chain. Atomic force microscopy and optical measurements show that the oligothiophenes form capsules with an H-type packing. The stability of the aggregates increases when the number of thiophene rings increases and when the stereocenter is further away from the thiophene segment. The chiral packing of the oligothiophenes was investigated by circular dichroism. The aggregation of the thiophenes at the molecular level in an H-type helical fashion is presumably present as domains in the capsules at the macroscopic level. The sign of the Cotton effect depends on the absolute configuration of the stereocenter. Furthermore, the sign of the Cotton effect showed an odd-even effect with the distance of the stereocenter from the π -conjugated segment and alternates going from the pentamer to the heptamer having the same side chain. A unique diastereomeric transition is revealed in the case of odd-numbered oligothiophenes. Analysis of this stereomutation shows that the transition is entropically driven. The capsules could be deformed into oblate spheroids by means of a magnetic field that could be trapped in a gel-matrix.

CONTENTS	page
7.1 Introduction	102
7.2 Self-Assembly in Solution	103
7.2.1 Optical Properties	103
7.2.2 Odd-Even Effects in Chiral Packing	104
7.2.3 Stability of the Assemblies	105
7.2.4 Supramolecular Stereomutation	106
7.2.5 The Shape of the Assemblies	109
7.3 Nanomanipulation of Self-Assembled Sexthiophene Capsules	110
7.4 Conclusions	111

7.1 INTRODUCTION

Chiroptical techniques, such as circular dichroism (CD), are commonly used to probe the secondary and tertiary structures in biopolymers and have recently become a highly sensitive tool for investigating the degree of helical order in π -conjugated polymer assemblies.⁴¹⁵ Chiroptical properties of these assemblies are associated with an exciton coupled CD-effect and model compounds have been used to investigate the angle between the π -conjugated segments in the helical aggregates.³⁶⁵ Aggregation induced Cotton effects have been reported for chiral polydiacetylenes,^{416,417} poly(thienylenevinylene)s,⁴¹⁸⁻⁴²⁰ poly(terthiophene)s,⁴²¹ polythiophenes,^{422,423} poly(p-phenyleneethynylene)s,^{424,425} poly(p-phenylenevinylene)s^{426,427} and their related oligomers (Chapter 1). In the case of chirally substituted polythiophenes, the helical packing is dependent not only on the absolute configuration of the stereocenter in the side chain, but also on its distance from the rigid core.⁴²⁸ Furthermore, the optical activity of such polythiophenes could be reversed by adjusting the cooling rate or the solvent conditions.^{422,429-432} Helix inversion has been found for a range of synthetic polymers,⁴³³⁻⁴⁴⁶ natural polymers like DNA⁴⁴⁷ and in nematic phases.⁴³³ Only a few examples exist of supramolecular assemblies of π -conjugated oligomers (Chapter 3) and other organic molecules.⁴⁴⁸⁻⁴⁵⁰

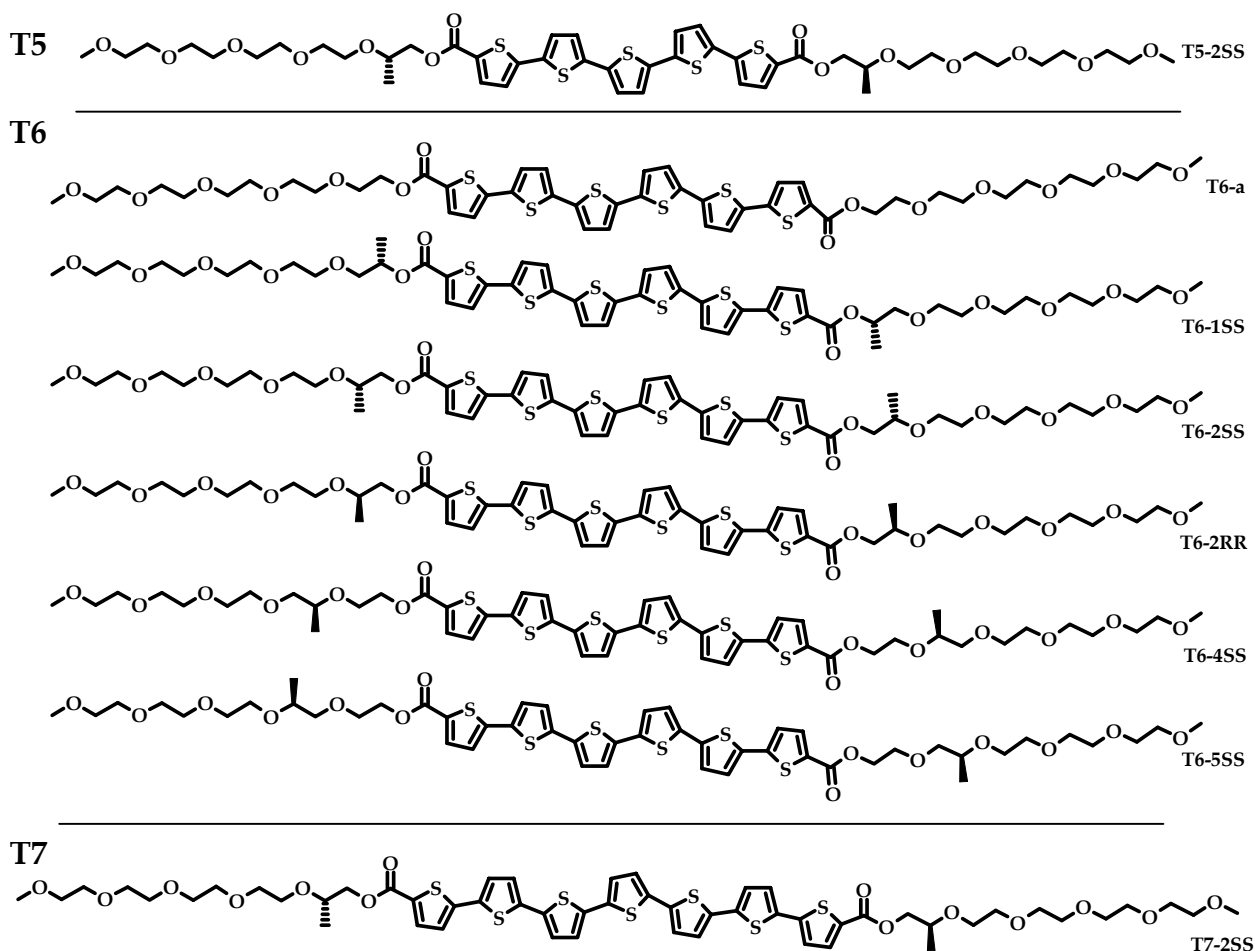


Chart 7.1: Oligothiophene derivatives under study in this Chapter and synthesized at the University of Durham by Dr. O. S. Henze and Dr. A. F. M. Kilbinger.

In Chapter 4, we have analyzed the aggregation of oligo(*p*-phenylenevinylene)s by temperature dependent circular dichroism. To investigate the general applicability of this approach, we report in this Chapter similar studies on chiral aggregates in polar solvents of α - α' linked oligothiophenes with five, six or seven thiophene rings and with penta(ethyleneoxide) substituents at the terminal α -positions with four different locations of the stereocenter (**T5**, **T6** and **T7**, Chart 7.1).^{243,451} These oligothiophenes self-assemble cooperatively in solution into capsules. The self-assembly process shows odd-even effects and a helix inversion. In addition, the aggregates could be deformed in a magnetic field. In earlier studies of these systems rod-like helical assemblies, reminiscent of the OPV aggregates discussed in Chapter 2, have been generated by slow evaporation of THF solutions, a good solvent for the oligothiophenes.²⁴³ This work will not be discussed further here.

7.2 SELF-ASSEMBLY IN SOLUTION

7.2.1 Optical Properties

The UV/vis absorption spectrum of **T5-2SS** in tetrahydrofuran (THF) shows a maximum at $\lambda = 433$ nm, for all **T6** derivatives, this maximum is located at $\lambda = 448$ nm while for **T7-2SS** it occurs at $\lambda = 447$ nm. In the fluorescence spectra, maxima are found at $\lambda = 511$, 530 and 548 nm for **T5-2SS**, **T6** and **T7-2SS**, respectively. The position of the maximum depends on the conjugation length and the shape of the spectra are similar to those reported earlier for molecularly dissolved α - α' terminally disubstituted oligothiophenes.⁴⁵² The self-assembly of the oligothiophenes was studied in *n*-butanol. A solution of **T5-2SS** in

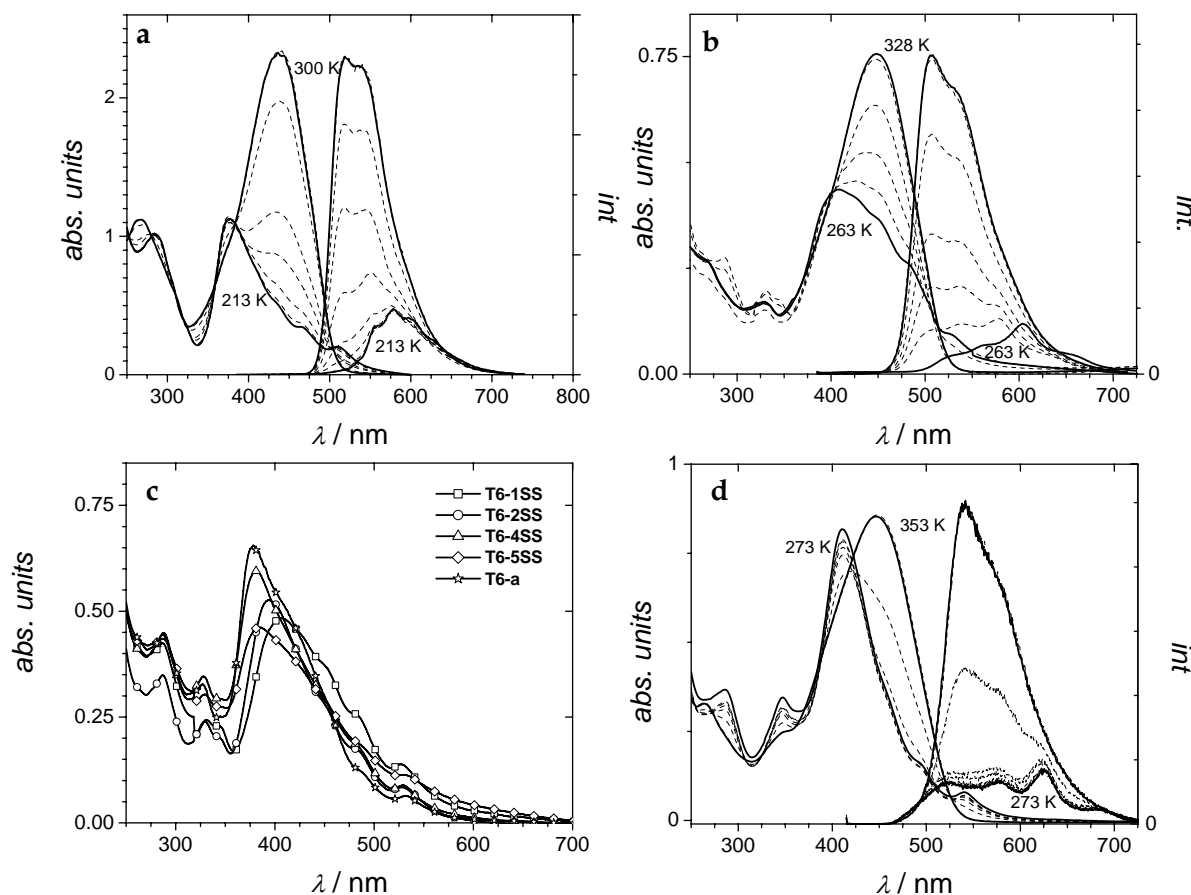


Figure 7.1: Temperature dependent UV/vis and emission spectra in *n*-butanol (2.6×10^{-5} M) for (a) **T5-2SS**, (b) **T6-1SS** and (d) **T7-2SS**. (c) UV/vis spectra at 283 K are plotted for all **T6** derivatives in *n*-butanol (2.6×10^{-5} M).

n-butanol at 300 K shows a UV/vis spectrum similar to that recorded in THF and the absorption maximum is located at $\lambda = 438$ nm (Figure 7.1a). Upon cooling to 213 K this band shifts to the blue by 63 nm to $\lambda = 375$ nm indicating H-type aggregation.^{243,452} For the **T6** derivatives, the shift upon cooling depends on the position of the stereocenter. The smallest blue shift is observed for **T6-1SS** (37 nm) while **T6-2SS** shifts 52 nm, **T6-4SS** 62 nm and **T6-5SS** 65 nm (Figure 7.1c). The largest shift (69 nm) was observed for **T6-a** indicating that the sexithiophenes, lacking the methyl group of the stereocenter, show a stronger exciton coupling probably as a result of a better packing.⁴⁵³ For **T7-2SS** in *n*-butanol, a similar blue shift from $\lambda = 450$ nm at 343 K to $\lambda = 410$ nm at 273 K is found (Figure 7.1d).

The fluorescence intensity of solutions of **T5-2SS** in *n*-butanol at 213 K was reduced when compared that found at 300 K and the maximum was red shifted to $\lambda = 579$ nm, typical for H-aggregates (Figure 7.1a). All **T6** derivatives show an emission maximum at $\lambda = 610$ nm below 300 K, while above 370 K, a much more intense emission is found having a maximum at $\lambda = 508$ nm (Figure 7.1b). In the case of **T7-2SS**, a similar red shift and quenching of the emission is observed going from $\lambda = 540$ nm at 343 K to $\lambda = 625$ nm at 273 K (Figure 7.1d).

7.2.2 Odd-Even Effects in Chiral Packing

For **T5-2SS**, a bisignated Cotton effect is found at 213 K, while at 300 K no Cotton effect exists. The Cotton effect showed a positive sign at lower energy ($\lambda_{[+]} = 410$ nm) and a negative Cotton effect at higher energy ($\lambda_{[-]} = 350$ nm) revealing a right-handed helical packing (Figure 7.2a). The zero-crossing at the absorption maximum of the chromophore indicates exciton coupling as a result of chiral aggregation. The sign of the Cotton effect of **T5-2SS** is opposite to that observed for the corresponding **T6-2SS** aggregates ($\lambda_{[-]} = 412$ nm and $\lambda_{[+]} = 380$ nm, left-handed helicity) but similar to that found for the aggregates of **T7-2SS** ($\lambda_{[+]} = 425$ nm and $\lambda_{[-]} = 394$ nm, right-handed helicity) (Figure 7.2a). As expected, the sign of the Cotton effect is reversed for aggregates of **T6-2RR** compared to **T6-2SS** having a stereocenter with the opposite configuration (Figure 7.2b). The sign of the Cotton effect also depends on the position of the stereocenter in the side chain (Figure 7.2b). For odd-numbered positions, *i.e.* **T6-1SS** and **T6-5SS**, the low energy side has a positive sign while the even numbered, *i.e.* **T6-2SS** and **T6-4SS**, have a negative sign. Interestingly, the intensity of the Cotton effect decreases upon moving the stereocenter away from the chromophore, compare **T6-5SS** with **T6-1SS** and **T6-4SS** with **T6-2SS**. The observed odd-even effects in the optical

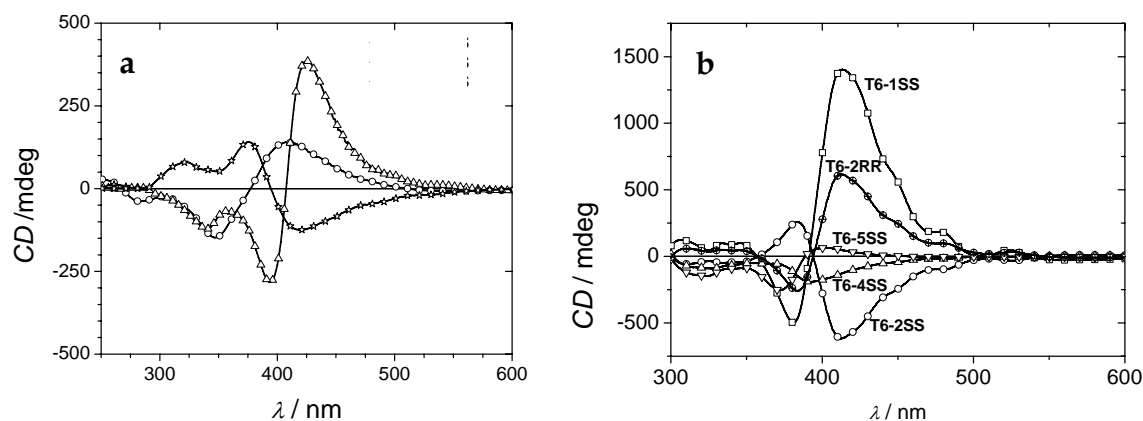


Figure 7.2: (a) CD spectra of **T5-2SS** (circles) **T6-2SS** (stars) and **T7-2SS** (triangles) in *n*-butanol (2.6×10^{-5} M). (b) CD spectra for all **T6** derivatives in *n*-butanol (8×10^{-5} M).

activity of the **T6** assemblies is similar to earlier reported odd–even effects found for β -substituted polythiophenes⁴²⁹ and in agreement with the established ROD–REL rules for cholesteric liquid crystals.⁴⁵⁴ In addition, the intensity of the Cotton effect increases upon extending the conjugation length and remarkably, the sign depends also on the number of thiophene rings, compare **T5–2SS**, **T6–2SS** and **T7–2SS** (Figure 7.2a).

7.2.3 Stability of the Assemblies

For all **T6** derivatives, measured for the same concentrations, is plotted in Figure 7.3a the shift of the absorption at $\lambda = 438$ nm upon heating with temperature intervals of 5 or 10 K. It should be noted that using such temperature intervals it is not possible to discriminate between an isodesmic and a non–isodesmic self–assembly process (Section 4.5). However, to compare the stability of the different assemblies of the sexithiophenes this discrimination is not necessary and, therefore the melting temperatures (T_m) have been calculated. The phase transition curves shift to higher temperatures as the stereocenter is moved further away from the thiophene segment. The T_m of the thiophene stacks is located at 288 K (**T6–1SS**), 316 K (**T6–2SS**), 323 K (**T6–4SS**), 328 K (**T6–5SS**) and 330 K (**T6–a**) showing that the achiral **T6** stacks are the most stable ones. The enthalpy gain computed from the slope of the curves (Figure 7.3a) is lowest for **T6–1SS** (–11 kJ/mol) and highest for **T6–a** (–28 kJ/mol). The differences in the transition curves reflect a better packing of the **T6** segments when the steric hindrance of the stereocenter in the side chains is absent. Not only the place of the stereocenter on the side chain, but also the conjugation length of oligothiophenes determines the stability of the stacks (Figure 7.3b); the T_m increases from 285 K for **T5–2SS** to $T_m = 336$ K for **T7–2SS**. The observation that more π – π interactions enhance the stability of the stacks, is similar to the earlier conclusion from the study of stacks of oligo(p–phenylenevinylene)s (OPVs, Chapter 4).

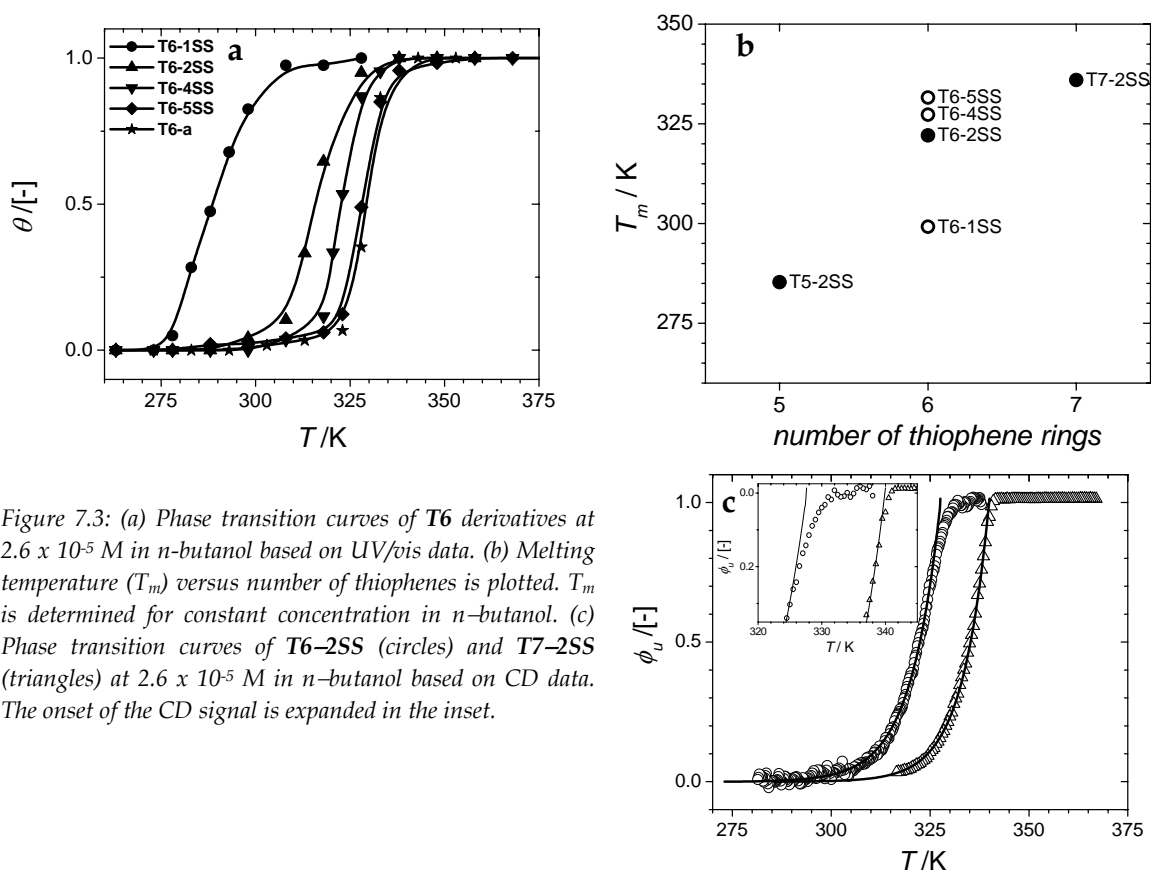


Figure 7.3: (a) Phase transition curves of **T6** derivatives at 2.6×10^{-5} M in *n*-butanol based on UV/vis data. (b) Melting temperature (T_m) versus number of thiophenes is plotted. T_m is determined for constant concentration in *n*-butanol. (c) Phase transition curves of **T6–2SS** (circles) and **T7–2SS** (triangles) at 2.6×10^{-5} M in *n*-butanol based on CD data. The onset of the CD signal is expanded in the inset.

When using similar conditions to measure the process of self-assembly in detail as described in Section 4.5, the aggregation curves (Figure 7.3c) reveal clearly a shape typical for a cooperative (non-isodesmic) self-assembly process. The curves are constructed from the normalized change of the Cotton effect intensity upon cooling solutions of **T6-2SS** and **T7-2SS**. The sharp transition observed at $T_e = 322$ K for **T6-2SS** is lower than that found for the **T7-2SS** assemblies ($T_e = 340$ K). The enthalpy of non-covalent bond formation during the self-assembly is highest for the **T7-2SS** (about -40 kJ/mol), which is smaller than that found for the OPVs described in Chapter 4. Interestingly, the data (inset, Figure 7.3c) gives an association constant, K_a , of 2×10^{-4} for **T7-2SS** and an average number aggregated monomers of about 300 to 350 at 300 K. These values are both in the same range as reported for the **OPV₄UT** 410 - 470 at 1.1×10^{-5} M (Section 4.5). In contrast, K_a for **T6-2SS** is much lower at 1×10^{-2} , *i.e.* less cooperative resulting in less assembled molecules. The results indicate that the self-assembly of the oligothiophenes follows a cooperative path involving the formation of pre-aggregates similar to that of the self-assembly process of **OPV₄UT**.

7.2.4 Supramolecular Stereomutation

The melting curves are fully reversible, however, much to our surprise we found that the sign of the Cotton effect of the aggregates of **T5-2SS** depends on the cooling rate. When a solution of **T5-2SS** was cooled from 300 K at 22.6 K/min a Cotton effect was found with a negative sign at $\lambda_{[-]} = 410$ nm (left-handed arrangement) while when the same solution was cooled at a rate of 10 K/hr the exactly opposite sign (right-handed arrangement) was observed having the same shape and with the zero-crossing at a similar position (Figure 7.4a). The helix that is formed upon fast cooling is presumably the kinetically controlled aggregate while the helix that is formed upon slow cooling is the thermodynamically stable aggregate. A similar stereomutational observation was obtained for **T7-2SS** (Figure 7.4b). Starting from 370 K, fast cooling gave $\lambda_{[-]} = 425$ nm, whereas slow cooling gave $\lambda_{[+]} = 425$ nm. For the **T6-2SS**, however, such a dependence is not observed.

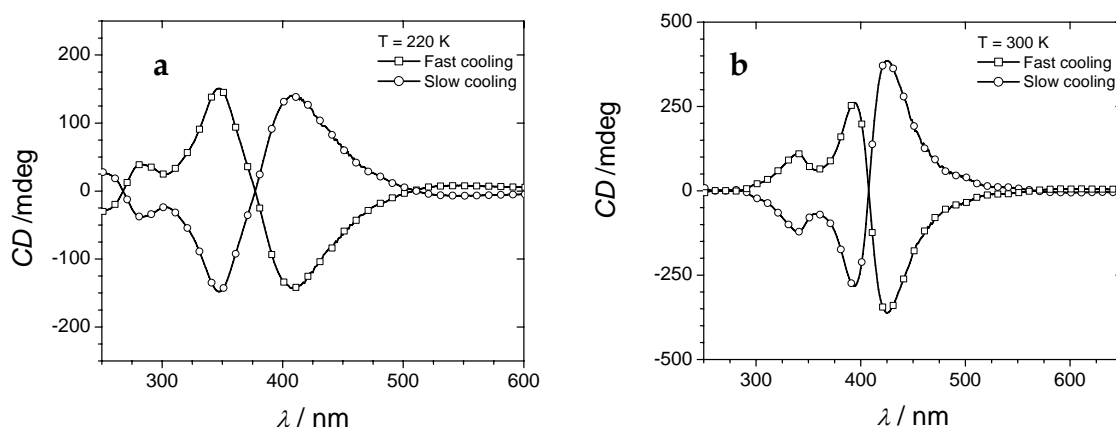


Figure 7.4: CD spectra for (a) **T5-2SS** and (b) **T7-2SS** in *n*-butanol (2.6×10^{-5} M) upon fast cooling (22.6 K/min) and slow cooling (10 K/hr) to 283 K.

The stereomutation can be followed by recording CD spectra as function of time for a **T7-2SS** solution cooled from 370 K to 300 K at a cooling rate of 22.6 K/min and subsequently heating to a temperature in the phase transition regime (Figure 7.5). The settings (scan-rate 200 nm/min, scan-range 600 - 300 nm, sensitivity 500 mdeg) allowed successive CD spectra to be recorded at 5 min. intervals. The appearance of isodichroic point at 0 mdeg suggest a transition between two types of aggregates that only differ in handedness in contrast to the

stereomutation reported for cartenoid assemblies where the non-zero crossing point implies a more radical restructuring.⁴⁵⁰ Moreover, the TM-AFM images of deposits of kinetic and thermodynamic aggregates of T7-2SS look identical.

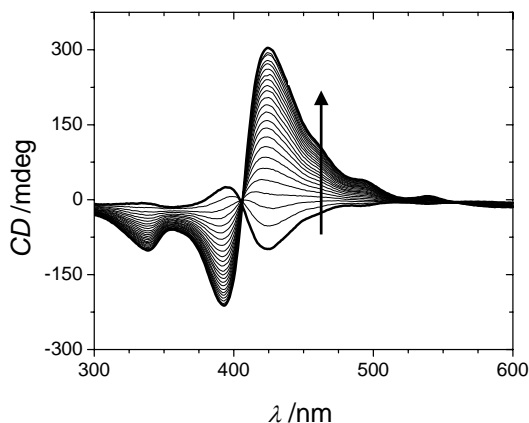


Figure 7.5: CD spectra of T7-2SS in *n*-butanol (2.6×10^{-5} M) at 320 K recorded at 5 min. interval (arrow indicates increase in time).

To study this remarkable stereomutation in more detail and in order to determine the process rate constant more precisely, the stereomutation at $\lambda = 425$ nm at different temperatures is followed in time (Figure 7.6). Below 321 K, the CD intensity after stereomutation is 340 mdeg (2.6×10^{-5} M) in all cases. At higher temperatures this value is lower, probably caused by partial melting of the aggregates (Figure 7.7) resulting in some molecularly dissolved heptathiophenes that do not contribute to the CD signal. Up to 320 K, the transition followed first order kinetics and went faster upon increasing the temperature. The sign reversal of the CD signal for T7-2SS, at 320 K, occurred with a rate constant of $k = 2.0 \times 10^{-4} \text{ s}^{-1}$ and was complete within 60 min (Figure 7.7). From the Eyring plot⁴⁵⁶ of the data up to 320 K (inset, Figure 7.7), was calculated the activation energy of this process of E_{act} (298 K) = 388 kJ/mol. The other kinetic parameters are ΔG^\ddagger (298 K) = 652 kJ/mol, $\Delta H^\ddagger = 390$ kJ/mol and $\Delta S^\ddagger = -880$ J/molK.

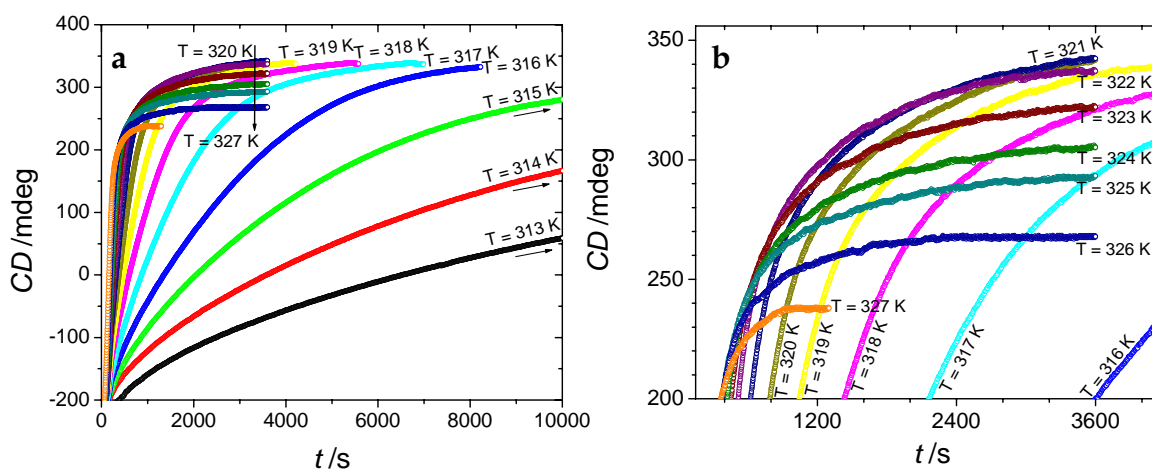


Figure 7.6: (a) Change in the intensity of the Cotton effect for T7-2SS (2.6×10^{-5} M, *n*-butanol) at $\lambda = 425$ nm as function of time; at varying temperatures (313 – 327 K, in steps of 1 K) in (b) an expanded plot showing the decrease in intensity of the Cotton effect at higher temperatures.

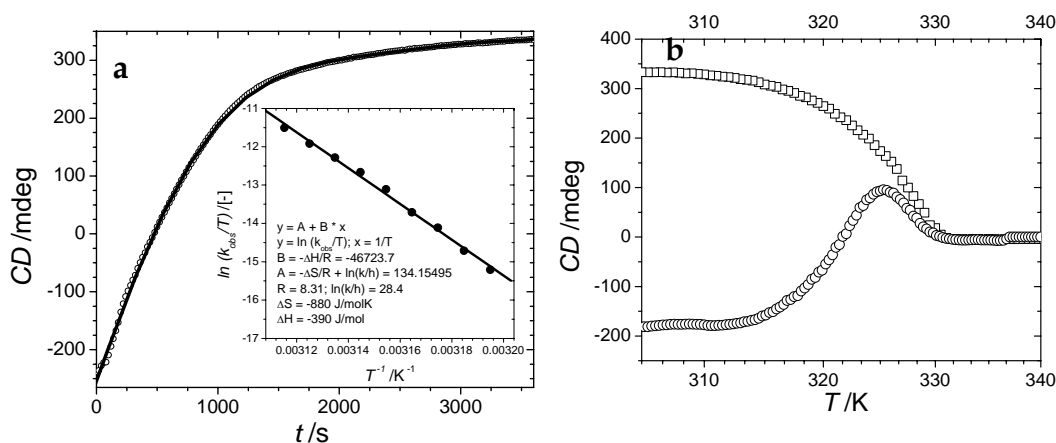


Figure 7.7: (a) The change of the Cotton effect of **T7-2SS** in *n*-butanol (followed at $\lambda = 425$ nm) at 320 K (open circles) and fitted to the first order kinetic model (solid line), inset shows Eyring plot for helix inversions up to 320 K. (b) Melting curves of **T7-2SS** by monitoring the Cotton effect at $\lambda = 425$ nm going from low to high temperatures starting from thermodynamically (open squares) and kinetically (open circles) controlled aggregates.

There are different explanations that may account for the observed entropy loss. One is that ΔS^\ddagger originates from a transition between two diastereomeric states that proceeds through a more molecularly ordered state; this seems unlikely and ignores the solvent entropy effects. Alternatively, a recent report provided a theoretical explanation for entropically driven helix formation on the basis of excluded volume interactions.⁴⁵⁷ When a polymer was modeled as a solid tube immersed in a solution of hard spheres, the tube rendered a region of space inaccessible to the spheres. The spheres' entropy increased as this excluded volume decreased by the overlap volume change during helix formation. The authors stated that maximizing the entropy can lead to one preferred geometry for the supramolecular aggregate. In our case, that would mean that during the process of stereomutation, the excluded volume increases as the overlap volume decreases, leading to a loss of entropy. Very recently, such contributions to the entropy change have been found to be a stronger driving force for protein assembly than the enthalpy change.⁴⁵⁸

The appearance of stereomutation only in the case of odd-numbered thiophenes **T5** and **T7** may be rationalized in terms of symmetry. Assuming a transoid arrangement of the thiophene rings, **T5** and **T7** have a C_2 -symmetry axis in the plane of the oligothiophene segment (left top Figure 7.8), whereas **T6** has a C_2 -symmetry axis in the oligothiophene stack direction (left bottom Figure 7.8). This difference in the position of the C_2 -symmetry axis could lead to a larger difference in energy barrier between the two diastereomeric stacks in the case of **T6**.

Preliminary molecular dynamics simulations for assemblies of **T7-2SS** molecules resulted in two stable helical structures with opposite handedness.^{459a} In both cases, the adjacent π -systems are separated by 0.37 nm, typical for π -stacking of oligothiophenes,^{459b} and with an angle of 6 to 8°. The potential energy calculated for the two structures favor the formation of the right-handed helical assembly. This is in line with the CD experiment showing the right-handed helix as the thermodynamically more favored assembly (right Figure 7.8).

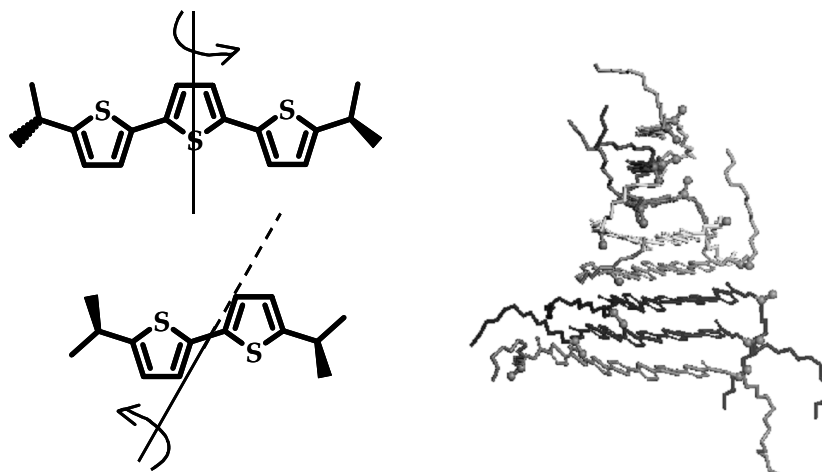


Figure 7.8: At the left are drawn the C_2 rotation axis in odd (top shows terthiophene derivative) and even (bottom shows a bithiophene derivative) numbered thiophenes carrying chiral side chains. At the right is given a side view of right-handed helical assembly of T7-2SS after molecular dynamics simulation. The upper molecule in the assembly is oriented perpendicularly to the paper. The lower molecule is oriented parallelly to the paper. Hydrogen atoms are omitted. Stereocenter and the methyl group attached to it, are represented as balls.

7.2.5 The Shape of the Assemblies

The shape of the assemblies of the oligothiophenes in butanol solutions were studied with dynamic light scattering (DLS). For T6-2SS spherical objects were revealed having an average radius of 55 nm at 293 K, which could be visualized by scanning electron microscopy (SEM, Figure 7.9a) and TM-AFM (Figure 7.9b,c). Clusters of the capsules were observed when a concentrated solution was applied to a mica surface (2×10^{-3} M, Figure 7.9b). The AFM images showed spherical objects of 100 nm diameter, based on the height using low forces at the tip. Isolated and much smaller spheres of 20 nm diameter were observed after depositing a 2×10^{-5} M solution (Figure 7.9c). AFM images on the other oligothiophene derivatives revealed similar objects (data not shown). The assemblies are supposed to be constructed from a layer of oligothiophene molecules forming capsules, *i.e.* hollow spheres, similar to those found for oligo(*p*-phenylenevinylene)s (Chapter 2) and oligothiophene based surfactants,^{246,460} which form vesicles in water. The aggregation of the thiophenes at the molecular level in an H-type helical fashion is presumably present as domains in the capsules at the macroscopic level.

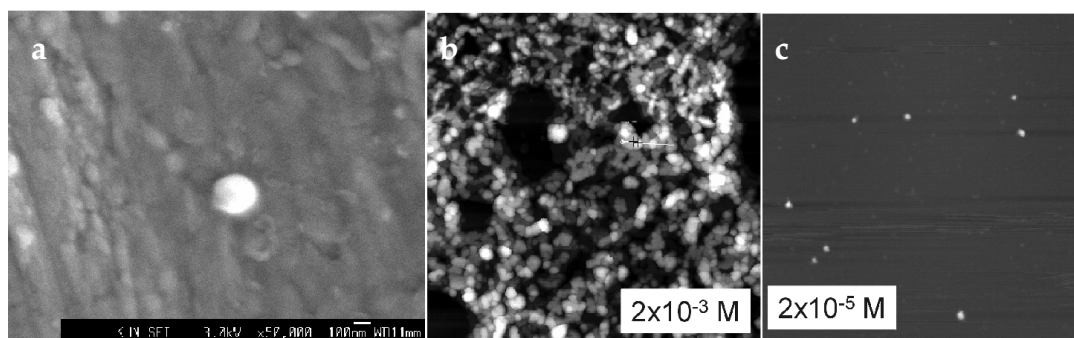


Figure 7.9: Images of drop cast solution of T6-2SS (*n*-butanol) (a) SEM image on an Al surface. TM-AFM images on glass, (b) height, $5 \times 5 \mu\text{m}^2$ z-scale 25 nm, (c) $1.8 \times 1.8 \mu\text{m}^2$ z-scale 15 nm.

7.3 NANOMANIPULATION OF SELF-ASSEMBLED SEXITHIOPHENE CAPSULES

The use of magnetic forces was investigated as a method of deforming simultaneously a collection of self-assembled **T6-2SS** capsules in a contact-free and non-invasive manner. Sexithiophenes have a large anisotropy in the diamagnetic susceptibility ($\Delta\chi \sim -4 \times 10^{-9} \text{ m}^3/\text{mol}$).⁴⁶¹ An external magnetic field (B) tends to orient such anisotropic molecules with their axis of lowest susceptibility (here the long axis of **T6-2SS**) along the field in order to minimize their magnetic energy $U_m = -\chi B^2$. However, the spherical aggregates of **T6-2SS** are composed of molecules that point in all directions, and therefore the overall magnetic susceptibility is isotropic, and no magnetic alignment of the capsules as a whole will occur. Instead, a magnetic field exerts a different torque on molecules that are parallel to the field (top and bottom of the sphere), compared to those perpendicular to the field (around the equator of the sphere). The sum of all these torques will deform the sphere into an oblate spheroid. The deformation leads to a decrease of the magnetic energy at the expense of an increased elastic energy. At equilibrium, the sum of the magnetic and the elastic energy is minimized, which occurs when the elastic deformation force is balanced by the magnetic force. The magnetic field induced deformation can be detected optically as a field-induced birefringence Δn . At fixed temperatures the absolute value of Δn increases with field, which directly proves that magnetic deformation of the **T6-2SS** capsules occurs (Figure 7.10a). When the field is removed Δn , and therefore the deformation, vanishes, which proves that the elastic deformation is a reversible process.

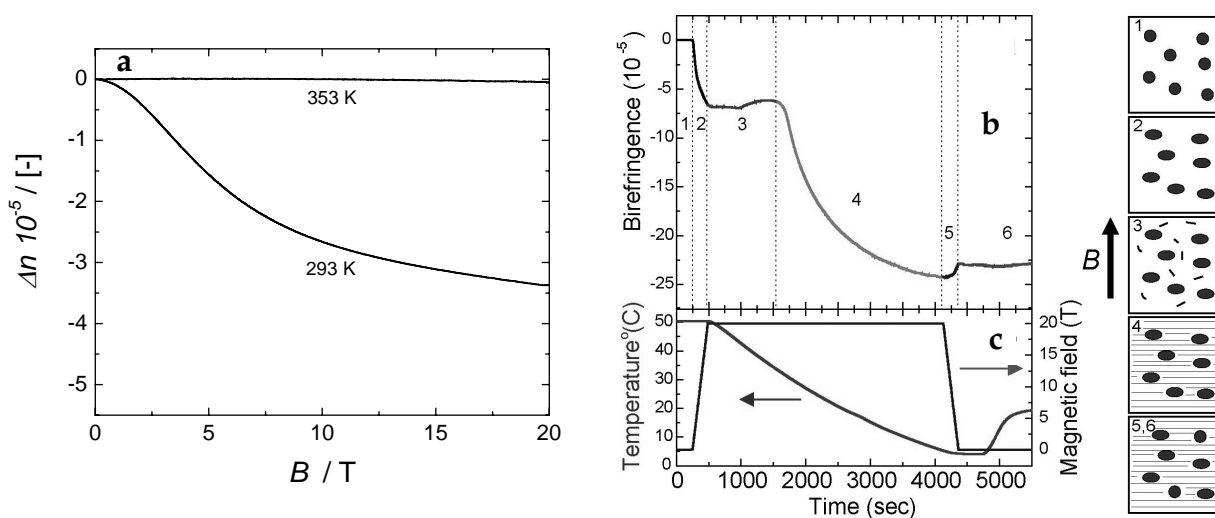


Figure 7.10: (a) Magnetic birefringence due to deformed nanocapsules. (b) Magnetic field induced birefringence during the fixation of deformed nanocapsules in a DDOA organogel. (c) Temperature and magnetic field versus time. Right panel: schematic representation of the six successive phases. The **T6-2SS** solution, containing DDOA, is heated to 50 °C (1), after which the field was ramped up to 20 T (2). At 20 T, the temperature is gradually reduced, causing gelation due to formation of DDOA fibers (3). Sufficiently long gel fibers are aligned, perpendicularly to the magnetic field, yielding a further decrease of the birefringence (4). At 5 °C the field is ramped down to zero (5). Finally, the gelled solution is heated to room temperature (6).

By trapping the deformed nanocapsules in a matrix, we could visualize a deformed capsule. 2,3-Bis-*n*-decyloxyanthracene (DDOA) was used as the matrix, it forms a fibrillar network in alcohols.⁴⁶² At 323 K, in a solution of **T6-2SS** and DDOA in isopropanol, nanocapsules of **T6-2SS** are present and dissolved DDOA molecules (Figure 7.10b). The capsules are deformed by the application of a magnetic field and the deformation is detected by field-induced birefringence. Subsequently, with the field on, the temperature is reduced slowly, triggering the gel formation. At 278 K, the gelation is complete and the resulting gel-sample is warmed to room temperature, during which most of the birefringence is preserved, and taken out of the magnet. Typical SEM photographs at zero magnetic field show that (Figure 7.11a) the **T6-2SS** spheres are embedded in randomly oriented DDOA fibres showing that such a matrix does not disturb the self-assemblies of **T6-2SS**, but traps them. In contrast, spheres gelled at 20 T are deformed into oblate spheroids contained in DDOA fibres oriented perpendicular to the magnetic field direction (Figure 7.10b). Apparently, the gelled DDOA solution in- and outside the deformed capsules provide sufficient stability to prevent the recovery of the spherical shape after the field is switched off.

T6-2SS molecules align with their thiophene rings parallel to the magnetic field. To maximize the number of molecules with their long axis along the field direction, the capsules must deform into an oblate shape, as indeed seen in the SEM images (Figure 7.11b). The negative sign of the birefringence implies that the molecules align with their optical axis parallel to the magnetic field direction, *i.e.* with the long molecular axis of **T6-2SS** along the field, leading to the observed oblate spheroids. Remarkably, three decades ago, Helfrich predicted that magnetic fields could be applied to deform phospholipid bilayer vesicles.^{463,464} Due to their symmetry spheres do not align in a field, but rather deform into ellipsoids of revolution, an effect which to date had not been observed experimentally.

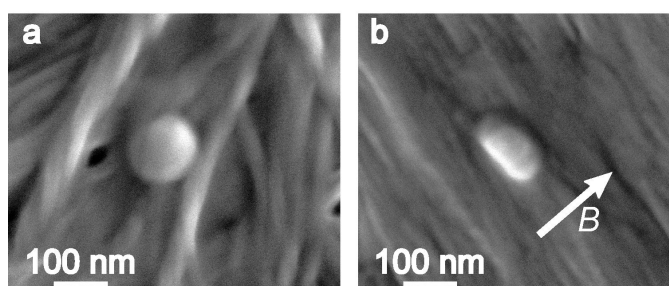


Figure 7.11: SEM images of spherical (a, 0 T) and deformed (b, 20 T) **T6-2SS** nanocapsules in a DDOA gel-network.

7.4 CONCLUSIONS

Optical studies show that the stability of the chiral self-assembled oligothiophenes depends on the π -conjugation length and on the position of the stereocenter relative to the π -conjugated core. Odd-even effects were observed in the sign of the Cotton effect and stereomutation occurs for odd-numbered oligothiophenes. Remarkably, this stereomutation is entropically driven. Such a stereomutation could be an elegant method for constructing two-state switchable materials. Furthermore, the controlled magnetic deformation of nanocapsules into oblate spheroids has been demonstrated showing that magnetic forces are a promising tool for the manipulation of supramolecular structures. The deformed capsules can be fixed in a compatible organogel, preserving their shape outside the magnetic field.

EXPERIMENTAL SECTION

Analytical techniques. Analytical thin layer chromatography (TLC) was performed on Kieselgel F-254 precoated silica plates. Column chromatography was carried out on Merck silica gel 60 (70–230 mesh). Preparative size exclusion chromatography was performed on BioRad Bio Beads S-X1 or S-X3 (200–400 mesh) swollen in tetrahydrofuran or dichloromethane. Matrix assisted laser desorption/ionization mass spectra were obtained (MALDI-TOF MS) using a α -cyano-4-hydroxycinnamic acid matrix on a PerSeptive Biosystems Voyager-DE PRO spectrometer. Elemental analyses were carried out on a Perkin Elmer 2400. Gas-chromatography mass spectrometry (GC-MS) measurements were performed on a Shimadzu GCMS QP5000. ^1H -NMR and ^{13}C -NMR spectra were recorded at room temperature on a Varian Gemini (300 MHz for ^1H -NMR, 75 MHz for ^{13}C -NMR) or a Varian Mercury (400 MHz for ^1H -NMR and 100 MHz for ^{13}C -NMR) spectrometer. Chemical shifts are given in ppm (δ) relative to tetramethylsilane using the deuterated solvent as internal standard. Abbreviations used for splitting patterns are s = singlet, d = doublet, dd = double doublet, t = triplet, m = multiplet and br = broad. **OPV₄T** was additionally analysed by ^{13}C -NMR (standard, inverse gated decoupled and gated decoupled), ^1H - ^1H COSY, HETCOR (^1J , ^2J and ^3J) and INADEQUATE, which were recorded in CDCl_3 at 25.0 °C on a Varian Gemini (300 MHz), a Varian Mercury (400 MHz) or a Varian Unity Inova (500 MHz). The acquisition parameters of the different experiments are as follows: (abbreviations used are np = number of data points in FID, sw = spectral width, pw = pulse width, d1 = relaxation time, nt = number of transients, ss = steady state transients, pp = 90° proton pulse in decoupler channel, sw1 = spectral width in the F1 direction, ni = number of increments, j1xh = coupling constant over one bond, jnxh = coupling constant over multiple bonds and jcc = coupling constant between two adjacent carbon nuclei): ^1H -NMR (300.08 MHz): np = 18×10^3 , sw = 4.50 kHz, pw = 32.3°, d1 = 3.0 s, nt = 16; ^{13}C -NMR (110.63 MHz): np = 60×10^3 , sw = 25.0 kHz, pw = 86.7°, d1 = 0 s, nt = 44×10^3 ; inverse gated decoupled ^{13}C -NMR (110.63 MHz): np = 60×10^3 , sw = 25.0 kHz, pw = 86.7°, d1 = 24 s, nt = 2.0×10^3 ; gated decoupled ^{13}C -NMR (125.69 MHz): np = 65×10^3 , sw = 25.0 kHz, pw = 45°, d1 = 10 s, nt = 1.5×10^3 ; ^1H - ^1H COSY (400.16 MHz): np = 1.0×10^3 , sw = 3.26 kHz, ss = 2, pw = 90°, d1 = 1.0 s, nt = 4, sw1 = 3.26 kHz, ni = 135; ^1J -HETCOR (125.69 MHz): np = 8.0×10^3 , sw = 25.0×10^3 , ss = 1, pw = 90°, d1 = 1.0 s, nt = 128, j1xh = 140.0 Hz, jnxh = 0 Hz, pp = 12.0 μs , sw1 = 5.14 kHz, ni = 256; ^2J HETCOR (125.69 MHz): np = 4.1×10^3 , sw = 24.1 kHz, ss = 1, pw = 90°, d1 = 1.0×10^3 , nt = 300, j1xh = 140.0 Hz, jnxh = 2.0 Hz, pp = 12.0 μs , sw1 = 5.20 kHz, ni = 256; ^3J -HETCOR (125.69 MHz): np = 4.1×10^3 , sw = 24.1 kHz, ss = 1, pw = 90°, d1 = 1.0 s, nt = 300, j1xh = 140.0 Hz, jnxh = 6.8 Hz, pp = 12.0 μs , sw1 = 5.20 kHz, ni = 256; INADEQUATE (125.69 MHz): np = 8.2×10^3 , sw = 25.0 kHz, ss = 8, pw = 90°, d1 = 13.0 s, nt = 56, jcc = 40.0 Hz, sw1 = 49.9 kHz, ni = 256.

Spectroscopic techniques. Infrared spectra were recorded using a Perkin Elmer 1600 FT-IR; UV/vis spectra using a Perkin Elmer Lambda 40P; fluorescence spectra using either a Perkin Elmer LS-50B or an Edinburgh Instrument FS920 double-monochromator spectrometer with a Peltier-cooled red-sensitive photomultiplier; circular-dichroism (CD) spectra using a JASCO J-600 spectropolarimeter, sensitivity, time constant, and scan-rate were chosen appropriately. If complete spectra were recorded at temperature-intervals, the time between two intervals was 30 min, wavelength steps of 1 nm. A PTC-348WI Peltier type temperature control system (263 – 383 K and adjustable temperature slope) was used to measure temperature variable CD spectra. A Peltier Temperature Programmer model 1 (PTP-1) was used to measure temperature variable UV/vis and fluorescence spectra. For recording the temperature variation at a selected wavelength, steps of $\Delta T = 0.01$ K and $\Delta T/t$ was chosen for complete overlap of up and down T-ramp. Time-correlated single-photon counting fluorescence studies were performed using an Edinburgh Instruments LifeSpec-PS spectrometer, consisting of a 400 nm picosecond laser (PicoQuant PDL 800B) operated at 2.5 MHz and a Peltier-cooled Hamamatsu micro-channel plate photomultiplier (R3809U-50). The width of the instrument response function amounts to 50 ps. Using a single channel analyzer, emission spectra can be recorded within a variable, narrow time window after the excitation pulse. The time-resolved emission spectra, the maximal count rate of photons was kept below 10^4 per second, have a spectral resolution of 5 nm. Spectra of films were directly measured after device operation. Transient absorption spectroscopy was carried out according to a literature procedure.^{335,340} Alkane solutions were prepared via heating. Aqueous solutions for optical measurements were prepared via a methanol injection method. The amphiphiles were dissolved in 50 μL methanol and this solution was injected into 5 mL demineralized water. After evaporation of the methanol, the temperature dependent optical spectra were recorded.

Materials. All solvents were of AR quality and commercial chemicals were used as received. Standard procedures were used to obtain dry solvents. Methyl(3,4,5-Tris(2-{2-[2-(2-methoxyethoxy)ethoxy]ethoxy}benzoate **1a**, (*E,E*)-4-{4-(3,4,5-Trisdodecyloxy)styryl}-2,5-bis[(*S*)-2-methylbutoxy]-styryl}-2,5-bis[(*S*)-2-methylbutoxy]benzaldehyde³³⁵ **5**, 2,5-bis[(*S*)-2-methylbutoxy]-1,4-dibromobenzene⁴⁶⁵ **8**,

formylbenzo-15-crown-5⁴⁶⁶ **1b**, 2,5-bis[(S)-2-methylbutoxy]-4-bromo-1-bromomethylbenzene³³⁵ **6** diethyl(2,5-bis[(S)-2-methylbutoxy]-4-bromobenzyl]phosphonate³³⁵ **7** were synthesized according to literature procedures. Compounds **13**, **14**, **OPV₃T** and **OPV₃UT** were provided by Ir. F. J. M. Hoeben. **T** and **UT** were kindly provided by Dr. Ir. J. H. K. Hirschberg. Perylene derivatives were provided by Z. Chen. Oligothiophene derivatives were provided by Dr. O. S. Henze and Dr. A. F. M. Kilbinger and have been or will be published elsewhere.²⁴⁴

(3,4,5-Tris(2-[2-[2-(2-methoxyethoxy)ethoxy]ethoxy]ethoxy)benzyl alcohol (2a).

Under an argon atmosphere, a solution of **1a** (17.59 g, 23.30 mmol) in 100 mL dry THF was added dropwise to a suspension of LiAlH₄ (0.97 g, 25.60 mmol) in 20 mL dry THF at 0°C. After refluxing overnight, the solution was poured on 100 mL crushed ice. Sulfuric acid (60 mL 10%) was added and the aqueous layer was extracted twice with dichloromethane. The collected organic layers were washed with brine and dried (Na₂SO₄), filtered and evaporated to dryness, resulting in 16.09 g (95%) of **2a**. ¹H-NMR (300 MHz, CDCl₃): δ 3.18 (s, 6H), 3.19 (s, 3H), 3.35-3.70 (m, 42H), 3.95 (m, 6H), 4.38 (s, 2H), 6.42 (s, 2H); ¹³C-NMR (100 MHz, CDCl₃): δ 25.0, 58.3, 63.9, 67.2, 68.2, 69.2, 69.8, 70.0, 70.0, 70.1, 71.3, 71.7, 105.6, 136.7, 136.7, 152.0; MALDI-TOF MS (M_w = 726.86) m/z = 749.57 [M+Na]⁺.

(3,4,5-Tris(2-[2-[2-(2-methoxyethoxy)-ethoxy]ethoxy]ethoxy)benzyl chloride (3a).

To a stirred solution of **2a** (10.0 g, 13.76 mmol) in 25 mL dry DCM, was added thionylchloride (4.9 g, 41.3 mmol) and three drops of DMF. The progress of the reaction was monitored with TLC. After 1h, the reaction was completed and the solvent was evaporated. The residue (10.0 g, 13.42 mmol) was not purified further. ¹H-NMR (400 MHz, CDCl₃): δ 3.25 (s, 6H), 3.26 (s, 3H), 3.43-3.75 (m, 42H), 4.10 (m, 6H), 4.40 (s, 2H), 6.53 (s, 2H); ¹³C-NMR (100 MHz, CDCl₃): δ 46.2, 58.5, 68.5, 69.3, 70.0, 70.1, 70.2, 70.4, 71.5, 71.9, 107.9, 132.3, 138.0, 152.2.

Diethyl(3,4,5-tris(2-[2-[2-(2-methoxyethoxy)-ethoxy]ethoxy]ethoxy)benzyl)phosphonate (4a).

A mixture of triethyl phosphite (13.85 g, 83.4 mmol) and **3a** (10.00 g, 13.42 mmol) was stirred at 160 °C for 8 h. During this time, ethylchloride was distilled from the reaction mixture. Subsequently, the mixture was cooled to 70 °C and the excess of triethylphosphite was distilled under reduced pressure. The product was used without further purification: ¹H NMR (300 MHz, CDCl₃) δ 1.21 (t, 6H), 3.02 (d, 2H), 3.34-3.80 (m, 51H), 3.98 (m, 4H), 4.10 (m, 6H), 6.53 (s, 2H); ³¹P-NMR (400 MHz, CDCl₃) δ 27.37.

(E,E,E)-1-[4-(3,4,5-Trisdodecyloxy)styryl]-2,5-bis[(S)-2-methylbutoxy]phenyl]-2-[4-(3,4,5-tris(2-[2-[2-(2-methoxyethoxy)ethoxy]ethoxy]ethoxy)styryl)-2,5-bis[(S)-2-methylbutoxy]phenyl]ethene (OPV₄b).

Phosphonate **4a** (77 mg, 0.09 mmol) was dissolved in 10 mL anhydrous DMF. Potassium tert-butoxide (t-BuOK) (60 mg, 0.54 mmol) was added to the solution under an argon atmosphere. After 15 min, a solution of aldehyde **5** (100 mg, 0.08 mmol) in 15 mL THF was added dropwise to the reaction mixture. The solution was stirred overnight at room temperature. 100 mL HCl (6N) was added and the aqueous layer was extracted three times with chloroform (200 mL). The collected organic layers were washed with HCl (3N) and dried over MgSO₄, filtered, then evaporated to dryness. The crude mixture was purified by column chromatography (silica gel, CH₂Cl₂/methanol 97/3) and dried thoroughly over P₂O₅ to afford 111 mg (73%) of **OPV₄b** as a red wax. M.p. 51°C; ¹H-NMR (400 MHz, CDCl₃): δ 0.90 (t, 9H, (CH₂)₉CH₃), 1.02 (m, 12H, CH₃), 1.13 (m, 12H, CH₃), 1.3 (m, 54H, OCH₂CH₂(CH₂)₉CH₃), 1.5 (m, 8H, CH₂), 1.7 (m, 2H, CH₂), 1.85 (m, 4H, CH), 1.96 (m, 4H, CH₂), 3.38 (s, 6H, OCH₃), 3.39 (s, 3H, OCH₃), 3.53-3.77 (m, 42H, OCH₂), 3.82-3.93 (m, 6H, OCH₂(CH₂)₁₀CH₃), 4.01 (m, 8H, OCH₂CH(CH₃)CH₂CH₃), 4.21 (m, 6H, ArOCH₂), 6.76 (s, 2H, ArH), 6.78 (s, 2H, ArH), 7.05 (d, 2H, J = 16.2 Hz, ArCH=CH), 7.11 (d, 2H, J = 5.1 Hz, ArCH=CH), 7.21 (s, 2H, ArH), 7.36 (d, J = 12.4 Hz, 1H, ArCH=CH), 7.41 (d, 1H, J = 12.4 Hz, ArCH=CH), 7.53 (s, 2H, ArH); ¹³C-NMR (100 MHz, CDCl₃) δ 11.69, 11.71, 11.76, 14.34, 17.02, 17.06, 17.09, 22.92, 26.36, 26.44, 26.62, 29.60, 29.63, 29.66, 29.85, 29.89, 29.94, 29.97, 29.99, 30.57, 32.15, 32.17, 35.22, 35.31, 35.38, 59.24, 68.86, 69.03, 69.31, 69.84, 70.00, 70.73, 70.74, 70.82, 70.90, 71.06, 72.15, 72.65, 73.78, 74.37, 74.41, 74.65, 105.29, 106.33, 109.99, 110.12, 110.65, 111.00, 122.73, 122.79, 122.9, 123.35, 126.75, 127.02, 127.64, 127.79, 128.61, 128.79, 133.46, 133.93, 138.36, 151.25, 151.30, 151.38, 152.97, 153.47; MALDI-TOF MS (M_w = 1900.73) m/z = 1900.43 [M], 1923.46 [M+Na]⁺, 1941.58 [M+K]⁺; Anal. Calcd. for C₁₁₃H₁₉₀O₂₂: C 71.41, H 10.08. Found: C 71.62, H 9.96.

Diethyl [2,5-bis[(S)-2-methylbutoxy]-4-bromobenzyl]phosphonate (7).

A mixture of triethyl phosphite (61.4 g, 370 mmol) and **6** (25 g, 59.5 mmol) was stirred at 160 °C for 8 h. During this time, ethylchloride was distilled from the reaction mixture. Subsequently, the mixture was cooled to 70 °C and the excess of triethyl phosphite was distilled under reduced pressure. The product was used without further purification. ¹H-NMR (300 MHz, CDCl₃) δ 1.00 (m, 6H), 1.10 (m, 6H), 1.28 (t, 6H), 1.36 (m, 2H), 1.65 (m, 2H), 1.95

(m, 2H), 3.23 (d, 2H), 3.79 (m, 4H), 4.07 (m, 4H), 7.01 (s, 1H), 7.07 (s, 1H); MALDI-TOF MS ($M_w = 418.43$) $m/z = 418.18$ [M]⁺

2,5-bis[(S)-2-methylbutoxy]-1,4-formylbenzene (9).

Under argon atmosphere at -10°C 36.75 mL of 1.6 M n-butyllithium in hexane was added dropwise to a solution of **8** (10 g, 24.5 mmol) in 200 mL dry diethylether. During the first 5 min, 4.55 mL of dry DMF was added. After stirring for 1 h, the reaction mixture was poured in 200 mL HCl (6 N) and extracted with diethylether (150 mL). The organic layer was washed 3 times with 200 mL HCl (1N), then with 300 mL water and followed by a saturated NaHCO₃ solution (300 mL). The organic layer was dried over MgSO₄, filtered and evaporated to dryness. The crude mixture was purified by two column chromatography procedures (silica gel, hexane/toluene 1/1 and silica gel, CH₂Cl₂). Recrystallization from hexane yielded pure **9** (3.93 g, 52%). ¹H-NMR (300 MHz, CDCl₃): δ 0.97 (t, 6H), 1.05 (d, 6H), 1.35 (m, 2H), 1.60 (m, 2H), 1.90 (m, 2H), 3.8 (m, 4H), 7.44 (s, 2H), 10.54 (s, 2H); ¹³C-NMR (100 MHz, CDCl₃): δ 11.24, 16.53, 26.08, 34.68, 73.88, 111.55, 129.29, 155.32, 189.30.

(E,E)-1,4-Bis[4-bromo-2,5-bis[(S)-2-methylbutoxy]styryl]-2,5-bis[(S)-2-methylbutoxy]benzene (10).

Dialdehyde **9** (4.80 g, 15.69 mmol) was dissolved in 100 mL dry DMF and slowly added, under an argon atmosphere, to a solution of **7** (16.94 g, 35.29 mmol) and t-BuOK (3.96 g, 35.68 mmol) in 220 mL dry DMF and THF (1/1 mixture). After stirring for 3 h at room temperature, the mixture was poured into ice and 250 mL HCl (6N) was added and extracted with chloroform. The organic layer was washed several times with 250 mL HCl (3N) and again with 200 mL water and subsequently dried over MgSO₄, filtered and evaporated to dryness. The crude mixture was purified by column chromatography (silica gel, CH₂Cl₂/pentane, 1/1). After recrystallisation from ethanol, 8.00 g (53%) of yellow **10** was obtained. ¹H-NMR (300 MHz, CDCl₃): δ 1.00 (m, 18H), 1.10 (m, 18H), 1.36 (m, 6H), 1.65 (m, 6H), 1.95 (m, 6H), 3.78-3.94 (m, 12H), 7.11 (s, 2H), 7.17 (s, 2H), 7.18 (s, 2H), 7.44 (d, 2H, $J = 16.7$ Hz) 7.52 (d, 2H, $J = 16.7$ Hz); ¹³C-NMR (100 MHz, CDCl₃): δ 11.33, 11.43, 16.59, 16.73, 16.79, 26.12, 26.29, 26.36, 34.84, 34.95, 35.01, 74.21, 74.47, 74.74, 110.10, 110.70, 111.47, 118.01, 122.38, 123.39, 127.26, 149.98, 150.97, 151.09; IR (KBr): ν (cm⁻¹) = 663, 717, 737, 772, 815, 855, 876, 916, 971, 982, 1027, 1048, 1200, 1236, 1289, 1325, 1344, 1388, 1419, 1462, 1500, 1563, 2050, 2874, 2920, 2959, 3060; MALDI-TOF MS ($M_w = 956.6$) $m/z = 956.6$ [M]; Anal. Calcd. for C₅₂H₇₆O₆Br₂: C 65.33, H 8.00 Found: C 65.03, H 7.75.

(E,E)-1,4-Bis[4-formyl-2,5-bis[(S)-2-methylbutoxy]styryl]-2,5-bis[(S)-2-methylbutoxy]benzene (11).

Dibromide **10** (2.00 g, 2.09 mmol) was dissolved in 20 mL THF. The solution was cooled to -10°C and 2.3 mL of a 2.5 M n-butyllithium solution in hexane was added slowly. After stirring for 5 min, the cooling bath was removed and 1 mL dry DMF was added dropwise. The reaction mixture was stirred for another hour at room temperature. After addition of 100 mL 6 M HCl, the organic layer was washed with water (2 × 150 mL), a saturated NaHCO₃ solution (150 mL) and again water (150 mL). The organic layer was dried over MgSO₄ and the solvent was evaporated. The residue was purified by column chromatography (silica, CH₂Cl₂/pentane 1/1) and recrystallisation from heptane yielded 1.23 g (69%) **11**. ¹H-NMR (300 MHz, CDCl₃): δ 1.00 (m, 18H), 1.10 (m, 18H), 1.36 (m, 6H), 1.65 (m, 6H), 1.95 (m, 6H), 3.81-4.03 (m, 12H), 7.24 (s, 2H), 7.26 (s, 2H), 7.35 (s, 2H), 7.54 (d, 2H, $J = 16.8$ Hz), 7.68 (d, 2H, $J = 16.8$ Hz), 10.5 (s, 2H); ¹³C-NMR (100 MHz, CDCl₃): δ 11.33, 11.43, 16.59, 16.73, 16.79, 26.12, 26.29, 26.36, 34.84, 34.95, 35.01, 73.70, 73.83, 74.12, 109.73, 110.19, 122.50, 123.11, 126.25, 127.42, 134.95, 150.67, 151.33, 156.38, 189.04; IR (KBr): ν (cm⁻¹) = 672, 723, 774, 814, 851, 874, 915, 970, 1007, 1041, 1124, 1152, 1200, 1263, 1343, 1390, 1423, 1463, 1504, 1595, 1668 (C=O), 2040, 2858, 2928, 2959, 3064; MALDI-TOF MS ($M_w = 855.21$) $m/z = 854.49$ [M]⁺; Anal. Calcd. for C₅₄H₇₈O₈: C 75.94, H 9.21. Found: C 75.62, H 9.46.

(E,E,E,E)-1,4-Bis[4-(3,4,5-tris(2-(2-(2-methoxyethoxy)ethoxy)ethoxy)styryl)-2,5-bis[(S)-2-methylbutoxy]styryl]-2,5-bis[(S)-2-methylbutoxy]benzene (OPV5a).

Under an argon atmosphere, phosphonate **4a** (925 mg, 1.08 mmol) was dissolved in 10 mL anhydrous DMF and t-BuOK (310 mg, 2.77 mmol) was added. After 15 min, a solution of dialdehyde **11** (310 mg, 0.36 mmol) in 7.5 mL THF was added dropwise to the reaction mixture. The solution was stirred overnight at room temperature. 100 mL HCl (6N) was added and the aqueous layer was extracted three times with chloroform (200 mL). The collected organic layers were washed with HCl (3N) and dried over MgSO₄, filtered and evaporated to dryness. The crude mixture was purified by column chromatography (silica gel, hexane/ethylacetate 2/1 and CH₂Cl₂/ethanol, gradient) and subsequently, size exclusion chromatography (bio beads, SX-1, CH₂Cl₂). Thoroughly drying over P₂O₅ afforded 435 mg (54%) of **OPV5a** as an orange wax. M.p. 82°C; ¹H-NMR (400 MHz, CDCl₃): δ 1.00 (m, 18H, CH₃), 1.10 (m, 18H, CH₃), 1.36 (m, 6H, CH₂), 1.65 (m, 6H, CH), 1.95 (m, 6H, CH₂), 3.36 (s, 12H, OCH₃), 3.39 (s, 6H, OCH₃), 3.5-3.8 (m, 84H, OCH₂), 3.8-3.9 (m, 12H, OCH₂CH(CH₃)CH₂CH₃), 4.21 (m, 12H, OCH₂), 6.76 (s, 4H, ArH),

7.03 (d, 2H, $J = 16.4$ Hz, ArCH=CH), 7.08 (s, 2H, ArH), 7.19 (s, 4H, ArH), 7.34 (d, 2H, $J = 16.4$ Hz, ArCH=CH), 7.52 (s, 4H, ArCH=CH); ^{13}C -NMR (100 MHz, CDCl_3): δ 11.33, 11.43, 16.81, 16.85, 26.38, 34.95, 35.01, 35.14, 59.00, 68.80, 69.77, 70.49, 70.53, 70.58, 70.59, 70.64, 70.65, 70.82, 71.91, 72.38, 74.15, 74.23, 74.43, 106.12, 109.83, 109.95, 110.75, 122.56, 122.75, 123.12, 126.50, 127.40, 127.59, 128.36, 133.69, 138.22, 151.03, 151.10, 151.20, 152.73; IR (KBr): ν (cm^{-1}) = 663, 692, 731, 773, 810, 852, 965, 1044, 1103, 1201, 1247, 1289, 1349, 1387, 1421, 1462, 1505, 1579, 2050, 2873, 2920, 2958, 3059; MALDI-TOF MS ($M_w = 2240.89$) $m/z = 2239.94$ $[\text{M}]^+$, 2262.92 $[\text{M}+\text{Na}]^+$, 2278.91 $[\text{M}+\text{K}]^+$; Anal. Calcd. for $\text{C}_{122}\text{H}_{198}\text{O}_{36}$: C 65.39, H 8.91. Found: C 65.27, H 9.05.

4-Hydroxymethylbenzo-15-crown-5 (2b).

Under argon atmosphere at 0 °C, solution of **1b** (2.93 g, 10.1 mmol) in 20 ml dry THF was added dropwise to a suspension of LiAlH_4 (0.421 g, 11.1 mmol) in 10 mL THF. After refluxing for 12 h, the solution was poured on 50 mL of crushed ice. Sulfuric acid (30 mL, 10%) was added and the aqueous layer was washed twice with 75 mL dichloromethane. The collected organic layers were washed with demineralised water and dried (MgSO_4), filtrated and evaporated to dryness, resulting in 1.24 g (42%) of **2b**. ^1H -NMR (300 MHz, CDCl_3) δ 3.78 (m, 8H), 3.94 (m, 4H), 4.17 (m, 4H), 4.63 (s, 2H), 6.87 (d, 1H), 6.91 (d, 1H), 6.95 (s, 1H).

4-Chloromethylbenzo-15-crown-5 (3b).

Under argon atmosphere, to a stirred solution of **2b** (1.18 g, 4.04 mmol) in 15 mL dry dichloromethane, were added a couple of droplets of DMF and thionylchloride (1.44 g, 12.12 mmol). After 2 h, the reaction was completed and the solvent was evaporated. The residu (1.25 g, 4.04 mmol) was not purified further. ^1H -NMR (300 MHz, CDCl_3): δ 3.83 (s, 8H), 3.98 (m, 4H), 4.21 (m, 4H), 4.60 (s, 2H), 6.87 (d, 1H), 6.91 (d, 1H), 6.95 (s, 1H).

4-Diethylphosphonatebenzo-15-crown-5 (4b).

A mixture of triethyl phosphite (4.15 g, 25 mmol) and **3b** (1.2 g, 3.87 mmol) was stirred at 160 °C for 12 h. During this time, ethylchloride was distilled off from the reaction mixture. Subsequently, the mixture was cooled to 70 °C and the excess of triethyl phosphite was distilled under reduced pressure. The product was used without further purification. ^1H -NMR (300 MHz, CDCl_3): δ 1.29 (t, 6H), 3.13 (d, 2H), 3.81 (s, 8H), 3.96 (m, 4H), 4.06 (m, 4H), 4.19 (m, 4H), 6.86 (s, 2H), 6.92 (s, 1H).

(*E,E,E,E*)-1,4-Bis[4-[(15-crown-5)styryl]-2,5-bis[(*S*)-2-methylbutoxy]-styryl]-2,5-bis[(*S*)-2-methylbutoxy]benzene (OPV₅b).

Under argon atmosphere, phosphonate **4b** (0.83 g, 2.1 mmol) was dissolved in 20 mL anhydrous DMF and $t\text{-BuOK}$ (0.8 g, 6.3 mmol) was added. After 15 minutes, a solution of dialdehyde **11** (0.59 g, 0.69 mmol) in 15 mL THF was added dropwise to the reaction mixture. The solution was stirred overnight at room temperature. 250 mL HCl (6 M) was added and the aqueous layer was extracted three times with dichloromethane. The collected organic layers were washed with HCl (3 M) and subsequently with demineralised water and dried over MgSO_4 , filtered and evaporated to dryness. The crude mixture was first purified by three times preparative size exclusion chromatography (bio beads, SX-1, CH_2Cl_2 (2x) and THF) and subsequently by column chromatography (silica gel, CH_2Cl_2 /ethanol, gradient). Precipitation in methanol of 0 °C yielded 0.11 g (12 %) of **OPV₅b**. Mp = 221 °C; ^1H -NMR (300 MHz, CDCl_3): δ 1.06 (t, 18H, CH_3), 1.18 (m, 18H, CH_3), 1.44 (m, 6H, CH_2), 1.73 (m, 6H, CH_2), 2.05 (m, 6H, CH_2), 3.84 (s, 16H, OCH_2), 3.92 (m, 8H, OCH_2), 3.98 (m, 12H, OCH_2) 4.23 (t, 4H, OCH_2), 4.28 (t, 4H, OCH_2), 6.93 (d, 2H, $J = 8.2$ Hz, $\text{CH}=\text{CH}$), 7.13 (d, 2H, $J = 8.8$ Hz, $\text{CH}=\text{CH}$), 7.14 (d, 2H, $J = 16.8$ Hz, $\text{CH}=\text{CH}$), 7.18 (s, 4H, ArH), 7.28 (s, 4H, ArH), 7.42 (d, 2H, $J = 16.5$ Hz, $\text{CH}=\text{CH}$), 7.51 (s, 4H, ArH). ^{13}C -NMR (400 MHz, CDCl_3): δ 11.39, 11.49, 11.52, 11.57, 16.87, 16.90, 26.24, 26.42, 35.05, 35.18, 69.05, 69.08, 69.62, 69.66, 70.54, 71.14, 74.19, 74.27, 74.49, 77.26, 109.85, 109.97, 110.59, 111.71, 114.03, 120.33, 121.86, 122.63, 126.90, 127.36, 127.45, 128.30, 131.79, 148.91, 149.25, 151.09, 151.13, 151.14; IR (KBr): ν (cm^{-1}) = 668, 751, 799, 852, 933, 963, 1047, 1174, 1138, 1203, 1214, 1256, 1269, 1306, 1355, 1389, 1421, 1463, 1513, 1581, 1599, 2873, 2925, 2959, 3019. MALDI-TOF MS ($M_w = 1383.87$) $m/z = 1382.92$ $[\text{M}]^+$, 1405.92 $[\text{M} + \text{Na}]^+$; Anal. Calcd. for $\text{C}_{84}\text{H}_{118}\text{O}_{16}$: C 72.19, H 8.59. Found: C 72.23, H 8.49.

Diethyl(4-cyanobenzyl)phosphonate.

A mixture of triethyl phosphite (2.54 g, 15.30 mmol) and 4-cyanobenzylbromide (2.00g, 10.20 mmol) was stirred at 160 °C for 2 h. During this time ethylbromide was distilled from the reaction mixture. Subsequently the mixture was cooled to 70 °C and the excess of triethylphosphite was distilled under reduced pressure. The product, diethyl(4-cyanobenzyl) phosphonate, was used without further purification: ^1H -NMR (CDCl_3) δ 7.55 (dd, 2H), 7.37 (dd, 2H), 3.98 (dt, 4H), 3.14 (d, 2H), 1.19 (t, 6H); ^{13}C -NMR (100 MHz, CDCl_3) δ 137.34 (d), 131.19 (d), 127.68, 118.43 (d), 110.55 (d), 62.17 (d), 33.78 (d), 16.07 (d); IR (UATR) ν (cm^{-1}) 2984, 2909, 2227, 1607, 1506, 1479, 1444, 1417, 1392, 1244, 1048, 1018, 958, 857, 824, 780 cm^{-1} ; GC-MS: 253.

(*E,E*)-4-{4-(3,4,5-Tridodecyloxystyryl)-2,5-bis[(*S*)-2-methylbutoxy]-styryl}-2,5-bis[(*S*)-2-methylbutoxy]benzaldehyde (5).

A literature procedure was followed,³³⁵ yielding 8.53 g (90%) of **5** as an orange solid: ¹H-NMR (CDCl₃) δ 1.18–0.90 (m, 33H), 1.89–1.18 (m, 68H), 2.05–1.90 (m, 4H), 4.10–3.80 (m, 14H), 6.77 (s, 2H), 7.08 (d, 1H), 7.13 (s, 1H), 7.9 (s, 1H), 7.25 (s, 1H), 7.34 (s, 1H), 7.41 (d, 1H), 7.53 (d, 1H), 7.66 (d, 1H), 10.48 (s, 1H); ¹³C-NMR (CDCl₃) δ 11.75, 11.91, 11.93, 14.55, 11.98, 17.05, 17.18, 17.21, 23.12, 26.56, 26.78, 29.79, 29.82, 29.85, 30.04, 30.08, 30.13, 30.16, 30.18, 30.77, 32.34, 32.36, 35.25, 35.31, 35.47, 35.53, 69.40, 73.83, 73.97, 74.19, 74.48, 74.56, 105.37, 109.77, 110.40, 110.49, 122.06, 122.50, 124.19, 126.52, 126.61, 127.98, 129.30, 133.24, 135.29, 138.44, 150.74, 151.20, 151.52, 153.37, 156.49, 188.93; IR (UATR) ν (cm⁻¹) 2957, 2922, 2853, 2676, 1593, 1501, 1465, 1422, 1386, 1333, 1242, 1201, 1116, 1041, 965, 852, 723; MALDI-TOF MS (M_w) 1206.98) m/z 1206.75 [M]⁺.

(*E,E,E*)-4-<4-{4-(3,4,5-Tridodecyloxystyryl)-2,5-bis[(*S*)-2-methylbutoxy]styryl}-2,5-bis[(*S*)-2-methylbutoxy]styryl>-2,5-bis[(*S*)-2-methylbutoxy]bromobenzene (15).

6 (60.1 mg, 0.362 mmol) was dissolved in 5 ml anhydrous DMF and under an argon atmosphere *t*-BuOK (0.46 g, 4.14 mmol) was added to the solution. After 15 min a solution of **5** (291 mg, 0.241 mmol) in 3.5 ml DMF/THF (2:1) was added dropwise to the reaction mixture. The solution was stirred for 4 h and subsequently poured onto 100 g of crushed ice. 80 mL of 3N HCl was added and the aqueous phase was extracted three times with chloroform (100 mL). The combined organic fractions were washed with 3N HCl solution (200 mL) and dried over MgSO₄. After evaporation of the solvent, the product was purified by column chromatography (silica gel, hexane/CH₂Cl₂ 1/2) to afford 337 mg (91%) of **15** as orange solid: ¹H-NMR (400 MHz, CDCl₃): δ 0.85 (t, 9H), 1.05 (m, 18H), 1.15 (t, 18H), 1.2–1.4 (m, 48H), 1.5 (m, 6H), 1.7 (m, 12H), 1.85 (m, 6H), 2.00 (m, 6H), 3.95–4.06 (m, 18H), 6.75 (s, 2H), 7.06 (d, J=16.4 Hz, 1H), 7.1–7.25 (m, 5H), 7.4 (d, J=16.4 Hz, 1H), 7.5–7.6 (m, 5H); IR (UATR) ν (cm⁻¹): 2958, 2918, 2873, 2859, 1507, 1463, 1420, 1386, 1347, 1250, 1202, 1050, 965, 840, 723; MALDI-TOF MS (M_w = 1534.1) m/z = 1534.21 [M]⁺.

(*E,E,E*)-4-<4-{4-(3,4,5-Tridodecyloxystyryl)-2,5-bis[(*S*)-2-methylbutoxy]styryl}-2,5-bis[(*S*)-2-methylbutoxy]styryl>-2,5-bis[(*S*)-2-methylbutoxy]benzaldehyde (16).

Bromide derivative **15** (337 mg, 0.220 mmol) was dissolved in 5 ml dry diethyl ether. The solution was cooled to -10 °C and 0.25 mL of a 1.6 M *n*-butyllithium solution in hexane was slowly added. The reaction mixture was stirred for 5 min., then, the cooling bath was removed and 0.1 mL dry DMF was added dropwise. The mixture was stirred for another hour at room temperature. After addition of 25 mL 6N HCl, the organic layer was washed with water (2x100 mL), a saturated NaHCO₃ solution (100 mL) and again water (100 mL). The organic layer was dried over MgSO₄ and the solvent was evaporated. Recrystallization from methanol/diethyl ether (5/1) yielded 287 mg (88%) of **16**. ¹H-NMR (400 MHz, CDCl₃): δ 0.85 (t, 9H), 1.05 (m, 18H), 1.15 (t, 18H), 1.2–1.4 (m, 48H), 1.5 (m, 6H), 1.7 (m, 12H), 1.85 (m, 6H), 2.00 (m, 6H), 3.95–4.06 (m, 18H), 6.8 (s, 2H), 7.1 (d, J=16.4 Hz, 1H), 7.16 (s, 1H) 7.24–7.29 (m, 3H), 7.38 (s, 1H), 7.46 (d, J=16.4 Hz, 1H), 7.55–7.6 (m, 4H), 7.7 (d, J=16.4 Hz, 1H), 10.52 (s, 1H); ¹³C-NMR (100 MHz, CDCl₃) δ 189.22, 156.72, 153.59, 151.77, 151.48, 150.98, 138.55, 135.50, 133.54, 128.98, 128.82, 127.60, 127.31, 126.75, 124.34, 123.51, 122.80, 122.20, 110.52, 110.29, 110.13, 109.95, 105.45, 74.70, 74.52, 74.42, 74.21, 74.01, 73.85, 69.41, 35.49, 35.42, 35.37, 35.22, 35.17, 32.25, 30.68, 29.99, 29.78, 29.69, 29.66, 26.72, 26.46, 23.00, 17.12, 16.93, 14.41, 11.47, 11.61; IR (UATR) ν (cm⁻¹): 1593; MALDI-TOF MS (M_w= 1482.30) m/z = 1482.33 [M]⁺.

(*E,E,E*)-4-[4-{4-(3,4,5-Tridodecyloxystyryl)-2,5-bis[(*S*)-2-methylbutoxy]styryl}-2,5-bis[(*S*)-2-methylbutoxy]styryl]phenylnitrile (12).

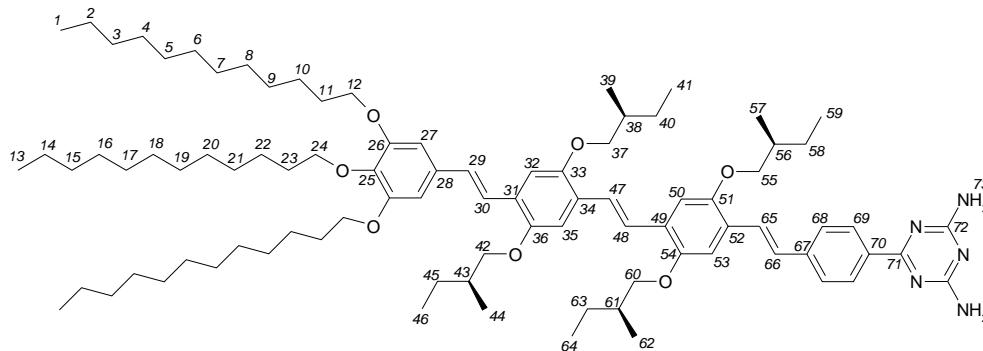
Diethyl(4-cyanobenzyl)phosphonate (0.79 g, 3.10 mmol) was dissolved in 5 ml anhydrous DMF and under an argon atmosphere, *t*-BuOK (0.46 g, 4.14 mmol) was added. After 15 min, a solution of **5** (2.50 g, 2.07 mmol) in 30 ml DMF/THF (2/1) was added dropwise to the reaction mixture. The solution was stirred for 4 h and subsequently poured onto 100 g of crushed ice. 80 ml of 3N HCl was added and the aqueous phase was extracted three times with diethyl ether. The collected organic fractions were washed with 3N HCl solution and dried over MgSO₄. After evaporation of the solvent, the product was purified by column chromatography (silica gel, hexane/CH₂Cl₂ 1/2) to afford 2.47 g (91%) of **12** as a orange solid: ¹H-NMR (400 MHz, CDCl₃): δ 0.95 (t, 9H), 1.05 (m, 12H), 1.15 (t, 12H), 1.3 (m, 54H), 1.5–1.7 (m, 8H), 1.8 (m, 2H), 1.9 (m, 4H), 2.00 (m, 4H), 3.95–4.06 (m, 14H), 6.75 (s, 2H), 7.06 (d, J=16.4 Hz, 1H), 7.1–7.2 (m, 6H), 7.4 (d, J=16.4 Hz, 1H), 7.5–7.6 (m, 6H). ¹³C-NMR (100 MHz, CDCl₃) δ 153.53, 151.96, 151.42, 151.17, 142.90, 138.46, 133.48, 132.66, 129.14, 128.97, 127.57, 127.40, 127.34, 126.93, 126.73, 125.54, 123.61, 122.70, 122.51, 119.37, 111.38, 110.60, 110.37, 110.11, 109.65, 105.35, 74.71, 74.58, 74.42, 74.15, 73.77, 69.32, 35.44, 35.43, 35.37, 35.22, 34.92, 32.21, 31.86, 30.64, 30.04, 30.03, 30.00, 29.95, 29.73, 29.69, 29.66, 29.32, 27.17, 26.68, 26.66, 26.63, 26.42, 25.52, 22.97, 22.92, 18.97, 17.11, 17.08, 17.02, 14.35, 11.78, 11.74, 11.66, 11.62; IR (UATR) ν (cm⁻¹) 2957, 2920, 2852, 2224, 1590, 1505, 1467, 1423, 1391, 1339, 1246, 1203, 1118, 1043, 1009, 966, 851, 821, 721 cm⁻¹; MALDI-TOF MS (M_w = 1306.02) m/z = 1306.22 [M]⁺.

(*E,E,E,E*)-4-[4-<4-[4-(3,4,5-Tridodecyloxystyryl)-2,5-bis[(*S*)-2-methylbutoxy]styryl]-2,5-bis[(*S*)-2-methylbutoxy]styryl]-2,5-bis[(*S*)-2-methylbutoxy]styryl]phenylnitrile (17).

Diethyl(4-cyanobenzyl)phosphonate (50 mg, 0.21 mmol) was dissolved in 1 mL anhydrous DMF under an argon atmosphere and *t*-BuOK (31 mg, 0.28 mmol) was added to the solution. After 15 min, a solution of **16** (200 mg, 0.135 mmol) in 4 mL DMF/THF (2/1) was added drop wise to the reaction mixture. The solution was stirred for 4 h and subsequently poured onto 25 g of crushed ice. 80 mL of 3N HCl was added and the aqueous phase was extracted three times with dichloromethane (100 mL). The collected organic fractions were washed with 3N HCl solution (150 mL) and dried over MgSO₄. After evaporation of the solvent the product was purified by column chromatography (silica gel, pentane/CH₂Cl₂ 2/1) to afford 174 mg (82%) of **17** as a orange solid: ¹H-NMR (400 MHz, CDCl₃): δ 0.85 (t, 9H), 1.05 (m, 18H), 1.15 (t, 18H), 1.2–1.4 (m, 48H), 1.5 (m, 6H), 1.7 (m, 12H), 1.85 (m, 6H), 2.00 (m, 6H), 3.95–4.06 (m, 18H), 6.74 (s, 2H), 7.03 (d, *J*=16.4 Hz, 1H), 7.12 (s, 1H), 7.15 (s, 1H), 7.19–7.22 (m, 5H), 7.39 (d, 1H), 7.5–7.65 (m, 9H). IR (UATR) ν (cm⁻¹) 2224; MALDI-TOF MS (*M*_w = 1581.22) *m/z* = 1581.37 [M]⁺.

2,4-Diamino-6-[(*E,E,E*)-4-[4-<4-[4-(3,4,5-tridodecyloxystyryl)-2,5-bis[(*S*)-2-methylbutoxy]styryl]-2,5-bis[(*S*)-2-methylbutoxy]styryl]-2,5-bis[(*S*)-2-methylbutoxy]styryl]phenyl-s-triazine (OPV₄T).

In a round-bottom flask 1.97 g (1.51 mmol) **12** and 0.13 g (1.54 mmol) dicyandiamide were dissolved in 20 mL 2-methoxyethanol. After adding 0.20 g (3.56 mmol) KOH, the solution was refluxed for 8 h. Purification was achieved with column chromatography (silica gel, EtOH/CH₂Cl₂ 2/98). After precipitation in methanol pure OPV₄T (1.55 g, 74%) was obtained. Peak assignment is based on combining the results of ¹H-NMR, ¹³C-NMR, ¹H-¹H COSY, ¹J-HETCOR and the ³J-HETCOR spectra, and is displayed below. ¹H-NMR: δ 0.9 (t, 9H, 1, 13), 1.0 (m, 12H, 41, 46, 59, 64), 1.1 (m, 12H, 39, 44, 57, 62), 1.2–1.4 (m, 24H, 2–9, 14–21), 1.5 (m, 6H, 10, 22), 1.7 (m, 8H, 40, 45, 58, 63), 1.8 (m, 6H, 11, 23), 2.0 (m, 4H, 38, 43, 56, 61), 3.8–3.95 (m, 8H, 37, 42, 55, 60), 3.95–4.05 (m, 6H, 12, 24), 5.25 (br, 4H, 73), 6.76 (s, 2H, 27), 7.06 (d, *J* = 16.2 Hz, 1H, 29), 7.13 (s, 1 H, 32), 7.16 (s, 1 H, 35), 7.19 (d, *J* = 16.6 Hz, 1H, 47), 7.23 (d, *J* = 16.5 Hz, 1H, 65), 7.25 (d, *J* = 16.6 Hz, 1H, 48), 7.41 (d, *J* = 16.2 Hz, 1H, 30), 7.55 (s, 2H, 50, 53), 7.63 (d, *J* = 8.4 Hz, 2H, 68), 7.63 (d, *J* = 16.5 Hz, 1H, 66), 8.34 (d, *J* = 8.4 Hz, 2H, 69); ¹³C-NMR: δ {11.43 (1C), 11.50 (1C), 11.55 (2C)} (41, 46, 59, 64), 14.13 (3C, 1, 13), {16.80 (1C), 16.87 (3C)} (39, 44, 57, 62), {22.71 (3C), [29.39, 29.41] (3C), 29.46 (3C), [29.65, 29.69, 29.73, 29.76] (12C), 31.95 (3C)} (2–9, 14–21), 26.15 (3C, 10, 22), 26.41 (4C, 40, 45, 58, 63), 29.78 (2C, 11), 30.36 (1C, 23), {35.00 (1C), 35.10 (1C), 35.16 (1C), 35.18 (1C)} (38, 43, 56, 61), 69.10 (2C, 12), 73.57 (1C, 24), {74.11 (1C), 74.20 (1C), 74.43 (1C), 74.48 (1C)} (37, 42, 55, 60), 105.1 (2C, 27), 109.6 (1C, 48), 109.9 (1C, 47), 110.4 (1C, 32), 110.9 (1C, 35), 122.5 (2C, 30, 50), 122.9 (1C, 53), 125.2 (1C, 52), 126.3 (1C, 66), 126.4 (2C, 68), 126.9 (1C, 49), 127.4 (1C, 34), 128.0 (1C, 31), 128.1 (1C, 65), 128.6 (1C, 29), 128.8 (2C, 69), 133.3 (1C, 28), 135.2 (1C, 70), 138.1 (1C, 25), 141.4 (1C, 67), {151.0 (1C), 151.1 (1C), 151.2 (1C), 151.5 (1C)} (33, 36, 51, 54), 153.3 (2C, 26), 167.6 (2 C,72), 172.0 (1C, 71); IR (KBr): ν (cm⁻¹) = 3170, 3401, 3475 (N-H stretch); MALDI-TOF MS (*M*_w = 1391.11) *m/z* = 1390.18 [M]⁺.



2,4-Diamino-6-[(*E,E,E*)-4-[4-<4-[4-(3,4,5-tridodecyloxystyryl)-2,5-bis[(*S*)-2-methylbutoxy]styryl]-2,5-bis[(*S*)-2-methylbutoxy]styryl]-2,5-bis[(*S*)-2-methylbutoxy]styryl]phenyl-s-triazine (OPV₅T).

In a round-bottom flask, 174 mg (0.11 mmol) **17** and 9.99 mg (0.12 mmol) dicyandiamide were dissolved in 5 mL 2-methoxyethanol. After adding 31 mg (0.55 mmol) KOH, the solution was refluxed for 8 h. After cooling the reaction mixture to room temperature 80 mL of brine was added and the aqueous phase was extracted three times with dichloromethane (100 mL). The collected organic fractions and dried over Na₂SO₄. After evaporation of the solvent the product was purified with column chromatography (silica gel, EtOH/CH₂Cl₂ 5/95). After precipitation in cold methanol pure OPV₅T (110 mg, 60%) was obtained. ¹H-NMR (400 MHz, CDCl₃): δ 0.85 (t, 9H), 1.05 (m, 18H), 1.15 (t, 18H), 1.2–1.4 (m, 48H), 1.5 (m, 6H), 1.7 (m, 12H), 1.85 (m, 6H), 2.00 (m, 6H), 3.95–4.06 (m, 18H), 5.24 (br, 4H), 6.74 (s, 2H), 7.03 (d, *J*=16.4 Hz, 1H), 7.12 (s, 1H), 7.15 (s, 1H), 7.19–7.22 (m, 5H), 7.39 (d, *J*=16.4 Hz, 1H), 7.52 (s, 2H), 7.54 (s, 2H), 7.59 (d, *J*=8.4 Hz, 2H), 7.62 (d, *J*=8.4 Hz, 1H), 8.32 (d, *J*=8.4 Hz, 2H); ¹³C-NMR (100 MHz, CDCl₃): δ 11.39, 11.47, 11.51, 14.10, 16.78, 16.85, 22.68, 26.14, 26.40, 29.36, 29.39, 29.44, 29.66, 29.70, 29.75, 30.35, 31.93,

35.00, 35.09, 35.16, 69.12, 73.56, 74.12, 74.22, 74.45, 77.21, 105.14, 109.70, 109.94, 110.47, 110.94, 122.53, 122.94, 125.18, 126.33, 126.89, 127.39, 128.00, 128.10, 128.62, 128.74, 133.24, 135.16, 138.21, 141.43, 151.01, 151.13, 151.18, 151.51, 153.26, 167.66, 172.02; IR (UATR) ν (cm⁻¹): (NH) 3545, 3491, 3422, 3303, 3225, 3210; MALDI-TOF MS (MW = 1665.26) m/z = 1665.41 [M]⁺.

2-Amino-4-butylureido-6-[(E,E,E)-4-<4-[4-(3,4,5-trisdodecyloxystyryl)-2,5-bis[(S)-2-methylbutoxy]styryl]-2,5-bis[(S)-2-methylbutoxy]styryl>]phenyl-s-triazine} (OPV₄UT).

1.35 g (0.97 mmol) of OPV₄T was dissolved in 20 ml dry pyridine at room temperature. 0.25 Equivalents of *n*-butylisocyanate (24.1 mg, 0.24 mmol) were added and the reaction mixture was refluxed for 8 h. After evaporation of the solvent, the mixture was flushed with toluene to remove the pyridine. Using column chromatography (silica gel, CH₂Cl₂/EtOH 98/2), pure OPV₄UT (0.839 g, 58%) was obtained. ¹H-NMR (400 MHz, CDCl₃): δ 0.9 (t, 9H), 1.02 (m, 12H), 1.1 (t, 12H), 1.3 (m, 54H), 1.5–1.7 (m, 15H), 1.8 (m, 2H), 1.9 (m, 4H), 2.00 (m, 4H), 3.5 (q, 2H), 3.95–4.06 (m, 14H), 5.46 (br, 1H), 6.75 (s, 2H), 7.03 (d, J=16.4 Hz, 1H), 7.1–7.2 (m, 6H), 7.4 (d, J=16.4 Hz, 1H), 7.5–7.6 (m, 4H), 8.22 (s, 1H), 8.24 (s, 1H), 9.28 (br, 1H), 9.90 (br, 1H), 10.24 (br, 1H); ¹³C-NMR (100 MHz, CDCl₃): δ 11.58, 11.65, 11.71, 14.00, 14.25, 16.89, 16.95, 16.98, 20.47, 22.81, 26.25, 26.52, 29.47, 29.50, 29.56, 29.75, 29.78, 29.81, 29.82, 29.85, 30.40, 30.47, 31.79, 32.03, 32.04, 35.11, 35.18, 35.27, 40.01, 69.05, 73.52, 73.94, 74.09, 74.34, 74.38, 77.21, 104.93, 109.26, 109.57, 110.23, 110.61, 122.12, 122.31, 122.66, 125.36, 125.79, 126.128, 126.70, 127.11, 127.18, 128.08, 128.40, 128.49, 133.07, 133.92, 137.95, 141.84, 150.73, 150.87, 150.94, 151.31, 153.03, 155.74, 163.53, 167.74, 169.77; MALDI-TOF MS (M_w = 1490.24) m/z = 1489.21 [M]⁺, 1512.03 [M+Na]⁺; IR (KBr): ν (cm⁻¹) = 1687 (C=O stretch), 3209, 3222, 3301, 3491 (N–H stretch); Anal. Calcd. for C₉₄H₁₄₈O₈N₆: C 72.05, H 10.26, N 5.09 Found: C 72.26, H 9.94, N 5.11.

2-Amino-4-butylureido-6-[(E,E,E,E)-4-[4-<4-[4-(3,4,5-tridodecyloxystyryl)-2,5-bis[(S)-2-methylbutoxy]styryl]-2,5-bis[(S)-2-methylbutoxy]styryl]-2,5-bis[(S)-2-methylbutoxy]styryl]phenyl-s-triazine} (OPV₅UT).

50 mg (0.030 mmol) of OPV₅T was dissolved in 5 mL dry pyridine at room temperature. *n*-Butylisocyanate (12 mg, 0.12 mmol) was added and the reaction mixture was refluxed for 8 h. After evaporation of the solvent, the mixture was flushed with toluene to remove the pyridine. Using column chromatography (silica gel, CH₂Cl₂/EtOH 98/2), pure OPV₅UT (28.3 mg, 53%) was obtained. ¹H-NMR (400 MHz, CDCl₃): δ 0.9 (t, 9H), 1.0 (m, 23H), 1.1 (m, 18H), 1.2–1.4 (m, 50H), 1.5 (m, 6H), 1.7 (m, 12H), 1.85 (m, 6H), 2.00 (m, 6H), 3.5 (m, 2H), 3.95–4.06 (m, 18H), 5.46 (br, 1H), 6.74 (s, 2H), 7.03 (d, J=16.4 Hz, 1H), 7.12 (s, 1H), 7.15 (s, 1H), 7.19–7.22 (m, 5H), 7.39 (d, J=16.4 Hz, 1H), 7.52 (s, 2H), 7.54 (s, 2H), 7.62 (d, J=8.4 Hz, 2H), 7.65 (d, J=8.4 Hz, 1H), 8.23 (d, J=8.4 Hz, 2H), 9.28 (br, 1H), 9.90 (br, 1H), 10.24 (br, 1H); ¹³C-NMR (100 MHz, CDCl₃): δ 11.58, 11.65, 11.71, 14.00, 14.25, 16.89, 16.95, 16.98, 20.47, 22.81, 26.25, 26.52, 29.47, 29.50, 29.56, 29.75, 29.78, 29.81, 29.82, 29.85, 30.40, 30.47, 31.79, 32.03, 32.04, 35.11, 35.18, 35.27, 40.01, 69.05, 73.52, 73.94, 74.09, 74.34, 74.38, 77.21, 104.93, 109.26, 109.57, 110.23, 110.61, 122.12, 122.31, 122.66, 125.36, 125.79, 126.128, 126.70, 127.11, 127.18, 128.08, 128.40, 128.49, 133.07, 133.92, 137.95, 141.84, 150.73, 150.87, 150.94, 151.31, 153.03, 155.74, 163.53, 167.74, 169.77; IR (UATR) ν (cm⁻¹): (CO) 1685; MALDI-TOF MS (M_w = 1764.29) m/z = 1764.26 [M]⁺; Anal. Calcd. for C₁₁₂H₁₇₄O₁₀N₆: C 76.25, H 9.94, N 4.76 Found: C 76.44, H 9.66, N 4.85.

1,6-Bis[2-amino-4-hexadiylureido-6-[(E,E,E)-4-<4-[4-(3,4,5-trisdodecyloxystyryl)-2,5-bis[(S)-2-methylbutoxy]styryl]-2,5-bis[(S)-2-methylbutoxy]styryl]phenyl-s-triazine} ((OPV₄UT)₂).

1.35 g (0.971 mmol) of OPV₄T was dissolved in 20 ml dry pyridine. Diisocyanatohexane (40.8 mg, 0.243 mmol) was added and the reaction mixture was refluxed for 8 h. After evaporation of the solvent, the mixture was flushed with toluene to remove the pyridine. Column chromatography (silica gel, CH₂Cl₂/EtOH 98/2) and size exclusion chromatography (2 times, bio-beads SX-1, THF) yielded pure (OPV₄UT)₂ (0.175 g, 14%). ¹H-NMR (300 MHz, CDCl₃): δ 0.9 (t, 18H), 1.02 (m, 24H), 1.1 (t, 24H), 1.3 (m, 108H), 1.5–1.7 (m, 28H), 1.8–2.0 (br, 12H), 3.5 (q, 4H), 3.95–4.06 (br, 28H), 5.46 (br, 2H), 6.75 (s, 4H), 7.1 (br, 16H), 7.4 (br, 8H), 8.0 (br, 4H), 9.5 (br, 2H), 9.90 (br, 2H), 10.24 (br, 2H); MALDI-TOF MS (M_w = 2950.41) m/z = 2949.09 [M]⁺, 2972.64 [M+Na]⁺; Anal. Calcd. for C₁₈₆H₂₉₀O₁₆N₁₂: C 74.89 H 9.97 N 5.57 Found: C 74.94 H 9.49, N 5.66.

N,N'',N'''-tris[3{3'-(E,E,E)-4-<4-[4-(3,4,5-trisdodecyloxystyryl)-2,5-bis[(S)-2-methylbutoxy]styryl]-2,5-bis[(S)-2-methylbutoxy]styryl}benzene-1,3,5-carboxamide (C₃-OPV₄)

To a solution of OPV amine³³⁵ (200 mg, 0.15 mmol) and triethylamine (21 μ l) in dry dichloromethane (10 mL) a solution of 1,3,5-benzenetricarboxylic acid chloride (11.8 mg, 0.045 mmol) was added in drops. The mixture was stirred for 6 hr and the solvent was evaporated. Purification by column chromatography (silica gel, CH₂Cl₂/pentane 3/1) and size exclusion chromatography (bio-beads SX-1, CH₂Cl₂) yielded pure C₃-OPV₄ (150 mg, 82 %). ¹H-NMR (400 MHz, CDCl₃): δ 0.89 (t, 27H), 1.03 (m, 36H), 1.13 (m, 36H), 1.2–1.4 (m, 72H), 1.5 (m, 18H), 1.68 (m, 24H), 1.84 (m, 18H), 2.0 (m, 12H), 3.85–3.95 (m, 24H), 3.95–4.05 (m, 18H), 6.75 (s, 6H), 7.02 (s, 3H), 7.06 (d, J

= 16.2 Hz, 3H), 7.11 (s, 3H), 7.15 (d, J = 15.8 Hz, 3H), 7.20 (d, J = 15.9 Hz, 3H), 7.24 (d, J = 15.8 Hz, 3H), 7.43 (d, J = 16.2 Hz, 3H), 7.50 (d, J = 15.9 Hz, 3H), 7.53 (s, 6H), 7.58 (d, J = 8.1 Hz, 6H), 7.73 (d, J = 8.1 Hz, 6H), 8.27 (s, 3H), 8.62 (s, 3H).

(*E,E,E,E*)-1,4-Bis[4-(cyanostyryl)-2,5-bis[(*S*)-2-methylbutoxy]styryl]-2,5-bis[(*S*)-2-methylbutoxy]benzene (18)

Diethyl(4-cyanobenzyl)phosphonate (336 mg, 1.4 mmol) was dissolved in 5 ml DMF and *t*-BuOK (210 mg, 1.87 mmol) was added. After 15 minutes, a solution of dialdehyde **11** (400 mg, 0.42 mmol) in 15 mL DMF was added dropwise to the reaction mixture. The solution was stirred for 4 h at room temperature. 100 mL HCl (6N) was added and the aqueous layer was extracted three times with chloroform. The collected organic layers were washed with HCl (3N) and dried over MgSO₄, filtered and evaporated to dryness. The crude mixture was purified by column chromatography (silica gel, CH₂Cl₂/pentane 1/1) and subsequently, size exclusion chromatography (bio-beads SX-1, CH₂Cl₂) was performed. After precipitation in methanol, 370 mg (84%) of **18** as a red solid was obtained. ¹H-NMR: δ 1.00, 1.10, 1.36, 1.65, 1.95, 3.78–3.94, 7.11, 7.17, 7.18, 7.56–7.64; MALDI-TOF MS (M_w =1053.5) m/z = 1052.7; IR (KBr): ν (cm⁻¹) = 2225.

(*E,E,E,E*)-1,4-Bis[4-(2,4-diamino-6-triazinephenyl)-2,5-bis[(*S*)-2-methylbutoxy]styryl]-2,5-bis[(*S*)-2-methylbutoxy]benzene OPV₅T₂.

In a round-bottom flask, 320 mg (0.31 mmol) **18** and 56.7 mg (0.67 mmol) dicyandiamide were dissolved in 12 ml 2-methoxyethanol. After adding 0.25 g (4.5 mmol) KOH, the solution was refluxed for 8 h. Much to our surprise the reaction mixture became turbid in the course of the reaction. After evaporation of the solvent, the obtained solid was redispersed into THF. The dispersion was centrifuged and further purification of the residue was hampered by the strong adhesion of the material to silica gel or aluminiumoxide. Despite this, purification was carried out on part of the residue by size exclusion chromatography (bio-beads SX-1, CH₂Cl₂). After precipitation in methanol OPV₅T₂ (25 mg, 8%) was obtained. Due to poor solubility, weak and broadened resonances in ¹H-NMR were observed at: δ 0.8–1.4, 1.6, 2.0, 3.75–4.0, 5.1, 6.9, 7.1–7.2, 7.4, 7.5–7.65, 8.35. MALDI-TOF MS (M_w =1221.65) m/z = 1221.69.

Small angle neutron scattering (SANS) experiments described in Chapter 3 were performed at the Paul Scherrer Institute (Villigen, Switzerland) using the small angle diffractometer SANS-II located at the SINQ. By using three instrumental settings with either λ = 1.9 nm and d = 6.0 m; λ = 4.55 nm and d = 1.0 m; λ = 4.55 nm and d = 5.0 m (where λ is the wavelength and d the sample-detector distance) the scattering vector $Q = 4\pi\sin(\theta/2)/\lambda$ covered a range between 0.01 and 4 nm⁻¹ (θ is the scattering angle). A mechanical selector used for monochromatization of the neutrons was set to a wavelength resolution of $\Delta\lambda/\lambda = 10\%$. SANS experiments described in Chapter 4 were performed at the Laboratoire Leon Brillouin (Saclay, France) using the small angle diffractometer PAXE located at the ORPHEE reactor. By using three instrumental settings with either λ = 1.2 nm and d = 5.04 m; λ = 0.6 nm and d = 5.04 m; λ = 0.5 nm and d = 5.04 m, Q covered a range between 0.03 and 3 nm⁻¹ and here $\Delta\lambda/\lambda = 8\%$. The solutions were measured in HELMA quartz cuvettes (path length 2 mm) and kept in a thermostatic sample holder (283 to 343 K), in both places.

The analysis of the data, from both places, follows the same approach. The scattering intensity from the solutions are described by $I(Q) = \phi V_n P(Q) S(Q)$ where $P(Q)$ represents the form factor of the aggregates and $S(Q)$ a contribution due to interparticle correlations. For the dilute solutions considered in the present case, it is assumed that $S(Q) \sim 1$ (indicating negligible correlation effects). The form factor contribution $P(Q)$ on the other hand was approximated by assuming an isotropic arrangement of cylindrical particles according to

$$P(Q) = \int_0^\infty (\Delta\rho)^2 \left(\frac{\sin(QH\cos\beta)}{QH\cos\beta} \right)^2 \left(\frac{2J_1(QR\sin\beta)}{QR\sin\beta} \right)^2 \sin\beta d\beta$$

with $2R$, the diameter of the columns and $2H$, their height. Provided that the aspect ratio of the aggregates is large, *i.e.* $H \gg R$, the form factor contribution should reveal a broad region in which $I(Q) \sim Q^{-1}$. Moreover, if the dimensions of the cross section of the aggregates are rather well-defined a secondary maximum at $Q \sim 4.49/R$ is expected at larger Q . The scattering patterns recorded were radially averaged and corrected with respect to the contributions arising from instrumental background, empty cells and solvent. Finally, the scattering data obtained as relative intensities were normalized to an absolute scale, using the incident beam flux as reference.

Differential scanning microcalorimetry (DSC) was performed on a VP-DSC from Health Scientific at a heating rate of 100 K/hr (minimum). Initial scans were discarded, five consecutive thereafter were averaged. Correction for solvent was carried out.

Cyclic voltammetry (CV) measurements were performed by others according to literature procedures.^{335,413a}

Scanning tunneling microscopy (STM) experiments were performed using a Discoverer scanning tunneling microscope (Topometrix Inc., Santa Barbara, CA) along with an external pulse/function generator (8111A, Hewlett Packard), with negative sample bias. Tips were electrochemically etched from a Pt/Ir wire (80%:20%, diameter 0.2 mm) in an aqueous 2N KOH/6N NaCN solution. STM images were acquired in the variable current mode under ambient conditions with the STM tip immersed in solution. In the STM images, the measured tunneling currents are converted into a gray scale: black (white) refers to a low (high) measured tunneling current. Experiments were repeated in several sessions using different tips to check for reproducibility and to avoid artifacts. Different settings for the tunneling current and the bias voltage were used, ranging from 0.3 nA to 1.0 nA and -0.1 V to -1.5 V, respectively. All STM images contain raw data and are not subjected to any manipulation or imaging processing. After registration of a monolayer structure, the underlying graphite surface was recorded at the same position by decreasing the bias voltage, serving as an *in-situ* calibration.

Atomic force microscopy (AFM) images were recorded under ambient conditions using a Digital Instrument Multimode Nanoscope IV or Dimension 3100 (equipped with a home-built phase detection system) operating in the tapping mode (TM) regime using micro-fabricated either silicon cantilever tips (NSG11a, 220–260 kHz, 11.5 N/m or NSG11b (NSG01), 150–175 kHz, 5.5 N/m or PPP-NCH, 300–330 kHz 42 N/m) or modified silicon cantilevers (NSG01/Pt, 155 kHz, 5.5 N/m or CSC12/W, 77 kHz, 1 N/m). Scanners 5962EV or 6007JVH were used with scan rates between 0.5 and 1.3 Hz and scan angles were mostly set to 90°, otherwise 0°. Integral and proportional gain were optimized. A_{sp}/A_o was adjusted to 0.9 unless stated otherwise. All AFM images shown are subjected to a first-order plane-fitting procedure to compensate for sample tilt. AFM samples were prepared by drop casting the solution under a solvent atmosphere on freshly cleaved HOPG. Drop casting the solutions occurred under a solvent atmosphere on freshly cleaved highly oriented pyrolytic graphite (HOPG) or muscovite mica, on glass slides, gold and silicon wafer with native oxide layer all cleaned by 15 min rinsing with isopropanol. For example, 3 μ L of a solution of 0.017 g/L **OPV4UT** in heptane was drop cast on a freshly cleaved HOPG surface. Subsequently, the solvent was allowed to evaporate under heptane atmosphere and ambient conditions. In approximately 25 s was needed for complete evaporation of the solvent. Devices were analyzed by AFM directly after device operation and spectroscopical studies.

Fluorescence microscopy (FM) images were obtained by focusing the output of an Argon ion laser ($\lambda = 457.9$ nm) by a 100x or 50x microscope objective to a 15 μ m spot on the sample surface and imaging the fluorescence emission ($\lambda = 564$ nm and 667 nm) on an intensified CCD camera, yielding a diffraction-limited picture (resolution $\sim \lambda/2 \sim 300$ nm for the 100x objective). To avoid photobleaching of the molecules a nitrogen flow was guided over the sample and the excitation power was kept as low as possible ($P < 800$ mWcm⁻²), yielding typical signals of $\ll 1$ photon/second. The colour-coded images are constructed from two consecutive measurements (capture time = 300 s, CCD intensifier gain = 150) with both excitation and detection polarizations either horizontal (0°) or vertical (90°) orientation with respect to the image. The colour coding corresponds to the intensity ratio of the two polarization orientations: $R = I_{\parallel}/I_{\perp}$ ranging from green ($R = 0$) to red ($R = \infty$) through yellow ($R = 1$). The orientation of the fibrils in the images is the true physical orientation of the fiber with respect to the polarizers and the image. High numerical aperture microscope objectives are known to have a considerable effect on the observed polarization degree.

Scanning electron microscopy (SEM) samples were dried, coated with a 2 nm Pt layer using a BALZERS BAE 121 Multicoating System and subsequently studied by a JEOL JSM T300 scanning electron microscope at 3 kV and a 1.2 nA probe current.

Contact angle measurements were carried on a Drop Shape Analysis DSA 10 apparatus from Krüss, using the sessile drop method at room temperature. Measurements were carried out within 30 s (2 records/s) after placing a water droplet on the film surface and were repeated 3 times on different positions of the same sample the following average contact angles were found for HOPG (80°), mica (20°), glass (30°), gold (90°), glass with 50 nm evaporated carbon (78°) and siliciumoxide wafer (70°).

Langmuir–Blodgett (LB) experiments were performed with a KSV-5000 LB instrument placed on an anti-vibration table in a controlled atmosphere room. 10 μ L of a chloroform solution (0.48 mM **OPV4b** and 0.27 mM **OPV5a**) was spreaded on the subphase (micro-filtered de-ionised water, resistivity = 18.2 M Ω cm) at 20°C. The Langmuir film compression (30 mm/min) started 30 minutes after spreading. The surface pressure was measured using the Wilhelmy plate method with plates made of filter paper. Brewster angle microscope experiments were carried out with a NFT BAM1 instrument, manufactured by Nano Film Technology, Göttingen, which was equipped with a 10 mV He–Ne laser (beam diameter of 0.68 mm, 632.8 nm).

1:2 binding model. Stepwise binding constants are defined as $K_1 = [HL]/[H][L]$, $K_2 = [HL_2]/[HL][L]$ and related through interaction parameter $\alpha = 4K_2/K_1$. If $\alpha = 1$; then independent binding sites, if $\alpha < 1$; then negative cooperativity, if $\alpha > 1$; then positive cooperativity. Overall binding constant $K_o = [HL_2]/[H][L]^2$; rewriting leads to $[H] = [H]_0 / (1 + K_1[L] + K_1K_2[L]^2)$

2:2 (1:2:1) binding model. Stepwise binding constants are defined as K_F (formation) = $[H_2L_2]/[H]^2[L]^2$, K_B (breaking) = $[H_2L]^2/[H_2L_2][L]^2$ and related through K (one ligand to one site) = $(K_F K_B)^{0.25}/16$. The concentration at which the sandwich is 50% dissociated is given by $c_{50} = (16K_F)^{-1/3}$.

Thermodynamics. The thermodynamic equilibrium constant (K) for any reaction can be expressed as a simple function of the standard Gibbs free energy change for the reaction as $K = \exp(-\Delta G/RT)$ with $\Delta G = -RT \ln K$ in which R is the gas constant and T is the temperature. The Gibbs function is defined as $\Delta G = \Delta H - T\Delta S$. Rearrangement leads to $\ln K = -\Delta H/RT + \Delta S/R$. By measuring K as a function of T , a plot of $\ln K$ versus $1/T$ can be constructed yielding a straight line with a slope of $-\Delta H/R$ and a y -intercept of $\Delta S/R$. This plot is called the Van 't Hoff plot and provides the enthalpy (ΔH) and entropy (ΔS) changes for a reaction. The Eyring equation describes the effect of the temperature on the rate of the reaction (k) by $k = (k_B T/h) \exp(-\Delta G^\ddagger/RT)$ where k_B is the Boltzmann constant and h is Planck's constant. ΔG^\ddagger is the free energy of activation and described by $\Delta G^\ddagger = \Delta H^\ddagger - T\Delta S^\ddagger$ and $\Delta G^\ddagger = -RT \ln K^\ddagger$. Filling this in the Eyring equation gives $k = (k_B T/h) \exp(-\Delta H^\ddagger/RT) \exp(\Delta S^\ddagger/R)$. By plotting $\ln(k/T)$ versus $1/T$ an Eyring plot is created providing the kinetic parameters ΔH^\ddagger from the slope ($\Delta H^\ddagger/R$) and ΔS^\ddagger from the y -intercept ($\Delta S^\ddagger/R + \ln(k_B/h)$). The activation energy E_{act} can be calculated from $E_{act} = \Delta H^\ddagger + RT$.

Dynamic oscillatory shear measurements were performed on a Rheometrics fluid spectrometer RFSII, with a plate-plate geometry (50 mm). Plate-plate distances were taken between 0.3 mm and 0.25 mm.

Photovoltaic cells were prepared onto a transparent ITO front electrode (140 nm) covered with a conducting layer of polyethylenedioxythiophene polystyrenesulfonate (PEDOT:PSS, filtered over a black rim FP 30/5,0 CN filter unit) using a Chemat Technology spin coater, model KW-4A: 500 rpm for 7 sec followed by 1500 rpm for 35 sec. The substrate was placed on a hot plate (100° C) for 1 minute to remove excessive water. On top of the PEDOT:PSS layer was spin coated at room temperature the mixture of (OPV₄UT)₂:PCBM in a ratio of 1:4 (by wt%). After the substrate is put on the chuck, the surface of the substrate is covered with solution, followed by spinning the samples at spin-rates of 500 rpm for 7 sec followed by 1500 rpm for 35 sec. After depositing LiF (1 nm) and an aluminium back electrode (100 nm) in vacuum the J/V characteristics were measured with a computer-controlled Keithley 2400 sourcemeter, sweeping in steps of 0.04 V with a delay of 0.10 s, in the dark and under white illumination. Four different device areas (0.1, 0.15, 0.33 and 1.0 cm²) were used for device preparation.

Field effect transistors were assembled on highly doped n⁺⁺-Si-gate electrode. An insulating thermal oxide layer was grown on one side of the substrate. A structure of interdigitated Au contacts, forming the source and drain electrodes, was realized on top of the insulating SiO₂ layer with a combination of photolithography and lift-off procedures. The films were spin cast under ambient conditions the organic solution via a two-step procedure employing a home-made chuck, which requires no vacuum, on a Chemat Technology spin coater model KW-4A placed in a laminar flowbox. First 7 seconds at 500 rpm followed by 60 seconds at 1500 rpm. The samples were stored in the dark before FET measurements. FET characterization was done using a HP4155B semiconductor parameter analyzer. A four-probe electrode pattern, with width and spacing of the electrodes was 200 nm, were made by electron-beam lithography. A double resist layer of poly (methyl methacrylate) (PMMA) was spun on silicon wafer with a 200 nm thick thermally grown oxide. The pattern was written with an electron beam pattern generator (EBPG5 HR 100kV FEG). Metal electrodes of Ti/Au₆₀Pd₄₀ were evaporated at liquid nitrogen temperature to ensure a smooth surface and lift-off was done in acetone. Isolated fibers were obtained by drop casting a 2 microliter organic solution under solvent saturated atmosphere.

X-ray photoelectron spectroscopy (XPS) samples were transported in a dry nitrogen atmosphere to a VG Ionex system equipped with a VG Clam II analyzer, and Mg/Al K α dual anode X-ray source. The XPS measurements were carried out using the Al anode. All C 1s peaks corresponding to hydrocarbon were calibrated at a binding energy of 285.0 eV to correct for the energy shift caused by charging. New bands appearing for the 4f-Au-band at 83.6 eV (84.4 eV in the pure Au) and the 3d-Pd-band at 334.7 eV (335.0 eV in pure Pd) in the surface of evaporated from an alloy of Au/Pd.

REFERENCES AND NOTES

- (1) Meijer, E. W.; Schenning, A. P. H. J. *Nature* **2002**, *419*, 353-4.
- (2) Tseng, G. Y.; Ellenbogen, J. C. *Science* **2001**, 1293-4.
- (3) Chen, J.; Reed, M. A.; Rawlett, A. M.; Tour, J. M. *Science* **1999**, 1550-2.
- (4) Gorman, C. B.; Carroll, R. L. *Angew. Chem. Int. Ed.* **2002**, 4378-400.
- (5) Sone, E. D.; Zubarev, E. R.; Stupp, S. I. *Angew. Chem. Int. Ed.* **2002**, *41*, 1705-9.
- (6) Duan, X.; Huang, Y.; Cui, Y.; Wang, J.; Lieber, C. M. *Nature* **2001**, 66-9.
- (7) Huang, Y.; Duan, X.; Cui, Y.; Lauhon, L. J.; Kim, K.-H.; Lieber, C. M. *Science* **2001**, 1313-7.
- (8) Postma, H. W. C.; Teepen, T.; Yao, Z.; Grifoni, M.; Dekker, C. *Science* **2001**, 76-9.
- (9) Bachtold, A.; Hadley, P.; Nakanishi, T.; Dekker, C. *Science* **2001**, 1317-20.
- (10) Kraft, A.; Grimsdale, A. C.; Holmes, A. B. *Angew. Chem. Int. Ed.* **1998**, *37*, 402-28.
- (11) Improved purity and a decreasing number of defects, such as tetrahedral carbon centers that interrupt conjugation, photodamage or end-groups, limit the conformational freedom of conjugated chains.
- (12) Becker, H.; Spreitzer, H.; Kreuder, W.; Kluge, E.; Schenk, H.; Parker, I.; Cao, Y. *Adv. Mater.* **2000**, *12*, 42-6.
- (13) Roex, H.; Adriaensens, P.; Vanderzande, D.; Gelan, J. *Macromolecules* **2003**, *36*, 5613-22.
- (14) Xing, K. Z.; Johansson, N.; Beamson, G.; Clark, D.T.; Brédas, J. L.; Salaneck, W. R. *Adv. Mater.* **1997**, *9*, 1027-31.
- (15) Sutherland, D. G. J.; Carlisle, J. A.; Elliker, P.; Fox, G.; Hagler, T. W.; Jimenez, I.; Lee, H. W.; Pakbaz, K.; Terminello, L. J.; Williams, S. C.; Himpel, F. J.; Shuh, D. K.; Tong, W. M.; Jia, J. J.; Callcott, T. A.; Ederer, D. L. *Appl. Phys. Lett.* **1996**, *68*, 2046-9.
- (16) Ma, L.; Wang, X.; Wang, B.; Wang, J.; Chen, J.; Huang, K.; Zhang, B.; Cao, Y.; Han, Z.; Qian, S.; Yao, S. *Chem. Phys.* **2002**, *285*, 85-92.
- (17) Kumar, P.; Mehta, A.; Dadmun, M. D.; Zheng, J.; Peyser, L.; Bartko, A. P.; Dickson, R. M.; Thundat, T.; Sumpter, B. G.; Noid, D. W.; Barnes, M. D. *J. Phys. Chem. B* **2003**, *107*, 6252-6.
- (18) Hu, D.; Yu, J.; Wong, K.; Bagchi, B.; Rossky, P. J.; Barbara, P. F. *Nature* **2000**, *405*, 1030-2.
- (19) McCullough, R. D. *Adv. Mater.* **1998**, *10*, 93-116.
- (20) Fischou, D. *Handbook of oligo- and polythiophenes*; Wiley-VCH: Weinheim, 1999.
- (21) Martens, H. C. F.; Blom, P. W. M.; Schoo, H. F. M. *Phys. Rev. B* **2000**, *61*, 7489-93.
- (22) Ruseckas, A.; Namdas, E. B.; Theander, M.; Svensson, M.; Yartsev, A.; Zigmantas, D.; Andersson, M. R.; Inganäs, O.; Sundström, V. *JPPA* **2001**, *144*, 3-12.
- (23) Jakubiak, R.; Collison, C. J.; Wan, W. C.; Rothberg, L. J.; Hsieh, B. R. *J. Phys. Chem. A* **1999**, *103*, 2394-8.
- (24) Kemerink, M.; van Duren, J. K. J.; Jonkheijm, P.; Pasveer, W. F.; Koenraad, P. M.; Janssen, R. A. J.; Salemink, H. W. M.; Wolter, J. H. *Nano Lett.* **2003**, *3*, 1191-6.
- (25) DiCesare, N.; Belletete, M.; Raymond, F.; Leclerc, M.; Durocher, G. *J. Phys. Chem. A* **1998**, *102*, 2700-7.
- (26) Raymond, F.; DiCesare, N.; Belletete, M.; Durocher, G.; Leclerc, M. *Adv. Mater.* **1998**, *10*, 599-602.
- (27) Krebs, F. C.; Jörgensen, M. *Macromolecules* **2003**, *36*, 4374-84.
- (28) Krebs, F. C.; Jörgensen, M. *Polymer Bulletin* **2003**, *51*, 127-34.
- (29) Grimsdale, A. C.; Leclère, P.; Lazzaroni, R.; MacKenzie, J. D.; Murphy, C.; Setayesh, S.; Silva, C.; Friend, R. H.; Müllen, K. *Adv. Funct. Mater.* **2002**, *12*, 729-33.
- (30) Winokur, M. J.; Chunwachirasiri, W. *J. Polym. Sci., Part B: Polym. Phys.* **2003**, *41*, 2630-48.
- (31) Schwartz, B. J. *Ann. Rev. Phys. Chem.* **2003**, *54*, 141-72.
- (32) Sirringhaus, H.; Wilson, R. J.; Friend, R. H.; Inbasekaran, M.; Wu, W.; Woo, E. P.; Grell, M.; Bradley, D. D. C. *Appl. Phys. Lett.* **2000**, *77*, 406-8.
- (33) Redecker, M.; Bradley, D. D. C.; Inbasekaran, M.; Woo, E. P. *Appl. Phys. Lett.* **1999**, *74*, 1400-3.
- (34) Brabec, C. J.; Winder, C.; Scharber, M. C.; Sariciftci, N. S.; Hummelen, J. C.; Svensson, M.; Andersson, M. R. *J. Chem Phys* **2001**, *115*, 7235-44.
- (35) Camaioni, N.; Ridolfi, G.; Casalbore-Miceli, G.; Possamai, G.; Maggini, M. *Adv. Mater.* **2002**, *14*, 1735-9.
- (36) Padinger, F.; Rittberger, R. S.; Sariciftci, N. S. *Adv. Funct. Mater.* **2003**, *13*, 85-8.
- (37) Liu, J.; F., G. T.; Yang, Y. *J. Appl. Phys.* **2002**, *91*, 1595-1600.
- (38) Heil, H.; Fimmberg, T.; von Malm, N.; Schmechel, R.; von Seggern, H. *J. Appl. Phys.* **2003**, *93*, 1636-41.
- (39) Teetsov, J.; Vanden Bout, D. A. *Langmuir* **2002**, *18*, 897-903.
- (40) Blatchford, J. W.; Gustafson, T. L.; Epstein, A. J.; Vanden Bout, D. A.; Kerimo, J.; Higgins, D. A.; Barbara, P. F.; Fu, D. K.; Swager, T. M.; MacDiarmid, A. G. *Phys. Rev. B* **1996**, *54*, R3683-R6.
- (41) Hassenkam, T.; Greve, D. R.; Björnholm, T. *Adv. Mater.* **2001**, *13*, 631-4.
- (42) Wei, P.-K.; Lin, Y.-F.; Fann, W.; Lee, Y.-Z.; Chen, S.-A. *Phys. Rev. B* **2001**, *63*, 045417/1-5.
- (43) Prins, L. J.; Reinhoudt, D. N.; Timmerman, P. *Angew. Chem. Int. Ed.* **2001**, *40*, 2383-426.
- (44) Sijbesma, R. P.; Meijer, E. W. *Chem. Commun.* **2003**, 5-16.
- (45) Martin, R. E.; Diederich, F. *Adv. Mater.* **1999**, *38*, 1350-77.
- (46) Tour, J. M. *Chem. Rev.* **1996**, *96*, 537-53.

- (47) Wöhrle, D.; Kreienhoop, L.; Schnurpfeil, G.; Elbe, J.; Tennigkeit, B.; Hiller, S.; Schlettwein, D. *J. Mater. Chem.* **1995**, *5*, 1819-29.
- (48) Garnier, F.; Yasser, A.; Hajlaoui, R.; Horowitz, G.; Deloffre, F.; Servet, B.; Ries, S.; Alnot, P. *J. Am. Chem. Soc.* **1993**, *115*, 8716-21.
- (49) Mushrush, M.; Facchetti, A.; Lefenfeld, M.; Katz, H. E.; Marks, T. J. *J. Am. Chem. Soc.* **2003**, *125*, 9414-23.
- (50) Geens, W.; Tsamouras, D.; Poortmans, J.; Hadziioannou, G. *Synth. Met.* **2001**, *122*, 191-2.
- (51) Melucci, M.; Gazzano, M.; Barbarella, G.; Cavallini, M.; Biscarini, F.; Maccagnani, P.; Ostojica, P. *J. Am. Chem. Soc.* **2003**, *125*, 10266-74.
- (52) van Hutten, P. F.; Wildeman, J.; Meetsma, A.; Hadziioannou, G. *J. Am. Chem. Soc.* **1999**, *121*, 5910-8.
- (53) Hong, Y.; Miller, L. L. *Chem. Mater.* **1995**, *7*, 1999-2000.
- (54) Kunugi, Y.; Miller, L. L.; Maki, T.; Canavesi, A. *Chem. Mater.* **1997**, *9*, 1061-2.
- (55) Jenekhe, S. A. *Macromolecules* **1990**, *23*, 2848-54.
- (56) Donat-Bouillud, A.; Mazerolle, L.; Gagnon, P.; Goldenberg, L.; Petty, M. C.; Leclerc, M. *Chem. Mater.* **1997**, *9*, 2815-21.
- (57) Henze, O.; Feast, W. J. *J. Mater. Chem.* **2003**, *13*, 1274-8.
- (58) Kilbinger, A. F. M.; Feast, W. J. *J. Mater. Chem.* **2000**, *10*, 1777-84.
- (59) Henze, O.; Fransen, M.; Jonkheijm, P.; Meijer, E. W.; Feast, W. J.; Schenning, A. P. H. J. *J. Polym. Sci., Part A: Polym. Chem.* **2003**, *41*, 1737-43.
- (60) Cacialli, F.; Feast, W. J.; Friend, R. H.; de Jong, M.; Lovenich, P. W.; Salaneck, W. R. *Polymer* **2002**, *43*, 3555-61.
- (61) Cacialli, F.; Friend, R. H.; Feast, W. J.; Lovenich, P. W. *Chem. Commun.* **2001**, 1778-9.
- (62) Neuteboom, E. E.; Meskers, S. C. J.; Meijer, E. W.; Janssen, R. A. J. *Macromolec. Chem. Phys.* **2004**, *205*, 217-22.
- (63) Neuteboom, E. E.; Janssen, R. A. J.; Meijer, E. W. *Synth. Met.* **2001**, *121*, 1283-4.
- (64) Li, W.; Maddux, T.; Yu, L. *Macromolecules* **1996**, *29*, 7329-34.
- (65) Hempenius, M. A.; Langeveld-Voss, B. M. W.; van Haare, J. A. E. H.; Janssen, R. A. J.; Sheiko, S. S.; Spatz, J. P.; Moeller, M.; Meijer, E. W. *J. Am. Chem. Soc.* **1998**, *120*, 2798-804.
- (66) Li, K.; Wang, Q. *Macromolecules* **2004**, *37*, 1172-4.
- (67) Kukula, H.; Ziener, U.; Schöps, M.; Godt, A. *Macromolecules* **1998**, *31*, 5160-3.
- (68) Chochos, C. L.; Tsolakis, P. K.; Gregoriou, V. G.; Kallitsis, J. K. *Macromolecules* **2004**, *37*, 2502-10.
- (69) Tew, G. N.; Li, L.; Stupp, S. I. *J. Am. Chem. Soc.* **1998**, *120*, 5601-2.
- (70) Tew, G. N.; Pralle, M. U.; Stupp, S. I. *J. Am. Chem. Soc.* **1999**, *121*, 9852-66.
- (71) Pralle, M. U.; Urayama, K.; Tew, G. N.; Neher, D.; Wegner, G.; Stupp, S. I. *Angew. Chem. Int. Ed.* **2000**, *39*, 1486-9.
- (72) Maddux, T.; Li, W.; Yu, L. *J. Am. Chem. Soc.* **1997**, *119*, 844-5.
- (73) Wang, H.; You, W.; Jiang, P.; Yu, L.; Wang, H. H. *Chem. Eur. J.* **2004**, *10*, 986-93.
- (74) Wang, H. H.; Wang, H.; Yu, L.; Thiyagarajan, P. *Polym. Mater. Sci. Eng.* **2000**, *85*, 20.
- (75) Urban, V.; Wang, H. H.; Thiyagarajan, P.; Littrell, K. C.; Wang, H. B.; Yu, L. *J. Appl. Cryst.* **2000**, *33*, 645-9.
- (76) Li, W.; Wang, H.; Yu, L.; Morkved, T. L.; Jaeger, H. M. *Macromolecules* **1999**, *32*, 3034-44.
- (77) Nawa, K.; Imae, I.; Noma, N.; Shirota, Y. *Macromolecules* **1995**, *28*, 723-9.
- (78) Imae, I.; Nawa, K.; Ohstedo, Y.; Noma, N.; Shirota, Y. *Macromolecules* **1997**, *30*, 380-6.
- (79) Ohstedo, Y.; Imae, I.; Shirota, Y. *J. Polym. Sci., Part B: Polym. Phys.* **2003**, *41*, 2471-84.
- (80) Shirota, Y.; Jeon, I.-R.; Noma, N. *Synth. Met.* **1993**, *55-57*, 803-6.
- (81) Mastrolilli, P.; Nobile, C. F.; Grisorio, R.; Rizzutti, A.; Suranna, G. P.; Acierno, D.; Amendola, E.; Iannelli, P. *Macromolecules* **2004**, *125*, 8434-37.
- (82) Schenning, A. P. H. J.; Fransen, M.; van Duren, J. K. J.; van Hal, P. A.; Janssen, R. A. J.; Meijer, E. W. *Macromolec. Rapid Commun.* **2002**, *23*, 271-5.
- (83) Hayakawa, T.; Horiuchi, S. *Angew. Chem. Int. Ed.* **2003**, *42*, 2285-9.
- (84) Funahashi, M.; Hanna, J. *Appl. Phys. Lett.* **2000**, *76*, 2574-6.
- (85) Katz, H. E.; Laquindanum, J. G.; Lovinger, A. J. *Chem. Mater.* **1998**, *10*, 633.
- (86) Ponomarenko, S.; Kirchmeyer, S. J. *Mater. Chem.* **2003**, *13*, 197-202.
- (87) Azumi, R.; Gotz, G.; Bäuerle, P. *Synth. Met.* **1999**, *101*, 544-5.
- (88) Lovinger, A. J.; Katz, H. E.; Dodabalapur, A. *Chem. Mater.* **1998**, *10*, 3275-7.
- (89) Garnier, F.; Hajlaoui, R.; El Kassami, A.; Horowitz, G.; Laigre, L.; Porzio, W.; Armanini, M.; Provasoli, F. *Chem. Mater.* **1998**, *10*, 3334-9.
- (90) Gray, G. W. *J. Chem. Soc.* **1955**, 236.
- (91) Hildebrandt, F.; Schröter, J. A.; Tschierske, C.; Festag, R.; Kleppinger, R.; Wendorff, J. H. *Angew. Chem. Int. Ed.* **1995**, *34*, 1631-3.
- (92) Hildebrandt, F.; Schröter, J. A.; Tschierske, C.; Festag, R.; Wittenberg, M.; Wendorff, J. H. *Adv. Mater.* **1997**, *9*, 564.
- (93) Liu, P.; Nakano, H.; Shirota, Y. *Liq. Cryst.* **2001**, *28*, 581-9.
- (94) Schenning, A. P. H. J.; El-Ghayoury, A.; Peeters, E.; Meijer, E. W. *Synth. Met.* **2001**, *121*, 1253-6.

- (95) Gill, R. E.; Meetsma, A.; Hadziioannou, G. *Adv. Mater.* **1996**, *8*, 212-14.
- (96) Eckert, J. F.; Nicoud, J. F.; Guillon, D.; Nierengarten, J. F. *Tet. Lett.* **2000**, *41*, 6411-4.
- (97) Eckert, J.-F.; Maciejczuk, U.; Guillon, D.; Nierengarten, J.-F. *Chem. Commun.* **2001**, 1278-9.
- (98) Chandrasekhar, S.; Sadashiva, B. K.; Suresh, K. A. *Pramana* **1977**, *9*, 471-80.
- (99) Malthete, J.; Destrade, C.; Tinh, N. H.; Jacques, J. *Mol. Crystallogr. Liq. Crystallogr. Lett.* **1981**, *64*, 233-8.
- (100) Destrade, C.; Nguyen, H. T.; Gasparoux, H.; Malthete, J.; Levelut, A. M. *Mol. Cryst. Liq. Cryst.* **1981**, *71*, 111-4.
- (101) Malthete, J.; Jacques, J.; Tinh, N. H.; Destrade, C. *Nature* **1982**, *298*, 46-8.
- (102) Adam, D.; Schuhmacher, P.; Simmerer, J.; Haeussling, L.; Siemensmeyer, K.; Etzbach, K. H.; Ringsdorf, H.; Haarer, D. *Nature* **1994**, *371*, 141-3.
- (103) Van de Craats, A. M.; Warman, J. M.; De Haas, M. P.; Adam, D.; Simmerer, J.; Haarer, D.; Schuhmacher, P. *Adv. Mater.* **1996**, *8*, 823-6.
- (104) Boden, N.; Bushby, R. J.; Cooke, G.; Lozman, O. R.; Lu, Z. *J. Am. Chem. Soc.* **2001**, *123*, 7915-6.
- (105) Pecchia, A.; Lozman, O. R.; Movaghar, B.; Boden, N.; Bushby, R. J.; Donovan, K. J.; Kreouzis, T. *Phys. Rev. B* **2002**, *65*, 104204/1-10.
- (106) Wegewijs, B. R.; Siebbeles, L. D. A.; Boden, N.; Bushby, R. J.; Movaghar, B.; Lozman, O. R.; Liu, Q.; Pecchia, A.; Mason, L. A. *Phys. Rev. B* **2002**, *65*, 245112/1-8.
- (107) Arikainen, E. O.; Boden, N.; Bushby, R. J.; Clements, J.; Movaghar, B.; Wood, A. *J. Mater. Chem.* **1995**, *5*, 2161-5.
- (108) Tang, B. Y.; Ge, J. J.; Zhang, A.; Calhoun, B.; Chu, P.; Wang, H.; Shen, Z.; Harris, F. W.; Cheng, S. Z. D. *Chem. Mater.* **2001**, *13*, 78-86.
- (109) Markovitsi, D.; Germain, A.; Millie, P.; Lecuyer, P.; Gallos, L.; Argyrakis, P.; Bengs, H.; Ringsdorf, H. *J. Phys. Chem.* **1995**, *99*, 1005-17.
- (110) Senthilkumar, K.; Grozema, F. C.; Bickelhaupt, F. M.; Siebbeles, L. D. A. *J. Chem. Phys.* **2003**, *119*, 9809-17.
- (111) Bengs, H.; Closs, F.; Frey, T.; Funhoff, D.; Ringsdorf, H.; Siemensmeyer, K. *Liq. Cryst.* **1993**, *15*, 565-74.
- (112) Van de Craats, A. M.; Warman, J. M.; Müllen, K.; Geerts, Y.; Brand, J. D. *Adv. Mater.* **1998**, *10*, 36-8.
- (113) van de Craats, A. M.; Warman, J. M. *Adv. Mater.* **2001**, *13*, 130-3.
- (114) Van De Craats, A. M.; Warman, J. M.; Fechtenkötter, A.; Brand, J. D.; Harbison, M. A.; Müllen, K. *Adv. Mater.* **1999**, *11*, 1469-72.
- (115) Lemaur, V.; da Silva Filho, D. A.; Coropceanu, V.; Lehmann, M.; Geerts, Y.; Piris, J.; Debije, M. G.; van de Craats, A. M.; Senthilkumar, K.; Siebbeles, L. D. A.; Warman, J. M.; Brédas, J.-L.; Cornil, J. *J. Am. Chem. Soc.* **2004**, *125*, 12020-21.
- (116) Berresheim, A. J.; Müller, M.; Müllen, K. *Chem. Rev.* **1999**, *99*, 1747-85.
- (117) Herwig, P.; Kayser, C. W.; Müllen, K.; Spiess, H. W. *Adv. Mater.* **1996**, *8*, 510-3.
- (118) Fechtenkötter, A.; Tchebotareva, N.; Watson, M.; Müllen, K. *Tetrahedron* **2001**, *57*, 3769-83.
- (119) Fechtenkötter, A.; Saalwächter, K.; Harbison, M. A.; Müllen, K.; Spiess, H. W. *Angew. Chem. Int. Ed.* **1999**, *38*, 3039-42.
- (120) Liu, C.-y.; Bard, A. J. *Chem. Mater.* **2000**, *12*, 2353-63.
- (121) van de Craats, A. M.; Stutzmann, N.; Bunk, O.; Nielsen, M. M.; Watson, M.; Müllen, K.; Chanzy, H. D.; Sirringhaus, H.; Friend, R. H. *Adv. Mater.* **2003**, *15*, 495-9.
- (122) Piris, J.; Debije, M. G.; Stutzmann, N.; van de Craats, A. M.; Watson, M. D.; Müllen, K.; Warman, J. M. *Adv. Mater.* **2003**, *15*, 1736-40.
- (123) Tracz, A.; Jeszka, J. K.; Watson, M. D.; Pisula, W.; Müllen, K.; Pakula, T. *J. Am. Chem. Soc.* **2003**, *125*, 1682-3.
- (124) Fleming, A. J.; Coleman, J. N.; Dalton, A. B.; Fechtenkötter, A.; Watson, M. D.; Müllen, K.; Byrne, H. J.; Blau, W. J. *J. Phys. Chem. B* **2003**, *107*, 37-43.
- (125) Wu, J.; Watson, M. D.; Zhang, L.; Wang, Z.; Müllen, K. *J. Am. Chem. Soc.* **2004**, *126*, 177-86.
- (126) Schlichting, P.; Rohr, U.; Müllen, K. *J. Mater. Chem.* **1998**, *8*, 2651-5.
- (127) Rohr, U.; Schlichting, P.; Bohm, A.; Gross, M.; Meerholz, K.; Brauchle, C.; Müllen, K. *Angew. Chem. Int. Ed.* **1998**, *37*, 1434-7.
- (128) Göltner, C.; Pressner, D.; Müllen, K.; Spiess, H. W. *Angew. Chem. Int. Ed.* **1993**, *32*, 1660-2.
- (129) Pressner, D.; Goeltner, C.; Spiess, H. W.; Müllen, K. *Acta Polym.* **1994**, *45*, 188-95.
- (130) Muller, G. R. J.; Meiners, C.; Enkelmann, V.; Geerts, Y.; Müllen, K. *J. Mater. Chem.* **1998**, *8*, 61-4.
- (131) Rohr, U.; Kohl, C.; Müllen, K.; van de Craats, A.; Warman, J. *J. Mater. Chem.* **2001**, *11*, 1789-99.
- (132) Liu, S.-G.; Sui, G.; Cormier, R. A.; Leblanc, R. M.; Gregg, B. A. *J. Phys. Chem. B* **2002**, *106*, 1307-15.
- (133) Cormier, R. A.; Gregg, B. A. *Chem. Mater.* **1998**, *10*, 1309-19.
- (134) Würthner, F.; Thalacker, C.; Diele, S.; Tschierske, C. *Chem. Eur. J.* **2001**, *7*, 2245-53.
- (135) Sautter, A.; Thalacker, C.; Würthner, F. *Angew. Chem. Int. Ed.* **2001**, *40*, 4425-8.
- (136) Struijk, C. W.; Sieval, A. B.; Dakhorst, J. E. J.; van Dijk, M.; Kimkes, P.; Koehorst, R. B. M.; Donker, H.; Schaafsma, T. J.; Picken, S. J.; van de Craats, A. M.; Warman, J. M.; Zuilhof, H.; Sudholter, E. J. *J. Am. Chem. Soc.* **2000**, *122*, 11057-66.
- (137) Katz, H. E.; Lovinger, A. J.; Johnson, J.; Kloc, C.; Siegrist, T.; Li, W.; Lin, Y.-Y.; Dodabalapur, A. *Nature* **2000**, *404*, 478-80.

- (138) Guan, Y.; Zakrevskyy, Y.; Stumpe, J.; Antonietti, M.; Faul, C. F. J. *Chem. Commun.* **2003**, 894-5.
- (139) Facchetti, A.; Mushrush, M.; Katz, H. E.; Marks, T. J. *Adv. Mater.* **2003**, *15*, 33-8.
- (140) Facchetti, A.; Yoon, M.-H.; Stern, C. L.; Katz, H. E.; Marks, T. J. *Angew. Chem. Int. Ed.* **2003**, *42*, 3900-3.
- (141) Lee, C.-H.; Yamamoto, T. *Mol. Cryst. Liq. Cryst. Sci. Techn., Mol. Cryst. Liq. Cryst.* **2002**, *378*, 13-21.
- (142) Lee, C. H.; Yamamoto, T. *Tet. Lett.* **2001**, *42*, 3993-6.
- (143) Attias, A.-J.; Cavalli, C.; Donnio, B.; Guillon, D.; Hapiot, P.; Malthete, J. *Chem. Mater.* **2002**, *14*, 375-84.
- (144) Pieterse, K.; Lauritsen, A.; Schenning, A. P. H. J.; Vekemans, J. A. J. M.; Meijer, E. W. *Chem. Eur. J.* **2003**, *9*, 5597-604.
- (145) Bock, H.; Babeau, A.; Seguy, I.; Jolinat, P.; Destruel, P. *ChemPhysChem* **2002**, *3*, 532-5.
- (146) Kestemont, G.; de Halleux, V.; Lehmann, M.; Ivanov, D. A.; Watson, M.; Geerts, Y. H. *Chem. Commun.* **2001**, 2074-5.
- (147) Pieterse, K.; van Hal, P. A.; Kleppinger, R.; Vekemans, J. A. J. M.; Janssen, R. A. J.; Meijer, E. W. *Chem. Mater.* **2001**, *13*, 2675-9.
- (148) Kumar, S.; Wachtel, E. J.; Keinan, E. *J. Org. Chem.* **1993**, *58*, 3821-7.
- (149) Boden, N.; Borner, R. C.; Bushby, R. J.; Clements, J. J. *Am. Chem. Soc.* **1994**, *116*, 10807-8.
- (150) Kumar, S.; Shankar Rao, D. S.; Krishna Prasad, S. *J. Mater. Chem.* **1999**, *9*, 2751-4.
- (151) Gearba, R. I.; Lehmann, M.; Levin, J.; Ivanov, D. A.; Koch, M. H. J.; Barbera, J.; Debije, M. G.; Piris, J.; Geerts, Y. H. *Adv. Mater.* **2003**, *15*, 1614-8.
- (152) Chuard, T.; Deschenaux, R. *Helv. Chim. Acta* **1996**, *79*, 736-41.
- (153) Chuard, T.; Deschenaux, R.; Hirsch, A.; Schoenberger, H. *Chem. Commun.* **1999**, 2103-4.
- (154) Tirelli, N.; Cardullo, F.; Habicher, T.; Suter, U. W.; Diederich, F. *J. Chem. Soc. Perkin Trans. 2* **2000**, *2*, 193-8.
- (155) Felder, D.; Heinrich, B.; Guillon, D.; Nicoud, J. F.; Nierengarten, J. F. *Eur. J. Org. Chem.* **2000**, *6*, 3501-7.
- (156) Dardel, S.; Guillon, D.; Heinrich, B.; Deschenaux, R. *J. Mater. Chem.* **2001**, *11*, 2814-31.
- (157) Chuard, T.; Deschenaux, R. *J. Mater. Chem.* **2002**, *12*, 1944-51.
- (158) Terech, P.; Weiss, R. G. *Chem. Rev.* **1997**, *97*, 3133-59.
- (159) Van Esch, J. H.; Feringa, B. L. *Angew. Chem. Int. Ed.* **2000**, *39*, 2263-6.
- (160) Ito, S.; Wehmeier, M.; Brand, J. D.; Kubel, C.; Epsch, R.; Rabe, J. P.; Müllen, K. *Chem. Eur. J.* **2000**, *6*, 4327-42.
- (161) Grimsdale, A. C.; Bauer, R.; Weil, T.; Tchebotareva, N.; Wu, J. S.; Watson, M.; Müllen, K. *Synthesis* **2002**, 1229.
- (162) Reitzel, N.; Hassenkam, T.; Balashev, K.; Jensen, T. R.; Howes, P. B.; Kjaer, K.; Fechtenkötter, A.; Tchebotareva, N.; Ito, S.; Müllen, K.; Bjørnholm, T. *Chem. Eur. J.* **2001**, *7*, 4894-4901.
- (163) Kubowicz, S.; Pietsch, U.; Watson, M. D.; Tchebotareva, N.; Müllen, K.; Thünemann, A. F. *Langmuir* **2003**, *19*, 5036-41.
- (164) Thünemann, A. F.; Ruppelt, D.; Ito, S.; Müllen, K. *J. Mater. Chem.* **1999**, *9*, 1055-7.
- (165) Thünemann, A. F.; Ruppelt, D.; Burger, C.; Müllen, K. *J. Mater. Chem.* **2000**, *10*, 1325-9.
- (166) Faul, C. F. J.; Antonietti, M. *Adv. Mater.* **2003**, *15*, 673-83.
- (167) Mizoshita, N.; Monobe, H.; Inoue, M.; Ukon, M.; Watanabe, T.; Shimizu, Y.; Hanabusa, K.; Kato, T. *Chem. Commun.* **2002**, 428-9.
- (168) Thünemann, A. F.; Kubowicz, S.; Burger, C.; Watson, M. D.; Tchebotareva, N.; Müllen, K. *J. Am. Chem. Soc.* **2003**, *125*, 352-6.
- (169) Desvergne, J.-P.; Brotin, T.; Meerschaut, D.; Clavier, G.; Placin, F.; Pozzo, J.-L.; Bouas-Laurent, H. *New J. Chem.* **2004**, *28*, 234-43.
- (170) Terech, P.; Meerschaut, D.; Desvergne, J. P.; Colomes, M.; Bouas-Laurent, H. *J. Col. Interf. Sci.* **2003**, *261*, 441-50.
- (171) Placin, F.; Desvergne, J.-P.; Belin, C.; Buffeteau, T.; Desbat, B.; Ducasse, L.; Lassegues, J.-C. *Langmuir* **2003**, *19*, 4563-72.
- (172) Kato, T.; Kutsuna, T.; Yabuuchi, K.; Mizoshita, N. *Langmuir* **2002**, *18*, 7086-8.
- (173) Pozzo, J.-L.; Desvergne, J.-P.; Clavier, G. M.; Bouas-Laurent, H.; Jones, P. G.; Perlstein, J. J. *J. Chem. Soc., Perkin Trans. 2* **2001**, 824-6.
- (174) Placin, F.; Desvergne, J. P.; Lassegues, J. C. *Chem. Mater.* **2001**, *13*, 117-21.
- (175) Terech, P.; Bouas-Laurent, H.; Desvergne, J.-P. *J. Coll. Int. Sci.* **1995**, *174*, 258-63.
- (176) Brotin, T.; Utermohlen, R.; Fages, F.; Bouas-Laurent, H.; Desvergne, J. P. *J. Chem. Soc., Chem. Commun.* **1991**, 416-18.
- (177) Kawano, S.-I.; Tamaru, S.-I.; Fujita, N.; Shinkai, S. *Chem. Eur. J.* **2004**, *10*, 343-51.
- (178) Shirakawa, M.; Kawano, S.; Fujita, N.; Sada, K.; Shinkai, S. *J. Org. Chem.* **2003**, *68*, 5037-44.
- (179) Hatano, T.; Takeuchi, M.; Ikeda, A.; Shinkai, S. *Chem. Lett.* **2003**, *32*, 314-5.
- (180) Hatano, T.; Takeuchi, M.; Ikeda, A.; Shinkai, S. *Org. Lett.* **2003**, *5*, 1395-8.
- (181) Tamaru, S.-I.; Uchino, S.-Y.; Takeuchi, M.; Ikeda, M.; Hatano, T.; Shinkai, S. *Tet. Lett.* **2002**, *43*, 3751-5.
- (182) Tamaru, S.-I.; Takeuchi, M.; Sano, M.; Shinkai, S. *Angew. Chem. Int. Ed.* **2002**, *41*, 853-6.
- (183) Tamaru, S.-I.; Nakamura, M.; Takeuchi, M.; Shinkai, S. *Org. Lett.* **2001**, *3*, 3631-4.
- (184) Arimori, S.; Takeuchi, M.; Shinkai, S. *Supramolec. Sci.* **1998**, *5*, 1-8.

- (185) de Witte, P. A. J.; Castriciano, M.; Cornelissen, J. J. L. M.; Scolaro, L. M.; Nolte, R. J. M.; Rowan, A. E. *Chem. Eur. J.* **2003**, *9*, 1775-81.
- (186) Lensen, M. C.; Castriciano, M.; Coumans, R. G. E.; Foekema, J.; Rowan, A. E.; Scolaro, L. M.; Nolte, R. J. M. *Tet. Lett.* **2002**, *43*, 9351-5.
- (187) Samori, P.; Engelkamp, H.; de Witte, P.; Rowan, A. E.; Nolte, R. J. M.; Rabe, J. P. *Angew. Chem. Int. Ed.* **2001**, *40*, 2348-50.
- (188) van der Boom, T.; Hayes, R. T.; Zhao, Y.; Bushard, P. J.; Weiss, E. A.; Wasielewski, M. R. *J. Am. Chem. Soc.* **2002**, *124*, 9582-90.
- (189) Lensen M. C.; Takazawa, K.; Elemans J. A. A. W.; Jeukens C. R. L. P. N.; Christianen P. C. M.; Maan J. C.; Rowan A. E.; Nolte R. J. M. *Chem. Eur. J.* **2004**, *10*, 831-9.
- (190) De La Escosura, A.; Martinez-Diaz, M. V.; Thordarson, P.; Rowan, A. E.; Nolte, R. J. M.; Torres, T. *J. Am. Chem. Soc.* **2003**, *125*, 12300-8.
- (191) Boamfa, M. I.; Christianen, P. C. M.; Maan, J. C.; Engelkamp, H.; Nolte, R. J. M. *Physica B* **2001**, *294&295*, 343-6.
- (192) Engelkamp, H.; Middelbeek, S.; Nolte, R. J. M. *Science* **1999**, *284*, 785-8.
- (193) van Nostrum, C. F.; Picken, S. J.; Schouten, A.-J.; Nolte, R. J. M. *J. Am. Chem. Soc.* **1995**, *117*, 9957-65.
- (194) Blanzat, B.; Barthou, C.; Tercier, N.; Andre, J. J.; Simon, J. *J. Am. Chem. Soc.* **1987**, *109*, 6193-4.
- (195) Zlatkin, A.; Yudin, S.; Simon, J.; Hanack, M.; Lehman, H. *Adv. Mater. Opt. and Electr.* **1995**, *5*, 259-63.
- (196) Engel, M. K.; Bassoul, P.; Bosio, L.; Lehmann, H.; Hanack, M.; Simon, J. *Liq. Cryst.* **1993**, *15*, 709-22.
- (197) Sirlin, C.; Bosio, L.; Simon, J. *J. Chem. Soc., Chem. Commun.* **1988**, 236-7.
- (198) Sirlin, C.; Bosio, L.; Simon, J.; Ahsen, V.; Yilmazer, E.; Bekaroglu, O. *Chem. Phys. Lett.* **1987**, *139*, 362-4.
- (199) Würthner, F.; Yao, S.; Beginn, U. *Angew. Chem. Int. Ed.* **2003**, *42*, 3247-50.
- (200) von Berlepsch, H.; Boettcher, C.; Daehne, L. *J. Phys. Chem. B* **2000**, *104*, 8792-9.
- (201) Würthner, F.; Yao, S.; Beginn, U. *Angew. Chem. Int. Ed.* **2003**, *42*, 3247-50.
- (202) Würthner, F.; Yao, S. *J. Org. Chem.* **2003**, *68*, 8943-9.
- (203) Wortmann, R.; Rosch, U.; Redi-Abshiro, M.; Würthner, F. *Angew. Chem. Int. Ed.* **2003**, *42*, 2080-3.
- (204) Würthner, F.; Yao, S.; Debaerdemaeker, T.; Wortmann, R. *J. Am. Chem. Soc.* **2002**, *124*, 9431-47.
- (205) Würthner, F.; Yao, S.; Schilling, J.; Wortmann, R.; Redi-Abshiro, M.; Mecher, E.; Gallego-Gomez, F.; Meerholz, K. *J. Am. Chem. Soc.* **2001**, *123*, 2810-24.
- (206) Würthner, F.; Yao, S.; Heise, B.; Tschierske, C. *Chem. Commun.* **2001**, 2260-1.
- (207) Prins, L. J.; Thalacker, C.; Würthner, F.; Timmerman, P.; Reinhoudt, D. N. *Proc. Natl. Acad. Sci. USA* **2001**, *98*, 10042-5.
- (208) Würthner, F.; Yao, S. *Angew. Chem. Int. Ed.* **2000**, *39*, 1978-81.
- (209) Babu, P.; Sangeetha, N. M.; Vijaykumar, P.; Maitra, U.; Rissanen, K.; Raju, A. R. *Chem. Eur. J.* **2003**, *9*, 1922-32.
- (210) Geiger, C.; Stanescu, M.; Chen, L.; Whitten, D. G. *Langmuir* **1999**, *15*, 2241-5.
- (211) Chen, H.; Farahat, M. S.; Law, K.-Y.; Whitten, D. G. *J. Am. Chem. Soc.* **1996**, *118*, 2584-94.
- (212) Chen, H.; Law, K.-Y.; Perlstein, J.; Whitten, D. G. *J. Am. Chem. Soc.* **1995**, *117*, 7257-8.
- (213) Wang, R.; Geiger, C.; Chen, L.; Swanson, B.; Whitten, D. G. *J. Am. Chem. Soc.* **2000**, *122*, 2399-400.
- (214) Whitten, D. G.; Chen, L.; Geiger, H. C.; Perlstein, J.; Song, X. *J. Phys. Chem. B* **1998**, *102*, 10098-111.
- (215) Ajayaghosh, A.; George, S. J. *J. Am. Chem. Soc.* **2001**, *123*, 5148-9.
- (216) George, S. J.; Ajayaghosh, A.; Jonkheijm, P.; Schenning, A. P. H. J.; Meijer, E. W. *Angew. Chem. Int. Ed.* **2004**, *43*, 3422-5.
- (217) Schoonbeek, F. S.; Van Esch, J. H.; Wegewijs, B.; Rep, D. B. A.; De Haas, M. P.; Klapwijk, T. M.; Kellogg, R. M.; Feringa, B. L. *Angew. Chem. Int. Ed.* **1999**, *38*, 1393-7.
- (218) Rep, D. B. A.; Roelfsema, R.; Van Esch, J. H.; Schoonbeek, F. S.; Kellogg, R. M.; Feringa, B. L.; Palstra, T. T. M.; Klapwijk, T. M. *Adv. Mater.* **2000**, *12*, 563-6.
- (219) Gesquière, A.; Abdel-Mottaleb, M. M. S.; De Feyter, S.; De Schryver, F. C.; Schoonbeek, F.; van Esch, J.; Kellogg, R. M.; Feringa, B. L.; Calderone, A.; Lazzaroni, R.; Brédas, J. L. *Langmuir* **2000**, *16*, 10385-91.
- (220) Gesquière, A.; De Feyter, S.; De Schryver, F. C.; Schoonbeek, F.; van Esch, J.; Kellogg, R. M.; Feringa, B. L. *Nano Lett.* **2001**, *1*, 201-6.
- (221) Liu, Y.; Li, Y.; Jiang, L.; Gan, H.; Liu, H.; Li, Y.; Zhuang, J.; Lu, F.; Zhu, D. *J. Org. Chem.* **2004**, *69*, 9049-54.
- (222) Varghese, R.; George, S. J.; Ajayaghosh, A. *Chem. Commun.* **2005**, 593-5.
- (223) El-Ghayoury, A.; Schenning, A. P. H. J.; Meijer, E. W. *J. Polym. Sci., Part A: Polym. Chem.* **2002**, *40*, 4020-3.
- (224) Dobrawa, R.; Würthner, F. *Chem. Commun.* **2002**, 1878-9.
- (225) Dobrawa, R.; Lysetska, M.; Ballester, P.; Grüne, M.; Würthner, F. *Macromolecules* **2005**, *38*, 1315 - 25.
- (226) Havinga, E. E.; Rotte, I. *Mol. Cryst. Liq. Cryst.* **1992**, *218*, 1-3.
- (227) DiCesare, N.; Belletete, M.; Marrano, C.; Leclerc, M.; Durocher, G. *J. Phys. Chem. A* **1999**, *103*, 795-802.
- (228) Martin, S. J.; Cadby, A. J.; Lane, P. A.; Bradley, D. D. C. *Synth. Met.* **1999**, *101*, 665-6.
- (229) Pope, M.; Swenberg, C. E. *Electronic Processes in Organic Crystals*; Clarendon Press: Oxford, 1982.
- (230) Davydov, A. S. *Theory of Molecular Excitons*; McGraw-Hill: New York, 1962.
- (231) Malenfant, P. R. L.; Groenendaal, L.; Fréchet, J. M. J. *J. Am. Chem. Soc.* **1998**, *120*, 10990-1.

- (232) Jestin, I.; Levillain, E.; Roncali, J. *Chem. Commun.* **1998**, 2655-6.
- (233) Miller, L. L.; Zinger, B.; Schlechte, J. S. *Chem. Mater.* **1999**, *11*, 2313-5.
- (234) Miller, L. L.; Schlechte, J. S.; Zinger, B.; Burrell, C. J. *Chem. Mater.* **2002**, *14*, 5081-9.
- (235) Apperloo, J. J.; Janssen, R. A. J.; Malenfant, P. R. L.; Fréchet, J. M. J. *Macromolecules* **2000**, *33*, 7038-43.
- (236) Apperloo, J. J.; Malenfant, P. R. L.; Fréchet, J. M. J.; Janssen, R. A. J. *Synth. Met.* **2001**, *121*, 1259-60.
- (237) Apperloo, J. J.; Janssen, R. A. J.; Malenfant, P. R. L.; Fréchet, J. M. J. *J. Am. Chem. Soc.* **2001**, *123*, 6916-24.
- (238) Lee, M.; Jeong, Y.-S.; Cho, B.-K.; Oh, N.-K.; Zin, W.-C. *Chem. Eur. J.* **2002**, *8*, 876-83.
- (239) Locklin, J.; Youk, J. H.; Xia, C.; Park, M.-K.; Fan, X.; Advincula, R. C. *Langmuir* **2002**, *18*, 877-83.
- (240) Xia, C.; Locklin, J.; Youk, J. H.; Fulghum, T.; Advincula, R. C. *Langmuir* **2002**, *18*, 955-7.
- (241) Sandberg, H.; Henze, O.; Kilbinger, A. F. M.; Sirringhaus, H.; Feast, W. J.; Friend, R. H. *Synth. Met.* **2003**, *137*, 885-6.
- (242) Leclère, P.; Surin, M.; Jonkheijm, P.; Henze, O.; Schenning, A. P. H. J.; Biscarini, F.; Grimsdale, A. C.; Feast, W. J.; Meijer, E. W.; Müllen, K.; Brédas, J. L.; Lazzaroni, R. *Eur. Polym. J.* **2004**, *40*, 885-92.
- (243) Schenning, A. P. H. J.; Kilbinger, A. F. M.; Biscarini, F.; Cavallini, M.; Cooper, H. J.; Derrick, P. J.; Feast, W. J.; Lazzaroni, R.; Leclère, P.; McDonnell, L. A.; Meijer, E. W.; Meskers, S. C. J. *J. Am. Chem. Soc.* **2002**, *124*, 1269-75.
- (244) Kilbinger, A. F. M.; Schenning, A. P. H. J.; Goldoni, F.; Feast, W. J.; Meijer, E. W. *J. Am. Chem. Soc.* **2000**, *122*, 1820-1.
- (245) Kilbinger, A. F. M.; Feast, W. J.; Cooper, H. J.; McDonnell, L. A.; Derrick, P. J.; Schenning, A. P. H. J.; Meijer, E. W. *Chem. Commun.* **2000**, 383-4.
- (246) Jiang, L.; Hughes, R. C.; Sasaki, D. Y. *Chem. Commun.* **2004**, 1028-9.
- (247) Arnaud, A.; Belleney, J.; Boue, F.; Bouteiller, L.; Carrot, G.; Wintgens, V. *Angew. Chem. Int. Ed.* **2004**, *43*, 1718-21.
- (248) Wang, W.; Han, J. J.; Wang, L.-Q.; Li, L.-S.; Shaw, W. J.; Li, A. D. Q. *Nano Lett.* **2003**, *3*, 455-8.
- (249) Gaylord, B. S.; Wang, S.; Heeger, A. J.; Bazan, G. C. *J. Am. Chem. Soc.* **2001**, *123*, 6417-8.
- (250) Xiong, H.; Qin, L.; Sun, J.; Zhang, X.; Shen, J. *Chem. Lett.* **2000**, *35*, 586-7.
- (251) Hulvat, J. F.; Sofos, M.; Tajima, K.; Stupp, S. I. *J. Am. Chem. Soc.* **2005**, *127*, 366-72.
- (252) Yoo, Y.-S.; Choi, J.-H.; Song, J.-H.; Oh, N.-K.; Zin, W.-C.; Park, S.; Chang, T.; Lee, M. *J. Am. Chem. Soc.* **2004**, *126*, 6294-300.
- (253) Brunsveld, L.; Folmer, B. J. B.; Meijer, E. W.; Sijbesma, R. P. *Chem. Rev.* **2001**, *101*, 4071-97.
- (254) El-Ghayoury, A.; Schenning, A. P. H. J.; Van Hal, P. A.; Van Duren, J. K. J.; Janssen, R. A. J.; Meijer, E. W. *Angew. Chem. Int. Ed.* **2001**, *40*, 3660-3.
- (255) El-Ghayoury, A.; Peeters, E.; Schenning, A. P. H. J.; Meijer, E. W. *Chem. Commun.* **2000**, 1969-70.
- (256) Sivakova, S.; Rowan, S. J. *Chem. Commun.* **2003**, 2428-29.
- (257) Kimizuka, N.; Kunitake, T. *J. Am. Chem. Soc.* **1989**, *111*, 3758-9.
- (258) Kimizuka, N.; Kawasaki, T.; Hirata, K.; Kunitake, T. *J. Am. Chem. Soc.* **1995**, *117*, 6360-1.
- (259) Würthner, F.; Thalacker, C.; Sautter, A. *Adv. Mater.* **1999**, *11*, 754-8.
- (260) Würthner, F.; Thalacker, C.; Sautter, A.; Schartl, W.; Ibach, W.; Hollricher, O. *Chem. Eur. J.* **2000**, *6*, 3871-86.
- (261) Thalacker, C.; Würthner, F. *Adv. Funct. Mater.* **2002**, *12*, 209-18.
- (262) Lehn, J.-M. *Chem. Eur. J.* **2000**, *6*, 2097-102.
- (263) Fendler, J. H. *Membrane Mimetic Chemistry*; Wiley: New York, 1982.
- (264) Bo, Z.; Zhang, C.; Severin, N.; Rabe, J. P.; Schlüter, A. D. *Macromolecules* **2000**, *33*, 2688-94.
- (265) Schenning, A. P. H. J.; Jonkheijm, P.; Hofkens, J.; De Feyter, S.; Asavei, T.; Cotlet, M.; De Schryver, F. C.; Meijer, E. W. *Chem. Commun.* **2002**, 1264-5.
- (266) Balogh, D. T.; Dhanabalan, A.; Dynarowicz-Latka, P.; Schenning, A. P. H. J.; Oliveira, O. N., Jr.; Meijer, E. W.; Janssen, R. A. J. *Langmuir* **2001**, *17*, 3281-5.
- (267) Schenning, A. P. H. J.; Peeters, E.; Meijer, E. W. *J. Am. Chem. Soc.* **2000**, *122*, 4489-95.
- (268) Breitenkamp, R. B.; Tew, G. N. *Macromolecules* **2004**, *37*, 1163-5.
- (269) Cimrová, V.; Remmers, M.; Neher, D.; Wegner, G. *Adv. Mater.* **1996**, *8*, 146-9.
- (270) Kim, J.; McHugh, S. K.; Swager, T. M. *Macromolecules* **1999**, *32*, 1500-7.
- (271) Björnholm, T.; Greve, D. R.; Reitzel, N.; Hassenkam, T.; Kjaer, K.; Howes, P. B.; Larsen, N. B.; Bögelund, J.; Jayaraman, M.; Ewbank, P. C.; McCullough, R. D. *J. Am. Chem. Soc.* **1998**, *120*, 7643-4.
- (272) Björnholm, T.; Hassenkam, T.; Greve, D. R.; McCullough, R. D.; Jayaraman, M.; Savoy, S. M.; Jones, C. E.; McDevitt, J. T. *Adv. Mater.* **1999**, *11*, 1218-21.
- (273) Reitzel, N.; Greve, D. R.; Kjaer, K.; Howes, P. B.; Jayaraman, M.; Savoy, S.; McCullough, R. D.; McDevitt, J. T.; Björnholm, T. *J. Am. Chem. Soc.* **2000**, *122*, 5788-800.
- (274) Boggild, P.; Grey, F.; Hassenkam, T.; Greve, D. R.; Björnholm, T. *Adv. Mater.* **2000**, *12*, 947-50.
- (275) Kim, J.; Swager, T. M. *Nature* **2001**, *411*, 1030-4.
- (276) De Feyter, S.; De Schryver, F. C. *Chem. Soc. Rev.* **2003**, *32*, 139-50.
- (277) Bäuerle, P.; Fischer, T.; Bidlingmeier, B.; Stabel, A.; Rabe, J. P. *Angew. Chem. Int. Ed.* **1995**, *34*, 303-7.
- (278) Stabel, A.; Rabe, J. P. *Synth. Met.* **1994**, *67*, 47-53.

- (279) Müller, H.; Petersen, J.; Strohmaier, R.; Gompf, B.; Eisenmenger, W.; Vollmer, M. S.; Effenberger, F. *Adv. Mater.* **1996**, *8*, 733-7.
- (280) Vollmer, M. S.; Effenberger, F.; Stecher, R.; Gompf, B.; Eisenmenger, W. *Chem. Eur. J.* **1999**, *5*, 96-101.
- (281) Azumi, R.; Gotz, G.; Debaerdemaeker, T.; Bäuerle, P. *Chem. Eur. J.* **2000**, *6*, 735-44.
- (282) Mena-Osteritz, E.; Meyer, A.; Langeveld-Voss, B. M. W.; Janssen, R. A. J.; Meijer, E. W.; Bäuerle, P. *Angew. Chem. Int. Ed.* **2000**, *39*, 2680-4.
- (283) Samori, P.; Francke, V.; Müllen, K.; Rabe, J. P. *Chem. Eur. J.* **1999**, *5*, 2312-7.
- (284) Samori, P.; Severin, N.; Müllen, K.; Rabe, J. P. *Adv. Mater.* **2000**, *12*, 579-82.
- (285) Francke, V.; Raeder, H. J.; Geerts, Y.; Müllen, K. *Macromolec. Rapid Commun.* **1998**, *19*, 275-81.
- (286) Marsitzky, D.; Brand, T.; Geerts, Y.; Klapper, M.; Müllen, K. *Macromolec. Rapid Commun.* **1998**, *19*, 385-9.
- (287) Bianchi, C.; Cecchetto, E.; Francois, B. *Synth. Met.* **1999**, *102*, 916-7.
- (288) Marsitzky, D.; Klapper, M.; Müllen, K. *Macromolecules* **1999**, *32*, 8685-8.
- (289) Leclère, P.; Calderone, A.; Marsitzky, D.; Francke, V.; Geerts, Y.; Müllen, K.; Brédas, J. L.; Lazzaroni, R. *Adv. Mater.* **2000**, *12*, 1042-6.
- (290) Leclère, P.; Parente, V.; Brédas, J. L.; Francois, B.; Lazzaroni, R. *Chem. Mater.* **1998**, *10*, 4010-4.
- (291) Leclère, P.; Hennebicq, E.; Calderone, A.; Brocorens, P.; Grimsdale, A. C.; Müllen, K.; Brédas, J. L.; Lazzaroni, R. *Progr. in Polym. Sci.* **2002**, *28*, 55-81.
- (292) McQuade, D. T.; Pullen, A. E.; Swager, T. M. *Chem. Rev.* **2000**, *100*, 2537-74.
- (293) Morgado, J.; Cacialli, F.; Friend, R. H.; Chuah, B. S.; Moratti, S. C.; Holmes, A. B. *Synth. Met.* **2000**, *111-112*, 449-52.
- (294) Luo, Y.-H.; Liu, H.-W.; Xi, F.; Li, L.; Jin, X.-G.; Han, C. C.; Chan, C.-M. *J. Am. Chem. Soc.* **2003**, *124*, 1202-3.
- (295) Meier, H.; Stalmach, U.; Kolshorn, H. *Acta Polym.* **1997**, 379-83.
- (296) Gesquière, A.; Abdel-Mottaleb, M. M.; De Feyter, S.; De Schryver, F. C.; Sieffert, M.; Müllen, K.; Calderone, A.; Lazzaroni, R.; Brédas, J.-L. *Chem. Eur. J.* **2000**, *6*, 3739-46.
- (297) Lazzaroni, R.; Calderone, A.; Brédas, J. L.; Rabe, J. P. *J. Chem. Phys.* **1997**, 99-105.
- (298) Stevens, F.; Dyer, D. J.; Walba, D. M. *Angew. Chem. Int. Ed.* **1996**, *8*, 900-1.
- (299) Walba, D. M.; Stevens, F.; Clark, N. A.; Parks, D. C. *Acc. Chem. Res.* **1996**, 591-7.
- (300) Giancarlo, L. C.; Flynn, G. W. *Acc. Chem. Res.* **2000**, *33*, 491-501.
- (301) De Feyter, S.; Gesquière, A.; De Schryver, F.; Meiners, C.; Sieffert, M.; Müllen, K. *Langmuir* **2000**, *16*, 9887-94.
- (302) De Feyter, S.; Gesquière, A.; Wurst, K.; Amabilino, D. B.; Veciana, J.; De Schryver, F. C. *Angew. Chem., Int. Ed.* **2001**, *40*, 3217-20.
- (303) Feast, W. J.; Goldoni, F.; Kilbinger, A. F. M.; Meijer, E. W.; Petty, M. C.; Schenning, A. P. H. J. *Macromolec. Symp.* **2001**, *175*, 151-8.
- (304) The critical aggregation concentration could not be determined since the optical techniques were not sensitive enough to measure more diluted concentrations than 10^{-8} mol/L.
- (305) Samori, P.; Francke, V.; Mangel, T.; Müllen, K.; Rabe, J. P. *Opt. Mater.* **1998**, *9*, 390-3.
- (306) See Experimental Section and Taylor, P. N. and Anderson, H. L. *J. Am. Chem. Soc.*, **1999**, *121*, 11538-45.
- (307) Broeren, M. A. C.; Dongen, J. v.; Genderen, M. v.; Meijer, E. W. *Angew. Chem. Int. Ed.* **2004**, 333-5.
- (308) Ashkin, A. *Phys. Rev. Lett.* **1970**, *24*, 156-9.
- (309) Bong, D. T.; Clark, T. D.; Granja, J. R.; Ghadiri, M. R. *Angew. Chem., Int. Ed.* **2001**, *40*, 988-1011.
- (310) Jeffrey, G. A. *An Introduction to hydrogen bonding*; Oxford University Press: Oxford, 1997.
- (311) Zerkowski, J. A.; Whitesides, G. M. *J. Am. Chem. Soc.* **1994**, 4298.
- (312) Ranganathan, A.; Pedireddi, V. R.; Rao, C. N. R. *J. Am. Chem. Soc.* **1999**, *121*, 1752-3.
- (313) Prins, L. J.; De Jong, F.; Timmerman, P.; Reinhoudt, D. N. *Nature* **2000**, *408*, 181-4.
- (314) Whitesides, G. M.; Simanek, E. E.; Mathias, J. P.; Seto, C. T.; Chin, D. N.; Gordon, D. M. *Acc. Chem. Res.* **1995**, 37.
- (315) Highfill, M. L.; Chandrasekaran, A.; Lynch, D. E.; Hamilton, D. G. *Cryst. Gr. Des.* **2002**, *2*, 15-20.
- (316) Kolotuchin, S. V.; Zimmerman, S. C. *J. Am. Chem. Soc.* **1998**, *120*, 9092-3.
- (317) Marsh, A.; Silvestri, M.; Lehn, J. M. *Chem. Commun.* **1996**, 1527.
- (318) Hibino, M. S. A.; Tsuchiya, H.; Hatta, I. *J. P. C. B.*, *102*, 4544; *J. Phys. Chem. B* **1998**, 4544.
- (319) De Feyter, S.; Gesquière, A.; Abdel-Mottaleb, M. M.; Grim, P. C.; De Schryver, F. C.; Meiners, C.; Sieffert, M.; Valiyaveetil, S.; Müllen, K. *Acc. Chem. Res.* **2000**, *33*, 520-31.
- (320) De Feyter, S.; Gesquière, A.; Klapper, M.; Müllen, K.; De Schryver, F. C. *Nano Lett.* **2003**, *3*, 1485-8.
- (321) Griessl, S.; Lackinger, M.; Edelwirth, M.; Hietschold, M.; Heckl, W. M. *Single Molec.* **2002**, *3*, 25-31.
- (322) Dmitriev, A.; Lin, N.; Weckesser, J.; Barth, J. V.; Kern, K. *J. Phys. Chem. B* **2002**, *106*, 6907-12.
- (323) Li, C.-J.; Zeng, Q.-D.; Wang, C.; Wan, L.-J.; Xu, S.-L.; Wang, C.-R.; Bai, C.-L. *J. Phys. Chem. B* **2003**, *107*, 747-50.
- (324) Barth, J. V.; Weckesser, J.; Cai, C.; Gunter, P.; Burgi, L.; Jeandupeux, O.; Kern, K. *Angew. Chem. Int. Ed.* **2000**, *39*, 1230-4.
- (325) Keeling, D. L.; Oxtoby, N. S.; Wilson, C.; Humphry, M. J.; Champness, N. R.; Beton, P. H. *Nano Lett.* **2003**, *3*, 9-12.

- (326) Theobald, J. A.; Oxtgoby, N. S.; Philips, M. A.; Champness, N. R.; Beton, P. H. *Nature* **2003**, 1029.
- (327) Kimizuka, N.; Fujikawa, S.; Kuwahara, H.; Kunitake, T.; Marsh, A.; Lehn, J.-M. *J. Chem. Soc., Chem. Commun.* **1995**, 2103-4.
- (328) Schönherr, H.; Paraschiv, V.; Zapotoczny, S.; Crego-Calama, M.; Timmerman, P.; Frank, C. W.; Vancso, G. J.; Reinhoudt, D. N. *Proc. Natl. Acad. Sci. USA* **2002**, *99*, 5024-7.
- (329) Gottarelli, G.; Mezzina, E.; Spada, G. P.; Carsughi, F.; Di Nicola, G.; Mariani, P.; Sabaticci, A.; Bonazzi, S. *Helv. Chim. Acta* **1996**, 220-34.
- (330) Yang, W.; Chai, X.; Chi, L.; Liu, X.; Cao, Y.; Lu, R.; Jiang, Y.; Tang, X.; Fuchs, H.; Li, T. *Chem. Eur. J.* **1999**, *5*, 1144-9.
- (331) Zubarev, E. R.; Pralle, M. U.; Sone, E. D.; Stupp, S. I. *J. Am. Chem. Soc.* **2001**, *123*, 4105-6.
- (332) Fenniri, H.; Deng, B.-L.; Ribbe, A. E. *J. Am. Chem. Soc.* **2002**, *124*, 11064-72.
- (333) Hirschberg, J. H. K. K.; Brunsveld, L.; Ramzi, A.; Vekemans, J. A. J. M.; Sijbesma, R. P.; Meijer, E. W. *Nature* **2000**, *407*, 167-70.
- (334) Jonkheijm, P.; Hoeben, F. J. M.; Kleppinger, R.; Van Herrikhuyzen, J.; Schenning, A. P. H. J.; Meijer, E. W. *J. Am. Chem. Soc.* **2003**, *125*, 15941-9.
- (335) Peeters, E. *Mesoscopic order in conjugated materials*, Technische Universiteit Eindhoven, 2000.
- (336) Interestingly, the formation of hydrogen-bonded hexameric structures of melamines was previously proposed in literature: Thalacker, C.; Würthner, F. *Adv. Funct. Mater.* **2002**, *12*, 209-18.
- (337) Fournier, J.-H.; Maris, T.; Wuest, J. D. *J. Org. Chem.* **2004**, 1862.
- (338) Brunet, P.; Simard, M.; Wuest, J. D. *J. Am. Chem. Soc.* **1997**, 2717.
- (339) Sauriat-Dorizon, M.; Maris, T.; Wuest, J. D. *J. Org. Chem.* **2003**, 240.
- (340) Peeters, E.; Marcos, A.; Meskers, S. C. J.; Janssen, R. A. J. *J. Phys. Chem. B* **2000**, 9445-54.
- (341) Concentration dependent UV/vis measurements in dodecane show that OPV₄T starts to aggregate at 5×10^{-5} M while the self-assembly of OPV₃T starts at 2.5×10^{-5} M.
- (342) Bouman, M. M.; Meijer, E. W. *Adv. Mater.* **1995**, 7.
- (343) Brunsveld, L.; Zhang, H.; Glasbeek, M.; Vekemans, J. A. J. M.; Meijer, E. W. *J. Am. Chem. Soc.* **2000**, *122*, 6175-82.
- (344) With STM and AFM we observe different types of structures on graphite. This might be the result of the different solvents applied. Another possibility could be that in the case of the AFM studies first a monolayer of rosettes is formed and that on top of this layer fibers are present. We have not investigated this in detail.
- (345) The broadening can be estimated by using a simple model based on a spherical tip apex (radius R) and a rectangular cross section of the fiber (height H) with $2[H(2R-H)]^{0.5}$ as in Samori, P.; Francke, V.; Mangel, T.; Müllen, K.; Rabe, J. *Opt. Mater.* **1998**, *9*, 390. For the present height and a terminal radius of commercial tips of 20 nm the broadening is about 29 nm. Therefore, the 'true' width is obtained by subtracting the broadening from the apparent width and is about 10 nm.
- (346) See Section 1.2.
- (347) See Section 1.3.1.1.
- (348) Percec, V.; Glodde, M.; Bera, T. K.; Miura, Y.; Shiyonovskaya, I.; Singer, K. D.; Balagurusamy, V. S. K.; Heiney, P. A.; Schnell, I.; Rapp, A.; Spiess, H. W.; Hudson, S. D.; Duan, H. *Nature* **2002**, *419*, 384-7.
- (349) See Section 1.3.2.3.
- (350) This offset has been determined by comparison of the propagation direction of the lamellae with respect to the graphite substrate underneath, by measuring subsequently the monolayer and graphite substrate.
- (351) a) Davydov, A. S. *Zhur. Ekspil. I Teoret. Fiz.* **1948**, 210-8. b) Peeters, E. *Mesoscopic order in conjugated materials*, Technische Universiteit Eindhoven, 2000, p. 70-72.
- (352) Sijbesma, R. P.; Beijer, F. H.; Brunsveld, L.; Folmer, B. J. B.; Hirschberg, J. H. K. K.; Lange, R. F. M.; Lowe, J. K. L.; Meijer, E. W. *Science* **1997**, *278*, 1601-4.
- (353) Dynamic oscillatory shear measurements show a fluidlike behavior for diluted solutions of OPV₃UT at ambient temperature. At all frequencies is the $G' < G''$, whereas, in concentrated solutions, a crossover is observed at 6 rad/s.
- (354) a) Oosawa, F.; Kasai, M. *J. Mol. Biol.* **1962**, *4*, 10-21. b) Aggeli, A.; Nyrkova, I. A.; Bell, M.; Harding, R.; Carrick, L.; McLeish, T. C. B.; Semenov, A. N.; Boden, N. *Proc. Natl. Acad. Sci. USA* **2001**, *98*, 11857-62.
- (355) Brunsveld, L. *Supramolecular Chirality*, Technische Universiteit Eindhoven, 2001.
- (356) Zimm, B.; Bragg, J. K. *J. Chem. Phys.* **1959**, *31*, 526.
- (357) van der Schoot, P. In *Supramolecular Polymers*; 2nd ed.; Ciferri, A., Ed.; CRC Press, Baton Rouge, 2005.
- (358) K_n (dimensionless) takes on the role of the cooperativity parameter σ in the helical aggregation models based on Zimm-Bragg theory.
- (359) CD melting curves were corrected for concentration and volume fraction (density is taken is 1.1 g/mL).
- (360) Prokhorenko, V. I.; Steengaards, D. B.; Holzwarth, A. R. *Biophys. J.* **2003**, *85*, 3173-86.
- (361) Didraga, C.; Klugkist, J. A.; Knoester, J. *J. Phys. Chem. B* **2002**, *106*, 11474-86.
- (362) Hannah, K. C.; Armitage, B. A. *Acc. Chem. Res.* **2004**, *37*, 845-53.
- (363) Zahn, S.; Swager, T. M. *Angew. Chem. Int. Ed.* **2002**, *41*, 4225-30.

- (364) Craig, M. R.; Jonkheijm, P.; Meskers, S. C. J.; Schenning, A. P. H. J.; Meijer, E. W. *Adv. Mater.* **2003**, *15*, 1435-8.
- (365) Langeveld-Voss, B. M. W.; Beljonne, D.; Shuai, Z.; Janssen, R. A. J.; Meskers, S. C. J.; Meijer, E. W.; Brédas, J.-L. *Adv. Mater.* **1998**, *10*, 1343-8.
- (366) a) Beljonne, D.; Hennebicq, E.; Daniel, C.; Herz, L. M.; Silva, C.; Scholes, G. D.; Hoeben, F. J. M.; Jonkheijm, P.; Schenning, A. P. H. J.; Meskers, S. C. J.; Philips, M. A.; Friend, R. H.; Meijer, E. W. *J. Phys. Chem. B* **2005**, accepted. b) Daniel, C.; Herz, L. M.; Silva, C.; Hoeben, F. J. M.; Jonkheijm, P.; Schenning, A. P. H. J.; Meijer, E. W. *Phys. Rev. B* **2003**, *68*, 235212/1-/9.
- (367) Absorbance melting curves were normalized between 310 and 375 K.
- (368) Palmans, A. R. A.; Vekemans, J. A. J. M.; Havinga, E. E.; Meijer, E. W. *Angew. Chem. Int. Ed.* **1997**, *36*, 2648-51.
- (369) Palmans, A. R. A. *Supramolecular structures based on the intramolecular H-bonding in the 3,3'-di(acylamino)-2,2'-bipyridine unit*, Technische Universiteit Eindhoven, 1997 and refs therein.
- (370) Brunsveld, L.; Schenning, A. P. H. J.; Broeren, M. A. C.; Janssen, H. M.; Vekemans, J. A. J. M.; Meijer, E. W. *Chem. Lett.* **2000**, 292-3.
- (371) See Chapter 1.
- (372) van Gorp, J. J.; Vekemans, J. A. J. M.; Meijer, E. W. *J. Am. Chem. Soc.* **2002**, *124*, 14759-69.
- (373) Sherrington, D. C.; Taskinen, K. A. *Chem. Soc. Rev.* **2001**, *30*, 83-93.
- (374) Ciferri, A. *Macromol. Rapid Commun.* **2002**, *23*, 511-29.
- (375) Hartgerink, J. D.; Zubarev, E. R.; Stupp, S. I. *Curr. Opin. Solid State Mater. Science* **2001**, *5*, 355-61.
- (376) Pralle, M. U.; Whitaker, C. M.; Braun, P. V.; Stupp, S. I. *Macromolecules* **2000**, *33*, 3550-6.
- (377) Klok, H.-A.; Jolliffe, K. A.; Schauer, C. L.; Prins, L. J.; Spatz, J. P.; Möller, M.; Timmerman, P.; Reinhoudt, D. N. *J. Am. Chem. Soc.* **1999**, *121*, 7154-5.
- (378) Zerkowski, J. A.; Seto, C. T.; Wierda, D. A.; Whitesides, G. M. *J. Am. Chem. Soc.* **1990**, *112*, 9025-6.
- (379) Mio, M. J.; Prince, R. B.; Moore, J. S.; Kuebel, C.; Martin, D. C. *J. Am. Chem. Soc.* **2000**, 6134-5.
- (380) Percec, V.; Ahn, C. H.; Ungar, G.; Yeardley, D. J. P.; Möller, M.; Sheiko, S. S. *Nature* **1998**, *391*, 161-4.
- (381) Rapaport, H.; Kim, H. S.; Kjaer, K.; Howes, P. B.; Cohen, S.; Als-Nielsen, J.; Ghadiri, M. R.; Leiserowitz, L.; Lahav, M. *J. Am. Chem. Soc.* **1999**, *121*, 1186-91.
- (382) Kawasaki, T.; Tokuhira, M.; Kimizuka, N.; Kunitake, T. *J. Am. Chem. Soc.* **2001**, *123*, 6792-800.
- (383) Liu, D.; De Feyter, S.; Cotlet, M.; Wiesler, U.-M.; Weil, T.; Herrmann, A.; Müllen, K.; De Schryver, F. C. *Macromolecules* **2003**, *36*, 8489-98.
- (384) Spano, F. C. *J. Chem. Phys.* **2002**, *115*, 5877-91.
- (385) a) See Experimental Section for more detail. b) For some fibrils we have also measured two consecutive images with polarization orientations of 45° and 135° in order to rule out any ambiguities in the polarization orientation of the light. In that case, the green color represents $R' = I_{135}/I_{45} = 0$, and red represents $R' = \infty$.
- (386) The mathematics of the model are beyond the scope of this thesis and will be published by: Jeukens, C. R. L. P. N.; Jonkheijm, P.; Wijnen, F. J. P.; Gielen, J. C.; Christianen, P. C. M.; Schenning, A. P. H. J.; Meijer, E. W.; Maan, J. C. *J. Am. Chem. Soc.* accepted.
- (387) Jeukens, C. R. L. P. N.; Lensen, M. C.; Wijnen, F. J. P.; Elemans, J. A. A. W.; Christianen, P. C. M.; Rowan, A. E.; Gerritsen, J. W.; Nolte, R. J. M.; Maan, J. C. *Nano Lett.* **2004**, *4*, 1401-6.
- (388) a) Craig, M. R.; Kok, M. M. d.; Hofstraat, J. W.; Schenning, A. P. H. J.; Meijer, E. W. *J. Mater. Chem.* **2003**, *13*, 2861-2. b) Breemen, A. J. J. M. v.; Herwig, P. T.; Chlon, C. H. T.; Sweelsen, J.; Schoo, H. F. M.; Benito, E. M.; Leeuw, D. M. d.; Tanase, C.; Wildeman, J.; Blom, P. W. M. *Adv. Funct. Mater.* **2005**, *15*, 872-6.
- (389) Salomon, A.; Cahen, D.; Lindsay, S.; Tomfohr, J.; Engelkes, V. B.; Frisbie, C. D. *Adv. Mater.* **2003**, 1881.
- (390) Herz, L. M.; Daniel, C.; Silva, C.; Hoeben, F. J. M.; Schenning, A. P. H. J.; Meijer, E. W.; Friend, R. H.; Phillips, R. T. *Phys. Rev. B* **2003**, *68*, 045203/1-/7.
- (391) Solid-state CD measurements (only measured on films on glass) show a Cotton effect similar to the shape found earlier in solution whereas the film from chloroform did not reveal a Cotton effect.
- (392) According to $I_{SD} = (WC_i/2L) \times \mu \times (V_G - V_T)^2$ with $W = 5 \text{ mm}$, $L = 1000 \text{ mm}$ and $C_i = 10^{-8} \text{ F/cm}^2$
- (393) The morphology of (OPV₄UT)₂ from toluene on ITO/PEDOT:PSS substrates revealed very smooth surfaces with a fibrillar network consisting of typical features of about 5 to 6 nm wide, in agreement with the morphology obtained on films on glass. Also pure PCBM films appear as smooth films. Apparently, the hydrophilicity of the surface has negligible influence on the supramolecular organization. This is in agreement with our assumption that the fibrillar structures are formed in solution, and that the deposition process does not cause a significant change in the supramolecular organization.
- (394) SEM observations also identified circularly shaped structures with a variety of dimensions and distributions in agreement with AFM. Related blends of PPV and C₆₀ also show coarse demixing, see next two refs.
- (395) Hoppe, H.; Glatzel, T.; Niggemann, M.; Hinsch, A.; Lux-Steiner, M. C.; Sariciftci, N. S. *Nano Letters* **2005**, *5*, 269-74.
- (396) Yang, X.; van Duren, J. K. J.; Janssen, R. A. J.; Michels, M. A. J.; Loos, J. *Macromolecules* **2004**, *37*, 2151-8.

- (397) Films spun from chlorobenzene and o-xylene have a much smoother surface; the rms-roughness decreased to 15 nm and 9 nm respectively, with a peak-to-peak distance of 73 nm and 48 nm respectively, however, no signature of a semicontinuous fibrillar network was observed on larger AFM magnifications. Apparently, polarity and boiling point effect the supramolecular morphology - toluene (111 °C, $\epsilon = 2.4$), chlorobenzene (132 °C, $\epsilon = 5.6$), o-xylene (140 °C, $\epsilon = 2.6$) and o-dichlorobenzene (ODCB, 180 °C, $\epsilon = 9.9$).
- (398) a) Fill factor is defined as $(J_{\max}V_{\max})/(J_{\text{sc}}V_{\text{oc}})$ with V_{\max} and J_{\max} as the voltage and current at maximal power. b) van Duren, J. K. J. *Polymer:Fullerene Bulk-Heterojunction Solar Cells*, Technische Universiteit Eindhoven, 2004.
- (399) Chesterfield, R. J.; Newman, C. R.; Pappenfus, T. M.; Ewbank, P. C.; Haukaas, M. H.; Mann, K. R.; Miller, L. L.; Frisbie, C. D. *Adv. Mater.* **2003**, *15*, 1278-82.
- (400) Rost, C.; Karg, S.; Riess, W.; Loi, M. A.; Murgia, M.; Muccini, M. *Appl. Phys. Lett.* **2004**, 1613-5.
- (401) Meijer, E. J.; De Leeuw, D.; Setayesh, S.; van Veenendaal, E.; Huisman, B.-H.; Blom, P. W. M.; Hummelen, J. C.; Scherf, U.; Kadam, J.; Klapwijk, T. M. *Nature Mater.* **2003**, *2*, 678-82.
- (402) Locklin, J.; Shinbo, K.; Onishi, K.; Kaneko, K.; Bao, Z.; Advincula, R. C. *Chem. Mater.* **2003**, *15*, 1404-12.
- (403) Dodabalapur, A.; Katz, H. E.; Torsi, L.; Haddon, R. C. *Science* **1995**, 1560.
- (404) Anthopoulos, T. D.; Tanase, C.; Setayesh, S.; Meijer, E. J.; Hummelen, J. C.; Blom, P. W. M.; De Leeuw, D. *Adv. Funct. Mater.* **2004**, *16*, 2174-79.
- (405) Yoon, M.-H.; DiBenedetto, S. A.; Facchetti, A.; Marks, T. J. *J. Am. Chem. Soc.* **2005**, *127*, 1348-9.
- (406) Chua, L.-L.; Zausmell, J.; Chang, J.-F.; Ou, E. C.-W.; Ho, P. K.-H.; Sirringhaus, H.; Friend, R. H. *Nature* **2005**, *434*, 194-9.
- (407) Hoeben, F. J. M.; Jonkheijm, P.; Meijer, E. W.; Schenning, A. P. H. J. *Chem. Rev.* **2005**, *105*, 1491-546.
- (408) Yamaguchi, T.; Ishii, N.; Tashiro, K.; Aida, T. *J. Am. Chem. Soc.* **2003**, *125*, 13934-5.
- (409) Würthner, F.; Thalacker, C.; Sautter, A. *Adv. Mater.* **1999**, *11*, 754-8.
- (410) The phenoxy substituents in the bay area can lead to a torsion angle of 30° between the two naphthalene imide half units leading to weak molecule-substrate interactions Würthner, F.; Sautter, A.; Thalacker, C. *Angew. Chem. Int. Ed. Engl.* **2000**, *39*, 1243. b) Hofkens, J.; Vosch, T.; Maus, M.; Kohn, F.; Cotlet, M.; Weil, T.; Herrman, A.; Müllen, K.; De Schryver, F. C. *Chem. Phys. Lett.* **2001**, *333*, 255. In contrast, the parent flat PBI has been successfully imaged under UHV conditions by a) Ludwig, C.; Gompf, B.; Petersen, J.; Strohmaier, R.; Eisenmenger, W. *Z. J. Phys. Chem. B* **1994**, *93*, 365. b) Uder, B.; Ludwig, C.; Petersen, J.; Gompf, B.; Eisenmenger, W. *J. Phys. Chem. B* **1995**, *97*, 389.
- (411) A binding constant of $K_a = 243 \text{ M}^{-1}$ was determined for OPV and a related diimide acceptor e.g. N-2,5-di-tert-butylphenyl-1,5-dicarboxy-N'-hydrogen-4,8-dicarboxynaphthalenediimide.
- (412) Würthner, F.; Thalacker, C.; Diele, S.; Tschierske, C. *Chem. Eur. J.* **2001**, *7*, 2245-53.
- (413) Here, the negative CD signal of the perylene band can be related to the preferential formation of M enantiomers formed by means of a left-handed helical stacking of the complex. Chirality originates from the non-planar structure of bay-substituted perylenes. In the crystalline state, P and M enantiomers could be directly observed, where close contacts between the molecules of opposite chirality are preferred. In the non-aggregated state (dilute solution), the same amount of P and M enantiomers are present and interconversion is rapid on the NMR time-scale. Upon aggregation, this interconversion is presumably slowed down and enrichment of one enantiomer is possible under the influence of the chiral OPV aggregates due to the formation of diastereomeric complexes. a) Chen, Z.; Debije, M. G.; Debaerdemaeker, T.; Osswald, P.; Würthner, F. *ChemPhysChem*, **2004**, *5*, 137-40 and b) Würthner, F.; Sautter, A.; Schilling, J. *J. Org. Chem.* **2002**, *67*, 3037-44.
- (414) Spector, M. S.; Selinger, J. V.; Schnur, J. M. In *Materials-Chirality pp.* 281-372; Green, M. M.; Nolte, R. J. M.; Meijer, E. W., Ed.; John Wiley & Sons, Inc.: Hoboken, New Jersey, 2003; Vol. 24 of Topics in Stereochemistry.
- (415) Pu, L. *Acta Polym.* **1997**, *48*, 116-41.
- (416) Li, Y.; Chu, B. *Macromolecules* **1991**, *24*, 4115-22.
- (417) Xu, R.; Chu, B. *Macromolecules* **1989**, *22*, 4523-8.
- (418) Cornelissen, J. J. L. M.; Peeters, E.; Janssen, R. A. J.; Meijer, E. W. *Acta Polymerica* **1998**, *49*, 471-6.
- (419) Goldoni, F.; Janssen, R. A. J.; Meijer, E. W. *Polym Prepr.* **1998**, *39*, 1049-50.
- (420) Goldoni, F.; Janssen, R. A. J.; Meijer, E. W. *J. Polym. Sci., Part A: Polym. Chem.* **1999**, *37*, 4629-39.
- (421) Andreani, F.; Angiolini, L.; Caretta, D.; Salatelli, E. *J. Mater. Chem.* **1998**, *8*, 1109-11.
- (422) Bouman, M. M.; Havinga, E. E.; Janssen, R. A. J.; Meijer, E. W. *Mol. Cryst. Liq. Cryst. Sci. Technol.* **1994**, *256*, 439-48.
- (423) Langeveld-Voss, B. M. W.; Janssen, R. A. J.; Christiaans, M. P. T.; Meskers, S. C. J.; Dekkers, H. P. J. M.; Meijer, E. W. *J. Am. Chem. Soc.* **1996**, *118*, 4908-9.
- (424) Fiesel, R.; Scherf, U. *Macromol. Rapid Commun.* **1998**, *19*, 427-31.
- (425) Fiesel, R.; Halkyard, C. E.; Rampey, M. E.; Kloppenburg, L.; Studer-Martinez, S. L.; Scherf, U.; Bunz, U. H. F. *Macromolec. Rapid Commun.* **1999**, *20*, 107-11.
- (426) Harlev, E.; Wudl, F. *Conjugated polymers and related materials. The interconnections of chemical and electronic structure.*; Oxford University Press: Oxford, 1993.

- (427) Langeveld-Voss, B. M. W.; Peeters, E.; Janssen, R. A. J.; Meijer, E. W. *Synth. Met.* **1997**, *84*, 611-4.
- (428) Lermo, E. R.; Langeveld-Voss, B. M. W.; Janssen, R. A. J.; Meijer, E. W. *Chem. Commun.* **1999**, 791-2.
- (429) Ramos Lermo, M. E.; Langeveld-Voss, B. M. W.; Meijer, E. W. *Polym. Prepr.* **1998**, *39*, 1087-8.
- (430) Bidan, G.; Guillerez, S.; Sorokin, V. *Adv. Mater.* **1996**, *8*, 157-60.
- (431) Langeveld-Voss, B. M. W.; Christiaans, M. P. T.; Janssen, R. A. J.; Meijer, E. W. *Macromolecules* **1998**, *31*, 6702-4.
- (432) Langeveld-Voss, B. M. W.; Waterval, R. J. M.; Janssen, R. A. J.; Meijer, E. W. *Macromolecules* **1999**, *32*, 227-30.
- (433) Holmes, A. E.; Barcena, H.; Canary, J. W. *Supramolecular inversion of helical chirality*; Cerberus Press, Inc.: New York, 2002 and refs therein.
- (434) Watanabe, J.; Okamoto, S.; Satoh, K.; Sakajiri, K.; Furuya, H.; Abe, A. *Macromolecules* **1996**, *29*, 7084-8.
- (435) Sakajiri, K.; Satoh, K.; Kawaguchi, S.; Watanabe, J. *Macromolecules* **1999**, *476*, 1-8.
- (436) Maeda, K.; Okamoto, Y. *Macromolecules* **1998**, *32*, 974-80.
- (437) Maeda, K.; Okamoto, Y. *Macromolecules* **1999**, *31*, 5164-9.
- (438) Fujiki, M. *J. Am. Chem. Soc.* **2000**, *122*, 3336-43.
- (439) Tabei, J.; Nomura, R.; Sanda, F.; Masuda, T. *Macromolecules* **2004**, *37*, 1175-9.
- (440) Koe, J. R.; Fujiki, M.; Motonaga, M.; Nakashima, H. *Chem. Commun.* **2000**, 389-90.
- (441) Fujiki, M.; Koe, J. R.; Motonaga, M.; Nakashima, H.; Terao, K.; Teramoto, A. *J. Am. Chem. Soc.* **2001**, *123*, 6253-61.
- (442) Tang, T.; Green, M. M.; Cheon, K. S.; Selinger, J. V.; Garetz, B. A. *J. Am. Chem. Soc.* **2003**, *125*, 7313-23.
- (443) Yashima, E.; Maeda, J.; Sato, O. *J. Am. Chem. Soc.* **2001**, *123*, 8159-60.
- (444) Nakako, H.; Nomura, R.; Tabata, M.; Masuda, T. *Macromolecules* **2001**, *34*, 1496-502.
- (445) Tabei, J.; Nomura, R.; Masuda, T. *Macromolecules* **2003**, *36*, 573-7.
- (446) Cheon, K. S.; Selinger, J. V.; Green, M. M. *Angew. Chem. Int. Ed.* **2000**, *39*, 1482-5.
- (447) Pohl, F. M.; Jovin, T. M. *J. Mol. Biol.* **1972**, *67*, 375-96.
- (448) Dong, Y.; Wu, Y.; Zhao, Y.; Wang, H.; Ruan, Y.; Zhang, H.; Fang, X. *Carb. Res.* **2003**, *338*, 1699-705.
- (449) Prince, R. B.; Barnes, S. A.; Moore, J. S. *J. Am. Chem. Soc.* **2000**, *122*, 2758-62.
- (450) Simonyi, M.; Bikadi, Z.; Zsila, F.; Deli, J. *Chirality* **2003**, *15*, 680-98.
- (451) Kilbinger, A. F. M.; Schenning, A. P. H. J.; Goldoni, F.; Feast, W. J.; Meijer, E. W. *J. Am. Chem. Soc.* **2000**, *122*, 1820-1.
- (452) Bäuerle, P. *Electronic Materials: The oligomer approach*; VCH: Weinheim, 1998.
- (453) McRae, E. G.; Kasha, M. *J. Phys. Chem.* **1958**, 721.
- (454) Gray, G. W.; McDonell, D. G. *Mol. Cryst. Liq. Cryst.* **1977**, *34*, 211-7.
- (455) During monitoring the change of the CD the temperature of the solution was thermostatted by peltier elements driven by software.
- (456) See Experimental Section
- (457) Snir, Y.; Kamien, R. D. *Science* **2005**, *307*, 1067.
- (458) Dell'Orco, D.; Xue, W.-F.; Thulin, E.; Linse, S. *Biophys. J.* **2005**, *88*, 1991-2002.
- (459) a) Unpublished results from Gardebien, F.; Leclère, Ph.; Lazzaroni, R. b) Prosa, T. J.; Winokur, M. J.; Moulton, J.; Smith, P.; Heeger, A. J. *Macromolecules* **1992**, *25*, 4364-72.
- (460) Vriezema, D. M.; Hoogboom, J.; Velonia, K.; Takazawa, K.; Christianen, P. C. M.; Maan, J. C.; Rowan, A. E.; Nolte, R. J. M. *Angew. Chem. Int. Ed.* **2003**, *42*, 772-6.
- (461) Sutter, D. H.; Flygare, W. H. *J. Am. Chem. Soc.* **1969**, *91*, 4063-8.
- (462) Brotin, T.; Utermohlen, R.; Fages, F.; Bouas-Laurent, H.; Desvergne, J.-P. *Chem. Soc. Chem. Commun.* **1991**, 416-7.
- (463) Helfrich, W. *Z. Naturforsch.* **1973**, *28C*, 693-705.
- (464) Helfrich, W. *Phys. Lett.* **1973**, *43A*, 409-10.
- (465) Fiesel, R.; Scherf, U. *Acta Polym.* **1998**, *49*, 445-9.
- (466) Wada, F.; Hirayama, H.; Namiki, H.; Kikukawa, K.; Matsuda, T. *Bull. Chem. Soc. Jpn.* **1980**, 1473-7.

SUMMARY

The successful use of organic semiconductors in opto-electronic applications such as light emitting diodes, field effect transistors and photovoltaic cells is demonstrated in recent years. Many research groups study the effect of the chemical structure and organization of these functional organic components on the performance of the devices. The lack of control over the organization going from π -conjugated molecules to macroscopic materials hampers the performance of these materials in devices.

The objective of the work described in this thesis is the programmed self-assembly of π -conjugated oligomers into architectures at the nanometer-scale using several secondary interactions simultaneously, thus following nature's paradigm. The construction of such architectures is thought to be not only important for plastic electronics but also for the new field of supramolecular electronics. This relatively unexplored field of research relies on structures having controlled dimension and shape, *e.g.* wires; 5 nm in diameter and 100 nm long. An introduction to the field is given in Chapter 1.

Chapter 2 describes the influence of hydrophobic/hydrophilic balance in a series of chiral oligo(*p*-phenylenevinylene)s (OPVs) on the self-assembly of these molecules in solution and in the solid state. A variety of self-assembled architectures were found using the same building blocks; namely monolayers, rods, helical fibers and vesicles, depending on the method of preparation. Pre-organizing the π -conjugated oligomers in solution offered a valuable tool to control the shape of the assemblies and the properties in the solid state; the emission from a single vesicle on a glass surface was similar to emission from the vesicles in water. Interestingly, such vesicles could be manipulated by optical tweezers providing a tool to position nanoscopic architectures.

Enhanced control over the position of the building blocks in the self-assembled objects was achieved by introducing hydrogen-bonding interactions as described in Chapter 3. The synthesized series of OPVs, carrying a hydrogen-bonding diaminotriazine unit, self-assemble into dimeric or hexameric structures on graphite surfaces as studied by scanning tunneling microscopy (STM). Weak interactions that determine the packing of molecules in a crystal can be applied to the supramolecular organization in solution. Optical techniques and small angle neutron scattering (SANS) showed the presence of long helical columnar aggregates in apolar solutions comprising of stacked rosettes. These tubules have a perfect space filling and are still soluble due to the apolar shell that surrounds the stacks. These tubules could be visualized in the solid state by atomic force microscopy (AFM).

In Chapter 4, OPVs of different conjugation length have been synthesized carrying a strong self-complementary hydrogen-bonding motif. Dimers are formed as studied with STM and ^1H -NMR spectroscopy. SANS data showed the formation rigid cylindrical objects. Stacks of the tetramer have a persistence length of 150 nm and a diameter of 6 nm. The trimer shows rigid columnar domains of 90 nm with a diameter of 5 nm. Temperature and concentration variable measurements show that the stability of the stacks increases with the conjugation length as a result of more favorable π - π interactions. Detailed photophysical measurements revealed different phases during the self-assembly of the OPV oligomers. It is shown, for the first time, that the the initial formation of small pre-aggregates is essential for the growth into long helical stacks. The self-assembly could be described by a nucleation-elongation assembly model reflecting the high cooperativity. The helix formation is enthalpy-driven and a

cooperative length of about 440 dimers is found. At high concentration, evidence of clustered assemblies is found in agreement with the SANS and AFM results.

Single isolated cylinders are visualized by AFM at the surface having similar diameters and persistence lengths as in solution. The transfer of the single cylinders from solution to a solid support as isolated objects is one of the first examples of single organic fibers consisting of self-assembled chromophores. The details of the transfer process, described in Chapter 5, are important for the construction of devices and showed that the transfer is only possible when specific concentrations and specific solid supports are used. At higher concentrations, an intertwined network is formed, while, at low concentration, ill-defined globular objects are observed. Only inert substrates (graphite and siliconoxide) tolerate single fibers. In the case of the repulsive surfaces (mica and glass) clustering of the stacks occurs while at an attractive surface (gold) the stacks are destroyed. Fluorescence microscopy measurements on OPV fibrils on a graphite surface showed a polarized optical emission evidencing that the chiral organization and the orientation of OPV dimers in the stacks is preserved during deposition. The control of the internal order within self-assembled fibers, and the ability to measure it, is a crucial step forward to construct uniform organic fibers that can be applied in nanosized electronics. The fibers cover nanosized FETs electrode patterns, however, no current was measured. This is presumably the result of bad contact between the fiber and the electrodes and/or a low intrinsic charge carrier mobility. The morphology of bulk FET devices could be controlled by the solvent. Thick films of self-assembled fibers show a better charge carrier mobility in the order of 10^{-6} cm²/Vs in comparison with non self-assembled oligomers (10^{-7} cm²/Vs).

The presence of an aliphatic covalent linker between two OPV units resulted in disordered stacks. This behavior is presumably the outcome of a competition between favorable π - π interactions and restricted conformational freedom due to the linker. The length of these polymers as well as the chiral order in the assemblies can be controlled by the addition of chain-stoppers. Films with uniform domains containing rods of the OPVs were preserved when blended with a C₆₀ derivative. Stable photovoltaic devices, despite considerable phase separation, were made.

In Chapter 6, complementary hydrogen-bond interactions are used to selectively join electron donor (OPVs) and acceptor (perylenebisimide) units. The hydrogen-bonded complexes form well-ordered aggregates in apolar solvents. Based on cyclic voltammetry and transient absorption spectroscopy, fluorescence quenching of OPV and perylene in the assembly can be related to photo-induced electron transfer that takes place even in apolar solvents. The film morphology of the active layer on device-relevant substrates could be controlled by programmed self-assembly of the two components in solution resulting in supramolecularly positioned π -conjugated donor and acceptor building blocks. In such a way, ideal pathways for charge transport are created and ambipolar charge transport was demonstrated by the construction of field effect transistors.

Chapter 7 reports the formation of aggregates in alcohols of a series of α - α' penta(ethyleneoxide) functionalized oligothiophenes that vary in the number of thiophene rings, ranging from five to seven, and in the location of the stereocenter in the ethyleneoxide side chain. AFM and optical measurements show that the oligothiophenes form capsules with an H-type packing. The stability of the aggregates increases when the number of thiophene rings increases and when the stereocenter is further away from the thiophene segment. The chiral packing of the oligothiophenes was investigated by circular dichroism. The aggregation

of the thiophenes at the molecular level in an H-type helical fashion is present as domains in the capsules at the macroscopic level. The sign of the Cotton effect depends on the absolute configuration of the stereocenter. Furthermore, the sign of the Cotton effect showed an odd–even effect in the distance of the stereocenter to the π -conjugated segment. Moreover, the sign alternates going from the pentamer to the heptamer having the same side chain. A unique diastereomeric transition is revealed in the case of odd-numbered oligothiophenes. Analysis of this stereomutation shows that the transition is entropically driven. Such a stereomutation can be an elegant method for constructing two-state switchable materials. The capsules could be manipulated by a magnetic field into oblate spheroids which could be trapped in a gel-matrix.

The construction and properties of nanoscopic supramolecular architectures based on π -conjugated oligomers is of great scientific importance. When in such well-ordered chromophoric assemblies energy traps are incorporated, fundamental scientific issues such as light harvesting, exciton diffusion length and energy transfer processes can be investigated within nanometer dimensions. Furthermore, a detailed understanding of the process to build supramolecular structures from small organic molecules will be invaluable for investigating and designing biological complex structures. In addition, the concept of controlling the position of π -conjugated molecules in the solid state, either in single fibers or in the bulk (films), by programmed self-assembly in solution is in principle applicable to all kinds of π -conjugated oligomers, and provides an attractive approach to construct nanoscopic (fibers) or microscopic (films) electronic devices. Successful implementation of self-assembled π -conjugated systems in nanoscopic devices depends largely on the other layers and electrodes present in the devices. The design of such nanoscopic devices must be such that all components behave as inert surfaces towards self-assembled fibers. To increase the compatibility and simplify processability, it is a dream to self-assemble all components at once like nature does.

SAMENVATTING

Het succesvol gebruik van organische halfgeleiders in optisch–electronische toepassingen, zoals displays, transistoren en zonnecellen, is gedurende de laatste jaren aangetoond. Vele onderzoeksgroepen bestuderen het effect van de chemische structuur en de organisatie van deze functionele organische componenten op de efficiëntie van deze toepassingen. Het gebrek aan controle in het hiërarchisch structureren van kleine π –geconjugeerde moleculen tot goed geordende macroscopische films hindert de efficiëntie van zulke toepassingen.

Het doel van het werk dat in dit proefschrift staat beschreven is de voor–geprogrammeerde zelf–assemblage van π –geconjugeerde oligomeren tot architecturen op de nanometerschaal door gebruik te maken van verscheidene secundaire interacties tegelijkertijd, aldus het paradigma van de natuur volgend. Het construeren van zulke architecturen is niet alleen van belang voor plastic elektronica, maar ook voor het nieuwe veld van supramoleculaire elektronica. Dit relatief onbekende onderzoeksveld steunt op structuren met een gecontroleerde dimensie en vorm, bijv. draden; 5 nm in diameter en 100 nm lang. Een introductie tot dit onderzoeksveld wordt gegeven in Hoofdstuk 1.

Hoofdstuk 2 beschrijft de invloed van de hydrofobe/hydrofiele balans in een serie van chirale oligo(p–fenylenevinyleen) (OPV)s op de zelf–assemblage van deze moleculen in oplossing en in de vaste toestand. De OPV–bouwstenen leveren een verscheidenheid aan zelf–geassembleerde architecturen op, namelijk monolagen, staafjes, helische draden en vesikels, afhankelijk van de bereidingsmethode. De methode van het pre–organiseren van π –geconjugeerde oligomeren in oplossing resulteert in een waardevol instrument om de vorm van de aggregaten en daarmee ook de eigenschappen in de vaste toestand te sturen; de emissie van een enkele vesikel op een glasoppervlak is gelijk aan emissie van de vesikels in water. Een aantrekkelijke manier om de nano–architecturen te positioneren is de mogelijkheid zulke vesikels met optical tweezers te kunnen manipuleren.

Verhoogde controle over de positie van de bouwstenen in de zelf–geassembleerde objecten is verkregen door het introduceren van waterstofbrug interacties zoals beschreven in Hoofdstuk 3. De serie OPVs, gesubstitueerd met waterstofbrug vormende diaminotriazine groepen, zelf–assembleren tot dimeren of hexameren op grafiet zoals bestudeerd met scanning tunneling microscopy (STM). Zwakke interacties die de pakking van moleculen in een kristal bepalen, kunnen worden toegepast op de supramoleculaire organisatie in oplossing. Optische technieken en kleine hoek verstrooiing van neutronen (SANS) tonen de vorming van lange helische buisvormige aggregaten in apolaire oplossingen. De aggregaten zijn opgebouwd uit gestapelde rozetten. Deze aggregaten hebben een perfecte ruimtevulling en zijn oplosbaar dankzij de apolaire schil aan de buitenkant van het aggregaat. Deze aggregaten werden met behulp van atomic force microscopy (AFM) afgebeeld in de vaste toestand.

In Hoofdstuk 4 wordt de synthese van OPVs met verschillende conjugatielengte beschreven die een sterke zelf–complementaire waterstofbrugvormend motief dragen. De vorming van dimeren is bestudeerd met STM en NMR spectroscopie. SANS data laat de vorming van rigide cilindrische objecten zien. Cylinders van het tetrameer hebben een persistentielengte van 150 nm en een diameter van 6 nm. Het trimeer geeft rigide cilindrische domeinen van 90 nm met een diameter van 5 nm. Temperatuur en concentratie afhankelijke metingen laten zien dat de stabiliteit van de cylinders toeneemt met de conjugatielengte tengevolge van een meer gunstige π – π interactie. Gedetailleerde optische metingen die het

proces van zelf-assemblage volgen, hebben voor de eerste keer een gedetailleerd inzicht verschaft in de beschrijving van de zelf-assemblage; namelijk een nucleatie-elongatie aggregatie of cooperatieve zelf-assemblage. De initiële isodesmische associatie van de OPV dimeren in kleine pre-aggregaten gaat vooraf aan de snelle associatie tot lange helische aggregaten. De helix vorming is enthalpie-gedreven en een cooperatieve lengte van ongeveer 440 dimeren is gevonden. Bij hoge concentraties is de klustervorming van aggregaten zichtbaar in overeenstemming met de SANS en AFM resultaten.

Enkele geïsoleerde cilindres werden afgebeeld op het oppervlak met behulp van AFM. Deze structuren hebben dezelfde afmetingen als de structuren in oplossing. De overdracht van enkele cilindres van oplossing naar een vaste drager als geïsoleerde objecten is één van de eerste voorbeelden van een enkele organische draad die zelf-geassembleerde chromoforen bevat. De details van het overdrachtsproces, beschreven in Hoofdstuk 5, zijn belangrijk voor de constructie van nano-elektronica en laten zien dat de overdracht slechts mogelijk is wanneer specifieke concentraties en specifieke vaste dragers worden gebruikt. Bij hogere concentraties wordt een verweven netwerk gevormd, terwijl bij lagere concentraties slecht gedefinieerde objecten werden waargenomen. Alleen inerte substraten (grafiet en siliciumoxide) tolereren draden. In het geval van repulsieve oppervlakken (mica en glas), groeperen de draden zich terwijl op attractieve oppervlakken (goud) de draden zijn vernietigd. Fluorescentie microscopie metingen van de OPV draden op een grafiet oppervlak laten gepolariseerde optische emissie zien, hetgeen een bewijs is dat de chirale organisatie en de orientatie van de OPV dimeren in de draden gehandhaafd blijft tijdens het deponeren. De controle van de interne structuur in zelf-geassembleerde draden, en de mogelijkheid dit te meten, is een cruciale stap voorwaarts in de constructie van uniforme organische draden die kunnen worden toegepast in nano-elektronica. Hoewel de draden over een nanoscopisch transistor elektrode patroon zijn gelegd, is geen stroom gemeten. Dit is waarschijnlijk het resultaat van slecht contact tussen de draad en/of de elektroden of een lage intrinsieke geleiding. De film morfologie van bulk transistors kan worden gecontroleerd door de keuze van het oplosmiddel. Dikke films van zelf-geassembleerde draden lieten een beter gatentransport, met een mobiliteit van 10^{-6} cm²/Vs, zien in vergelijking met niet zelf-geassembleerde oligomeren.

De aanwezigheid van een alifatische covalente verbinding tussen twee OPVs resulteert in wanorderlijke stapels. Dit gedrag is waarschijnlijk het gevolg van de competitie tussen de gunstige π - π interacties en beperkte bewegingsvrijheid opgelegd door de verbinding. Zowel de lengte van deze polymeren als de chirale orde in deze aggregaten kan worden gecontroleerd door het toevoegen van ketenstoppers. Films met uniforme domeinen van OPV-draden zijn behouden gebleven in blends met een C₆₀ derivaat. Stabiele zonnecellen zijn gemaakt, ondanks de aanzienlijke fasescheiding.

In Hoofdstuk 6 zijn complementaire waterstofbrug interacties gebruikt om selectief elektron donoren (OPVs) en acceptoren (perylenebisimide) te verenigen. De waterstofbrug complexen vormen goed geordende aggregaten in apolaire oplosmiddelen. Gebaseerd op cyclische voltammetrie en tijdsafhankelijke absorptie spectroscopie kon de uitdoving van de fluorescentie worden gerelateerd aan foto-geïnduceerde elektronenoverdracht die zelfs plaatsvindt in apolaire oplosmiddelen. De morfologie van de actieve laag op relevante substraten voor optisch-elektronische toepassingen kan worden gecontroleerd door de geprogrammeerde zelf-assemblage van de twee componenten in oplossing resulterend in supramoleculair gepositioneerde π -geconjugeerde donor en acceptor bouwstenen. Op deze

manier worden ideale kanalen voor ladingstransport gecreëerd en ambipolair ladingstransport werd gedemonstreerd met het fabriceren van transistoren.

Hoofdstuk 7 rapporteert de vorming van aggregaten in alcoholen in een serie α - α' penta(ethyleenoxide) gefunctionaliseerde oligothiofenen die variëren in het aantal thiofeenringen, van vijf tot zeven, en in de lokatie van het stereocenter in de ethyleenoxide zijketen. AFM en optische metingen laten zien dat de oligothiofenen capsules vormen met een H-type pakking. De stabiliteit van de aggregaten neemt toe naarmate het aantal thiofeenringen toeneemt en wanneer het stereocenter verder weg staat van het thiofeensegment. De chirale pakking van de oligothiofenen werd bestudeerd met behulp van circulair dichroïsme. Waarschijnlijk is het op moleculair niveau aggregeren van de thiofenen in een H-type helisch pakking op macroscopisch niveau aanwezig als domeinen in de capsules. Het teken van het Cotton effect hangt af van de absolute configuratie van het stereocenter en verder liet het teken van het Cotton effect een even-oneven afhankelijkheid zien in de afstand van het stereocenter tot het π -geconjugeerde segment. Bovendien alterneert het teken gaande van het pentameer tot het heptameer met dezelfde zijketen. Een uniek diastereomere overgang is gevonden in het geval van oneven genummerde oligothiofenen. Analyse van deze stereomutatie laat zien dat de overgang entropisch gedreven is. Een dergelijke stereomutatie kan een elegante methode zijn voor de constructie van bistabiele schakelbare materialen. De capsules kunnen worden gemanipuleerd met magnetische velden tot afgeplatte bollen die kunnen worden ingesloten in een gel-matrix.

De constructie en eigenschappen van nanoscopische supramoleculaire architecturen gebaseerd op π -geconjugeerde oligomeren is van groot wetenschappelijk belang. Wanneer men erin slaagt energiefuiken te bouwen in dergelijke goed geordende aggregaten, kunnen fundamentele wetenschappelijke onderwerpen welke gerelateerd zijn aan de foto-synthese worden bestudeerd met nanoscopische precisie; te denken valt aan het invangen van licht, de exciton diffusielengte en energieoverdrachtsprocessen. Bovendien zal een gedetailleerd begrip van het opbouwproces van dergelijke supramoleculaire structuren, het ontrafelen en ontwerpen van biologische complexe structuren een stapje dichterbij brengen. Verder is het concept van de controle over positionering van π -geconjugeerde moleculen in de vaste toestand, in enkele draden ofwel in de bulk (film), door geprogrammeerde zelf-assemblage in oplossing in principe van toepassing op allerlei π -geconjugeerde oligomeren en voorziet in een aantrekkelijke benadering om nanoscopische (draden) of microscopische (films) elektronische toepassingen te fabriceren. Succesvolle implementatie van zelf-geassembleerde π -geconjugeerde systemen in elektronische toepassingen hangt grotendeels af van andere lagen en elektroden die aanwezig zijn. Het ontwerp van dergelijke nanoscopische toepassingen moet zodanig zijn dat alle componenten zich gedragen als inerte oppervlakken naar zelf-geassembleerde aggregaten. Om de verenigbaarheid te vergroten en de verwerkbaarheid te vereenvoudigen zou het een droom zijn alle componenten in een enkel proces te assembleren net zoals in de natuur plaats vindt.

CURRICULUM VITAE



Pascal Jonkheijm werd geboren op 12 juni 1978 te Hontenisse. Na de VWO-opleiding aan het Zeldenrust-Steelant College te Terneuzen werd in 1996 begonnen aan de studie Scheikundige Technologie aan de Technische Universiteit Eindhoven. Na een korte stage aan het Shell Research and Technology Centre te Louvain-la-Neuve (België) in het voorjaar van 2000, werd in augustus 2001 het afstudeerproject binnen de vakgroep Macromoleculaire en Organische Chemie afgerond. Vanaf september 2001 was hij werkzaam als promovendus in dezelfde vakgroep onder leiding van prof.dr. E. W. Meijer and dr. A. P. H. J. Schenning. Gedurende deze jaren lag zijn onderzoeksinteresse in de macromoleculaire engineering van π -geconjugeerde oligomeren met behulp van supramoleculaire interacties tot nanoscopische structuren. De belangrijkste resultaten van dit onderzoek, waarvan een gedeelte is uitgevoerd aan de universiteit van Leuven in samenwerking met prof.dr. F. De Schryver en dr. S. De Feyter, staan beschreven in dit proefschrift. Hij is een laureaat van de DSM awards voor chemie en technologie (2004).

Pascal Jonkheijm was born in Hontenisse, the Netherlands on June 12th, 1978. He attended the Zeldenrust-Steelant College where he obtained his VWO (pre-university education) degree. In 1996 he started to study Chemical Engineering and Chemistry at the Eindhoven University of Technology. After a short stay at the Shell Research and Technology Centre in Louvain-la-Neuve (Belgium) in spring 2000, he graduated in August 2001 after the graduation project at the laboratory of Macromolecular and Organic Chemistry. In September 2001, he started as a Ph.D. student in the same group with prof.dr. E. W. Meijer and dr. A. P. H. J. Schenning as advisors. During these years his research interest have been in macromolecular engineering of π -conjugated oligomers through supramolecular interactions into nanoscopic structures. The most important results of the research, part of which is performed at the University of Leuven in cooperation with prof.dr. F. De Schryver and dr. S. De Feyter, are described in this thesis. He is a laureate of the DSM awards for chemistry and technology (2004).

List of Publications

Jeukens, C. R. L. P. N.; Jonkheijm, P.; Wijnen, F. J. P.; Gielen, J. C.; Christianen, P. C. M.; Schenning, A. P. H. J.; Meijer, E. W.; Maan, J. C. *J. Am. Chem. Soc.* accepted.

Shklyarevskiy, I. O.; Jonkheijm, P.; Christianen, P. C. M.; Schenning, A. P. H. J.; Meijer, E. W.; Henze, O.; Kilbinger, A. F. M.; Feast, W. J.; Del Guerzo, A.; Desvergne, J.-P.; Maan, J. C. *J. Am. Chem. Soc.* **2005**, *127*, 1112-3.

Shklyarevskiy, I. O.; Jonkheijm, P.; Christianen, P. C. M.; Schenning, A. P. H. J.; Del Guerzo, A.; Desvergne, J.-P.; Meijer, E. W.; Maan, J. C. *Langmuir* **2005**, *21*, 2108-12.

Miura, A.; Jonkheijm, P.; De Feyter, S.; Schenning, A. P. H. J.; Meijer, E. W.; De Schryver, F. C. *Small* **2005**, *1*, 131-7

Hoeben, F. J. M.; Jonkheijm, P.; Meijer, E. W.; Schenning, A. P. H. J. *Chem. Rev.* **2005**, *105*, 1491-546.

- De Feyter, S.; Miura, A.; Yao, S.; Chen, Z.; Würthner, F.; Jonkheijm, P.; Schenning, A. P. H. J.; Meijer, E. W.; De Schryver, F. C. *Nano Lett.* **2005**, *5*, 77-81.
- Daniel, C.; Herz, L. M.; Westenhoff, S.; Makereel, F.; Beljonne, D.; Hoeben, F. J. M.; Jonkheijm, P.; Schenning, A. P. H. J.; Meijer, E. W.; Silva, C. *Chem. Phys.* **2005**, *79*, 281-3.
- Würthner, F.; Chen, Z.; Hoeben, F. J. M.; Osswald, P.; You, C.-C.; Jonkheijm, P.; van Herrikhuyzen, J.; Schenning, A. P. H. J.; van der Schoot, P. P. A. M.; Meijer, E. W.; Beckers, E. H. A.; Meskers, S. C. J.; Janssen, R. A. J. *J. Am. Chem. Soc.* **2004**, *126*, 10611-8.
- Schenning, A. P. H. J.; Jonkheijm, P.; Hoeben, F. J. M.; Van Herrikhuyzen, J.; Meskers, S. C. J.; Meijer, E. W.; Herz, L. M.; Daniel, C.; Silva, C.; Phillips, R. T.; Friend, R. H.; Beljonne, D.; Miura, A.; De Feyter, S.; Zdanowska, M.; Uji-I, H.; De Schryver, F. C.; Chen, Z.; Würthner, F.; Mas-Torrent, M.; Den Boer, D.; Durkut, M.; Hadley, P. *Synth. Met.* **2004**, *147*, 43-8.
- Leclère, P.; Surin, M.; Jonkheijm, P.; Henze, O.; Schenning, A. P. H. J.; Biscarini, F.; Grimsdale, A. C.; Feast, W. J.; Meijer, E. W.; Müllen, K.; Brédas, J. L.; Lazzaroni, R. *Eur. Polym. J.* **2004**, *40*, 885-92.
- Leclère, P.; Surin, M.; Lazzaroni, R.; Kilbinger, A. F. M.; Henze, O.; Jonkheijm, P.; Biscarini, F.; Cavallini, M.; Feast, W. J.; Meijer, E. W.; Schenning, A. P. H. J. *J. Mater. Chem.* **2004**, *14*, 1959-63.
- Hoeben F. J. M.; Herz L. M.; Daniel, C.; Jonkheijm, P.; Schenning A. P. H. J.; Silva, C.; Meskers S. C. J.; Beljonne, D.; Phillips R. T.; Friend R. H.; Meijer, E. W. *Angew. Chem. Int. Ed.* **2004**, *43*, 1976-9.
- Jonkheijm, P.; Miura, A.; Zdanowska, M.; Hoeben, F. J. M.; De Feyter, S.; Schenning, A. P. H. J.; De Schryver, F. C.; Meijer, E. W. *Angew. Chem. Int. Ed.* **2004**, *43*, 74-8.
- Jonkheijm, P.; Schenning, A. P. H. J.; Meijer, E. W. *Polym. Prepr.* **2004**, *91*, 131-2.
- Gesquière, A.; Jonkheijm, P.; Hoeben, F. J. M.; Schenning, A. P. H. J.; De Feyter, S.; De Schryver, F. C.; Meijer, E. W. *Nano Lett.* **2004**, *4*, 1175-9.
- George, S. J.; Ajayaghosh, A.; Jonkheijm, P.; Schenning, A. P. H. J.; Meijer, E. W. *Angew. Chem. Int. Ed.* **2004**, *43*, 3422-5.
- Daniel, C.; Herz, L. M.; Beljonne, D.; Hoeben, F. J. M.; Jonkheijm, P.; Schenning, A. P. H. J.; Meijer, E. W.; Phillips, R. T.; Silva, C. *Synth. Met.* **2004**, *147*, 29-35.
- van Hal, P. A.; Wienk, M. M.; Kroon, J. M.; Verhees, W. J. H.; Slooff, L. H.; van Gennip, W. J. H.; Jonkheijm, P.; Janssen, R. A. J. *Adv. Mater.* **2003**, *15*, 118-21.
- Miura, A.; Chen, Z.; Uji-i, H.; De Feyter, S.; Zdanowska, M.; Jonkheijm, P.; Schenning, A. P. H. J.; Meijer, E. W.; Würthner, F.; De Schryver, F. C. *J. Am. Chem. Soc.* **2003**, *125*, 14968-9.
- Masuda, M.; Jonkheijm, P.; Sijbesma, R. P.; Meijer, E. W. *J. Am. Chem. Soc.* **2003**, *125*, 15935-40.
- Kemerink, M.; van Duren, J. K. J.; Jonkheijm, P.; Pasveer, W. F.; Koenraad, P. M.; Janssen, R. A. J.; Salemink, H. W. M.; Wolter, J. H. *Nano Lett.* **2003**, *3*, 1191-6.
- Jonkheijm, P.; Hoeben, F. J. M.; Kleppinger, R.; Van Herrikhuyzen, J.; Schenning, A. P. H. J.; Meijer, E. W. *J. Am. Chem. Soc.* **2003**, *125*, 15941-9.
- Henze, O.; Fransen, M.; Jonkheijm, P.; Meijer, E. W.; Feast, W. J.; Schenning, A. P. H. J. *J. Polym. Sci., Part A: Polym. Chem.* **2003**, *41*, 1737-43.
- Gesquière, A.; Jonkheijm, P.; Schenning, A. P. H. J.; Mena-Osteritz, E.; Bäuerle, P.; de Feyter, S.; de Schryver, F. C.; Meijer, E. W. *J. Mater. Chem.* **2003**, *13*, 2164-7.

Daniel, C.; Herz, L. M.; Silva, C.; Hoeben, F. J. M.; Jonkheijm, P.; Schenning, A. P. H. J.; Meijer, E. W. *Phys. Rev. B* **2003**, *68*, 235212/1-/9.

Craig, M. R.; Jonkheijm, P.; Meskers, S. C. J.; Schenning, A. P. H. J.; Meijer, E. W. *Adv. Mater.* **2003**, *15*, 1435-8.

Bulle-Lieuwma, C. W. T.; van Gennip, W. J. H.; van Duren, J. K. J.; Jonkheijm, P.; Janssen, R. A. J.; Niemantsverdriet, J. W. *Appl. Surf. Sc.* **2003**, *203-204*, 547-50.

Schenning, A. P. H. J.; Jonkheijm, P.; Hofkens, J.; De Feyter, S.; Asavei, T.; Cotlet, M.; De Schryver, F. C.; Meijer, E. W. *Chem. Commun.* **2002**, 1264-5.

Schenning, A. P. H. J.; van Herrikhuyzen, J.; Jonkheijm, P.; Chen, Z.; Würthner, F.; Meijer, E. W. *J. Am. Chem. Soc.* **2002**, *124*, 10252-3.

Schenning, A. P. H. J.; Jonkheijm, P.; Peeters, E.; Meijer, E. W. *J. Am. Chem. Soc.* **2001**, *123*, 409-16.

Jonkheijm, P.; Fransen, M.; Schenning, A. P. H. J.; Meijer, E. W. *J. Chem. Soc., Perkin Trans. 2* **2001**, 1280-6.

